Astronomy & Astrophysics manuscript no. hrs˙photometry
December 5, 2012

Submillimetre Photometry of 323 Nearby Galaxies from the *Herschel*⋆ Reference Survey.

L. Ciesla[1], A.Boselli[1], M. W. L. Smith[2], G. J. Bendo[3], L. Cortese[4], S. Eales[2], S. Bianchi[5], M. Boquien[1], V. Buat[1], J. Davies[2], M. Pohlen[2], S. Zibetti[5,6], M. Baes[7], A. Cooray[8,9], I. de Looze[7], S. di Serego Alighieri[5], M. Galametz[10], H. L. Gomez[2], V. Lebouteiller[11], S. C. Madden[11], C. Pappalardo[5], A. Remy[11], L. Spinoglio[12], M. Vaccari[13,14], R. Auld[2], D. L. Clements[15].

[1] Laboratoire d'Astrophysique de Marseille - LAM, Université d'Aix-Marseille & CNRS, UMR7326, 38 rue F. Joliot-Curie, 13388 Marseille Cedex 13, France
[2] School of Physics and Astronomy, Cardiff University, Queens Buildings The Parade, Cardiff CF24 3AA, UK
[3] UK ALMA Regional Centre Node, Jodrell Bank Centre for Astrophysics, School of Physics and Astronomy, University of Manchester, Oxford Road, Manchester M13 9PL, United Kingdom
[4] European Southern Observatory, Karl Schwarzschild Str. 2, 85748 Garching bei Muenchen, Germany
[5] INAF-Osservatorio Astrofisico di Arcetri, Largo Enrico Fermi 5, 50125 Firenze, Italy
[6] Dark Cosmology Centre, Niels Bohr Institute University of Copenhagen, Juliane Maries Vej 30, DK-2100 Copenhagen, Denmark
[7] Sterrenkundig Observatorium, Universiteit Gent, Krijgslaan 281 S9, 9000, Gent, Belgium
[8] Department of Physics & Astronomy, University of California, Irvine, CA 92697, USA 10
[9] California Institute of Technology, 1200 E. California Blvd, Pasadena, CA 91125, USA
[10] Institute of Astronomy, University of Cambridge, Madingley Road, Cambridge CB3 0HA
[11] CEA/DSM/IRFU/Service d'Astrophysique, CEA, Saclay, Orme des Merisiers, Batiment 709, F-91191 Gif-sur-Yvette, France
[12] Istituto di Fisica dello Spazio Interplanetario, INAF, Via Fosso del Cavaliere 100, I-00133 Roma, Italy
[13] Dipartimento di Astronomia, Università di Padova, vicolo Osservatorio, 3, 35122 Padova, Italy
[14] Astrophysics Group, Physics Department, University of the Western Cape, Private Bag X17, 7535, Bellville, Cape Town, South Africa
[15] Astrophysics Group, Imperial College, Blackett Laboratory, PrinceConsort Road, London SW7 2AZ, UK

Received; accepted

ABSTRACT

The *Herschel* Reference Survey (HRS) is a guaranteed time *Herschel* key project aimed at studying the physical properties of the interstellar medium in galaxies of the nearby universe. This volume limited, K-band selected sample is composed of galaxies spanning the whole range of morphological types (from ellipticals to late-type spirals) and environments (from the field to the centre of the Virgo Cluster). We present flux density measurements of the whole sample of 323 galaxies of the HRS in the three bands of the Spectral and Photometric Imaging Receiver (SPIRE), at 250 μm, 350 μm and 500 μm. Aperture photometry is performed on extended galaxies and point spread function (PSF) fitting on timeline data for unresolved objects; we carefully estimate errors and upper limits. The flux densities are found to be in good agreement with those of the HeViCS and KINGFISH key projects in all SPIRE bands, and of the *Planck* consortium at 350 μm and 550 μm, for the galaxies in common. This submillimetre catalogue of nearby galaxies is a benchmark for the study of the dust properties in the local universe, giving the zero redshift reference for any cosmological survey.

Key words. Galaxies: ISM; Infrared: galaxies; Surveys; Catalogs

1. Introduction

Dust grains in the interstellar medium (ISM) of galaxies profoundly affect our view of these systems by absorbing the ultraviolet (UV) and optical stellar emission and re-emitting it in the infrared, from ∼5 μm to ∼1 mm. Dust is produced by the aggregation of metals injected into the interstellar medium by massive stars, through stellar winds (Höfner 2009; Gomez et al. 2010b), supernovae (Clayton et al. 1997; Bianchi & Schneider 2007; Matsuura et al. 2011; Gomez et al. 2012), or less massive stars in their final evolution stages, such as asymptotic giant branch stars (Gehrz 1989; Dwek 1998; Galliano et al. 2008). Generally intermixed with gas in the ISM, dust is thus a good tracer of the cold molecular and atomic phases of the ISM and contains a significant fraction of metals. Dust plays an important role in the interstellar medium as it acts as a catalyst in the transformation process of the atomic to molecular hydrogen, shields the UV radiation field preventing the dissociation of molecular clouds, and contributes to the cooling and heating of the ISM in photodissociation regions (Wolfire et al. 1995). The 5-70 μm spectral range corresponds to the emission of the hot dust generally associated with star formation whereas at longer wavelengths, up to ∼1mm, the submillimetre emission is generally dominated by the emission from the cold dust (e.g. Bendo et al. 2010, 2012a; Boquien et al. 2011). *IRAS* (Neugebauer et al. 1984), *COBE* (1989), *ISO* (Kessler et al. 1996), *Spitzer* (Werner et al. 2004), and *AKARI* (Murakami et al. 2007) allowed us to study the emission of the dust up to 240 μm. However, most of the cold dust emission is drowned by warm dust at wavelengths shorter than 240 μm.

⋆ *Herschel* is an ESA space observatory with science instruments provided by European-led Principal Investigator consortia and with important participation from NASA.

An accurate determination of dust masses requires submillimetre data (Devereux & Young 1990; Gordon et al. 2010; Galametz et al. 2011; Bendo et al. 2012a). Ground-based facilities, such as SCUBA on *JCMT* (Holland et al. 1999), reveal the submillimetre domain but observations of large samples of normal galaxies such as ours is still prohibitive due to the long integration times needed for these instruments. The *Herschel* Space Observatory (Pilbratt et al. 2010), launched in May 2009, opens a new window on the far-infrared/submillimetre spectral domain (55 to 672 μm) and allows us to probe the cold dust component in large numbers of nearby galaxies.

To characterize the dust properties in the local universe, the Spectral and Photometric Imaging Receiver (SPIRE) (Griffin et al. 2010) Local Galaxies Working Group (SAG 2) has selected 323 galaxies to be observed as part of the *Herschel* Reference Survey (HRS) (Boselli et al. 2010b). The HRS is a guaranteed time key project and a benchmark study of dust in the nearby universe. The goals of the survey are to investigate (i) the dust content of galaxies as a function of Hubble type, stellar mass and environment, (ii) the connection between the dust content and composition and the other phases of the interstellar medium, and (iii) the origin and evolution of dust in galaxies. The HRS spans the whole range of morphological types including ellipticals to late-type spirals, with a few irregular dwarf galaxies, and environments (from relatively isolated field galaxies to members of the core of the Virgo Cluster). The sample is ideally defined also because of the availability of a large set of ancillary data. Multiwavelength data, from the literature, are available for about 90% of HRS galaxies from *IRAS* (Sanders et al. 2003; Moshir & et al. 1990; Thuan & Sauvage 1992; Soifer et al. 1989; Young et al. 1996); optical and near-infrared from SDSS (Abazajian et al. 2009) and 2MASS (Jarrett et al. 2003), and radio from NVSS (Condon et al. 1998) and FIRST (Becker et al. 1995). Most of these data are available on NED and GOLDMine (Gavazzi et al. 2003). Some of them are already released or currently analysed by our team such as UV data from *GALEX* (Boselli et al. 2011, Cortese et al., submitted), *Spitzer*/IRAC (Ciesla et al., in prep), and *Spitzer*/MIPS (Bendo et al. 2012b). Hα imaging (Boselli et al., in prep), CO(J=1-0) spectroscopy (Boselli et al., in prep), optical integrated spectroscopy (Boselli et al., submitted), CO(J=3-2) *JCMT* mapping (Smith et al. in prep), and gas metallicities (Hughes et al. 2012, submitted) will be soon available.

The first scientific results, based on a subsample of HRS data obtained during the Science Demonstration Phase (SDP) data, were presented in the A&A *Herschel* Special Issue (2010). Statistical studies based on this data set investigate the far-infrared/submillimetre colours (Boselli et al. 2012), the dust scaling relations as a function of environment and galaxy type (Cortese et al. 2012), and the properties of the early-type galaxies in the sample (Smith et al. 2012). A preliminary analysis of the spectral energy distributions (SEDs) was done as part of the SDP (Boselli et al. 2010a) while the complete analysis and modelling of the SEDs of the whole sample is in preparation (Ciesla et al., in prep). Thanks to the high angular resolution of *Herschel* ($\sim$18$''$ at 250 μm, leading to a resolution of a few kpc at 20 Mpc), studies of large resolved HRS galaxies (with angular sizes between 2$'$ and 10$'$) within kiloparsec-sized subregions are also possible (Bendo et al. 2012a; Boquien et al. 2012).

The aim of this paper is to present the HRS catalogue of the flux densities at 250, 350 and 500 μm. The paper is organised as follows. In Section 2, we briefly describe the HRS sample. Section 3 gives the description of the *Herschel*/SPIRE observations and data reduction. Section 4 details the techniques used for the flux extraction. In Section 5, we provide flux densities of the whole sample and in Section 6, we compare our results to those available in the literature.

2. The sample

The HRS galaxies are selected according to several criteria fully described in Boselli et al. (2010b). The HRS is a volume limited sample composed of galaxies at a distance between 15 and 25 Mpc. The galaxies are selected according to their K band magnitude, whose luminosity is a proxy for the total stellar mass (Gavazzi et al. 1996). Based on the optical extinction studies and far-infrared observations at wavelength shorter than 200 μm, we expect late-type galaxies to have a larger content of dust than early-types (Sauvage & Thuan 1994). Thus, two different K_{mag} limits have been adopted: $K_{mag} \leq$12 for late-types and $K_{mag} \leq$8.7 for early-types (in Vega magnitudes). Finally, to limit any contamination from Galactic cirrus, we selected galaxies at high Galactic latitude ($b > +55$ deg) and with low Galactic extinction regions ($A_B < 0.2$ Schlegel et al. 1998). The final sample contains 323[1] galaxies, 62 early-types and 261 late-types.

3. *Herschel*/SPIRE observations and data reduction

3.1. Observations

We observed the 323 HRS galaxies with SPIRE (Griffin et al. 2010) in three wide bands at 250, 350 and 500 μm. In order not to duplicate *Herschel* observations, 79 galaxies out of 323 were observed as part of the open time key project the *Herschel* Virgo Cluster Survey (HeViCS, Davies et al. 2010).

For the 239 galaxies outside the Virgo cluster plus 4 Virgo galaxies observed during the Science Demonstration Phase, the observations are carried out using the SPIRE scan-map mode with a nominal scan speed of 30$''$s^{-1}. The sizes of the images depend on the optical extent of the targets and have been chosen to cover 1.5 times the optical diameter, D_{25}[2], of the galaxies, which is the full area over which the infrared emission is expected. Previous observations of spiral discs indeed indicated that the infrared emission of late-type galaxies can be more extended than the optical disc (Bianchi et al. 2000). For galaxies with an optical diameter smaller than $\sim$ 3$'$, the small scan-map mode is used to provide a homogeneous coverage of a circular area of $\sim$ 5$'$ diameter. For galaxies with an optical diameter larger than $\sim$ 3$'$, the large scan-map mode is used to cover, at least, $1.5 \times D_{25}$. The resulting sizes of the maps are thus 8$' \times$ 8$'$, 12$'\times$12$'$, and 16$'\times$16$'$, depending on the optical size of the target. As early-type galaxies are known to contain less dust than late-types (Ferrarese et al. 2006), longer integration times were used on this subsample (Smith et al. 2012). For late-types, 3 pairs of cross-linked scan maps are made, while 8 pairs for early-types.

HeViCS covers 55 deg^2 at full depth (84 deg^2 in total), of the centre of the Virgo cluster at five wavelengths, from 100 to 500 μm, using the PACS/SPIRE parallel mode, down to the confusion limit in the SPIRE bands (Davies et al. 2012). For the 79 HRS galaxies observed by HeViCS, the PACS/SPIRE parallel mode scan map is used with a scan speed of 60$''$ s^{-1} done with 4 pairs of perpendicular scans. Regions around each of the 79 galaxies are cut off from the large fields to perform the aperture

[1] With respect to the original sample given in Boselli et al. (2010b), the galaxy HRS 228 should be removed from the complete sample because its updated redshift on NED indicates it as a background object.

[2] The diameter at 25 mag arcsec^{-2}.

photometry. They are large enough to provide a good estimate of the background emission.

3.2. Data reduction

The complete description of the data reduction and map-making procedures will be presented in a dedicated paper by Smith et al. (in prep). Here, we just give a brief summary of the different steps carried out within the *Herschel* Interactive Pipeline Environment software (HIPE; Ott 2011). The SPIRE data are processed up to Level-1, the level where the pointed photometre timelines are derived, with a script adapted from the official scan map pipeline (Griffin et al. 2009; Dowell et al. 2010). The only difference to the Level-1 product is that we use the optimised deglitcher setting available for the observing mode. The typical SPIRE pipeline performs the following data processing steps on the timelines:

1. Application of the glitch removal procedure to delete the cosmic rays that affect all detectors in an individual array, and then application of the wavelet glitch removal of cosmic rays from individual detectors (WaveletDeglitcher) for HRS data. For HeViCS data, the sigmaKappaDeglitcher is used.
2. Application of an electrical low pass filter response correction, to correct for the delay in the data coming out of the electronics; this matches the detector timelines to the astrometric pointing timelines.
3. Reapplication of the wavelet glitch removal for the HRS data; this additional step improves the removal of all glitches.
4. Application of an additional time response correction.
5. Flux calibration, which includes nonlinearity corrections.
6. Removal of the temperature drift where all bolometers are brought to the same level using a custom method called BriGAdE (Smith et al. in prep).
7. Corrections of the bolometer time response, which adjusts the bolometer detector timelines to account for the fact that the bolometers do not respond instantaneously to signal.
8. Creation of the final maps using the naive map maker included in the standard pipeline.

The pipeline also performs some steps related to associating the astrometry with the bolometer timeline data and performs some minor time corrections before the mapmaking step.

The pixel sizes and FWHM values of the final maps are provided in Table 1. By default, the pipeline applies a correction to the maps, called K_4p, that converts the flux densities weighted by the relative spectral response function (RSRF) in monochromatic flux densities, corresponding to spectra where νS_ν is constant. In doing this, the pipeline considers all sources as point-like objects. However, the RSRF changes for extended sources, so we need to divide the data by the K_4p for point sources, automatically applied by the pipeline, and apply the K_4e for extended sources instead. For such extended sources, the resulting correction is thus K_4e/K_4p, and their values are provided by the SPIRE Observer Manual[3]. There are, in our sample, galaxies which are almost point-like that would not need this K_4[4] correction. Defining if a source is barely resolved can be subjective, thus for clarity, we defined two groups: one for point-like sources, one for extended sources using a quantitive criterion (see Section 4.1). We apply this K_4 correction for extended sources on all resolved galaxies of the HRS sample.

To update the maps product for the present work to the latest calibration (HIPE v8, SPIRE calibration tree v8.1), we multiply all 350 μm measurements by 1.0067, the most recent flux calibration (SPIRE photometry cookbook[5], Bendo et al. 2011). These corrections are listed in Table 1, we define the total correction $corr_\lambda$ as the combination of correction for extension (K_4) and the correction for updated calibration.

3.3. Colour corrections

The SPIRE flux calibration assumes that the sources have a spectrum with νS_ν constant across the filter. This assumption does not correspond to the SEDs of the objects observed (Boselli et al. 2010a). The observed SEDs of the target galaxies are close to a modified black body with a spectral index ranging from $\beta \sim 1.0$ to 2.0 (Boselli et al. 2012). Tuned colour corrections could thus be required. To quantify these colour corrections, we assume that the far-infrared spectrum can be farely well represented by a modified black body with a spectral index β of 1.5 or 2.0 Table 2 lists the colour corrections that should be applied for different sets of β and T. They were obtained by integrating a modified blackbody of given β and T over the SPIRE spectral response function for each band. For extended sources, the spectral response functions have been weighted by λ^2 (SPIRE Observer Manual) thus resulting in different sets of colour corrections for extended sources with respect to point sources. Indeed, for feedhorn bolometers in general and for the detectors in SPIRE specifically, the relative spectral responsivity function (RSRF) changes between point-like and extended sources as explained in Section 5.2.1 of the SPIRE Observers' Manual. The colour corrections rely upon the integral of the product of the spectrum and the RSRF, then if the RSRF changes, the colour corrections will also change. We give the values for both point-like and extended sources. They are multiplicative corrections. Given the still poorly constrained shape of the SED of the target galaxies, these corrections listed in Table 2 are not applied to the set of data given in Table A.2.

4. Flux extraction

As we chose long integration times in order to reach the confusion limit, the images include faint background sources. Furthermore, despite a high Galactic latitude selection, some images show the presence of Galactic cirrus. Our sample contains large extended galaxies, point-like sources and non-detected galaxies. These technical aspects, related to the nature of the emitting source and of the sky background emission around it, prevent us from performing an automatic photometry. Three methods are needed to accurately measure the flux for all of objects: a first method for point-like sources (PSF fitting on timeline data), a second for extended ones (aperture photometry) and the third for the determination of upper limits.

4.1. Point-like sources

SPIRE is calibrated using a timeline-based PSF fitting approach. It is then possible to extract the flux densities of point-like sources directly from the timeline data using a PSF fitting method. The PSF fitter fits a two-dimensional Gaussian function

[3] http://herschel.esac.esa.int/Docs/SPIRE/html/spire_om.html

[4] For simplicity, here we define K_4=K_4e/K_4p, for the exact definition refer to the SPIRE Observer Manual

[5] http://herschel.esac.esa.int/twiki/pub/Public/SpireCalibrationWeb/SPIREPhotometryCookbook_jul2011_2.pdf

Table 1: Summary of the properties of SPIRE image data.

	250 μm	350 μm	500 μm
Pixel size ($pixsize_\lambda$)	6″	8″	12″
Map FWHM	18.2″	24.5″	36.0″
Beam area ($beam_\lambda$)	423 arcsec^2	751 arcsec^2	1587 arcsec^2
Correction for extension (K_4)	0.98279	0.98344	0.97099
Correction for updated calibration	1.	1.0067	1.
Total correction ($corr_\lambda$)	0.98279	0.99003	0.97099

Table 2: The colour corrections for the SPIRE data for extended and point-like sources.

		Extended			Point like		
		250 μm	350 μm	500 μm	250 μm	350 μm	500 μm
$\beta = 2$	$T = 10K$	1.026	1.025	1.044	1.023	0.995	0.959
	$T = 15K$	1.019	1.009	1.021	0.984	0.959	0.917
	$T = 20K$	1.005	0.996	1.007	0.955	0.938	0.896
	$T = 25K$	0.994	0.988	0.999	0.937	0.925	0.884
	$T = 30K$	0.985	0.983	0.994	0.924	0.917	0.876
$\beta = 1.5$	$T = 10K$	1.021	1.025	1.049	1.026	1.004	0.977
	$T = 15K$	1.022	1.014	1.031	0.995	0.972	0.940
	$T = 20K$	1.011	1.004	1.020	0.970	0.953	0.920
	$T = 25K$	1.002	0.998	1.014	0.953	0.942	0.909
	$T = 30K$	0.995	0.993	1.009	0.941	0.934	0.902
	$T = 35K$	0.990	0.990	1.006	0.933	0.929	0.897
	$T = 40K$	0.986	0.987	1.003	0.926	0.925	0.893
	$T = 45K$	0.983	0.985	1.001	0.922	0.922	0.890
	$T = 50K$	0.981	0.984	1.000	0.918	0.919	0.888

Notes. Multiplicative factors to apply to correct values for galaxies with spectral energy distributions well represented by a modified black body with a grain emissivity parameter β and a temperature T in the given ranges. Color corrections for $\beta = 2$ and $T = 15, 20, 25K$, are consistent with those given in Davies et al. (2012); in that paper, however, the K_4 correction is included in the color correction for extended sources, while here it is included in the fluxes.

to the signal and position timeline data. For unresolved sources, the peak of the Gaussian function from the fit corresponds to the flux density of the source. For more information, see Bendo et al. (2012, in prep). Based on tests of aperture photometry versus timeline-based PSF fitting for SPIRE data, there is significantly worse accuracy and precision for aperture photometry on unresolved sources. Moreover, there are some systematic effects that are actually due to the mapping technique (related to where bolometers tend to cross over the unresolved sources). Timeline-based PSF fitting actually avoids those biases for point sources. The SPIRE-ICC (Instrument Control Center) strongly recommends the use of PSF fitting on timeline data for unresolved sources (SPIRE Observer's Manual[6] Section 5.2.11).

To identify point-like sources and measure their flux densities, we proceed with the following method. All of the images are inspected in order to make a list of point-like sources candidates. We run the timeline-based PSF fitter program and use the criterion given by the SPIRE photometry cookbook. For a given band, if the FWHM of the resulting gaussian fitted to the timeline data is smaller than 20″, 29″and 37″at 250, 350 and 500 μm, respectively, then the source is considered as point-like. These limits for the FWHM were determined empirically by adding artificial randomly-placed sources to timeline data and then performing timeline-based PSF fits to those data. The resulting distribution of FWHM indicates that 20″, 29″and 37″are acceptable upper limits for the typical FWHM that will be measured for sources. According to this criterium, in the whole HRS sample, there are 10, 10 and 9 point-like sources at 250, 350 and 500 μm, respectively. As the timeline data are calibrated in Jy/beam, the timeline fits for these data give amplitudes that correspond to the flux densities of the sources. These will be the most accurate flux densities that can be measured for these sources, as the measurement technique matches the method applied to the primary and secondary sources used for SPIRE flux calibration. As the pipeline is optimised for point sources, their flux densities do not need to be corrected with the K_4 correction described in Section 3.2 and provided in Table 1. However, the 350 μm measurements are corrected for the HIPE v8 updated calibration, thus they are multiplied by 1.0067.

4.2. Extended sources

The aperture photometry of extended sources is carried out using the DS9/Funtools program "Funcnts". This task performs a basic aperture photometry, summing all pixels within a defined elliptical region. The mean value of the background is calculated in a given annulus and then subtracted from the counts of the aperture. With "Funcnts", we can extract the counts in elliptical regions adapted to match the shape of the galaxies.

To understand and quantify the contribution of background features in the measurements, we choose three different objects as representative examples, as illustrated in Figure 1. There are three extreme cases. The first one is M99 (HRS 102) which is a bright resolved face-on spiral. The second one is NGC 3945 (HRS 71), a nearly face-on barred spiral, lying in a region polluted by a strong cirrus emission. The last one is NGC 4550 (HRS 210), an unresolved faint early-type galaxy. This source is treated as all point-like sources, but we choose to include it as a comparison with the two previous extended galaxies.

[6] http://herschel.esac.esa.int/Docs/SPIRE/html/spire_om.html

Different growth curves are obtained when the background is estimated in different regions, as depicted in Figure 1. Here the different growth curves (colored lines) are obtained when the sky background is estimated in annuli of constant width of 60″ but of 30″ increasing radii. M99 (HRS 102) is a prototypical case with no particular problems since its growth curve reaches a plateau. Indeed, M99 is very bright, thus its flux density is not affected by faint background sources at large radii. On the contrary, the presence of Galactic cirrus strongly affects the flux density measurements, as for NGC 3945 (HRS 71). In this case, the growth curves do not saturate after a given radius. The curves of NGC 4550 (HRS 210) clearly show the contribution of background features at radii greater than $0.3 \times a_{opt}$, where a_{opt} is the optical semi major axis taken from NED. Furthermore, as NGC 4550 (HRS 210) is in a crowded field, several background sources contribute to any background region chosen. The HRS sample is composed of galaxies of different properties such as those shown in Figure 1. It is thus clear that a standard, automatic procedure cannot be blindly applied for the extraction of the flux densities of all the sources. We thus need to define appropriate apertures for each object.

To define the apertures, we apply two different methods, one for the extended sources, mainly late-type galaxies, and another one for resolved but compact object, generally early-types. We inspect the infrared images and compare them with the optical ones. For most of the late-types, the infrared disk is more extended than its optical counterpart. We find that taking an elliptical diameter of 1.4 times the optical one is large enough to contain all the infrared emission of these galaxies. However, in some particular cases, this standard aperture needs to be adapted, especially for galaxies which are interacting, galaxies with a companion or a strong background source within the standard aperture. For instance, HI-deficient[7] spiral galaxies of the Virgo cluster have truncated dust disks (Cortese et al. 2010). Furthermore, edge-on spirals have an optical semi-minor axis b_{opt} very small and $1.4 \times b_{opt}$ is not large enough to include the extended structure due to the side-lobes of the SPIRE beams (a typical example is NGC 4565-HRS 213 in Figure A.2). We thus modify the ellipticity of edge-on galaxies of the aperture to include all the infrared emission.

Elliptical galaxies, even if resolved, have a faint compact infrared emission concentrated in the center. Lenticulars are the intermediate type between ellipticals and spirals. They contain extended dust but generally not beyond the optical emission. For all of these galaxies, the apertures are adapted to match the emission and avoid any major background contamination.

For all galaxies, the background contribution is measured in a region defined as a circular annulus of inner radius $1.55 \times a_{opt}$, with a 60″ width. This choice is dictated by the fact that we want to quantify any possible contribution of large scale fluctuations in the sky background on source, but at the same time extract flux densities sufficiently far from the target to avoid any contamination of the galaxy to the sky background estimate. The width of the annulus is taken as a good compromise between the will of having a reliable statistic to estimate the background, and the will of avoiding as much as possible contamination from background sources and images features. We performed a detailed check on every background region to avoid or minimize any kind of source contamination (companion galaxy, strong background sources, etc).

[7] The HI-deficiency is defined as the difference, in logarithmic units, between the HI mass expected from an isolated galaxy with the same morphological type and optical diameter and the observed HI mass (Haynes et al. 1984).

Table 3: Median, mean and chosen infrared to optical aperture ratios of detected galaxies according to their morphological type.

	Median ratio	Mean ratio	Chosen ratio
E	0.38	0.29	0.30
S0, S0a, S0/Sa	0.76	0.88	0.80
Late-types	1.40	1.41	1.40

Notes. The chosen ratios are used to calculate upper limits of sources not detected with SPIRE.

The ellipses used for the aperture photometry and the circular annuli used for the background estimation are listed in Table A.1, organized as follows:

- Column 1: *Herschel* Reference Survey name (HRS).
- Column 2: Zwicky name, from the Catalogue of Galaxies and of Cluster of Galaxies, (Zwicky et al. 1968, CGCG).
- Column 3: Virgo Cluster Catalogue name, (Binggeli et al. 1985, VCC).
- Column 4: Uppsala General Catalogue name, (Nilson 1973, UGC).
- Column 5: New General Catalogue name, (Dreyer 1888, NGC).
- Column 6: Index Catalogue name, (Dreyer 1895, IC).
- Column 7: Right Ascension J2000 (RA).
- Column 8: Declination J2000 (Dec).
- Column 9: Semi major axis of the aperture, in arcseconds (a_{IR}).
- Column 10: Semi minor axis of the aperture, in arcseconds (b_{IR}).
- Column 11: Position Angle, in degree (PA) (from North to East).
- Column 12: Inner radius of the background circular annulus, in arcseconds (r_{in}^{bck}).
- Column 13: Outer radius of the background circular annulus, in arcseconds (r_{out}^{bck}).

Figure A.2 shows the optical and infrared images of the HRS galaxies, along with the apertures used. Table 3 gives the mean and median infrared to optical aperture diameter ratios for elliptical, lenticular and late-type galaxies respectively, where the infrared diameter is the one listed in Table A.1.

4.3. Aperture correction

As defined in Section 4.2, these apertures have been expressly chosen to include all of the infrared emission of the galaxies. Studying the emission of extended galaxies observed with *Herschel*, Dale et al. (2012) have shown that, at low surface brightness, the shape of the PSF can affect the emission at the edge of any object. They empirically defined the aperture correction as the ratio between the flux density measured on the IRAC 8.0 μm unsmoothed image, and the flux density measured on the same image smoothed to a *Herschel* band PSF. They found a median value of 1.0 at all wavelengths, with maximum corrections between 7% and 13% for SPIRE. To quantify the effect of the wings of the PSF on our measurements, and understand whether a specific correction is required, we do the following exercise. The maximal effect is expected for an extended galaxy with a flat radial profile and a sharp edge at 500 μm. We create a mock galaxy on an image with the *Herschel*

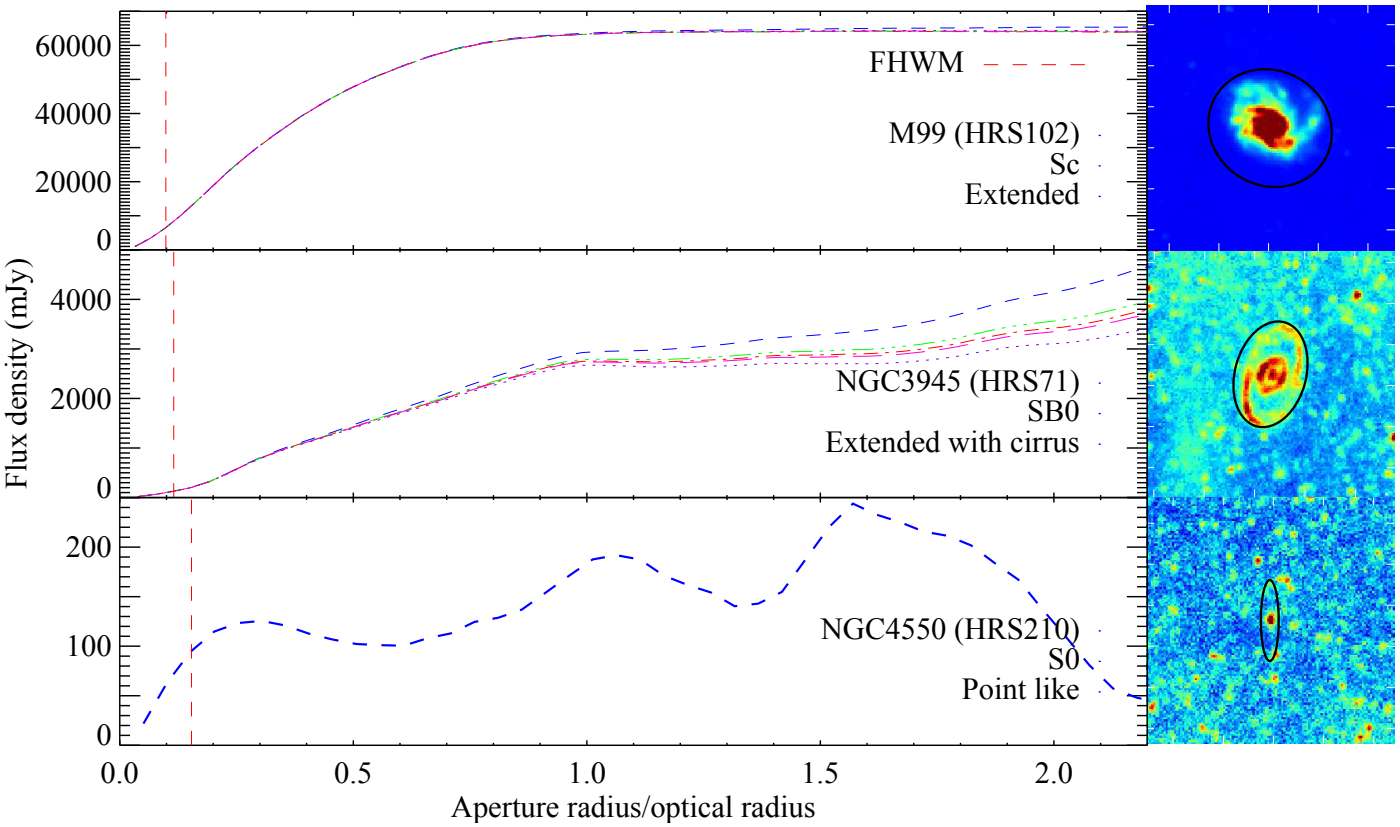

Fig. 1: Growth curves at 250 μm of the galaxies M 99 (HRS 102), NGC 3945 (HRS 71), and NGC 4550 (HRS 210). The different colored curves are obtained by changing the background estimate region as described in the text. The vertical red dashed lines correspond to the FWHM of the SPIRE beam at 250 μm. The right panels show the 250 μm images of the three galaxies, the black ellipses indicate the optical shapes of the galaxies.

500 μm resolution, and with a constant surface brightness of 1 Jy beam^{-1} dropping to 0 at a radius of 204″. Using the 500 μm PSF provided by Sibthorpe et al.[8], we convolve the mock galaxy with the SPIRE 500 μm PSF. We carry out the photometry using circular apertures from 12″ to 480″ in steps of 12″ on both the original and convolved images (Figure 2). The largest aperture correction is $\sim$ 5% at the radius of the original source (204″). For a linear decreasing surface brightness profile, more physical but still extreme, the correction drops to $<$ 2%. These 2%-5% corrections can be considered as an upper limit for our data because: i) a flat radial profile is quite unphysical and ii) our apertures have been expressly chosen larger than the infrared size of the galaxies. As we always choose the aperture greater than the infrared emission of the galaxy (except for galaxies in particular configurations like NGC 4567-HRS 215 and NGC 4568-HRS 216), the aperture correction is thus much smaller than $<$ 2%. As the calibration errors ($\sim$7%) are greater than the aperture corrections, we choose not to apply them on our measurements and consider our flux densities as integrated values.

4.4. Photometric uncertainties

There are two sources of uncertainty when carrying out photometry on SPIRE images, the systematic errors due to the absolute flux calibration and the stochastic errors related to the flux extraction technique. The calibration errors are (1) the uncertainty on the models used to determine the flux density of Neptune (5%), (2) a 2% random uncertainty that is measured from the standard deviation in the ratio of the measured Neptune flux density to the model Neptune flux density. The resulting calibration error is 7% in all bands (Swinyard et al. 2010; SPIRE Observer's Manual). Technically, the errors should add together quadratically, but the SPIRE team decided to use 7% as a conservative upper limit on the flux calibration. As the methods used for point-like and extended source photometry are different, the stochastic error estimation is computed in different ways.

4.4.1. Point-like sources

The uncertainty for point-like sources is calculated by performing tests in which artificial point sources with the same flux density as the target were added to the timeline data at random locations within a 0.3 deg box centered on each source. The artificial sources were then fit with the timeline-based source fitter using the same settings as were applied to each target galaxy. A hundred iterations of adding artificial sources to the fields around each galaxy were performed, and the standard deviation of the flux densities of the artificial sources was used as the uncertainty in the flux density measurement of the target galaxy. The highest value of the point-like source errors is 5 mJy for sources with a flux density less than 200 mJy.

[8] ftp://ftp.sciops.esa.int/pub/hsc-calibration/SPIRE/PHOT/Beams/

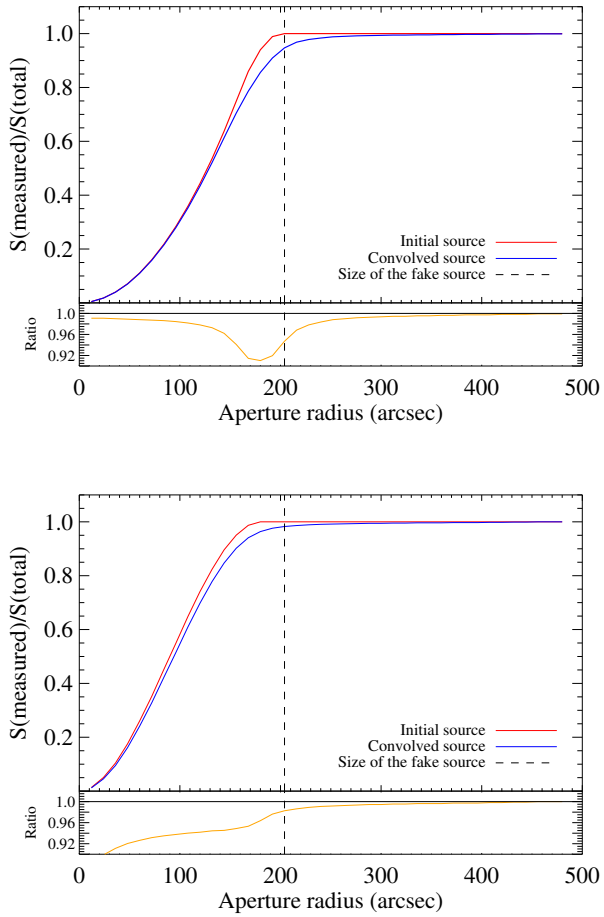

Fig. 2: Simulation of the photometry of an extended face-on spiral galaxy at 500 μm. Upper panel: a flat extended source. In red, the integrated radial profile of the original source, and in blue of the convolved source. In orange, the convolved to original source flux density ratios. The dashed line marks the size of the original source. Lower panel: an extended galaxy with a linear surface brightness profile.

4.4.2. Extended sources

For aperture photometry of extended sources, the stochastic total error, $err_{\rm tot}$, depends mainly on (1) the instrumental error, $err_{\rm inst}$, (2) the confusion error, $err_{\rm conf}$ and (3) the error on the determination of the sky background, $err_{\rm sky}$. We calculate the errors on our flux density measurements according to the formula:

$$err_{\rm tot} = \sqrt{err_{\rm inst}^2 + err_{\rm conf}^2 + err_{\rm sky}^2}, \quad (1)$$

The instrumental error: $err_{\rm inst}$

The instrumental error is due to the noise of the instrument which depends on the number of scans crossing a pixel. Assuming it independent from pixel to pixel, the instrumental error is:

$$err_{\rm inst} = \sqrt{\sum_{\rm i=1}^{N_{\rm pix}} \sigma_{\rm inst,i}^2}, \quad (2)$$

where $N_{\rm pix}$ is the number of pixels within the aperture and $\sigma_{\rm inst}$ is the pixel per pixel uncertainty measured in the aperture on the error map provided by the pipeline. Mean values of $err_{\rm inst}$ are 1.2%, 1.4% and 2.4% of the total flux density at 250, 350 and 500 μm, respectively.

The confusion error: $err_{\rm conf}$

The confusion error is due to the presence of background sources (i.e. faint point-like sources) within the aperture. As the beam size is larger than the pixel size, this uncertainty is correlated between neighboring pixels. A point-like background source will then affect several pixels. The confusion error is:

$$err_{\rm conf} = \sigma_{\rm conf}^{\lambda} \times \sqrt{\frac{N_{\rm pix} \times pixsize_{\lambda}^2}{beam_{\lambda}}}, \quad (3)$$

where $\sigma_{\rm conf}^{\lambda}$ is the confusion noise. Here, we assume the values estimated by Nguyen et al. (2010), i.e. 5.8, 6.3 and 6.8 mJy/beam at 250, 350 and 500 μm respectively. The pixel size of the images $pixsize_{\lambda}$ and the beam area $beam_{\lambda}$ are given in Table 1. Mean values of $err_{\rm conf}$ are 4.2%, 5.8% and 9.2% of the total flux density at 250, 350 and 500 μm, respectively. They are thus dominant with respect to the instrument noise.

The background error: $err_{\rm sky}$

The uncertainty on the sky background comes from large scale structures not removed during the map-making procedure. These large scale structures, for instance, can be due to Galactic cirrus, as those evident in Figure 1 of Davies et al. (2012) in the Virgo Cluster. Indeed, despite the fact that the galaxies are selected at high Galactic latitude, some images are contaminated by cirrus (see Figure 1). They contribute to the galaxy emission and/or to the background determination. To determine $\sigma_{\rm sky}$, the uncertainty on the background, we take 13 × 13 pixel boxes around the galaxy in the image map for all of the three bands, we calculate the standard deviation of the mean values of the same boxes, as described in Boselli et al. (2003). Ideally we would estimate $\sigma_{\rm sky}$ from boxes with a similar number of pixels to the apertures used for the photometry. This was not possible due to the sizes of the images. The effect of using smaller boxes will be to give us a conservative estimate of $\sigma_{\rm sky}$. The number of boxes depends on the size of the galaxy and on the size of the image; the mean numbers of boxes are 16, 14 and 11 at 250, 350 and 500 μm. The error on the sky determination is:

$$err_{\rm sky} = N_{\rm pix}\sigma_{\rm sky}, \quad (4)$$

where $\sigma_{\rm sky}$ is the uncertainty of the background. Mean values of $err_{\rm sky}$ are 8.0%, 9.6% and 10.3% of the total flux density at 250, 350 and 500 μm, respectively. $err_{\rm sky}$ is thus the dominant error for extended galaxies.

Figure 3 shows the influence of each error component as a function of the number of pixels of the aperture, assuming mean values of $\sigma_{\rm inst}$ and $\sigma_{\rm sky}$ ($\sigma_{\rm conf}$ is constant at a given band). The background error is the dominant source of uncertainty for extended galaxies of size larger than 80 pixels, which is the case for more than 90% of the galaxies of our sample.

Independent measurements

As part of the Science Demonstration Phase, 15 extended galaxies were observed in both the HRS and HeViCS projects.

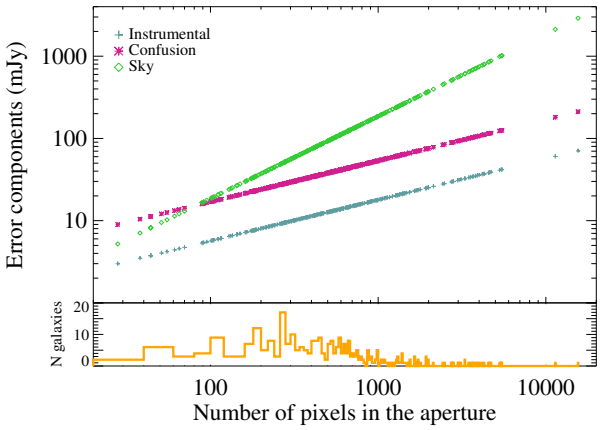

Fig. 3: Error components versus the number of pixels of the aperture and the histogram of the number of pixels.

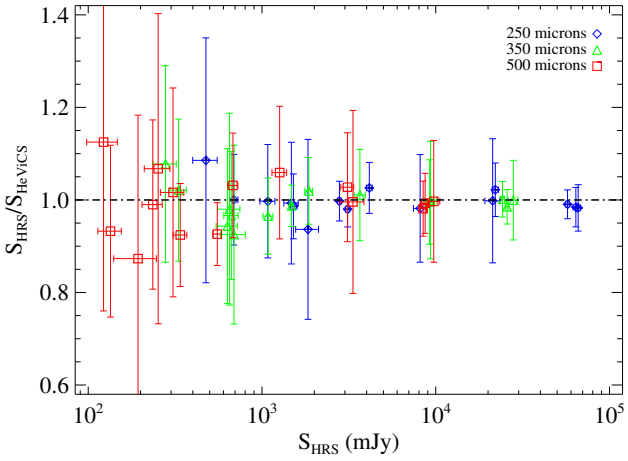

Fig. 4: Ratio between flux density measurements of 15 galaxies from HRS images and measurements of the same 15 galaxies from HeViCS images. Blue diamonds are for 250 μm flux densities, green triangles are for 350 μm and red squares are for 500 μm.

To test the reproducibility of our measurements and the accuracy of our errors, we compare the flux densities of the two sets of data. Indeed, we have two sets of independent images of the same galaxies produced by two different SPIRE scan modes. We perform the photometry on these two sets and compare the flux densities measured in exactly the same conditions (same apertures, same background regions and same photometric procedure). The names and flux densities of these sources from both HRS and HeViCS data are listed in Table 4. Figure 4 shows the ratio between the flux densities from HRS images and the flux densities from HeViCS images in the three bands. The median differences between the flux densities are 1.6%, 1.9% and 3.0% at 250, 350 and 500 μm, respectively. We can consider these values as a lower limits to the photometric uncertainty on the flux densities measured in this work.

Table 5 indicates the mean total stochastic error for the extended sources within the HRS, for early-types and late-types galaxies separately, and for different flux density ranges.

Table 5: Mean stochastic errors ($err_{\rm tot}$) on the HRS flux densities for extended galaxies.

	250 μm	350 μm	500 μm
All	6.2%	8.2%	11.1%
E	20.2%	25.8%	20.9%
S0, S0a, S0/Sa	9.0%	13.2%	19.1%
Late-types	5.9%	7.6%	10.5%
S < 200 mJy	21.8%	24.6%	21.6%
200 mJy < S < 1000mJy	10.2%	10.9%	10.2%
S > 1000 mJy	4.6%	5.9%	5.9%

Calibration errors are not included. Adding the calibration errors, the mean total errors are 9, 11 and 13% at 250, 350 and 500 μm, respectively, which is consistent with the 10, 10 and 15% estimated by Davies et al. (2012).

4.5. Undetected sources

Bona fide detected galaxies are identified through a visual inspection of the images rather than following strict signal to noise criteria. This choice is dictated by the fact that, given the different nature of the sky background and of the emitting source, we might have strong detections but with a very low signal to noise (this is for instance the case of HRS 71 which has an uncertain flux density measurement since lying in a cirrus dominated region) or very high signal to noise sources with uncertain values (point like sources which can be easily confused with background objects). If we limit our sample to extended sources with no cirrus contamination nor nearby companions, our detection threshold is S/N $\sim$ 3, 2 and 2 at 250, 350 and 500 μm, respectively, where the S/N is defined as the ratio of the flux density S over the total uncertainty err_{tot}.

For the undetected galaxies (39, 42 and 47 galaxies at 250, 350 and 500 μm, respectively), an upper limit is determined as:

$$S_{\rm limit(\lambda)} = 3 err_{\rm tot}, \quad (5)$$

where $err_{\rm tot}$ is estimated as in Equation 1. The measure of $err_{\rm tot}$ requires the adoption of a representative aperture, $N_{\rm pix}$, for each undetected source. We make three different assumptions according to the morphology of the undetected galaxies. We form 3 groups: (a) type E, (b) type S0, S0a, S0/Sa and (c) late-types. For both group (a) and (b), we calculate the ratio between the semi-major axis of the infrared elliptical aperture and the semi-major axis of the optical diameter of the detected galaxies of the same morphological type (Table 3). Given the mean values measured for detected sources, we decided to adopt $0.3 \times a_{opt}$ for ellipticals and $0.8 \times a_{opt}$ for S0 and S0/Sa. We take $1.4 \times a_{opt}$ for late-type galaxies, as we do for detected late-types. The radii of the circular region used for the calculation of upper limits are then 0.3, 0.8 or 1.4 times the optical semi-major axis for ellipticals, lenticular and spiral galaxies, respectively. For galaxies detected only in one or two bands, but not in the others, we use the aperture defined at these bands and take a_{IR} as the radius of the circular aperture to calculate the upper limit in the other bands. A minimum conservative and independent of λ radius for upper limit apertures has been set to 22.5″ not to have apertures smaller than the SPIRE resolution.

To test whether these upper limits are realistic, we plot in Figure 5 the surface brightness of the galaxies versus their stellar mass calculated as in Boselli et al. (2009) (for details,

Table 4: The 15 extended galaxies observed in both HRS and HeViCS projects for the *Herschel* Science Demonstration Phase.

HRS	Name	HRS			HeViCS		
		250 μm	350 μm	500 μm	250 μm	350 μm	500 μm
		mJy	mJy	mJy	mJy	mJy	mJy
102	NGC 4254	64026.1 ± 2329.3	25753.9 ± 599.1	8685.7 ± 406.2	65039.2 ± 1525.8	26143.0 ± 778.7	8750.1 ± 399.3
106	NGC 4276	1476.4 ± 139.5	650.7 ± 95.8	252.7 ± 42.6	1486.6 ± 137.9	664.0 ± 100.9	236.7 ± 62.7
122	NGC 4321	66006.4 ± 2209.8	27948.0 ± 1792.0	9742.4 ± 817.0	67163.5 ± 2583.7	27962.1 ± 1602.6	9773.1 ± 995.4
152	NGC 4412	2790.7 ± 73.6	1084.2 ± 71.7	338.6 ± 30.7	2797.8 ± 95.1	1123.4 ± 60.4	366.4 ± 29.0
158	NGC 4423	1079.9 ± 107.3	632.9 ± 88.8	307.6 ± 47.4	1082.9 ± 78.3	670.9 ± 72.9	302.7 ± 48.4
160	NGC 4430	4145.2 ± 156.3	1859.9 ± 96.1	680.6 ± 45.8	4040.2 ± 154.0	1824.5 ± 87.7	659.9 ± 57.2
162	NGC 4435	1839.0 ± 276.7	690.0 ± 112.8	193.5 ± 53.3	1963.9 ± 280.9	745.9 ± 96.9	221.6 ± 49.7
163	NGC 4438	8132.3 ± 684.6	3660.7 ± 271.1	1263.9 ± 122.7	8284.0 ± 689.8	3622.2 ± 230.6	1193.3 ± 112.6
165	UGC 7579	688.5 ± 38.8	331.0 ± 35.5	134.3 ± 20.7	688.3 ± 55.0	324.2 ± 34.2	144.0 ± 18.2
182	NGC 4480	3112.1 ± 84.2	1478.6 ± 42.8	553.1 ± 31.7	3175.4 ± 90.4	1497.8 ± 52.2	597.2 ± 27.3
190	NGC 4501	57336.0 ± 1379.6	24221.3 ± 645.1	8461.8 ± 366.1	57884.4 ± 1172.9	24183.9 ± 666.2	8623.7 ± 367.5
206	IC 3521	1516.8 ± 72.8	666.2 ± 63.3	235.3 ± 31.3	1538.2 ± 80.7	689.5 ± 73.8	237.7 ± 30.5
217	NGC 4569	22023.9 ± 894.2	9219.8 ± 580.8	3105.1 ± 265.6	21550.7 ± 850.8	9261.9 ± 619.2	3022.1 ± 230.6
220	NGC 4579	21263.2 ± 2091.8	9340.7 ± 802.9	3339.0 ± 526.2	21301.7 ± 1950.3	9343.3 ± 874.4	3353.2 ± 405.0
223	UGC 7802	475.8 ± 76.5	278.6 ± 42.4	122.5 ± 24.6	438.3 ± 80.3	258.5 ± 32.4	108.9 ± 27.7

Table 6: Detection rates in each band for different morphology classes.

	250 μm	350 μm	500 μm
E	32%	32%	23%
S0, S0a, S0/Sa	60%	58%	55%
Late-types	97%	96%	95%

see Boselli et al. 2012). The surface brightness is calculated by dividing flux densities by the infrared size of galaxies, i.e. the aperture size. The detection limit in surface brightness of our survey is $\sim$ 0.03, 0.02 and 0.008 mJy arcsec^{-2} at 250, 350 and 500 μm, respectively. The only extended galaxy with a surface brightness below this threshold is M86 (HRS150) whose dust emission comes from a peculiar feature probably stripped from a nearby star forming system (Gomez et al. 2010a). At 350 μm, the other detected galaxy with a low surface brightness is NGC4636 (HRS241) which is a faint, clearly detected, compact source. Few sources have a relatively high surface brightness at 250 μm but are non detected at 350 and 500 μm. These sources are close to point-like and are well detected at 250 μm. However, at 350 and 500 μm, they become as faint as the background sources, with a comparable surface brightness. To be conservative, we thus consider them as undetected sources. These two galaxies are particular cases, thus we consider that our upper limits are realistic as they lie at the lower limit of the detections.

Table 6 gives the detection rate in each band for the 3 groups: ellipticals (E), lenticulars (S0, S0a, S0/Sa) and late types.

5. Flux densities calculation

SPIRE maps are in Jy/beam. Flux densities, upper limits and errors of extended sources are thus converted into mJy using Equation 6.

$$S_\lambda(mJy) = S_\lambda(Jy/beam)\frac{pixsize_\lambda^2 \times 1000}{beam_\lambda} \times corr_\lambda, \quad (6)$$

where the pixel size of the images, $pixsize_\lambda$, the beam area, $beam_\lambda$, and the correction, $corr_\lambda$ (latest HIPE v8 calibration[9] and extended sources corrections) are given in Table 1.

5.1. The data table

The flux densities of the 323 HRS galaxies in the three SPIRE bands (without colour corrections applied) are given in Table A.2, organized as follows:

- Column 1: HRS name.
- Column 2: Flag of the 250 μm flux density (f_{250}); 0: Non-detection, 1: Detection (extended source), 2: Detection (point-like source), 3: Overestimation of the flux density due to the presence of a strong background source or a companion galaxy, 4: Presence of Galactic cirrus.
- Column 3: Flux density at 250 μm (S_{250}) in mJy.
- Column 4: Flag of the 350 μm flux density (f_{350}); see Column 2.
- Column 5: Flux density at 350 μm (S_{350}) in mJy.
- Column 6: Flag of the 500 μm flux density (f_{500}); see Column 2.
- Column 7: Flux density at 500 μm (S_{500}) in mJy.
- Column 8: Number of pixels in the 250 μm aperture (N_{250}).
- Column 9: Number of pixels in the 350 μm aperture (N_{350}).
- Column 10: Number of pixels in the 500 μm aperture (N_{500}).
- Column 11: Instrumental error at 250 μm, determined as in Equation 2 ($err^{250}_{\rm inst}$).
- Column 12: Instrumental error at 350 μm, determined as in Equation 2 ($err^{350}_{\rm inst}$).
- Column 13: Instrumental error at 500 μm, determined as in Equation 2 ($err^{500}_{\rm inst}$).
- Column 14: Confusion error at 250 μm, determined as in Equation 3 ($err^{250}_{\rm conf}$).
- Column 15: Confusion error at 350 μm, determined as in Equation 3 ($err^{350}_{\rm conf}$).
- Column 16: Confusion error at 500 μm, determined as in Equation 3 ($err^{500}_{\rm conf}$).
- Column 17: Sky error at 250 μm, determined as in Equation 4 ($err^{250}_{\rm sky}$).

[9] http://herschel.esac.esa.int/twiki/bin/genpdf/Public/HipeWhatsNew8x?pdforientation=portrait&pdftoclevels=3

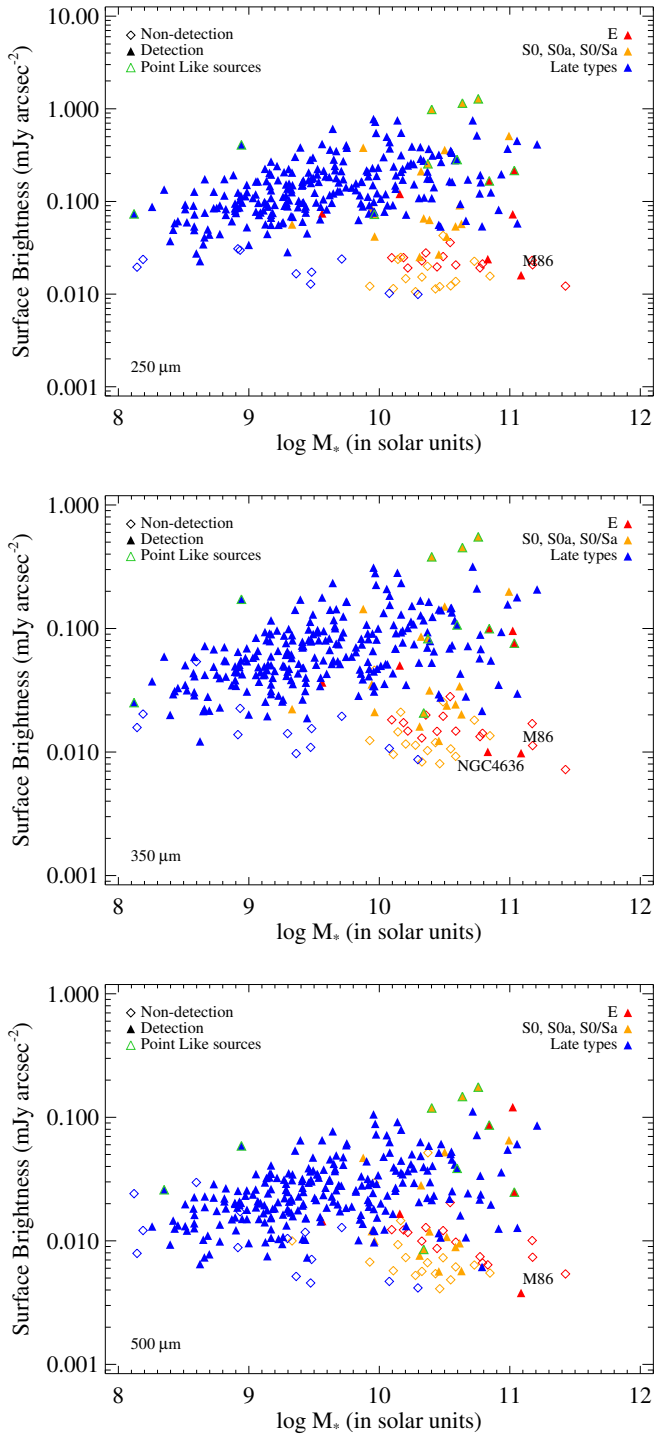

Fig. 5: The surface brightness versus the stellar mass at 250 (top panel), 350 (middle panel) and 500 μm (bottom panel). Filled triangles are for detections, empty triangles for non-detections. Red, orange and blue colors are for elliptical, lenticular and late-type galaxies, respectively. Triangles with a green contour are point-like sources.

- Column 18: Sky error at 350 μm, determined as in Equation 4 ($err_{\rm sky}^{350}$).
- Column 19: Sky error at 500 μm, determined as in Equation 4 ($err_{\rm sky}^{500}$).

The $err_{\rm inst}$, $err_{\rm conf}$ and $err_{\rm sky}$ are not provided for point-like galaxies (i.e. flag 2) as their errors are calculated with a different method (see Section 4.4.1). The total errors provided in Table A.2 do not contain the calibration error of 7% which can be added in quadrature.

6. Comparison with the literature

Submillimetre photometry in the ~ 250-550 μm spectral domain is available for some HRS galaxies from Davies et al. (2012), Auld et al. (submitted), Dale et al. (2012) and Planck Collaboration et al. (2011).

Comparison with the HeViCS Bright Galaxy Catalogue

We compare our results with those of Davies et al. (2012) (Figure 6) who used a different method to perform the photometry. They carried out a study on 78 bright Virgo galaxies as part of the HeViCS. Before extracting flux densities, they smoothed and re-gridded the 250 μm and 350 μm images to the 500 μm resolution and pixel scale. They defined "by eye" elliptical apertures and a concentric annulus (for background estimation) on the 500 μm image and used them at all bands. For consistency with our work, we apply the K_4 corrections to their measurements, using the values given in Table 1. For the 59 galaxies in common to both the HRS and HeViCS surveys, mean values of the flux density ratios between their measurements on HeViCS fields and in this work are 1.00 ± 0.07, 1.01 ± 0.07 and 0.99 ± 0.08 at 250, 350 and 500 μm. Thus our fluxes and those of Davies et al. (2012) are consistent with each other. Auld et al. (2012, submitted) present a comparison between the flux densities of the optically selected Virgo galaxies, from the Virgo Cluster Catalogue (VCC), and HRS ones, for galaxies in common. Despite the different techniques used (automatic for Auld et al. 2012), the measurements are in good agreement.

Comparison with KINGFISH

KINGFISH (Key Insights on Nearby Galaxies: A Far-Infrared Survey with *Herschel*; Kennicutt et al. 2011) is a survey of 61 nearby galaxies observed in PACS and SPIRE bands. Dale et al. (2012) provide the flux densities of this sample in which six galaxies are in common with the HRS. The comparison is important as the images of the targets are the same but the data reduction, map-making, and flux extraction use different methods. They carried out aperture photometry using ellipses and applied aperture correction, which are of the order of a few percents (Dale, private communication). They also applied Galactic extinction corrections to their measurements. These corrections are however very small since they do not exceed 0.4%, where this value has been determined for an object $b = 10$ deg. The background is estimated by taking the mean value of several regions circumscribing the galaxy. The K_4 correction is applied to their flux densities to have consistency between their and our measurements.

Flux densities are compared in Figure 7 (left panel). Mean HRS to KINGFISH flux density ratios are 1.00±0.02, 1.01±0.03 and 0.93 ± 0.04 at 250, 350, and 500 μm. At 250 and 350 μm the results are in very good agreement but not at 500 μm. This 7% discrepancy can be due to the differences in the data reduction and map-making or in the flux extraction procedures. To understand if its origin comes from the method used to perform

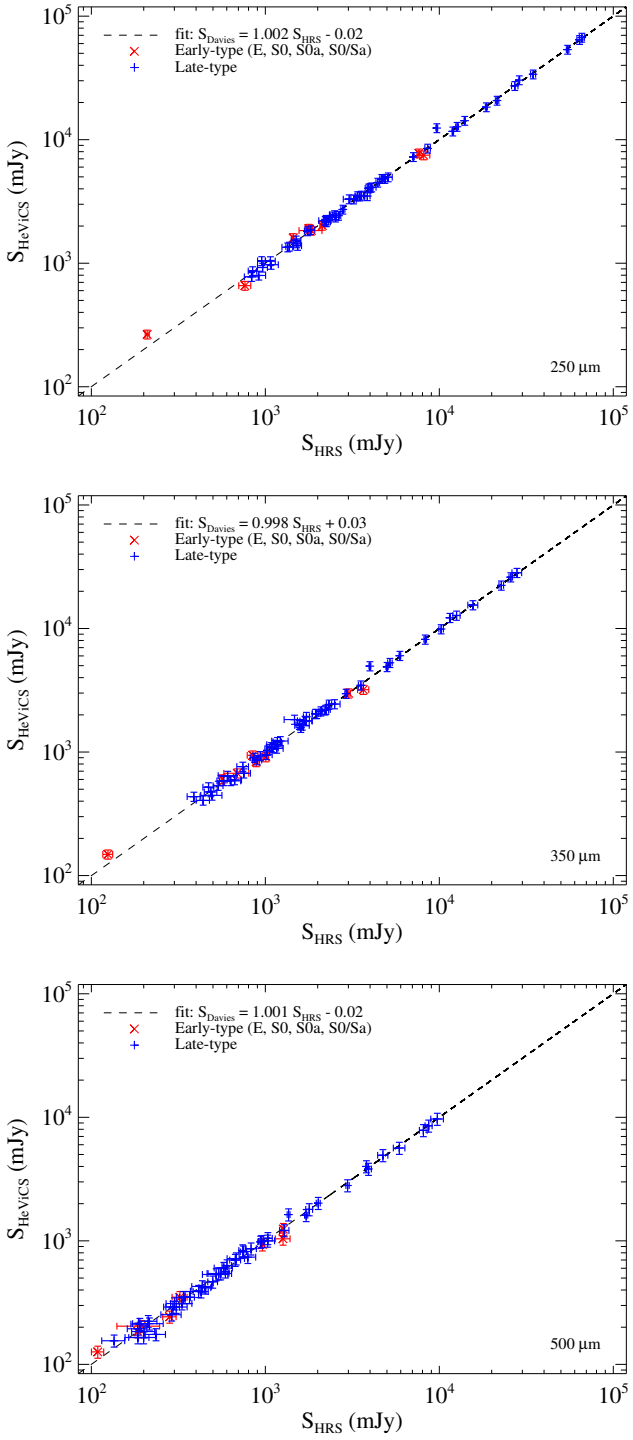

Fig. 6: A comparison of the flux densities of the 59 sources common to both the HRS sample and the HeViCS Virgo bright galaxy sample (Davies et al. 2012) at 250, 350 and 500 μm. Red triangles are for early type galaxies, blue triangles for late type galaxies. The dashed line indicates the linear fit.

the photometry, we apply our flux extraction technique on the public KINGFISH images. On Figure 7 (right panel), we show the flux density ratio of the measurements obtained in this work to those given by Dale et al. (2012) (crosses), as well as to those that we have extracted using our own procedure on the public KINGFISH images (diamonds). At 250 μm, all sets of data are consistent. At 350 μm, the flux densities measured on KINGFISH images with our procedure are $\sim$ 4% higher than ours. As the same method to extract fluxes is employed, this difference is due to the data reduction and map-making procedure applied by the SAG2 and the KINGFISH team. We note also a $\sim$ 4% systematic difference between Dale et al. (2012) measurements and ours on the same images. This is due to the different flux extraction methods. At 500 μm, the flux densities measured on KINGFISH images with our procedure are $\sim$ 3% lower than our measurements, this discrepancy comes from the different production of the images. As at 350 μm, we note the $\sim$ 4% systematic error due to the different methods used to perform the photometry. The discrepancies observed between HRS and KINGFISH flux densities is thus a combination between differences in the production of the images and differences in the way the photometry is performed.

Comparison with Planck

We also compare our measurements with the *Planck* Early Release Compact Source Catalog (ERCSC) of the *Planck* Collaboration (Planck Collaboration et al. 2011). The catalogue contains flux densities derived from several method. To be consistent with this work, we use the measurements determined from aperture photometry. Cross-matching the two catalogues, we find 155 galaxies in common at 350 μm and 76 galaxies in common at 550 μm. The *Planck* FWHM are 4.23′ at 350 μm and 4.47′ at 550 μm. The photometry on the *Planck* compact sources was carried out using the FWHM of the band as the radius of the aperture. After visually inspecting each HRS galaxy with a corresponding *Planck* source, we excluded 11 sources because the *Planck* measurements may have potentially included other bright sources that lie within 5′of the galaxies.

The comparison between the data taken from the Planck catalogues and those presented here in Table A.2 is shown in Figure 8. Mean *Herschel* to *Planck* flux density ratios are 0.91 and 1.13 at 350 and 500 μm, respectively. At 500 μm, *Herschel* flux densities are on average higher than those of *Planck* at 550 μm. The discrepancy at 500 μm is in part due to the difference of wavelength. If we assume a modified black body with a β of 1.5, T =20K, and assuming the relative colour corrections (1.02 for the SPIRE data, 0.91 for the *Planck* one, as indicated by the ERCSC Explanatory Supplement), we expect a flux density ratio of $S(500)_{SPIRE}/S(550)_{Planck}$ = 1.15. Once correcting the *Planck* data for this difference, the same ratio drops to 0.98 at 500 μm and 0.96 at 350 μm. Colour corrections thus explain the mean differences between the two independent sets of data. They do not however explain other systematic differences such as those related to aperture effects. The major differences between the *Planck* measurements and ours are due to the different aperture sizes. Higher ratios correspond to galaxies that have a size larger than the *Planck* 350 μm FWHM. Lower ratios can be explained by the contribution of background sources, visible on *Herschel* images, present in the *Planck* beam (Figure 9). At low flux densities, *Planck* data are systematically higher than those of *Herschel*, probably due to the important contamination of background sources (Figure 8). Davies et al. (2012) also compared their results with those of the *Planck* Collaboration at 350 μm. The result of their linear fit is given in Figure 8, upper left panel (flux densities are not color corrected).

To understand this strong systematic difference between *Planck* measurements and ours, we carried out the photometric method used for the *Planck* catalogue on HRS images of the galaxies in common but using the aperture and sky annu-

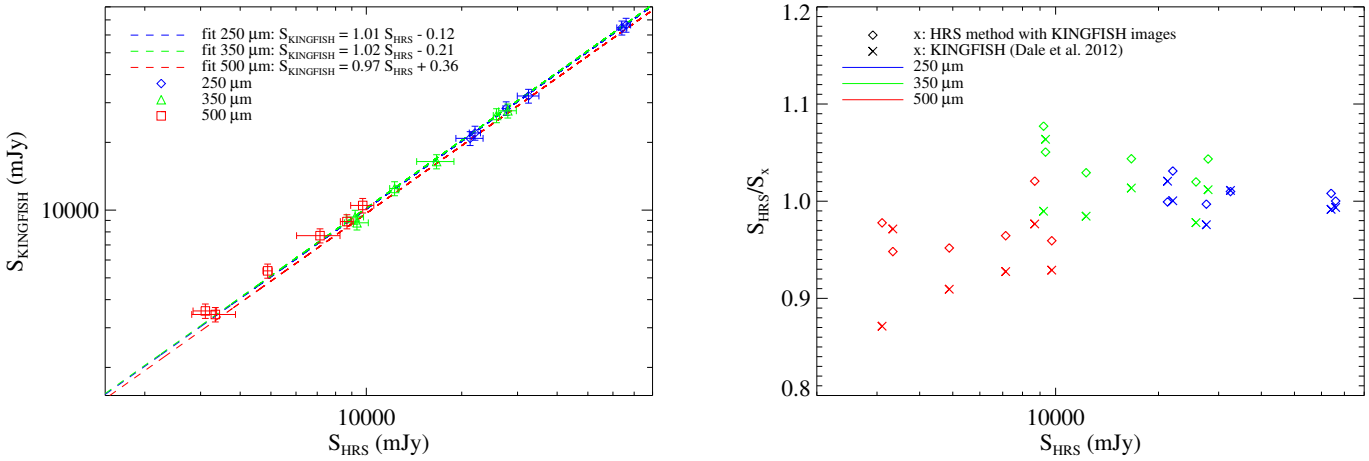

Fig. 7: Left panel: Comparison between KINGFISH (Dale et al. 2012) and HRS flux densities of six common galaxies: NGC 4254 (HRS 102), NGC 4321 (HRS 122), NGC 4536 (HRS 205), NGC 4569 (HRS 217), NGC 4579 (HRS 220) and NGC 4725 (HRS 263) in the three SPIRE bands. Blue diamonds, green triangles and red squares are for the 250, 350 and 500 μm measurements respectively. The dashed lines give the linear fits. Right panel: the flux density ratio obtained in this work to those given by Dale et al. (2012) (crosses), as well as to those that we have extracted using our own procedure from the public KINGFISH images (diamonds).

Table 7: Flux densities from different sources for the 4 galaxies shown in Figure 9, at 350 μm.

	HRS mJy	*Planck* mJy	HRS in *Planck* beam mJy
HRS 64	683 ± 62	1400 ± 132	1372 ± 810
HRS 213	31070 ± 687	24342 ± 1431	25504 ± 922
HRS 263	16657 ± 2242	11974 ± 574	14144 ± 815
HRS 276	1229 ± 90	2028 ± 147	1904 ± 809

lus defined by the *Planck* consortium. A circular aperture with a radius of 4.23′(4.47′) at 350 μm (500 μm) is used, and the background region is defined as a circular annulus with an inner radius of 4.23′(4.47′) at 350 μm (500 μm) and outer radius of 2×4.23′(2×4.47′) at 350 μm (500 μm). This is a rough approximation, and a more precise work would require a convolution of the *Herschel* images to the resolution of *Planck* which is beyond the purpose of the present paper. We rejected flux densities of galaxies with sizes bigger than the *Planck* beam, or faint galaxies contaminated by strong background sources within the *Planck* beam. Figure 8 (lower panels) shows the *Planck* photometry versus HRS photometry measured in *Planck* apertures only for galaxies with good flux density measurements, the associated flux densities are in Table 7. The results of the linear least squares fits show the consistency of the two sets of measurements. The HRS photometry in the beam of *Planck* is in good agreement with the flux densities of the *Planck* catalogue. Furthermore, the calibration error of *Planck* at 350 and 550 μm *Planck* is 7% (Planck HFI Core Team et al. 2011), associated with the calibration error of *Herschel*, we obtain 10%. We can conclude that, despite differences due to the choice of the aperture, our measurements are consistent with the *Planck* data. However, because of the various photometry issues but particularly the source blending issues, *Herschel* measurements should be used instead of *Planck* measurements for these galaxies whenever possible.

7. Data access

The table is available on the SAG2 *Herschel* Database in Marseille (HeDaM; Roehlly et al. in preparation) at http://hedam.oamp.fr/HRS/. An electronic version of the catalogue and a README file can be downloaded there. The README describes how the photometry is performed for both extended and point-like sources. Through this database, we plan in the next future to give access to the community to all *Herschel* and ancillary data of the HRS galaxies.

8. Conclusion

We present the flux densities of the 323 galaxies of the *Herschel* Reference Survey in the three SPIRE bands. For extended galaxies, aperture photometry on elliptical regions is performed using the "Funcnts" DS9/Funtools task. The background contribution is estimated calculating the mean value of the pixels within a concentric circular annulus. A different technique is used for point-like sources, where a PSF fitting is directly performed on timeline data. We compare our results with those of Davies et al. (2012), KINGFISH (Dale et al. 2012) and the *Planck* Early Science Compact Source Catalog (Planck Collaboration et al. 2011). Our measurements and those of Davies et al. (2012) and Dale et al. (2012) are consistent. Despite the different size of PSF between SPIRE and *Planck*, our flux densities and those of the *Planck* Consortium are in a good agreement. The catalogue is publicly available on the HeDaM database.

Acknowledgements. We thank the referee for precious comments and suggestions which helped improving the quality of the manuscript. LC thanks Daniel Dale for enlightening discussions about the photometry of extended galaxies. LC also thanks Samuel Boissier and Sébastien Heinis for useful discussions. AB thanks the ESO visiting program committee for inviting him at the Garching headquarters for a two months staying. SB, SdiSA and CP acknowledge financial support by ASI through the ASI-INAF grants I/016/07/0 and I/009/10/0. SPIRE has been developed by a consortium of institutes led by Cardiff Univ. (UK) and including Univ. Lethbridge (Canada); NAOC (China); CEA, LAM (France); IFSI, Univ. Padua (Italy); IAC (Spain); Stockholm Observatory (Sweden); Imperial College London, RAL, UCL-MSSL, UKATC, Univ. Sussex (UK); Caltech, JPL, NHS C, Univ. Colorado (USA). This development has been supported by national funding agencies: CSA (Canada);

NAOC (China); CEA, CNES, CNRS (France); ASI (Italy); MCINN (Spain); SNSB (Sweden); STFC, UKSA (UK); and NASA (USA). This research has made use of the NASA/IPAC ExtraGalactic Database (NED) which is operated by the Jet Propulsion Laboratory, California Institute of Technology, under contract with the National Aeronautics and Space Administration. The research leading to these results has received funding from the European Communitys Seventh Framework Programme (/FP7/2007-2013/) under grant agreement No 229517. This research has made use of the NASA/IPAC ExtraGalactic Database (NED) which is operated by the Jet Propulsion Laboratory, California Institute of Technology, under contract with the National Aeronautics and Space Administration and of the GOLDMine database (http://goldmine.mib.infn.it/). The Dark Cosmology Centre is funded by the Danish National Research Foundation.

References

Abazajian, K. N., Adelman-McCarthy, J. K., Agüeros, M. A., et al. 2009, ApJS, 182, 543
Baes, M., Clemens, M., Xilouris, E. M., et al. 2010, A&A, 518, L53
Becker, R. H., White, R. L., & Helfand, D. J. 1995, ApJ, 450, 559
Bendo, G. J., Boselli, A., Dariush, A., et al. 2012a, MNRAS, 419, 1833
Bendo, G. J., Galliano, F., & Madden, S. C. 2012b, ArXiv e-prints, 1202.4629
Bendo, G. J., Wilson, C. D., Warren, B. E., et al. 2010, MNRAS, 402, 1409
Bianchi, S., Alton, P. B., & Davies, J. I. 2000, in ESA Special Publication, Vol. 455, ISO Beyond Point Sources: Studies of Extended Infrared Emission, ed. R. J. Laureijs, K. Leech, & M. F. Kessler, 149
Bianchi, S. & Schneider, R. 2007, MNRAS, 378, 973
Binggeli, B., Sandage, A., & Tammann, G. A. 1985, AJ, 90, 1681
Boquien, M., Buat, V., Boselli, A., et al. 2012, ArXiv e-prints, 1201.2405
Boquien, M., Calzetti, D., Combes, F., et al. 2011, AJ, 142, 111
Boselli, A., Boissier, S., Cortese, L., et al. 2009, ApJ, 706, 1527
Boselli, A., Boissier, S., Heinis, S., et al. 2011, A&A, 528, A107
Boselli, A., Ciesla, L., Buat, V., et al. 2010a, A&A, 518, L61
Boselli, A., Ciesla, L., Cortese, L., et al. 2012, ArXiv e-prints, 1201.2305
Boselli, A., Eales, S., Cortese, L., et al. 2010b, PASP, 122, 261
Boselli, A., Sauvage, M., Lequeux, J., Donati, A., & Gavazzi, G. 2003, A&A, 406, 867
Clayton, D. D., Arnett, D., Kane, J., & Meyer, B. S. 1997, ApJ, 486, 824
Condon, J. J., Cotton, W. D., Greisen, E. W., et al. 1998, AJ, 115, 1693
Cortese, L., Ciesla, L., Boselli, A., et al. 2012, ArXiv e-prints, 1201.2762
Cortese, L., Davies, J. I., Pohlen, M., et al. 2010, A&A, 518, L49
Dale, D. A., Aniano, G., Engelbracht, C. W., et al. 2012, ApJ, 745, 95
Davies, J. I., Bianchi, S., Cortese, L., et al. 2012, MNRAS, 419, 3505
Devereux, N. A. & Young, J. S. 1990, in NASA Conference Publication, Vol. 3084, NASA Conference Publication, ed. D. J. Hollenbach & H. A. Thronson Jr., 92
Dowell, C. D., Pohlen, M., Pearson, C., et al. 2010, in Society of Photo-Optical Instrumentation Engineers (SPIE) Conference Series, Vol. 7731, Society of Photo-Optical Instrumentation Engineers (SPIE) Conference Series
Dreyer, J. L. E. 1888, MNRAS, 49, 1
Dreyer, J. L. E. 1895, MNRAS, 51, 185
Dwek, E. 1998, ApJ, 501, 643
Ferrarese, L., Côté, P., Jordán, A., et al. 2006, ApJS, 164, 334
Galametz, M., Madden, S. C., Galliano, F., et al. 2011, A&A, 532, A56
Galliano, F., Dwek, E., & Chanial, P. 2008, ApJ, 672, 214
Gavazzi, G., Boselli, A., Donati, A., Franzetti, P., & Scodeggio, M. 2003, A&A, 400, 451
Gavazzi, G., Pierini, D., & Boselli, A. 1996, A&A, 312, 397
Gehrz, R. 1989, in IAU Symposium, Vol. 135, Interstellar Dust, ed. L. J. Allamandola & A. G. G. M. Tielens, 445
Gomez, H. L., Baes, M., Cortese, L., et al. 2010a, A&A, 518, L45
Gomez, H. L., Clark, C. J. R., Nozawa, T., et al. 2012, MNRAS, 2206
Gomez, H. L., Vlahakis, C., Stretch, C. M., et al. 2010b, MNRAS, 401, L48
Gordon, K. D., Galliano, F., Hony, S., et al. 2010, A&A, 518, L89
Griffin, M., Ade, P., André, P., et al. 2009, in EAS Publications Series, Vol. 34, EAS Publications Series, ed. L. Pagani & M. Gerin, 33–42
Griffin, M. J., Abergel, A., Abreu, A., et al. 2010, A&A, 518, L3
Haynes, M. P., Magri, C. A., & Giovanelli, R. 1984, in Bulletin of the American Astronomical Society, Vol. 16, Bulletin of the American Astronomical Society, 882
Höfner, S. 2009, in Astronomical Society of the Pacific Conference Series, Vol. 414, Cosmic Dust - Near and Far, ed. T. Henning, E. Grün, & J. Steinacker, 3
Holland, W. S., Robson, E. I., Gear, W. K., et al. 1999, MNRAS, 303, 659
Jarrett, T. H., Chester, T., Cutri, R., Schneider, S. E., & Huchra, J. P. 2003, AJ, 125, 525
Kennicutt, R. C., Calzetti, D., Aniano, G., et al. 2011, PASP, 123, 1347
Matsuura, M., Dwek, E., Meixner, M., et al. 2011, Science, 333, 1258
Moshir, M. & et al. 1990, in IRAS Faint Source Catalogue, version 2.0 (1990)
Murakami, H., Baba, H., Barthel, P., et al. 2007, PASJ, 59, 369
Nguyen, H. T., Schulz, B., Levenson, L., et al. 2010, A&A, 518, L5
Nilson, P. 1973, Uppsala general catalogue of galaxies, ed. Nilson, P.
Ott, S. 2011, in Astronomical Society of the Pacific Conference Series, Vol. 442, Astronomical Data Analysis Software and Systems XX, ed. I. N. Evans, A. Accomazzi, D. J. Mink, & A. H. Rots, 347
Planck Collaboration, Ade, P. A. R., Aghanim, N., et al. 2011, A&A, 536, A7
Planck HFI Core Team, Ade, P. A. R., Aghanim, N., et al. 2011, A&A, 536, A6
Sanders, D. B., Mazzarella, J. M., Kim, D.-C., Surace, J. A., & Soifer, B. T. 2003, AJ, 126, 1607
Sauvage, M. & Thuan, T. X. 1994, ApJ, 429, 153
Schlegel, D. J., Finkbeiner, D. P., & Davis, M. 1998, ApJ, 500, 525
Smith, M. W. L., Gomez, H. L., Eales, S. A., et al. 2012, ArXiv e-prints, 1112.1408
Soifer, B. T., Boehmer, L., Neugebauer, G., & Sanders, D. B. 1989, AJ, 98, 766
Swinyard, B. M., Ade, P., Baluteau, J.-P., et al. 2010, A&A, 518, L4
Thuan, T. X. & Sauvage, M. 1992, A&AS, 92, 749
Wolfire, M. G., Hollenbach, D., McKee, C. F., Tielens, A. G. G. M., & Bakes, E. L. O. 1995, ApJ, 443, 152
Young, J. S., Allen, L., Kenney, J. D. P., Lesser, A., & Rownd, B. 1996, AJ, 112, 1903
Zwicky, F., Herzog, E., & Wild, P. 1968, Catalogue of galaxies and of clusters of galaxies, ed. Zwicky, F., Herzog, E., & Wild, P.

Appendix A: Tables

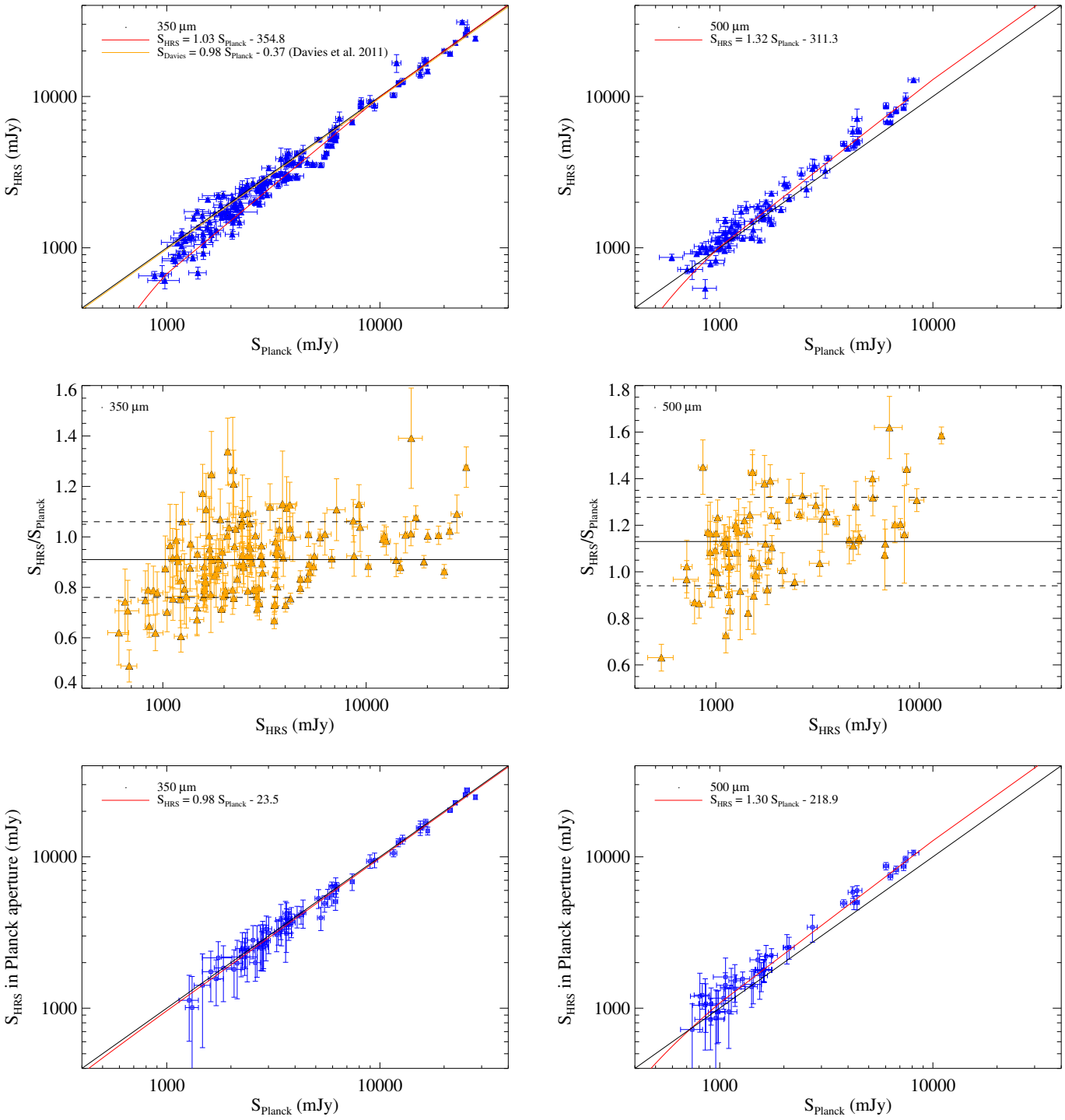

Fig. 8: Upper panels: the HRS versus *Planck* flux densities of 144 bright galaxies at 350 μm and 76 bright galaxies at 500 μm. The black lines are the one to one relationship in log scale. The red lines are the results of the linear fit; the orange line, on the 350 μm plot, is the result of Davies et al. (2012) linear least squares fit. Middle panels: the HRS/*Planck* flux density ratio versus the HRS flux densities at 350 μm and 500 μm. The black line corresponds to the mean ratio, the dashed lines correspond to the standard deviation of the ratios. Lower panels: *Planck* flux densities versus HRS flux densities measured in the aperture used by the *Planck* Consortium at 350 μm and 500 μm.

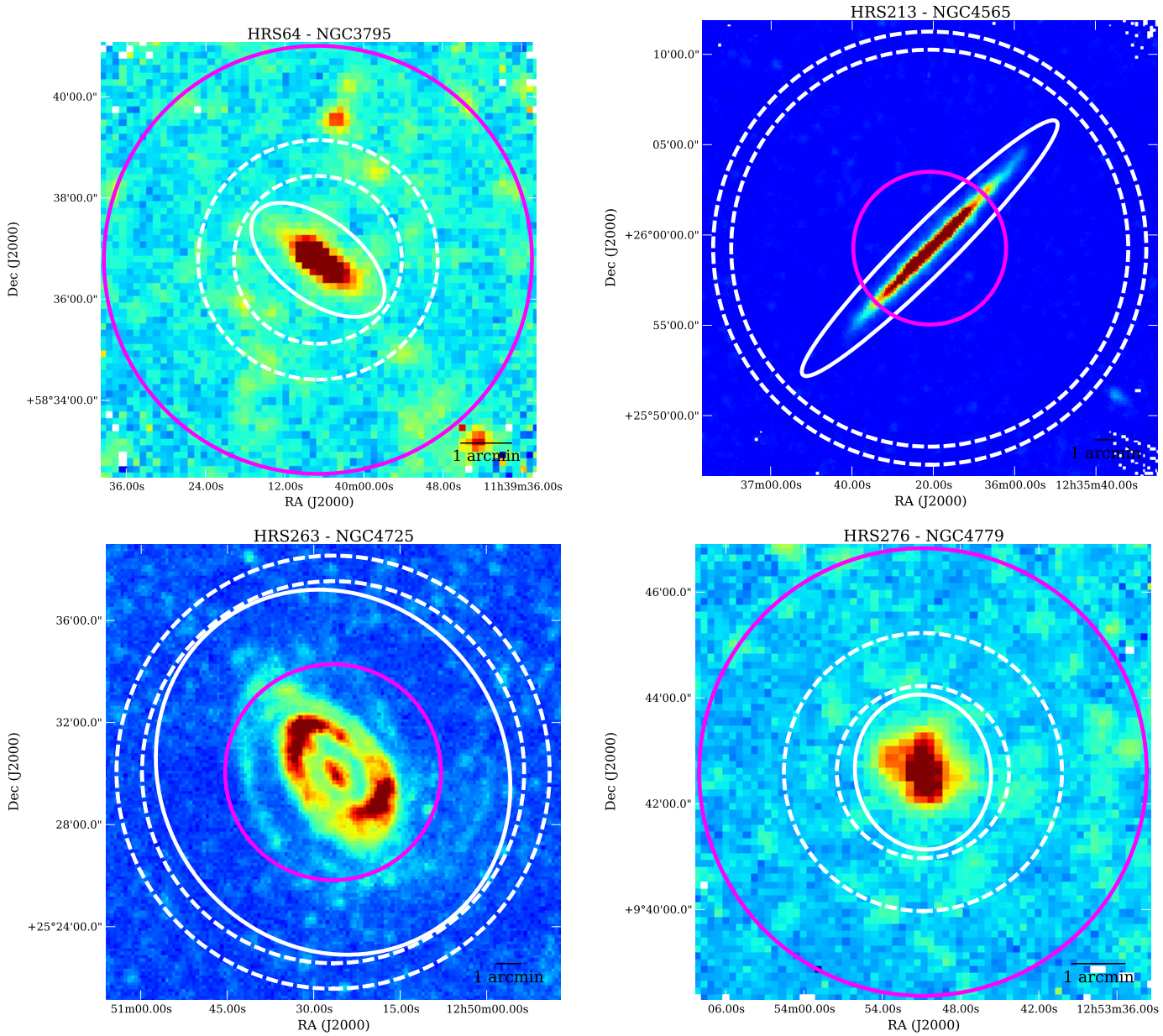

Fig. 9: Comparison between *Planck* and *Herschel* aperture photometry on 350 μm SPIRE images, with in white, the apertures used for *Herschel* photometry and in dashed white for the background estimation, in magenta the aperture used by the *Planck* consortium on *Planck* images.

Table A.1: Apertures used for the on source and sky background estimates (see Section 4.2).

HRS	CGCG	VCC	UGC	NGC	IC	RA	Dec	a_{IR} (arcsec)	b_{IR} (arcsec)	PA (degree)	r_{in}^{bck} (arcsec)	r_{out}^{bck} (arcsec)
1	123035	-	-	-	-	154.415	22.8100	47	40	170	46	106
2	124004	-	5588	-	-	155.238	25.3650	46	45	40	62	103
3	94026	-	5617	3226	-	155.863	19.8980	39	38	15	300	354
4	94028	-	5620	3227	-	155.877	19.8650	117	97	155	249	309
5	94052	-	-	-	610	156.618	20.2280	80	47	28	86	146
6	154016	-	5662	3245	-	156.755	28.6390	125	45	150	153	213
7	154017	-	5663	3245	-	156.827	28.5070	20	20	-	150	210
8	154020	-	5685	3254	-	157.333	29.4910	210	66	46	232	292
9	154026	-	5731	3277	-	158.231	28.5120	81	73	25	90	150
10	183028	-	5738	-	-	158.624	35.2570	55	43	30	74	148
11	124038	-	5742	3287	-	158.697	21.6480	87	41	20	97	157
12	124041	-	-	-	-	158.925	26.1260	28	22	20	31	91
13	183030	-	5753	3294	-	159.068	37.3250	149	76	115	165	225
14	124045	-	5767	3301	-	159.234	21.8820	42	42	55	165	225
15	65087	-	5826	3338	-	160.531	13.7470	247	152	100	273	333
16	94116	-	5842	3346	-	160.912	14.8720	112	98	108	125	185
17	95019	-	5887	3370	-	161.767	17.2740	132	74	150	146	206
18	155015	-	5906	3380	-	162.051	28.6020	71	56	20	79	139
19	184016	-	5909	3381	-	162.103	34.7110	85	78	55	94	154
20	184018	-	5931	3395	2613	162.459	32.9830	83	62	50	125	192
21	155028	-	5958	-	-	162.816	27.8490	78	45	180	86	127
22	155029	-	5959	3414	-	162.818	27.9750	81	71	10	165	225
23	184028	-	5972	3424	-	162.943	32.9010	108	59	110	131	191
24	184029	-	5982	3430	-	163.048	32.9500	167	94	35	185	245
25	125013	-	5995	3437	-	163.149	22.9340	101	67	117	116	176
26	184031	-	5990	-	-	163.160	34.4830	58	34	15	62	122
27	184034	-	6001	3442	-	163.284	33.9100	55	47	178	79	143
28	155035	-	6023	3451	-	163.587	27.2400	79	48	50	79	139
29	95060	-	6026	3454	-	163.623	17.3440	90	51	115	91	144
30	95062	-	6028	3455	-	163.630	17.2850	99	61	70	110	170
31	267027	-	6024	3448	-	163.663	54.3050	236	74	65	261	321
32	95065	-	6030	3457	-	163.703	17.6210	38	38	-	167	217
33	95085	-	6077	3485	-	165.010	14.8420	88	76	60	97	157
34	95097	-	6116	3501	-	165.697	17.9890	166	52	30	180	240
35	267037	-	6115	3499	-	165.796	56.2220	34	30	20	37	97
36	155049	-	6118	3504	-	165.797	27.9730	112	87	150	125	185
37	155051	-	6128	3512	-	166.012	28.0370	68	63	138	75	135
38	38129	-	6167	3526	-	166.736	7.1740	82	44	55	88	148
39	66115	-	6169	-	-	166.764	12.0600	80	39	180	86	146
40	67019	-	6209	3547	-	167.483	10.7210	80	39	7	107	148
41	96011	-	6267	3592	-	168.613	17.2600	73	41	117	82	142
42	96013	-	6277	3596	-	168.776	14.7870	170	162	180	188	248
43	96022	-	6299	3608	-	169.246	18.1490	28	28	-	146	206
44	96026	-	6320	-	-	169.572	18.8470	54	51	107	65	117
45	291054	-	6330	3619	-	169.840	57.7580	78	75	115	125	185
46	96029	-	6343	3626	-	170.016	18.3570	58	54	160	125	185
47	156064	-	6352	3629	-	170.133	26.9630	96	68	65	106	166
48	268021	-	6360	3631	-	170.262	53.1700	210	200	118	232	292
49	39130	-	6368	3640	-	170.279	3.2350	35	35	-	185	245
50	96037	-	6396	3655	-	170.728	16.5900	76	52	30	92	149
51	96038	-	6405	3659	-	170.939	17.8190	86	61	55	97	157
52	268030	-	6406	3657	-	170.982	52.9210	60	54	160	67	127
53	67071	-	6420	3666	-	171.109	11.3420	183	50	95	203	263
54	96045	-	6445	3681	-	171.624	16.8630	94	75	165	104	164
55	96047	-	6453	3684	-	171.797	17.0300	121	84	125	134	194
56	291072	-	6458	3683	-	171.883	56.8770	82	64	128	86	146
57	96049	-	6460	3686	-	171.933	17.2240	133	104	25	148	208
58	96050	-	6464	3691	-	172.039	16.9210	52	41	30	78	140
59	67084	-	6474	3692	-	172.100	9.4080	132	48	95	135	186
60	268051	-	6547	3729	-	173.456	53.1260	118	80	15	131	191
61	292009	-	6575	-	-	174.110	58.1910	82	24	171	186	245
62	186012	-	6577	3755	-	174.139	36.4100	132	57	115	146	206
63	268063	-	6579	3756	-	174.200	54.2940	175	87	179	193	253
64	292017	-	6629	3795	-	175.029	58.6130	92	48	53	99	142
65	292019	-	6640	3794	-	175.223	56.2020	94	60	120	104	164
66	186024	-	6651	3813	-	175.328	36.5470	94	46	85	104	164
67	268076	-	6706	3846	-	176.062	55.0350	83	55	60	107	158
68	186045	-	-	-	-	176.608	34.8530	20	20	-	75	113
69	268088	-	6787	3898	-	177.314	56.0840	183	107	108	203	263
70	-	-	-	-	2969	178.130	-3.8720	61	51	105	229	278
71	292042	-	6860	3945	-	178.307	60.6760	220	145	165	244	304
72	-	-	-	3952	2972	178.419	-3.9970	81	48	79	85	142
73	269013	-	6870	3953	-	178.454	52.3270	243	129	13	321	381

Table A.1: continued.

HRS	CGCG	VCC	UGC	NGC	IC	RA	Dec	a_{IR} (arcsec)	b_{IR} (arcsec)	PA (degree)	r_{in}^{bck} (arcsec)	r_{out}^{bck} (arcsec)
74	269019	-	6918	3982	-	179.117	55.1250	98	85	38	108	168
75	269020	-	6919	-	-	179.156	55.6330	51	40	90	70	131
76	269022	-	6923	-	-	179.206	53.1600	84	34	170	93	153
77	13033	-	6993	4030	-	180.098	-1.1000	175	126	31	193	253
78	98019	-	6995	4032	-	180.137	20.0740	78	76	176	175	252
79	69024	-	7001	4019	755	180.293	14.1040	107	52	145	147	195
80	69027	-	7002	4037	-	180.349	13.4010	105	85	15	203	267
81	13046	-	7021	4045	-	180.676	1.9770	126	93	5	139	199
82	98037	-	-	-	-	180.900	16.0560	57	54	105	63	109
83	41031	-	7035	-	-	180.917	2.6410	47	45	150	51	111
84	69036	-	7048	4067	-	181.048	10.8540	50	37	45	55	115
85	243044	-	7095	4100	-	181.536	49.5820	225	74	163	249	309
86	41041	-	7111	4116	-	181.903	2.6920	159	100	163	176	236
87	69058	-	7117	4119	-	182.040	10.3790	68	50	150	190	250
88	41042	-	7116	4123	-	182.046	2.8780	210	162	105	232	292
89	69088	66	7215	4178	-	183.193	10.8660	224	78	30	248	308
90	13104	-	7214	4179	-	183.217	1.3000	91	91	-	176	236
91	98108	92	7231	4192	-	183.451	14.9000	410	109	155	454	514
92	69101	131	7255	-	3061	183.768	14.0290	101	51	120	120	180
93	187029	-	7256	4203	-	183.771	33.1970	103	84	180	157	217
94	69104	145	7260	4206	-	183.820	13.0240	205	51	180	237	297
95	69107	152	7268	4207	-	183.877	9.5850	82	37	120	91	151
96	69110	157	7275	4212	-	183.914	13.9020	151	84	75	167	227
97	69112	167	7284	4216	-	183.977	13.1490	383	90	19	424	484
98	69119	187	7291	4222	-	184.094	13.3070	144	47	55	163	223
99	69123	213	7305	-	3094	184.233	13.6250	39	29	92	61	111
100	98130	226	7315	4237	-	184.298	15.3240	84	48	105	93	153
101	158060	-	7338	4251	-	184.535	28.1750	87	87	-	168	228
102	98144	307	7345	4254	-	184.707	14.4160	258	235	60	285	345
103	42015	341	7361	4260	-	184.843	6.0990	68	35	45	83	128
104	99015	-	7366	-	-	184.869	17.2300	50	50	-	55	115
105	99014	355	7365	4262	-	184.877	14.8780	44	44	-	52	146
106	42032	393	7385	4276	-	185.031	7.6920	88	88	-	97	157
107	42033	404	7387	-	-	185.072	4.2010	81	39	15	86	136
108	42037	434	-	4287	-	185.202	5.6400	76	34	70	77	131
109	42038	449	7403	4289	-	185.259	3.7220	180	37	1	201	261
110	70024	465	7407	4294	-	185.324	11.5110	165	52	160	183	243
111	99024	483	7412	4298	-	185.387	14.6060	101	75	140	287	402
112	42044	492	7413	4300	-	185.423	5.3850	90	29	40	147	189
113	99027	497	7418	4302	-	185.427	14.5980	270	59	177	313	373
114	42045	508	7420	4303	-	185.479	4.4740	276	224	162	306	366
115	42047	517	7422	-	-	185.505	5.1000	57	36	170	65	125
116	70031	522	7432	4305	-	185.515	12.7410	109	109	-	120	180
117	70029	524	7431	4307	-	185.523	9.0440	160	46	25	159	219
118	42053	552	7439	-	-	185.613	4.5660	79	60	170	80	98
119	99029	559	7442	4312	-	185.631	15.5380	214	52	170	237	297
120	70034	570	7445	4313	-	185.661	11.8010	214	48	143	237	297
121	70035	576	7447	4316	-	185.676	9.3320	107	46	110	107	160
122	99030	596	7450	4321	-	185.729	15.8220	383	340	30	424	484
123	42063	613	7451	4324	-	185.776	5.2500	147	42	53	149	223
124	70039	630	7456	4330	-	185.822	11.3680	246	60	64	345	422
125	42068	648	7461	4339	-	185.896	6.0820	22	22	-	107	167
126	99036	654	7467	4340	-	185.897	16.7220	86	86	-	167	227
127	42070	656	7465	4343	-	185.911	6.9540	108	43	130	109	160
128	42072	667	7469	-	3259	185.952	7.1870	79	39	15	87	147
129	99038	685	7473	4350	-	185.991	16.6930	20	20	-	148	208
130	70045	692	7476	4351	-	186.007	12.2050	83	62	70	100	178
131	42079	697	7474	-	3267	186.023	7.0410	65	65	-	72	132
132	42080	699	7477	-	3268	186.031	6.6070	81	57	22	90	150
133	158099	-	7483	4359	-	186.046	31.5220	149	48	105	219	295
134	70048	713	7482	4356	-	186.061	8.5360	135	36	40	148	208
135	42083	731	7488	4365	-	186.118	7.3170	78	78	-	405	465
136	42089	758	7492	4370	-	186.229	7.4450	73	36	80	81	141
137	70057	759	7493	4371	-	186.231	11.7040	122	122	-	237	297
138	70058	763	7494	4374	-	186.266	12.8870	20	20	-	139	265
139	42093	787	7498	4376	-	186.325	5.7410	77	44	135	85	145
140	42092	785	7497	4378	-	186.325	4.9250	128	104	160	142	202
141	70061	792	7503	4380	-	186.342	10.0170	147	73	155	163	223
142	99044	801	7507	4383	-	186.356	16.4700	109	54	20	120	180
143	42095	827	7513	-	-	186.428	7.2170	156	43	155	167	227
144	70068	836	7520	4388	-	186.445	12.6620	214	52	90	237	297
145	70067	849	7519	4390	-	186.461	10.4590	91	76	125	101	161
146	42098	851	7518	-	3322	186.475	7.5550	91	38	160	100	160

Table A.1: continued.

HRS	CGCG	VCC	UGC	NGC	IC	RA	Dec	a_{IR} (arcsec)	b_{IR} (arcsec)	PA (degree)	r_{in}^{bck} (arcsec)	r_{out}^{bck} (arcsec)
147	42099	859	7522	-	-	186.493	3.4300	121	40	130	135	195
148	99049	865	7526	4396	-	186.495	15.6720	141	57	125	156	216
149	70071	873	7528	4402	-	186.531	13.1130	165	48	90	183	243
150	70072	881	7532	4406	-	186.549	12.9460	129	113	130	430	495
151	70076	912	7538	4413	-	186.634	12.6110	122	73	15	135	195
152	42104	921	7536	4412	-	186.650	3.9650	79	65	76	87	147
153	42105	938	7541	4416	-	186.695	7.9190	91	85	145	111	157
154	70082	939	7546	-	-	186.697	8.8850	103	98	165	152	213
155	70080	944	7542	4417	-	186.711	9.5840	86	86	-	167	227
156	99054	958	7551	4419	-	186.735	15.0470	147	58	133	163	223
157	42106	957	7549	4420	-	186.744	2.4940	86	50	8	93	153
158	42107	971	7556	4423	-	186.787	5.8800	128	50	20	142	202
159	70090	979	7561	4424	-	186.798	9.4210	85	80	100	201	261
160	42111	1002	7566	4430	-	186.860	6.2630	93	89	120	225	316
161	70093	1003	7568	4429	-	186.861	11.1070	20	20	-	377	437
162	70098	1030	7575	4435	-	186.919	13.0790	83	77	10	96	148
163	70097	1043	7574	4438	-	186.940	13.0090	134	118	27	327	404
164	70099	1047	7581	4440	-	186.973	12.2930	84	84	-	93	153
165	42117	1048	7579	-	-	186.981	5.7210	77	35	130	87	147
166	70100	1062	7583	4442	-	187.016	9.8040	121	121	-	234	294
167	70104	1086	7587	4445	-	187.066	9.4360	93	33	105	103	208
168	70108	1091	7590	-	-	187.078	8.7290	57	37	175	127	174
169	99063	-	7595	-	3391	187.114	18.4150	63	50	95	66	125
170	99062	1110	7594	4450	-	187.124	17.0850	258	169	171	285	345
171	70111	1118	7600	4451	-	187.169	9.2590	82	40	170	91	151
172	99065	1126	7602	-	3392	187.180	14.9990	122	48	40	135	195
173	42124	1145	7609	4457	-	187.246	3.5710	95	94	165	135	195
174	70116	1154	7614	4459	-	187.250	13.9790	20	20	-	156	216
175	70115	1158	7613	4461	-	187.262	13.1840	84	84	-	163	223
176	70121	1190	7622	4469	-	187.367	8.7500	84	48	85	201	261
177	42132	1205	7627	4470	-	187.407	7.8240	77	48	180	85	145
178	42134	1226	7629	4472	-	187.445	8.0010	92	92	-	476	536
179	70125	1231	7631	4473	-	187.454	13.4290	36	36	-	187	247
180	70129	1253	7638	4477	-	187.509	13.6360	55	44	35	95	148
181	70133	1279	7645	4478	-	187.573	12.3290	22	22	-	87	147
182	42139	1290	7647	4480	-	187.612	4.2470	83	60	170	93	153
183	70139	1316	7654	4486	-	187.706	12.3910	58	57	159	374	470
184	70140	1326	7657	4491	-	187.738	11.4840	79	39	148	87	147
185	42141	1330	7656	4492	-	187.749	8.0780	82	82	-	91	151
186	129005	-	7662	4494	-	187.850	25.7750	26	25	180	222	282
187	42144	1375	7668	4505	-	187.913	3.9390	199	158	70	221	281
188	99075	1379	7669	4498	-	187.915	16.8530	119	64	125	132	192
189	99077	1393	7676	-	797	187.978	15.1240	70	46	108	78	138
190	99076	1401	7675	4501	-	187.997	14.4200	303	162	140	336	396
191	99078	1410	7677	4502	-	188.014	16.6880	62	32	40	94	177
192	70152	1419	7682	4506	-	188.044	13.4200	36	29	105	100	160
193	70157	1450	7695	-	3476	188.174	14.0500	94	72	30	120	180
194	14063	-	7694	4517	-	188.190	0.1150	462	86	80	511	571
195	99087	1479	7703	4516	-	188.281	14.5750	90	90	-	100	160
196	70167	1508	7709	4519	-	188.376	8.6550	151	109	152	167	227
197	70168	1516	7711	4522	-	188.415	9.1750	169	42	33	187	247
198	159016	-	7714	4525	-	188.463	30.2770	126	67	65	159	214
199	99090	1532	7716	-	800	188.486	15.3550	82	59	150	91	151
200	42155	1535	7718	4526	-	188.513	7.6990	71	68	163	325	385
201	42156	1540	7721	4527	-	188.535	2.6540	246	78	67	272	332
202	70173	1549	7728	-	3510	188.562	11.0720	22	22	-	51	111
203	42158	1554	7726	4532	-	188.581	6.4680	112	51	166	120	180
204	42159	1555	7727	4535	-	188.585	8.1980	270	232	180	308	397
205	14068	1562	7732	4536	-	188.613	2.1880	303	137	140	336	396
206	42162	1575	7736	-	3521	188.664	7.1600	84	59	18	167	234
207	99093	1588	7742	4540	-	188.712	15.5510	79	66	145	132	202
208	99096	1615	7753	4548	-	188.860	14.4960	252	209	150	279	339
209	-	-	-	4546	-	188.873	-3.7930	104	75	80	135	188
210	70182	1619	7757	4550	-	188.878	12.2210	20	20	-	108	159
211	70184	1632	7760	4552	-	188.916	12.5560	65	65	-	336	396
212	99098	-	7768	4561	-	189.034	19.3230	77	62	110	87	147
213	129010	-	7772	4565	-	189.087	25.9880	595	80	135	659	719
214	70186	1664	7773	4564	-	189.113	11.4390	38	38	-	201	261
215	70189	1673	7777	4567	-	189.136	11.2580	86	41	75	204	265
216	70188	1676	7776	4568	-	189.143	11.2390	93	53	33	206	266
217	70192	1690	7786	4569	-	189.208	13.1630	258	157	23	498	558
218	42178	1692	7785	4570	-	189.223	7.2470	84	84	-	163	223
219	70195	1720	7793	4578	-	189.377	9.5550	90	90	-	175	235

Table A.1: continued.

HRS	CGCG	VCC	UGC	NGC	IC	RA	Dec	a_{IR} (arcsec)	b_{IR} (arcsec)	PA (degree)	r_{in}^{bck} (arcsec)	r_{out}^{bck} (arcsec)
220	70197	1727	7796	4579	-	189.431	11.8180	264	204	100	292	352
221	42183	1730	7794	4580	-	189.452	5.3680	83	73	160	100	160
222	70199	1757	7803	4584	-	189.574	13.1100	82	44	20	91	151
223	42186	1758	7802	-	-	189.587	7.8910	76	40	55	87	147
224	42187	1760	7804	4586	-	189.618	4.3190	181	48	115	201	261
225	70202	1778	7817	-	3611	189.767	13.3640	33	30	115	81	141
226	42191	1780	7821	4591	-	189.802	6.0120	82	37	40	91	151
227	14091	-	7819	4592	-	189.828	-0.5320	241	63	95	267	327
228	-	-	-	-	-	189.843	-5.6650	22	22	-	39	79
229	70204	1809	7825	-	3631	189.950	12.9740	46	46	-	51	111
230	99106	1811	7826	4595	-	189.966	15.2980	90	59	110	100	160
231	70206	1813	7828	4596	-	189.983	10.1760	20	20	-	221	281
232	70213	1859	7839	4606	-	190.240	11.9120	66	56	33	308	412
233	70216	1868	7843	4607	-	190.302	11.8870	163	56	4	280	376
234	70214	1869	7842	4608	-	190.305	10.1560	103	103	-	199	259
235	42205	1883	7850	4612	-	190.387	7.3150	51	51	-	100	160
236	70223	1903	7858	4621	-	190.510	11.6470	69	69	-	356	416
237	42208	1923	7871	4630	-	190.630	3.9600	97	67	10	102	147
238	14109	-	7869	4629	-	190.636	-1.3510	57	51	80	64	124
239	99112	1932	7875	4634	-	190.671	14.2960	119	51	156	309	390
240	70229	1938	7880	4638	-	190.698	11.4430	48	48	-	93	153
241	43002	1939	7878	4636	-	190.708	2.6880	36	35	90	447	507
242	70230	1943	7884	4639	-	190.718	13.2580	134	84	123	148	208
243	15008	-	7895	4643	-	190.834	1.9780	130	126	135	213	265
244	71015	1972	7896	4647	-	190.885	11.5830	109	90	105	120	180
245	71016	1978	7898	4649	-	190.917	11.5530	45	45	-	237	297
246	100004	-	7901	4651	-	190.928	16.3930	163	115	80	181	241
247	71019	1987	7902	4654	-	190.986	13.1270	209	109	128	232	292
248	71023	2000	7914	4660	-	191.133	11.1910	22	22	-	87	147
249	71026	2006	7920	-	3718	191.192	12.3510	38	30	72	120	180
250	43018	-	7924	4665	-	191.275	3.0560	108	108	-	209	269
251	15015	-	7926	4666	-	191.286	-0.4620	189	189	44	198	262
252	15016	-	7931	4668	-	191.384	-0.5350	99	51	5	120	186
253	15019	-	7951	4684	-	191.823	-2.7270	49	46	20	133	193
254	71043	2058	7965	4689	-	191.940	13.7630	246	186	164	272	332
255	43028	-	7961	4688	-	191.944	4.3360	150	137	35	204	264
256	15023	-	-	4691	-	192.057	-3.3330	83	74	105	131	191
257	71045	2070	7970	4698	-	192.096	8.4870	238	119	165	263	323
258	-	-	-	4697	-	192.150	-5.8010	20	20	-	260	314
259	43034	-	7975	4701	-	192.298	3.3890	151	125	40	167	227
260	100011	-	7980	4710	-	192.412	15.1650	103	60	27	199	259
261	43040	-	7982	-	-	192.459	2.8530	147	53	180	157	217
262	43041	-	7985	4713	-	192.491	5.3110	134	90	110	148	208
263	129027	-	7989	4725	-	192.611	25.5010	440	404	35	449	509
264	15027	-	7991	-	-	192.662	1.4640	93	34	170	101	170
265	-	-	-	4720	-	192.678	-4.1560	57	44	115	92	143
266	-	-	-	4731	-	192.755	-6.3930	277	136	90	307	367
267	129028	-	8005	4747	-	192.941	25.7770	165	76	30	183	243
268	71060	-	8007	4746	-	192.981	12.0830	92	51	120	102	162
269	71062	2092	8010	4754	-	193.073	11.3140	120	120	-	233	293
270	15029	-	8009	4753	-	193.092	-1.2000	202	120	105	280	340
271	100015	-	8014	4758	-	193.184	15.8490	129	58	160	139	199
272	71065	2095	8016	4762	-	193.234	11.2310	208	208	-	404	464
273	15031	-	8020	4771	-	193.339	1.2690	171	65	135	186	246
274	15032	-	8021	4772	-	193.372	2.1680	117	44	145	188	254
275	-	-	-	4775	-	193.440	-6.6220	89	84	50	99	159
276	71068	-	8022	4779	-	193.462	9.7100	88	76	10	97	157
277	43060	-	-	4791	-	193.683	8.0530	50	33	65	55	115
278	71071	-	8032	-	-	193.684	13.2370	115	39	165	127	187
279	15037	-	8041	-	-	193.803	0.1170	130	79	157	144	204
280	43066	-	8043	4799	-	193.815	2.8970	72	38	90	74	134
281	43068	-	8045	-	-	193.848	7.9090	38	30	105	42	102
282	43069	-	-	4803	-	193.890	8.2410	22	22	-	23	83
283	43071	-	8054	4808	-	193.954	4.3040	110	70	127	120	180
284	-	-	-	-	3908	194.169	-7.5630	90	43	170	84	144
285	15049	-	8078	4845	-	194.505	1.5760	218	68	100	241	301
286	71092	-	8102	4866	-	194.863	14.1710	294	54	87	415	521
287	15055	-	8121	4904	-	195.245	-0.0270	115	103	145	120	185
288	-	-	-	4941	-	196.055	-5.5520	152	81	15	168	228
289	-	-	-	4981	-	197.203	-6.7770	115	85	149	127	187
290	189037	-	8271	5014	-	197.880	36.2820	64	52	102	79	139
291	217031	-	8388	5103	-	200.125	43.0840	60	60	-	67	127
292	218010	-	8439	5145	-	201.308	43.2670	84	74	85	93	153

Table A.1: continued.

HRS	CGCG	VCC	UGC	NGC	IC	RA	Dec	a_{IR} (arcsec)	b_{IR} (arcsec)	PA (degree)	r_{in}^{bck} (arcsec)	r_{out}^{bck} (arcsec)
293	16069	-	8443	5147	-	201.582	2.1010	92	77	125	103	169
294	246017	-	8593	-	902	204.005	49.9610	93	46	160	101	161
295	73054	-	8616	5248	-	204.384	8.8850	260	187	140	288	348
296	190041	-	8675	5273	-	205.535	35.6540	56	56	95	94	149
297	246023	-	8711	5301	-	206.602	46.1070	181	71	150	193	253
298	218047	-	8725	5303	-	206.937	38.3050	65	53	85	42	102
299	45108	-	8727	5300	-	207.067	3.9510	163	107	140	180	240
300	218058	-	8756	-	-	207.650	42.5410	75	42	85	79	139
301	17088	-	8790	5334	4338	208.227	-1.1150	175	126	40	193	253
302	45137	-	8821	5348	-	208.547	5.2270	154	39	177	237	305
303	295024	-	8843	5372	-	208.692	58.6660	62	58	40	92	162
304	46001	-	8831	5356	-	208.744	5.3340	133	51	12	143	203
305	46003	-	8838	5360	958	208.911	4.9850	83	28	70	101	161
306	46007	-	8847	5363	-	209.030	5.2550	170	110	130	189	249
307	46009	-	8853	5364	-	209.050	5.0140	283	183	30	314	374
308	46011	-	8857	-	-	209.111	4.3970	20	20	-	42	102
309	272031	-	9036	5486	-	211.854	55.1030	44	43	125	150	195
310	47010	-	9172	5560	-	215.023	3.9910	149	50	115	172	232
311	47012	-	9175	5566	-	215.083	3.9340	197	103	35	449	525
312	47020	-	9183	5576	-	215.265	3.2710	31	31	-	165	225
313	47022	-	9187	5577	-	215.305	3.4360	154	64	55	157	217
314	19012	-	9215	-	-	215.863	1.7260	95	62	165	101	161
315	220015	-	9242	-	-	216.338	39.5400	211	34	71	382	451
316	47063	-	9308	5638	-	217.418	3.2330	24	24	-	125	185
317	47066	-	9311	-	1022	217.508	3.7730	51	41	165	51	111
318	47070	-	9328	5645	-	217.664	7.2750	100	63	105	111	171
319	75064	-	9353	5669	-	218.183	9.8920	167	118	61	185	245
320	47090	-	9363	5668	-	218.351	4.4500	152	144	17	198	276
321	47123	-	9427	5692	-	219.576	3.4100	49	33	40	62	124
322	47127	-	9436	5701	-	219.796	5.3640	153	148	90	293	382
323	48004	-	9483	-	1048	220.741	4.8900	100	47	163	104	164

Table A.2: Flux densities, numbers of pixels encompassed within the apertures, and errors of the HRS galaxies at 250, 350 and 500 μm, see Section 5.

HRS	f_{250}	S_{250}[1] (mJy)	f_{350}	S_{350}[1] (mJy)	f_{500}	S_{500}[1] (mJy)	N_{250}	N_{350}	N_{500}	err^{250}_{inst} (mJy)	err^{350}_{inst} (mJy)	err^{500}_{inst} (mJy)	err^{250}_{conf} (mJy)	err^{350}_{conf} (mJy)	err^{500}_{conf} (mJy)	err^{250}_{sky} (mJy)	err^{350}_{sky} (mJy)	err^{500}_{sky} (mJy)
1	1	498.3 ± 37.2	1	210.8 ± 29.1	1	79.3 ± 17.5	163	92	41	6.7	5.0	4.0	21.2	17.4	12.7	29.8	22.8	11.3
2	1	1163.0 ± 58.5	1	482.7 ± 36.2	1	153.0 ± 18.2	185	102	45	7.9	5.6	4.2	22.6	18.3	13.3	53.3	30.8	11.7
3	1	580.9 ± 33.8	1	241.8 ± 23.9	1	79.9 ± 13.8	135	75	32	3.5	2.5	2.0	19.3	15.7	11.2	27.5	17.9	7.7
4	1	12674.1 ± 209.9	1	5240.7 ± 140.6	1	1815.2 ± 68.2	993	560	251	16.2	8.7	6.2	52.4	42.9	31.5	202.6	133.6	60.2
5	1	2741.4 ± 57.0	1	1139.8 ± 44.6	1	361.6 ± 24.5	340	192	86	13.6	7.9	5.6	30.6	25.1	18.3	46.1	36.0	15.3
6	1	619.3 ± 71.6	1	385.1 ± 62.7	1	183.4 ± 38.3	501	281	127	10.9	8.0	6.5	37.2	30.4	22.4	60.2	54.3	30.4
7	2	1238.6 ± 5.0	2	478.3 ± 5.0	2	149.7 ± 8.0	456	256	114	0.0	0.0	0.0	0.0	0.0	0.0	0.0	0.0	0.0
8	1	3982.1 ± 299.1	1	2251.9 ± 150.7	1	1021.0 ± 55.7	1216	685	301	17.2	12.8	10.7	58.0	47.5	34.5	292.9	142.5	42.4
9	1	1433.8 ± 84.2	1	580.5 ± 60.2	1	183.0 ± 31.3	526	296	133	11.3	8.6	6.9	38.1	31.2	22.9	74.2	50.8	20.2
10	1	683.4 ± 44.1	1	300.4 ± 29.4	1	102.5 ± 20.1	207	115	53	7.2	5.6	4.4	23.9	19.5	14.5	36.4	21.3	13.2
11	1	3442.2 ± 70.4	1	1608.0 ± 48.4	1	610.5 ± 25.2	317	182	79	10.4	7.7	5.5	29.6	24.5	17.7	63.0	41.0	17.1
12	1	268.2 ± 15.7	1	118.2 ± 11.0	2	51.8 ± 9.0	55	29	13	3.7	2.9	0.0	12.3	9.8	0.0	8.9	4.0	0.0
13	1	12326.7 ± 132.1	1	5267.7 ± 109.7	1	1886.2 ± 45.6	994	561	248	18.9	13.2	10.0	52.4	43.0	31.3	119.8	100.1	31.6
14	3	215.5 ± 23.7	3	98.0 ± 24.0	3	33.4 ± 14.8	161	92	41	3.7	3.0	2.3	21.1	17.4	12.7	10.2	16.3	7.2
15	1	12895.0 ± 769.4	1	6272.0 ± 460.7	1	2443.8 ± 285.6	3290	1857	821	28.4	21.4	17.2	95.4	78.2	57.0	762.9	453.5	279.3
16	1	5596.0 ± 189.0	1	2602.1 ± 174.9	1	987.6 ± 65.8	967	543	242	15.7	11.3	9.0	51.7	42.3	30.9	181.1	169.4	57.4
17	1	6685.8 ± 193.3	1	2971.9 ± 121.8	1	1174.4 ± 58.5	869	485	216	17.4	11.3	9.0	49.0	40.0	29.2	186.1	114.5	49.9
18	1	1114.6 ± 49.6	1	507.7 ± 44.8	1	182.6 ± 21.5	350	199	84	9.4	7.2	5.5	31.1	25.6	18.2	37.5	36.0	10.0
19	1	2610.5 ± 123.5	1	1225.4 ± 74.4	1	469.5 ± 43.8	585	328	145	12.1	9.3	7.2	40.2	32.9	24.0	116.1	66.1	36.0
20[a]	3	6717.1 ± 109.3	3	2841.8 ± 66.4	3	1015.8 ± 34.8	458	258	116	14.7	8.8	6.6	35.6	29.1	21.4	102.3	59.0	26.6
21	1	550.6 ± 54.6	1	326.9 ± 46.3	1	162.3 ± 23.0	310	173	77	8.8	6.7	5.1	29.3	23.9	17.5	45.3	39.1	14.1
22	1	487.0 ± 86.6	1	223.9 ± 60.4	1	102.8 ± 29.2	509	284	125	6.6	5.0	4.0	37.5	30.6	22.2	77.7	51.9	18.5
23	1	8873.4 ± 123.8	1	3743.0 ± 73.6	1	1280.2 ± 40.1	562	318	139	29.0	13.5	8.5	39.4	32.4	23.5	113.8	64.7	31.4
24	1	8482.9 ± 284.5	1	3807.3 ± 166.5	1	1465.5 ± 86.5	1368	777	343	20.6	14.3	11.4	61.5	50.6	36.8	277.0	158.0	77.5
25	1	8680.5 ± 94.6	1	3549.9 ± 67.6	1	1274.2 ± 47.0	593	334	149	22.4	13.1	8.8	40.5	33.2	24.3	82.5	57.4	39.3
26	1	483.7 ± 34.0	1	269.5 ± 24.7	1	120.1 ± 14.8	179	102	44	6.9	5.1	3.9	22.2	18.3	13.2	24.8	15.8	5.4
27	1	1365.4 ± 46.7	1	547.8 ± 29.5	1	174.0 ± 18.0	230	128	56	8.8	6.1	4.6	25.2	20.5	14.9	38.4	20.2	9.0
28	1	2450.2 ± 70.4	1	1098.6 ± 43.1	1	392.9 ± 25.8	337	189	85	9.9	7.6	5.8	30.5	25.0	18.3	62.6	34.3	17.3
29	1	1809.4 ± 125.2	1	941.1 ± 71.0	1	369.2 ± 47.1	405	226	101	10.3	7.5	5.9	33.5	27.3	20.0	120.3	65.1	42.3
30	1	2308.6 ± 165.1	1	1160.8 ± 92.4	1	504.4 ± 60.6	539	300	133	12.8	8.6	7.2	38.6	31.4	22.9	160.0	86.4	55.6
31	1	5483.5 ± 329.9	1	2490.3 ± 199.8	1	1003.0 ± 98.7	1541	857	382	22.2	15.7	12.1	65.3	53.2	38.8	322.6	192.0	89.9
32	1	130.3 ± 30.3	0	< 64.8	0	< 48.0	129	71	31	5.3	4.2	3.5	18.9	15.1	11.4	23.1	14.9	10.7
33	1	3463.1 ± 104.3	1	1581.8 ± 81.1	1	597.5 ± 47.1	593	334	150	12.1	9.2	7.2	40.5	33.2	24.4	95.4	73.5	39.7
34	1	4922.8 ± 148.5	1	2458.8 ± 132.2	1	1012.2 ± 72.5	757	422	186	17.3	11.2	8.4	45.8	37.3	27.1	140.2	126.3	66.7
35	1	182.3 ± 21.1	1	71.9 ± 15.8	0	< 32.3	91	50	25	4.6	3.7	2.9	15.8	12.7	9.5	13.2	8.7	4.0
36	1	12200.6 ± 219.7	1	4746.5 ± 119.6	1	1565.1 ± 61.1	865	487	213	46.4	17.5	10.4	48.9	40.0	29.0	209.1	111.4	52.8
37	1	2525.4 ± 90.1	1	1085.9 ± 55.2	1	364.7 ± 27.1	375	216	95	10.2	7.7	6.3	32.2	26.7	19.4	83.5	47.7	17.9
38	1	1273.1 ± 52.5	1	678.2 ± 30.2	1	276.9 ± 21.1	320	184	80	9.1	6.9	5.3	29.8	24.6	17.8	42.3	16.1	10.0
39	1	836.7 ± 57.6	1	442.9 ± 35.1	1	201.7 ± 24.9	276	150	71	8.3	6.3	5.0	27.6	22.2	16.8	49.9	26.5	17.7
40	1	2037.2 ± 48.8	1	878.5 ± 35.0	1	308.3 ± 24.6	276	154	71	9.6	6.8	5.3	27.6	22.5	16.8	39.1	25.9	17.3
41	1	1080.9 ± 48.1	1	547.9 ± 36.0	1	220.2 ± 20.0	265	150	67	8.4	6.3	5.1	27.1	22.2	16.3	38.9	27.6	10.3
42	1	9344.5 ± 526.2	1	4353.9 ± 395.5	1	1754.2 ± 144.6	2431	1371	610	25.0	17.8	14.7	82.0	67.2	49.1	519.2	389.4	135.2
43	0	< 48.7	0	< 37.6	0	< 29.7	70	39	17	2.4	2.0	1.7	13.8	11.5	8.7	8.2	4.6	4.4
44	1	1109.7 ± 57.5	1	512.8 ± 37.7	1	196.3 ± 21.0	242	138	63	8.3	6.2	4.9	25.9	21.3	15.8	50.6	30.4	13.0
45[b]	3	1784.8 ± 105.7	3	821.3 ± 66.7	3	301.9 ± 37.6	510	286	126	6.8	5.2	4.3	37.6	30.7	22.3	98.5	59.0	30.0
46	1	2114.3 ± 52.6	1	857.3 ± 40.4	1	281.1 ± 20.5	277	155	68	6.2	4.2	3.1	27.7	22.6	16.4	44.3	33.3	11.9
47	1	1820.0 ± 131.1	1	919.8 ± 83.0	1	371.7 ± 42.7	570	324	142	18.1	8.9	7.0	39.7	32.7	23.7	123.6	75.8	34.8
48	1	19908.0 ± 744.6	1	8725.4 ± 700.4	1	3243.1 ± 358.9	3688	2074	922	33.8	23.2	18.2	101.0	82.6	60.4	737.0	695.1	353.4
49	0	< 79.3	0	< 59.3	0	< 35.0	111	62	27	3.0	2.6	2.0	17.5	14.6	10.3	19.6	13.0	5.1
50	1	9178.2 ± 87.6	1	3560.9 ± 46.9	1	1120.7 ± 36.7	352	197	86	22.3	12.5	7.5	31.2	25.5	18.4	78.7	37.4	30.9
51	1	2805.4 ± 106.4	1	1361.5 ± 95.6	1	546.3 ± 30.8	471	265	118	11.7	8.8	6.7	36.1	29.5	21.6	99.4	90.5	20.9
52	1	618.9 ± 46.8	1	276.0 ± 43.7	1	111.5 ± 20.7	286	159	70	8.4	6.6	5.5	28.1	22.9	16.6	36.5	36.7	11.0
53	1	5965.1 ± 184.2	1	2852.4 ± 134.2	1	1126.2 ± 54.3	805	454	206	17.0	11.4	8.9	47.2	38.7	28.5	177.3	128.0	45.4
54	1	2132.9 ± 126.0	1	962.6 ± 65.8	1	362.7 ± 39.8	618	351	156	11.8	9.1	7.3	41.3	34.0	24.8	118.4	55.6	30.3
55	1	5887.0 ± 161.6	1	2656.5 ± 146.2	1	982.4 ± 67.7	890	500	222	15.7	10.9	9.0	49.6	40.6	29.6	153.0	140.0	60.2
56	1	12586.1 ± 107.2	1	4741.2 ± 78.6	1	1537.0 ± 38.0	465	262	115	40.1	18.8	10.6	35.9	29.4	21.3	92.7	70.4	29.6
57	1	9835.9 ± 250.0	1	4221.3 ± 150.1	1	1515.8 ± 66.1	1220	686	305	18.4	12.6	10.1	58.1	47.5	34.7	242.5	141.8	55.3
58[c]	1	1325.8 ± 32.3	3	613.1 ± 30.7	3	229.3 ± 17.8	193	109	48	7.1	5.4	4.1	23.1	19.0	13.8	21.5	23.5	10.4
59	1	3309.0 ± 166.1	1	1664.8 ± 125.3	1	670.7 ± 52.2	560	316	141	13.1	9.2	7.2	39.3	32.3	23.6	160.8	120.7	46.0
60	1	5639.8 ± 115.8	1	2427.5 ± 86.5	1	864.0 ± 43.2	830	466	206	16.6	11.2	8.7	47.9	39.2	28.5	104.1	76.3	31.2
61	1	592.9 ± 35.0	1	324.1 ± 30.0	1	127.2 ± 20.0	181	102	46	6.6	5.0	4.3	22.4	18.3	13.5	26.0	23.2	14.1
62	1	2171.2 ± 118.3	1	1188.1 ± 80.8	1	535.5 ± 46.8	670	379	170	13.2	9.4	7.8	43.1	35.3	25.9	109.4	72.1	38.2
63	1	7391.9 ± 245.3	1	3604.1 ± 205.5	1	1423.7 ± 90.0	1339	746	338	19.1	13.3	10.8	60.8	49.5	36.6	236.8	199.0	81.5
64	1	1209.1 ± 98.7	1	683.4 ± 61.7	1	274.4 ± 26.8	390	217	96	10.0	7.4	5.9	32.8	26.7	19.5	92.5	55.1	17.5
65	1	1396.9 ± 111.6	1	756.5 ± 64.5	1	335.9 ± 43.1	498	278	125	11.1	8.4	6.6	37.1	30.3	22.2	104.7	56.4	36.3
66	1	10585.4 ± 63.4	1	4243.3 ± 42.8	1	1441.3 ± 26.8	378	210	93	18.3	11.4	7.2	32.3	26.3	19.2	51.3	31.8	17.3
67	1	892.7 ± 79.4	1	506.6 ± 67.1	1	218.1 ± 29.2	404	227	103	9.7	7.6	6.0	33.4	27.3	20.2	71.3	60.8	20.2
68	2	513.4 ± 5.0	2	216.9 ± 5.0	2	73.8 ± 7.0	116	63	28	0.0	0.0	0.0	0.0	0.0	0.0	0.0	0.0	0.0
69	1	3481.8 ± 419.8	1	1828.6 ± 260.5	1	718.9 ± 101.5	1732	978	430	20.9	15.6	12.8	69.2	56.8	41.2	413.5	253.8	91.9
70	1	1139.9 ± 39.3	1	544.9 ± 33.3	1	200.9 ± 19.5	276	157	70	8.3	6.6	5.2	27.6	22.7	16.6	26.7	23.4	8.7
71[d]	4	2432.3 ± 877.0	4	1214.2 ± 564.5	4	419.9 ± 321.3	2807	1574	698	16.1	12.0	9.6	88.1	72.0	52.5	872.4	559.7	316.8
72	1	921.3 ± 75.1	1	421.5 ± 61.5	1	149.6 ± 42.3	343	188	85	9.2	6.9	5.5	30.8	24.9	18.3	67.9	55.8	37.7

Table A.2: continued.

HRS	f_{250}	S_{250}[1] (mJy)	f_{350}	S_{350}[1] (mJy)	f_{500}	S_{500}[1] (mJy)	N_{250}	N_{350}	N_{500}	err^{250}_{inst} (mJy)	err^{350}_{inst} (mJy)	err^{500}_{inst} (mJy)	err^{250}_{conf} (mJy)	err^{350}_{conf} (mJy)	err^{500}_{conf} (mJy)	err^{250}_{sky} (mJy)	err^{350}_{sky} (mJy)	err^{500}_{sky} (mJy)
73	1	31441.6±1540.4	1	14040.4 ± 826.5	1	5093.4 ± 337.3	2730	1539	685	27.1	20.1	16.1	86.9	71.2	52.1	1537.7	823.1	332.8
74	1	7489.2 ± 226.0	1	3095.3 ± 205.5	1	1110.7 ± 89.2	735	417	182	21.9	14.0	10.2	45.1	37.1	26.8	220.3	201.6	84.5
75	1	352.1 ± 35.4	1	200.2 ± 31.8	1	90.9 ± 19.9	181	103	49	6.8	5.2	4.1	22.4	18.4	13.9	26.5	25.4	13.6
76	1	666.0 ± 49.6	1	377.8 ± 38.5	1	149.2 ± 20.0	260	145	65	7.9	6.1	5.0	26.8	21.9	16.0	40.9	31.1	10.9
77	1	36007.6 ± 500.5	1	14723.4 ± 311.4	1	5018.0 ± 168.3	1939	1090	484	43.8	23.5	16.5	73.2	59.9	43.8	493.2	304.7	161.7
78	1	1598.2 ± 172.5	1	828.4 ± 89.0	1	348.9 ± 39.5	518	292	133	11.0	8.4	6.7	37.8	31.0	22.9	167.9	83.0	31.5
79	1	785.7 ± 105.4	1	405.7 ± 68.1	1	174.9 ± 37.3	494	278	124	11.2	8.1	6.8	37.0	30.3	22.2	98.1	60.4	29.2
80	1	2028.1 ± 229.7	1	1051.4 ± 107.7	1	426.3 ± 78.4	788	439	195	13.4	10.2	8.5	46.7	38.0	27.8	224.5	100.2	72.9
81	1	8555.0 ± 210.2	1	3685.7 ± 104.2	1	1254.1 ± 42.7	1027	573	258	27.8	15.0	10.3	53.3	43.4	32.0	201.4	93.5	26.4
82	1	863.7 ± 62.5	1	368.8 ± 39.5	1	129.0 ± 21.4	276	152	68	9.0	6.5	5.0	27.6	22.4	16.4	55.4	32.0	12.8
83	1	394.1 ± 30.1	1	210.2 ± 30.0	1	84.8 ± 15.4	187	104	45	6.7	5.3	3.9	22.7	18.5	13.3	18.6	22.9	6.6
84	1	1326.1 ± 33.6	1	586.4 ± 25.1	1	208.5 ± 16.0	165	94	42	6.6	5.2	3.9	21.4	17.6	12.9	25.0	17.1	8.7
85	1	15287.9 ± 349.6	1	6772.1 ± 229.3	1	2577.8 ± 133.7	1473	828	367	29.7	17.8	12.8	63.8	52.2	38.1	342.5	222.5	127.5
86	1	5141.3 ± 270.8	1	2619.4 ± 158.5	1	1156.1 ± 52.0	1398	792	354	19.0	13.7	11.4	62.2	51.1	37.4	262.9	149.4	34.3
87	1	918.8 ± 94.4	1	383.6 ± 66.8	1	130.2 ± 29.0	303	165	77	6.8	4.9	3.8	35.5	29.0	21.0	87.2	60.0	19.6
88	1	8144.1 ± 486.8	1	3913.8 ± 293.7	1	1636.2 ± 146.1	2981	1674	745	28.6	20.5	16.3	90.8	74.2	54.3	477.4	283.4	134.7
89	1	9631.1 ± 238.5	1	5154.7 ± 180.4	1	2289.0 ± 68.7	1538	867	385	20.8	14.7	12.0	65.2	53.4	39.0	228.5	171.7	55.3
90	0	< 277.6	0	< 296.9	0	< 137.3	725	408	181	7.9	6.1	4.8	44.9	36.8	26.7	80.5	91.6	36.9
91	1	27168.9±1158.3	1	12563.7 ± 601.6	1	4741.7 ± 319.4	3915	2201	978	38.1	22.3	16.6	103.9	85.1	62.2	1153.0	595.1	312.8
92	1	1504.9 ± 95.0	1	742.6 ± 57.0	1	300.5 ± 31.7	455	253	114	10.4	7.1	5.7	35.5	28.9	21.1	87.6	48.5	22.9
93	1	1488.0 ± 154.5	1	672.3 ± 90.1	1	246.8 ± 52.3	771	431	193	8.0	6.2	5.0	46.2	37.7	27.7	147.2	81.6	44.1
94	1	3860.2 ± 140.0	1	2206.8 ± 103.7	1	1034.4 ± 61.8	902	508	235	14.5	10.2	8.1	50.6	40.9	30.5	129.8	94.7	53.2
95	1	3499.3 ± 58.7	1	1369.8 ± 33.4	1	441.7 ± 21.2	266	154	68	13.4	8.2	5.6	27.1	22.5	16.4	50.3	23.3	12.2
96	1	12655.3 ± 227.8	1	5205.6 ± 155.4	1	1788.3 ± 80.7	1116	624	283	21.9	12.9	9.2	55.5	45.7	33.5	219.8	148.0	72.8
97	1	21484.6 ± 486.3	1	10248.2 ± 308.4	1	3917.9 ± 151.6	3038	1709	760	31.2	20.1	15.2	91.6	75.0	54.8	476.6	298.4	140.5
98	1	3220.2 ± 119.5	1	1723.1 ± 68.5	1	740.7 ± 36.8	598	334	151	15.1	9.3	6.7	40.7	33.2	24.4	111.4	59.2	26.7
99	1	637.9 ± 23.1	1	258.5 ± 15.2	1	80.6 ± 10.8	103	56	26	5.7	3.4	2.6	16.5	13.6	10.1	15.1	5.8	2.7
100	1	7095.6 ± 76.4	1	2914.3 ± 50.5	1	940.1 ± 34.6	362	204	90	16.3	9.2	5.8	31.5	25.9	18.9	67.6	42.4	28.5
101	0	< 364.5	0	< 198.4	0	< 135.0	662	372	165	7.5	5.7	4.7	42.8	35.0	26.0	113.4	55.8	36.4
102	1	64026.1±2329.3	1	25753.9 ± 599.1	1	8685.7 ± 406.2	5304	2987	1324	44.0	29.6	23.1	121.1	99.2	72.4	2325.7	590.1	399.0
103[c]	1	844.6 ± 47.3	3	388.4 ± 33.1	3	135.1 ± 20.4	215	121	52	6.4	4.8	3.6	24.4	20.0	14.3	40.0	26.0	14.0
104	0	< 156.0	0	< 126.1	0	< 63.2	221	124	55	7.2	5.6	4.6	24.8	20.5	14.6	45.2	36.3	14.4
105	0	< 150.2	0	< 92.2	0	< 59.0	175	98	43	5.5	4.1	3.4	22.1	18.1	13.3	44.6	24.5	14.0
106	1	1476.4 ± 139.5	1	650.7 ± 95.8	1	252.7 ± 42.6	675	379	177	12.5	9.5	7.6	43.2	35.3	26.5	132.1	88.6	32.5
107	1	964.3 ± 63.2	1	486.0 ± 40.2	1	200.8 ± 30.4	279	159	70	8.4	5.6	4.4	27.8	22.3	16.5	56.2	33.0	25.2
108	1	595.2 ± 37.1	1	259.0 ± 30.2	1	87.9 ± 17.9	232	129	54	7.2	5.0	3.9	25.0	20.6	15.5	26.4	21.5	8.0
109	1	2239.0 ± 82.4	1	1173.7 ± 64.4	1	498.9 ± 32.2	594	336	146	14.0	8.8	6.3	40.5	33.3	24.0	70.3	54.4	20.4
110	1	4021.7 ± 133.6	1	1973.8 ± 110.3	1	828.0 ± 60.2	748	416	184	13.3	9.4	7.4	45.5	37.0	27.4	124.9	103.4	53.1
111	1	11959.2 ± 120.1	1	5008.5 ± 72.3	1	1716.6 ± 36.0	666	373	166	18.8	10.6	7.4	42.9	35.0	25.5	110.6	62.4	24.4
112	1	652.0 ± 45.6	1	291.7 ± 29.9	1	104.5 ± 17.8	239	132	60	7.3	5.1	3.8	25.6	21.1	15.4	37.0	20.7	8.0
113	1	18637.1 ± 244.7	1	8302.4 ± 142.5	1	2969.7 ± 64.6	1396	784	348	47.8	23.1	13.2	62.1	50.8	37.4	231.8	131.1	51.1
114	1	54637.8 ± 912.0	1	22717.1 ± 692.9	1	8098.4 ± 415.6	5423	3055	1358	47.8	26.5	19.8	122.4	100.2	73.3	902.5	685.1	408.6
115	1	642.3 ± 36.6	1	278.3 ± 27.5	1	92.5 ± 15.5	180	103	44	6.7	4.4	3.3	22.4	18.4	13.2	28.2	20.0	7.4
116	0	< 481.1	0	< 409.4	0	< 170.9	1040	585	260	13.2	9.8	8.0	53.7	43.8	31.8	150.5	128.9	46.6
117	1	4430.1 ± 106.4	1	1943.4 ± 84.0	1	672.2 ± 47.9	659	371	163	24.3	12.0	7.6	42.7	34.9	25.6	94.3	75.5	39.8
118	1	916.9 ± 86.2	1	494.2 ± 68.8	1	199.7 ± 35.7	416	236	102	8.6	6.4	5.2	33.9	27.7	20.3	78.8	62.6	28.9
119	1	4085.2 ± 243.6	1	1631.6 ± 156.2	1	521.6 ± 86.8	975	550	247	26.0	13.1	8.6	52.0	42.4	31.3	236.5	149.8	80.5
120	1	3928.7 ± 178.2	1	1689.4 ± 159.7	1	577.1 ± 69.0	910	514	230	18.3	11.2	8.0	50.2	41.0	30.2	170.0	153.9	61.6
121	1	4699.6 ± 65.4	1	2085.9 ± 51.2	1	749.1 ± 31.1	432	245	109	18.8	10.0	6.1	34.6	28.2	20.8	52.3	41.6	22.3
122	1	66006.4±2209.8	1	27948.0±1792.0	1	9742.4 ± 817.0	113876408		2849	65.4	43.0	32.6	177.4	145.3	106.2	2201.7	1785.6	809.4
123	1	1781.7 ± 88.8	1	846.5 ± 59.7	1	322.9 ± 31.8	540	308	139	10.5	7.5	5.9	38.6	31.9	23.5	79.3	50.0	20.6
124	1	3499.0 ± 226.4	1	1721.3 ± 140.8	1	680.8 ± 78.0	1312	735	330	18.8	12.3	9.4	60.2	49.2	36.1	217.4	131.4	68.5
125	0	< 44.3	0	< 31.7	0	< 20.4	44	24	11	3.2	2.2	2.1	10.9	8.7	6.0	9.4	5.6	2.6
126	0	< 344.7	0	< 272.5	0	< 172.0	651	366	162	7.5	5.7	4.6	42.6	34.7	25.5	106.5	83.8	51.1
127	1	3570.5 ± 96.0	1	1599.0 ± 59.0	1	589.7 ± 28.3	418	233	107	14.0	8.3	5.7	34.0	27.9	20.6	88.7	51.4	18.5
128	1	952.3 ± 50.2	1	471.5 ± 33.9	1	190.0 ± 21.2	274	153	69	7.5	5.3	4.3	27.5	22.6	16.6	41.4	24.7	12.5
129[e]	2	320.6 ± 5.4	2	104.1 ± 8.0	0	< 64.9	184	104	53	0.0	0.0	2.8	0.0	0.0	14.6	0.0	0.0	15.7
130	1	1532.7 ± 82.6	1	752.6 ± 68.5	1	289.5 ± 38.5	451	254	113	9.5	6.8	5.3	35.3	28.9	21.0	74.0	61.7	31.8
131	1	774.9 ± 60.0	1	341.2 ± 44.0	1	125.6 ± 29.0	376	213	97	8.2	6.1	5.0	32.1	26.5	19.6	50.0	34.6	20.8
132	1	834.7 ± 77.3	1	439.1 ± 38.3	1	185.2 ± 29.1	413	227	107	8.9	6.4	5.2	33.8	27.6	20.5	69.0	25.8	20.0
133	1	1893.9 ± 76.4	1	1249.6 ± 87.2	1	611.1 ± 47.1	639	361	160	12.7	9.4	7.6	42.0	34.5	25.2	62.5	79.6	39.1
134	1	1359.8 ± 87.6	1	597.3 ± 60.8	1	211.7 ± 32.8	430	242	109	11.8	7.1	5.5	34.5	28.2	20.8	79.7	53.4	24.7
135	0	< 449.8	0	< 329.5	0	< 195.2	538	303	134	21.7	16.1	13.1	87.6	71.7	52.1	119.8	81.6	36.7
136	1	1946.6 ± 53.3	1	771.7 ± 37.5	1	250.5 ± 18.8	233	132	59	16.0	7.2	4.4	25.7	20.9	15.5	43.8	30.3	9.7
137	0	< 940.4	0	< 484.0	0	< 313.7	1307	735	326	14.7	11.1	9.0	59.9	49.7	36.3	307.3	153.1	97.6
138	2	209.5 ± 5.6	2	125.3 ± 8.2	2	108.9 ± 8.8	105	58	25	0.0	0.0	0.0	0.0	0.0	0.0	0.0	0.0	0.0
139	1	1069.8 ± 70.3	1	535.9 ± 35.0	1	212.3 ± 25.7	302	167	79	7.9	5.7	4.8	29.1	23.5	17.7	63.6	25.4	18.1
140	1	3034.0 ± 228.3	1	1471.4 ± 189.2	1	554.2 ± 85.5	1169	657	290	14.3	10.6	8.5	56.9	46.6	33.9	220.7	183.0	78.0
141	1	4868.0 ± 162.7	1	2230.9 ± 130.5	1	793.5 ± 86.6	947	532	233	14.1	9.9	7.7	51.2	41.8	30.4	153.8	123.3	80.8
142[b]	3	4822.0 ± 105.5	3	1960.0 ± 60.8	3	659.1 ± 36.7	517	284	130	17.0	9.5	6.9	37.8	30.6	22.7	97.1	51.7	28.0
143	1	4675.3 ± 129.9	1	2323.6 ± 80.8	1	952.0 ± 37.2	605	339	150	17.3	10.7	7.1	40.9	33.2	24.4	122.1	72.9	27.3
144	1	8570.1 ± 314.2	1	3540.8 ± 113.8	1	1287.2 ± 79.2	982	542	243	31.2	15.1	9.1	51.8	42.7	31.0	308.3	104.4	72.3
145[b]	3	1820.4 ± 102.3	3	937.2 ± 83.2	3	413.2 ± 42.1	610	343	151	10.6	7.7	6.1	41.1	33.6	24.4	93.1	75.7	33.7

Table A.2: continued.

HRS	f_{250}	S_{250}[1] (mJy)	f_{350}	S_{350}[1] (mJy)	f_{500}	S_{500}[1] (mJy)	N_{250}	N_{350}	N_{500}	err^{250}_{inst} (mJy)	err^{350}_{inst} (mJy)	err^{500}_{inst} (mJy)	err^{250}_{conf} (mJy)	err^{350}_{conf} (mJy)	err^{500}_{conf} (mJy)	err^{250}_{sky} (mJy)	err^{350}_{sky} (mJy)	err^{500}_{sky} (mJy)
146	1	1749.9 ± 72.4	1	868.3 ± 49.8	1	345.5 ± 24.0	304	171	76	9.6	6.3	4.7	29.0	23.9	17.3	65.6	43.3	15.9
147	1	2556.2 ± 76.7	1	1309.7 ± 61.3	1	540.1 ± 28.7	433	243	107	11.7	8.0	6.4	34.6	28.3	20.6	67.4	53.8	18.9
148	1	3775.5 ± 145.2	1	2034.4 ± 110.5	1	899.6 ± 42.1	716	401	178	14.1	10.1	8.1	44.5	36.3	26.5	137.4	103.8	31.6
149	1	14005.7 ± 122.9	1	5933.2 ± 68.3	1	2014.7 ± 52.7	706	398	180	41.4	19.6	9.7	44.2	36.2	26.5	107.0	54.5	44.5
150[f]	1	744.4 ± 262.2	1	455.7 ± 154.5	1	176.2 ± 76.8	1293	725	324	14.1	10.8	8.9	80.2	65.7	47.9	249.2	139.5	59.4
151	1	2503.0 ± 167.4	1	1133.8 ± 114.3	1	434.1 ± 56.4	784	445	196	12.4	8.8	7.3	46.6	38.3	27.9	160.3	107.4	48.5
152	1	2790.7 ± 73.6	1	1084.2 ± 71.7	1	338.6 ± 30.7	452	258	113	11.4	8.6	6.5	35.3	29.1	21.1	63.6	65.0	21.2
153	1	2536.9 ± 108.4	1	1162.6 ± 102.9	1	427.1 ± 42.4	683	385	174	11.9	8.4	6.6	43.5	35.6	26.2	98.5	96.2	32.7
154	1	2208.1 ± 180.4	1	1220.1 ± 131.4	1	539.7 ± 77.5	889	497	219	12.5	9.2	7.5	49.6	40.5	29.6	173.0	124.7	71.3
155	0	< 322.0	0	< 216.7	0	< 144.4	651	366	162	10.7	7.8	6.3	42.3	34.8	25.5	98.0	62.8	40.3
156	1	8487.4 ± 168.5	1	3367.5 ± 120.4	1	1096.9 ± 51.0	755	424	189	27.2	14.1	9.5	45.7	37.4	27.3	159.9	113.6	42.0
157	1	4100.9 ± 79.9	1	1788.0 ± 60.7	1	650.5 ± 31.3	383	215	97	11.6	8.4	6.2	32.5	26.6	19.6	72.0	53.9	23.6
158	1	1079.9 ± 107.3	1	632.9 ± 88.8	1	307.6 ± 47.4	568	319	144	11.3	8.7	7.0	39.6	32.4	23.9	99.1	82.2	40.3
159	1	2636.6 ± 77.7	1	1014.8 ± 79.5	1	331.9 ± 46.4	593	334	150	16.3	9.1	6.3	40.5	33.2	24.4	64.2	71.7	38.9
160	1	4145.2 ± 156.3	1	1859.9 ± 96.1	1	680.6 ± 45.8	736	414	183	13.9	9.9	8.0	45.1	36.9	26.9	149.0	88.2	36.1
161	2	1610.6 ± 4.4	2	694.1 ± 4.2	2	220.8 ± 5.7	224	125	55	0.0	0.0	0.0	0.0	0.0	0.0	0.0	0.0	0.0
162	1	1839.0 ± 276.7	1	690.0 ± 112.8	1	193.5 ± 53.3	559	317	141	10.4	6.4	4.6	39.3	32.3	23.6	273.7	107.9	47.6
163[g]	1	8132.3 ± 684.6	1	3660.7 ± 271.1	1	1263.9 ± 122.7	1392	782	346	16.9	10.4	7.1	62.0	50.8	37.0	681.6	266.1	116.8
164	0	< 228.1	0	< 239.6	0	< 105.2	621	349	155	10.1	7.7	6.1	41.3	33.9	24.4	63.0	71.9	24.5
165	1	688.5 ± 38.8	1	331.0 ± 35.5	1	134.3 ± 20.7	242	138	62	7.9	6.1	4.7	25.9	21.3	15.7	27.8	27.8	12.7
166	0	< 722.6	0	< 625.5	0	< 253.2	1281	721	320	14.7	11.0	8.9	59.5	48.8	35.8	232.9	202.4	75.9
167	1	1374.7 ± 62.5	1	576.8 ± 49.7	1	184.7 ± 23.9	275	154	65	9.7	5.9	4.1	27.6	22.5	16.0	55.2	44.0	17.2
168	1	612.0 ± 45.7	1	295.7 ± 31.1	1	123.9 ± 17.4	186	107	47	6.2	4.4	3.5	22.9	18.8	13.6	39.1	24.4	10.3
169	1	1168.7 ± 59.8	1	556.7 ± 54.8	1	210.6 ± 27.5	284	157	73	8.4	6.4	5.7	28.0	22.7	17.0	52.2	49.5	20.8
170	1	8521.2 ± 1158.7	1	3878.6 ± 686.5	1	1470.2 ± 196.4	3822	2152	958	30.8	22.9	18.4	102.8	84.2	61.6	1153.7	680.9	185.5
171	1	2240.9 ± 61.8	1	898.5 ± 54.5	1	294.3 ± 26.2	291	162	73	13.5	7.2	4.7	28.4	23.1	16.9	53.2	48.9	19.5
172	1	2665.8 ± 148.1	1	1106.7 ± 101.7	1	347.4 ± 36.1	523	291	130	13.9	9.3	6.7	38.0	31.0	22.7	142.5	96.4	27.3
173	1	5023.5 ± 192.1	1	1990.5 ± 77.9	1	633.7 ± 50.0	789	443	196	10.0	6.5	5.4	46.7	38.2	27.9	186.1	67.6	41.2
174	2	1447.5 ± 5.0	2	568.4 ± 5.8	2	185.3 ± 5.4	266	152	67	0.0	0.0	0.0	0.0	0.0	0.0	0.0	0.0	0.0
175	0	< 222.6	0	< 194.9	0	< 93.3	622	350	155	10.3	7.6	6.1	41.6	34.0	25.0	60.6	54.9	17.4
176	1	2126.8 ± 68.6	1	887.5 ± 37.8	1	282.0 ± 25.0	357	201	90	15.9	7.8	5.2	31.4	25.7	18.9	58.9	26.6	15.6
177	1	2428.9 ± 64.6	1	1027.6 ± 34.0	1	366.7 ± 24.5	328	182	82	10.8	6.7	4.9	29.8	24.5	18.0	56.3	22.6	15.8
178	0	< 326.7	0	< 193.0	0	< 144.3	742	417	185	11.4	8.4	6.7	45.2	37.2	27.1	98.4	51.8	39.2
179	0	< 85.8	0	< 61.4	0	< 40.6	115	64	28	4.4	3.2	2.9	17.9	14.6	11.2	21.9	13.9	6.9
180	1	441.9 ± 48.0	1	156.0 ± 38.1	1	44.0 ± 22.4	216	118	55	7.6	5.4	4.4	29.2	23.9	17.5	37.3	29.3	13.4
181	0	< 39.3	0	< 29.0	0	< 19.6	44	24	11	2.7	2.0	1.4	10.9	8.7	6.0	6.7	3.7	2.3
182	1	3112.1 ± 84.2	1	1478.6 ± 42.8	1	553.1 ± 31.7	443	248	110	10.8	8.4	6.4	35.0	28.6	20.9	75.8	30.7	22.9
183[h]	1	763.9 ± 60.5	1	1006.5 ± 36.9	1	1269.2 ± 21.7	293	164	76	7.7	6.9	8.7	28.5	23.2	17.3	52.8	27.8	9.8
184	1	823.0 ± 91.1	1	307.1 ± 56.8	1	100.5 ± 28.1	265	158	64	9.6	5.5	4.2	27.1	22.3	16.3	86.5	51.9	22.6
185	1	1344.6 ± 98.9	1	607.7 ± 71.8	1	215.7 ± 43.1	593	332	145	10.5	7.6	6.1	40.5	33.1	24.2	89.6	63.3	35.1
186	3	84.9 ± 19.8	3	34.7 ± 14.5	0	< 25.0	61	37	14	2.4	1.8	1.4	13.0	11.0	7.2	14.8	9.3	4.0
187[i]	1	8470.5 ± 403.3	1	4212.1 ± 291.0	1	1737.3 ± 161.1	2763	1560	693	27.4	19.5	16.1	87.4	71.7	52.4	392.8	281.4	151.5
188	1	3930.0 ± 127.1	1	1885.4 ± 81.2	1	767.2 ± 43.9	670	373	166	13.4	9.4	8.1	43.0	35.1	25.6	118.8	72.6	34.7
189	1	1568.4 ± 46.3	1	718.9 ± 40.5	1	266.0 ± 25.0	294	164	72	9.0	6.6	5.4	28.5	23.2	16.9	35.4	32.5	17.6
190	1	57336.0±1379.6	1	24221.3 ± 645.1	1	8461.8 ± 366.1	4299	2414	1083	38.9	27.2	21.8	109.0	89.1	65.4	1374.8	638.3	359.6
191	1	381.2 ± 41.8	1	202.3 ± 35.2	1	77.4 ± 20.1	175	97	43	6.5	4.9	4.0	22.0	17.9	13.0	34.9	29.9	14.8
192	1	320.6 ± 25.2	1	136.8 ± 23.7	1	44.1 ± 12.3	95	53	22	4.9	3.2	2.3	16.2	13.2	9.3	18.6	19.4	7.7
193	1	2237.8 ± 125.8	1	1103.9 ± 83.1	1	450.6 ± 35.0	600	338	151	11.5	8.0	6.0	40.7	33.4	24.1	118.4	75.7	24.6
194	1	33388.0±1108.5	1	17557.5 ± 445.9	1	7599.0 ± 224.1	3473	1955	863	39.4	26.2	19.8	98.0	80.2	58.4	1103.4	437.8	215.5
195	0	< 428.7	0	< 251.5	0	< 133.3	718	403	179	12.7	9.7	7.7	44.6	36.5	26.6	135.2	74.8	34.7
196	1	5086.1 ± 275.8	1	2500.9 ± 188.1	1	1031.3 ± 98.4	1444	815	357	17.1	12.0	9.5	63.2	51.4	37.6	268.0	180.5	90.4
197	1	3392.6 ± 78.9	1	1570.1 ± 67.1	1	601.8 ± 38.1	620	352	158	16.8	9.8	6.7	41.4	34.0	24.8	65.0	57.0	28.1
198	1	1774.6 ± 67.2	1	938.0 ± 64.1	1	414.4 ± 36.2	740	417	182	12.9	10.1	7.9	45.2	37.1	26.8	48.0	51.3	23.0
199	1	873.0 ± 123.1	1	394.1 ± 82.3	1	150.4 ± 34.9	424	241	110	10.2	7.7	6.2	34.2	28.2	20.9	117.8	77.0	27.3
200	1	7778.6 ± 89.2	1	3038.0 ± 61.9	1	995.0 ± 27.3	422	237	108	62.3	24.2	9.4	28.4	23.5	16.5	57.1	51.9	19.6
201	1	45589.8 ± 429.1	1	19242.9 ± 200.9	1	6776.4 ± 113.8	1687	947	420	68.6	31.4	16.6	68.3	55.9	40.8	418.1	190.4	104.9
202	0	< 47.4	0	< 35.9	0	< 27.4	44	24	11	3.2	2.4	2.1	13.5	10.6	8.5	7.5	4.9	2.5
203	1	6901.7 ± 117.7	1	3088.4 ± 71.2	1	1175.1 ± 47.1	504	282	124	20.0	12.0	9.4	37.4	30.5	22.1	109.8	63.2	40.5
204	1	34624.3±1146.6	1	15607.8±1019.1	1	5891.4 ± 450.2	5476	3084	1362	41.0	24.9	18.7	123.1	100.8	73.4	1139.2	1013.8	443.8
205	1	27619.4 ± 623.9	1	12281.5 ± 431.3	1	4883.1 ± 162.1	3642	2055	915	57.8	29.6	19.7	100.4	82.3	60.2	613.1	422.4	149.2
206	1	1516.8 ± 72.8	1	666.2 ± 63.3	1	235.3 ± 31.3	432	247	106	10.8	8.0	6.2	34.6	28.5	20.5	63.1	55.9	22.9
207	1	4029.4 ± 105.6	1	1741.1 ± 69.6	1	611.4 ± 40.4	460	259	116	11.3	8.4	6.7	35.7	29.2	21.4	98.8	62.6	33.5
208	1	15625.3±1675.7	1	7154.1 ± 739.7	1	2664.2 ± 276.8	4605	2595	1155	33.6	25.2	20.5	112.8	92.4	67.6	1671.5	733.5	267.6
209	3	583.0 ± 96.1	3	291.2 ± 84.6	3	128.7 ± 52.7	687	385	174	7.7	5.8	4.7	43.6	35.6	26.2	85.3	76.5	45.5
210	2	91.4 ± 4.2	0	< 57.8	0	< 37.1	104	63	28	0.0	3.2	2.6	0.0	14.3	10.9	0.0	12.5	5.3
211	0	< 255.2	0	< 177.5	0	< 99.0	369	207	92	7.8	5.9	4.7	32.2	26.2	18.7	78.4	52.7	26.8
212	1	1453.9 ± 76.8	1	756.5 ± 72.1	1	305.0 ± 37.1	423	242	107	10.2	7.9	6.1	34.2	28.2	20.6	68.0	65.9	30.2
213	1	62058.5±1177.0	1	31069.7 ± 686.3	1	12870.2 ± 288.9	4174	2348	1047	52.2	31.8	23.0	107.4	87.9	64.4	1170.9	679.9	280.7
214	0	< 108.9	0	< 62.0	0	< 47.5	132	74	33	4.6	3.4	2.7	19.0	15.6	11.2	30.6	13.1	10.8
215[j]	3	9674.8 ± 109.2	3	3991.5 ± 48.0	3	1360.2 ± 25.3	314	177	78	18.8	9.5	6.8	34.6	28.2	21.0	101.8	37.7	12.4
216[j]	3	28827.2 ± 163.7	3	11511.9 ± 68.5	3	3813.1 ± 33.1	433	239	109	75.2	33.7	17.0	37.8	31.0	22.5	140.4	50.9	17.3
217	1	22023.9 ± 894.2	1	9219.8 ± 580.8	1	3105.1 ± 265.6	3548	1993	887	40.2	24.9	18.9	99.0	81.0	59.2	887.8	574.6	258.2
218	0	< 255.5	0	< 267.4	0	< 121.6	622	350	155	7.2	5.6	4.5	41.6	34.1	24.8	74.0	82.2	31.8

Table A.2: continued.

HRS	f_{250}	S_{250}[1] (mJy)	f_{350}	S_{350}[1] (mJy)	f_{500}	S_{500}[1] (mJy)	N_{250}	N_{350}	N_{500}	err^{250}_{inst} (mJy)	err^{350}_{inst} (mJy)	err^{500}_{inst} (mJy)	err^{250}_{conf} (mJy)	err^{350}_{conf} (mJy)	err^{500}_{conf} (mJy)	err^{250}_{sky} (mJy)	err^{350}_{sky} (mJy)	err^{500}_{sky} (mJy)
219	0	< 295.1	0	< 246.0	0	< 147.4	714	401	178	7.8	6.1	4.8	44.6	36.7	26.6	87.3	73.1	41.0
220	1	21263.2±2091.8	1	9340.7 ± 802.9	1	3339.0 ± 526.2	4712	2643	1177	35.0	25.5	20.6	114.2	93.3	68.2	2088.4	797.1	521.4
221	1	3992.5 ± 96.2	1	1742.9 ± 55.5	1	607.6 ± 28.1	533	300	131	13.3	9.6	7.2	38.4	31.4	22.8	87.2	44.8	14.8
222	1	508.9 ± 64.4	1	222.6 ± 44.0	1	85.7 ± 22.5	317	176	79	8.7	6.6	5.2	29.6	24.1	17.7	56.5	36.3	12.9
223	1	475.8 ± 76.5	1	278.6 ± 42.4	1	122.5 ± 24.6	268	151	67	8.1	6.0	4.9	27.2	22.3	16.3	71.0	35.5	17.7
224	1	2159.0 ± 199.6	1	992.6 ± 107.4	1	343.8 ± 63.8	769	434	193	14.1	10.2	8.2	46.1	37.8	27.6	193.7	100.0	56.9
225	1	88.6 ± 21.2	0	< 174.0	0	< 95.9	90	268	119	4.4	8.0	6.2	15.8	29.7	21.6	13.5	49.2	22.7
226	1	1328.5 ± 48.2	1	629.5 ± 35.2	1	240.3 ± 23.7	270	151	68	8.4	6.3	5.1	27.3	22.3	16.4	38.8	26.5	16.3
227	1	4231.6 ± 229.1	1	2463.5 ± 131.5	1	1165.4 ± 73.8	1340	756	335	18.4	13.6	11.1	60.9	49.9	36.4	220.1	120.9	63.2
228	0	< 37.7	0	< 32.3	0	< 19.3	28	16	7	3.1	2.5	2.0	10.9	9.3	6.0	5.5	4.8	1.4
229	0	< 206.9	0	< 92.8	0	< 59.2	186	104	46	6.5	5.1	4.0	22.6	18.2	13.3	64.8	24.4	14.0
230	1	2294.8 ± 106.6	1	1048.0 ± 72.1	1	373.4 ± 31.9	474	262	120	11.0	8.4	6.4	36.2	29.4	21.8	99.6	65.3	22.4
231	2	356.3 ± 8.8	2	134.4 ± 10.5	2	48.6 ± 20.7	143	83	37	0.0	0.0	0.0	0.0	0.0	0.0	0.0	0.0	0.0
232	1	1524.0 ± 87.1	1	611.4 ± 48.2	1	205.9 ± 35.6	325	185	80	10.6	6.9	5.2	30.0	24.7	17.8	81.0	40.8	30.4
233	1	5224.3 ± 208.3	1	2203.1 ± 107.2	1	751.4 ± 68.4	809	450	199	21.1	12.6	9.0	47.3	38.5	28.1	201.7	99.3	61.7
234	0	< 403.9	0	< 269.4	0	< 137.1	929	522	232	8.7	6.7	5.4	50.6	41.4	30.4	124.4	79.4	33.7
235	0	< 102.9	0	< 104.7	0	< 56.9	234	131	58	4.5	3.5	2.8	25.4	20.9	15.5	22.6	27.8	10.5
236	0	< 317.3	0	< 212.5	0	< 99.2	415	233	103	6.1	4.5	3.7	33.9	27.8	20.1	100.0	65.0	26.0
237	1	3453.6 ± 164.2	1	1473.2 ± 116.5	1	509.6 ± 50.5	571	323	142	12.6	9.2	7.2	39.7	32.6	23.7	158.9	111.5	44.0
238	1	351.5 ± 58.3	1	187.9 ± 36.9	1	87.7 ± 20.7	260	151	66	7.7	6.2	4.9	26.8	22.3	16.2	51.2	28.7	12.0
239	1	6684.3 ± 127.1	1	2739.4 ± 86.4	1	938.7 ± 33.1	533	297	136	23.3	12.0	8.1	38.4	31.3	23.2	118.9	79.7	22.2
240	0	< 182.5	0	< 153.8	0	< 106.6	203	114	50	9.9	7.6	6.1	56.1	46.0	33.6	21.3	21.4	9.8
241	1	97.0 ± 30.8	1	40.8 ± 22.8	0	< 26.0	111	66	27	3.2	2.6	1.2	17.5	14.7	6.0	25.1	17.1	6.2
242	1	4008.9 ± 223.0	1	1916.3 ± 163.4	1	764.8 ± 75.2	994	558	250	16.0	11.4	9.3	52.4	42.9	31.5	216.2	157.3	67.6
243	1	3278.1 ± 239.1	1	1635.0 ± 182.9	1	618.5 ± 85.2	1438	811	357	10.9	8.4	6.7	63.1	51.7	37.6	230.4	175.2	76.1
244	1	11627.9 ± 191.5	1	4833.0 ± 86.5	1	1612.2 ± 51.6	861	488	215	11.9	7.9	6.1	48.8	40.1	29.2	184.8	76.3	42.2
245	0	< 137.2	0	< 74.7	0	< 48.8	183	103	45	4.3	3.1	3.1	22.7	18.7	13.2	39.5	16.2	9.0
246	1	12459.9 ± 405.2	1	5559.6 ± 214.2	1	2128.2 ± 115.2	1653	932	411	22.6	15.3	12.5	67.6	55.4	40.3	398.9	206.3	107.1
247	1	27785.6 ± 418.1	1	12088.0 ± 272.4	1	4533.9 ± 134.9	1996	1124	499	27.8	18.7	14.3	74.3	60.8	44.4	410.5	264.9	126.6
248	0	< 39.4	0	< 27.5	0	< 19.5	44	24	11	1.8	1.5	1.3	10.9	8.9	6.3	7.1	1.6	1.1
249	1	153.5 ± 25.8	1	83.6 ± 20.5	1	27.5 ± 11.5	102	60	24	4.7	4.1	3.0	16.8	14.1	9.7	19.0	14.4	5.4
250	0	< 1571.7	0	< 934.2	0	< 267.5	3117	1753	779	16.4	12.7	10.1	92.9	76.0	55.6	515.3	301.7	69.0
251	1	50616.9 ± 226.4	1	20088.2 ± 204.0	1	6816.0 ± 70.7	1394	784	350	72.9	32.4	18.6	62.1	50.8	37.2	205.1	194.9	57.2
252	1	1220.7 ± 77.0	1	648.0 ± 87.0	1	295.6 ± 32.7	450	258	115	10.1	7.7	6.4	35.3	29.1	21.3	67.7	81.6	24.0
253	1	476.6 ± 40.9	2	150.4 ± 6.0	2	61.9 ± 9.0	199	111	48	4.5	0.0	0.0	23.5	0.0	0.0	33.2	0.0	0.0
254	1	11189.7 ± 781.8	1	4931.9 ± 536.2	1	1734.5 ± 245.2	4003	2254	1000	32.2	23.5	18.8	105.2	86.2	62.9	774.0	528.7	236.3
255	1	2203.5 ± 393.5	1	1304.8 ± 187.7	1	621.8 ± 79.2	1948	1096	486	20.9	15.4	12.5	70.6	57.8	42.1	386.6	177.9	65.8
256	1	7379.6 ± 79.9	1	2793.1 ± 57.7	1	913.1 ± 27.8	539	307	134	12.5	7.1	4.6	38.6	31.8	22.9	68.8	47.6	14.9
257	1	4785.2 ± 434.5	1	2465.2 ± 304.6	1	949.1 ± 129.0	2481	1394	622	24.2	18.6	14.9	82.8	67.8	49.6	425.9	296.4	118.1
258	2	271.7 ± 5.0	2	95.7 ± 6.0	2	31.2 ± 10.0	456	255	113	0.0	0.0	0.0	0.0	0.0	0.0	0.0	0.0	0.0
259	1	4066.4 ± 262.3	1	2118.2 ± 141.8	1	945.3 ± 87.7	1652	930	412	20.8	15.3	12.1	67.6	55.3	40.4	252.6	129.6	76.9
260	1	7119.3 ± 156.8	1	2985.4 ± 98.3	1	1035.0 ± 42.6	552	307	136	22.5	9.1	5.2	39.1	31.8	23.2	150.1	92.5	35.3
261	1	1989.5 ± 116.6	1	1039.7 ± 124.3	1	415.0 ± 59.3	683	387	174	13.8	9.7	7.9	43.4	35.7	26.2	107.4	118.7	52.6
262	1	6725.1 ± 188.9	1	3055.0 ± 175.9	1	1160.3 ± 101.7	1061	600	261	16.4	12.3	9.9	54.2	44.5	32.1	180.2	169.8	96.0
263	1	32493.1±2546.8	1	16657.1±2242.4	1	7142.4 ± 1118.3	15566	8751	3884	60.8	46.0	36.9	207.5	169.8	123.9	2537.6	2235.5	1110.8
264	1	720.3 ± 49.0	1	410.0 ± 30.7	1	183.9 ± 19.7	277	157	71	8.2	6.1	4.9	27.7	22.7	16.8	39.5	19.7	9.0
265	1	1018.4 ± 43.8	1	438.1 ± 32.2	1	143.9 ± 18.0	223	121	55	8.0	5.9	4.4	24.8	20.0	14.8	35.1	24.6	9.3
266	1	7614.5 ± 737.4	1	4064.4 ± 425.7	1	1852.1 ± 170.0	3294	1845	825	28.8	21.2	17.3	95.4	77.9	57.1	730.6	417.9	159.1
267	1	3433.7 ± 178.5	1	1717.0 ± 101.8	1	701.1 ± 53.4	1099	616	273	18.1	13.2	10.2	55.1	45.1	32.9	168.8	90.3	40.8
268	1	6293.5 ± 89.6	1	2690.4 ± 61.5	1	985.3 ± 25.4	418	238	107	20.9	11.2	7.3	34.0	28.0	20.6	80.2	53.6	12.9
269[d]	0	< 1035.2	0	< 830.0	0	< 291.8	1271	715	317	10.6	7.9	6.4	59.3	48.5	35.4	339.8	272.3	90.4
270	1	6235.2 ± 576.9	1	2691.3 ± 256.7	1	964.5 ± 107.8	2135	1196	533	25.8	18.1	14.6	76.8	62.8	45.9	571.2	248.2	96.5
271	1	2735.8 ± 140.6	1	1444.8 ± 102.2	1	610.1 ± 46.8	658	366	161	14.0	9.7	8.2	42.6	34.7	25.2	133.2	95.7	38.5
272	0	< 1681.8	0	< 1453.7	0	< 663.2	3804	2140	951	18.4	13.9	11.3	102.6	83.9	61.5	550.8	477.1	212.0
273	1	4701.2 ± 189.2	1	2283.6 ± 158.1	1	888.6 ± 91.7	984	554	243	16.8	11.9	9.4	52.2	42.7	31.0	181.1	151.8	85.7
274	1	2237.0 ± 103.8	1	1120.7 ± 68.7	1	438.9 ± 33.5	456	255	114	11.0	7.8	6.9	35.5	29.0	21.2	96.9	61.8	25.0
275	1	5155.7 ± 152.4	1	2383.8 ± 99.2	1	903.3 ± 53.6	661	368	167	12.7	9.6	7.7	42.8	34.8	25.7	145.8	92.3	46.4
276	1	2681.0 ± 110.1	1	1228.5 ± 90.4	1	452.5 ± 44.9	588	330	150	12.2	9.3	7.2	40.3	33.0	24.4	101.7	83.7	37.1
277	1	240.8 ± 44.1	1	100.1 ± 29.6	1	39.0 ± 16.7	150	85	38	6.1	4.6	3.7	20.4	16.7	12.3	38.6	24.0	10.7
278[k]	3	998.3 ± 106.5	3	452.6 ± 45.7	3	159.3 ± 30.8	393	218	97	10.3	7.4	5.9	33.0	26.8	19.6	100.7	36.3	23.0
279	1	2762.0 ± 189.7	1	1601.7 ± 127.9	1	730.4 ± 69.7	908	510	230	15.0	10.9	9.1	50.1	41.0	30.2	182.4	120.6	62.2
280	1	1988.2 ± 47.7	1	863.9 ± 30.6	1	306.2 ± 20.0	250	137	61	10.7	6.7	4.8	26.3	21.2	15.5	38.4	20.9	11.7
281	1	407.6 ± 26.8	1	182.5 ± 16.9	1	59.3 ± 12.4	101	58	26	5.0	3.9	3.1	16.8	13.8	10.1	20.3	8.9	6.5
282	0	< 38.1	0	< 31.0	0	< 20.4	38	21	9	3.0	2.5	1.8	10.9	8.9	6.3	5.8	4.7	1.9
283	1	9262.6 ± 135.4	1	4010.6 ± 81.2	1	1499.4 ± 47.2	678	381	174	18.0	11.1	8.5	43.3	35.4	26.2	127.0	72.2	38.3
284	1	7546.1 ± 68.3	1	2898.7 ± 45.5	1	956.0 ± 25.3	343	193	84	23.7	11.9	7.1	30.8	25.2	18.2	56.2	36.0	16.1
285	1	13012.2 ± 260.2	1	5510.5 ± 167.6	1	1872.9 ± 76.7	1310	736	330	65.2	27.5	13.9	60.2	49.2	36.1	244.6	157.9	66.2
286	1	1281.3 ± 278.7	1	819.1 ± 201.2	1	386.7 ± 120.8	1417	798	351	13.8	10.4	8.4	76.3	62.8	45.3	267.7	190.9	111.7
287	1	4592.5 ± 129.8	1	2072.7 ± 67.2	1	781.7 ± 47.1	1046	588	261	16.3	12.1	9.6	53.8	44.0	32.1	117.0	49.3	33.1
288	1	5837.5 ± 252.9	1	2699.8 ± 148.8	1	998.4 ± 63.3	1087	611	275	16.9	11.9	9.9	54.8	44.9	33.0	246.3	141.4	53.1
289	1	8041.8 ± 151.6	1	3532.7 ± 113.2	1	1296.2 ± 60.7	864	483	214	16.0	10.9	8.8	48.9	39.9	29.1	142.6	105.4	52.5
290	1	1650.4 ± 54.3	1	652.2 ± 45.7	1	220.4 ± 26.3	313	173	79	10.5	7.0	5.6	28.5	23.1	17.2	44.9	38.8	19.1
291	0	< 201.3	0	< 180.6	0	< 82.5	323	182	80	8.9	6.8	5.4	30.0	26.9	18.1	59.4	53.5	19.9

Table A.2: continued.

HRS	f_{250}	S_{250}[1] (mJy)	f_{350}	S_{350}[1] (mJy)	f_{500}	S_{500}[1] (mJy)	N_{250}	N_{350}	N_{500}	err^{250}_{inst} (mJy)	err^{350}_{inst} (mJy)	err^{500}_{inst} (mJy)	err^{250}_{conf} (mJy)	err^{350}_{conf} (mJy)	err^{500}_{conf} (mJy)	err^{250}_{sky} (mJy)	err^{350}_{sky} (mJy)	err^{500}_{sky} (mJy)
292	1	5546.6 ± 83.6	1	2235.1 ± 72.1	1	719.9 ± 45.8	546	311	138	23.5	12.2	7.6	38.9	32.0	23.4	70.1	63.5	38.6
293	1	4384.8 ± 108.6	1	2021.9 ± 65.3	1	786.2 ± 39.1	621	353	153	12.7	9.6	7.3	41.5	34.1	24.7	99.5	54.8	29.4
294	1	2098.3 ± 56.3	1	1049.3 ± 49.0	1	398.8 ± 27.8	380	216	96	11.4	8.2	6.0	32.4	26.7	19.5	44.5	40.2	18.9
295	1	38865.7±1154.7	1	16601.7 ± 673.0	1	5922.3 ± 288.8	4264	2406	1075	49.1	30.5	21.3	108.6	89.0	65.2	1148.6	666.4	280.6
296	1	419.0 ± 41.2	1	211.2 ± 34.9	1	100.0 ± 19.4	282	154	69	5.0	3.9	3.1	27.9	22.5	16.5	29.8	26.4	9.7
297	1	7826.9 ± 169.3	1	3747.1 ± 109.7	1	1514.6 ± 74.6	1133	637	282	19.6	13.1	10.3	56.0	45.8	33.4	158.6	98.8	65.9
298	1	2629.9 ± 71.4	1	1049.1 ± 33.2	1	352.6 ± 20.9	304	168	77	12.2	7.3	5.6	29.0	23.5	17.5	64.1	22.3	10.0
299	1	5049.0 ± 260.2	1	2611.8 ± 253.4	1	1139.4 ± 140.4	1540	862	381	19.5	14.3	11.6	65.3	53.3	38.8	251.1	247.3	134.4
300	1	567.6 ± 63.5	1	290.7 ± 43.0	1	105.2 ± 23.9	282	161	73	8.1	6.5	5.2	27.9	23.0	17.0	56.5	35.8	15.9
301	1	5174.5 ± 457.8	1	2867.7 ± 275.2	1	1317.9 ± 119.6	1933	1092	484	21.7	16.1	13.1	73.1	60.0	43.8	451.4	268.1	110.5
302	1	1462.0 ± 113.5	1	853.4 ± 53.4	1	389.9 ± 33.9	531	300	136	11.9	8.5	6.9	38.3	31.4	23.2	106.2	42.3	23.7
303	1	1499.9 ± 57.6	1	572.9 ± 41.4	1	173.7 ± 21.2	317	178	78	11.1	7.5	5.4	29.6	24.2	17.6	48.2	32.7	10.5
304	1	3676.8 ± 94.7	1	1734.4 ± 66.2	1	635.9 ± 40.0	595	333	146	14.3	9.7	7.4	40.6	33.1	24.0	84.4	56.5	31.1
305	1	332.6 ± 58.1	1	163.8 ± 45.8	1	59.0 ± 19.5	212	116	54	7.3	5.3	4.5	24.2	19.5	14.6	52.3	41.1	12.1
306	1	3199.0 ± 288.8	1	1277.5 ± 194.1	1	364.8 ± 95.8	1645	931	415	21.5	14.9	12.1	67.4	55.4	40.5	280.0	185.5	86.0
307	1	17755.3 ± 803.5	1	8647.4 ± 639.7	1	3501.9 ± 308.0	4550	2557	1134	33.8	25.1	20.3	112.2	91.8	67.0	794.9	632.6	299.9
308	2	92.4 ± 6.0	2	31.6 ± 6.0	0	< 30.3	65	38	15	0.0	0.0	2.8	0.0	0.0	9.1	0.0	0.0	3.4
309	1	786.0 ± 32.6	1	418.5 ± 28.2	1	177.7 ± 16.1	177	97	45	6.4	5.2	4.2	22.1	17.9	13.3	23.2	21.1	8.0
310	1	3073.6 ± 146.6	1	1287.9 ± 114.7	1	468.6 ± 54.5	660	367	165	14.3	9.8	7.7	42.7	34.8	25.5	139.5	108.9	47.5
311	1	7815.5 ± 383.2	1	3672.6 ± 303.2	1	1382.8 ± 135.8	1780	1002	446	21.6	16.0	12.8	70.1	57.4	42.0	376.1	297.3	128.5
312	0	< 115.6	0	< 90.2	0	< 65.5	89	50	22	6.5	4.7	3.8	35.5	28.8	21.2	13.5	7.2	3.3
313	1	3052.5 ± 149.3	1	1596.4 ± 79.4	1	670.7 ± 50.5	875	491	218	15.2	11.0	8.9	49.2	40.2	29.4	140.1	67.6	40.1
314	1	2048.1 ± 80.3	1	1118.4 ± 51.8	1	494.0 ± 45.6	518	294	132	11.4	8.5	6.8	37.8	31.1	22.9	69.8	40.6	38.9
315	1	522.8 ± 125.8	1	280.8 ± 78.5	1	149.5 ± 47.2	638	364	163	12.6	9.9	7.6	42.0	34.6	25.4	117.9	69.7	39.0
316	0	< 46.8	0	< 35.9	0	< 22.3	51	28	12	2.2	1.6	1.3	12.0	9.6	6.6	9.7	7.0	3.2
317	1	333.6 ± 56.0	1	187.5 ± 25.4	1	73.7 ± 18.0	187	105	47	6.8	5.2	4.1	22.7	18.6	13.6	50.7	16.5	11.1
318	1	3268.5 ± 119.2	1	1611.6 ± 105.8	1	652.5 ± 46.3	560	317	140	12.3	9.3	7.1	39.3	32.3	23.5	111.9	100.3	39.2
319	1	5099.6 ± 334.4	1	2672.5 ± 219.7	1	1155.6 ± 89.2	1725	971	435	20.7	15.3	12.3	69.1	56.5	41.5	326.5	211.7	78.0
320	1	6699.0 ± 358.1	1	3578.2 ± 213.9	1	1582.6 ± 100.8	1921	1079	482	21.9	16.0	13.0	72.9	59.6	43.7	349.9	204.8	89.9
321	1	1390.6 ± 31.9	1	600.5 ± 25.1	1	210.7 ± 14.9	145	81	36	7.2	5.3	3.9	20.0	16.3	11.9	23.8	18.3	8.0
322	1	2972.6 ± 380.4	1	1701.2 ± 313.4	1	769.5 ± 138.6	1985	1120	497	13.4	10.0	8.1	74.1	60.7	44.3	372.9	307.3	131.1
323	1	4047.4 ± 63.5	1	1857.5 ± 49.0	1	707.0 ± 24.4	410	233	103	14.1	9.2	6.7	33.7	27.8	20.2	52.0	39.3	12.0

Notes. Errors in this table do not contain the 7% calibration errors. Flux densities in this table do not contain colour corrections.
[(a)] Presence of a companion galaxy; flux densities are overestimated.
[(b)] Presence of a background source that cannot be separated at 250, 350 and 500 μm; flux densities are overestimated.
[(c)] Presence of a background source that cannot be separated at 350 and 500 μm; flux densities are overestimated.
[(d)] Presence of a strong cirrus.
[(e)] The source is considered point like; however in the PLW band (500 μm), even if there is a detection, the emission of the galaxy is dominated by a background source; the 500 μm flux density is thus an upper limit.
[(f)] Particular aperture adapted to take into account M86's structures (Gomez et al. 2010a; Cortese et al. 2010).
[(g)] Aperture is off-centered to match the particular shape of NGC 4438 (Cortese et al. 2010).
[(h)] Flux densities in SPIRE bands dominated by synchrotron emission (Baes et al. 2010; Boselli et al. 2010a)
[(i)] Presence of the companion NGC 4496B; flux densities are overestimated.
[(j)] NGC 4567 and NGC 4568, the two galaxies are overlapping; flux densities are overstimated.
[(k)] Presence of a background source that cannot be separated at 500 μm; flux are overestimated.

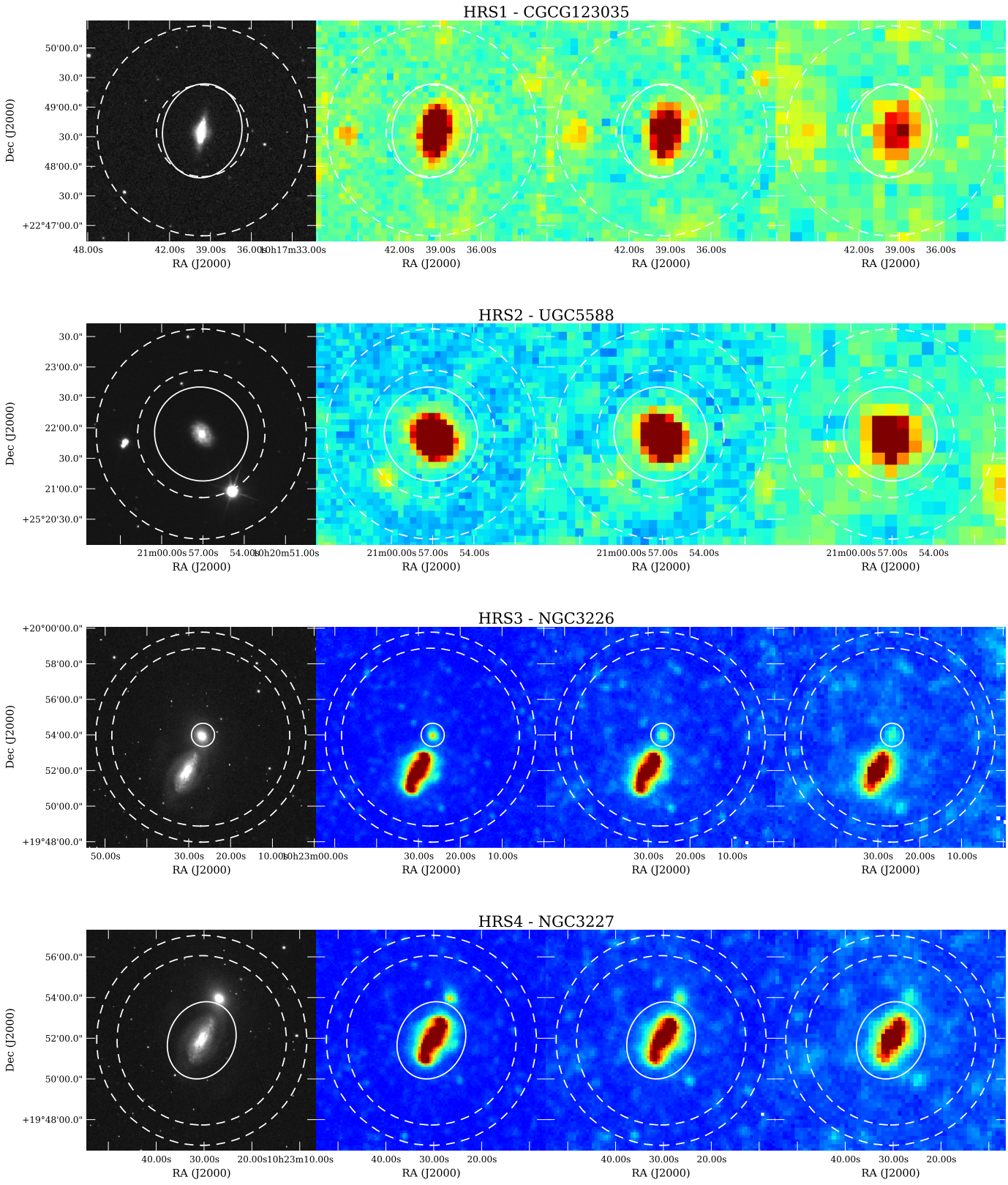

Fig. A.1: Images of the HRS galaxies. From left to right: SDSS *r'* band image, 250, 350, and 500 μm *Herschel* images. The aperture used for the photometry is indicated by the solid line and the annulus, where the background is estimated, is indicated in dashed lines.

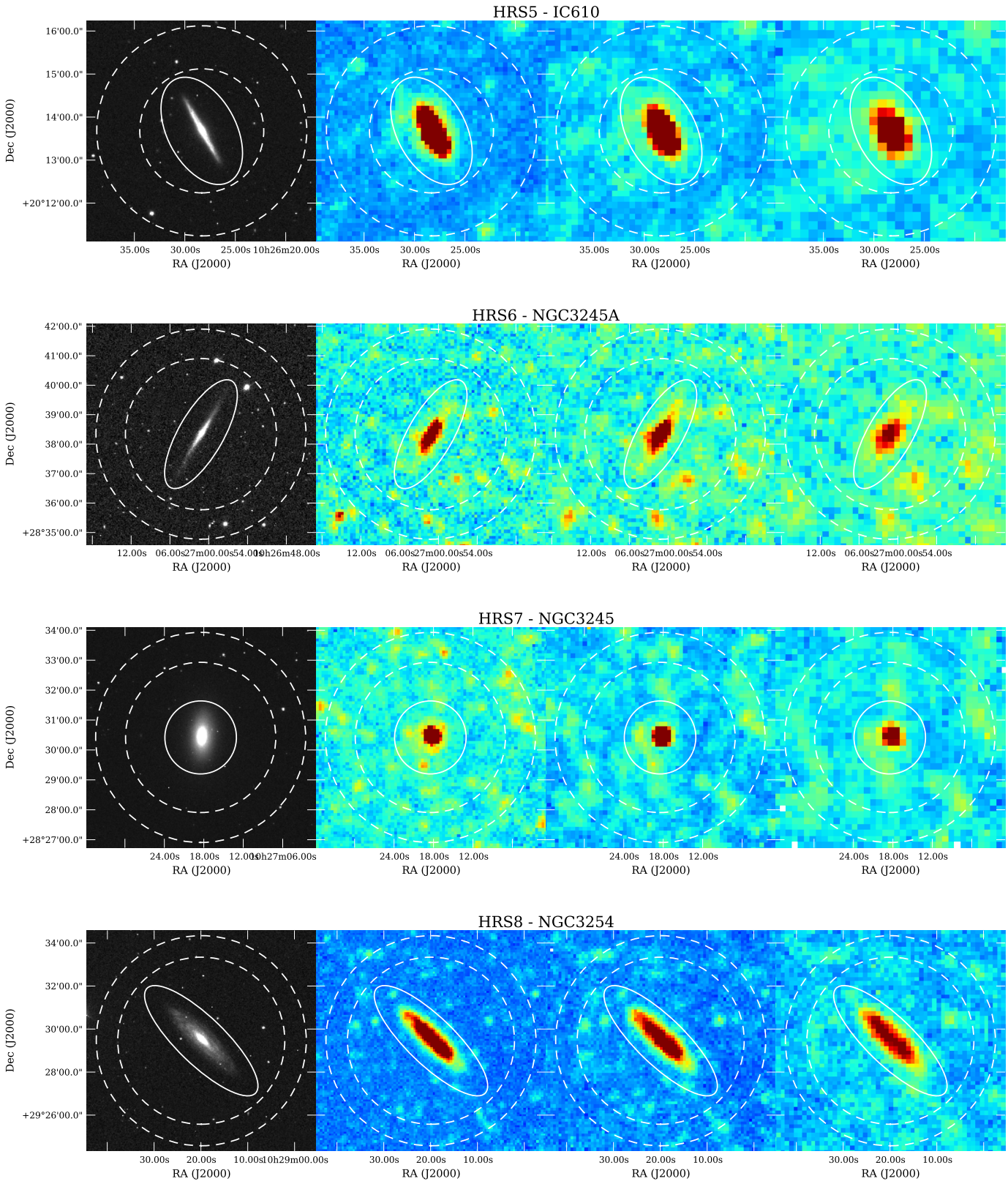

Fig. A.1: Images of the HRS galaxies. From left to right: SDSS *r'* band image, 250, 350, and 500 μm *Herschel* images. The aperture used for the photometry is indicated by the solid line and the annulus, where the background is estimated, is indicated in dashed lines.

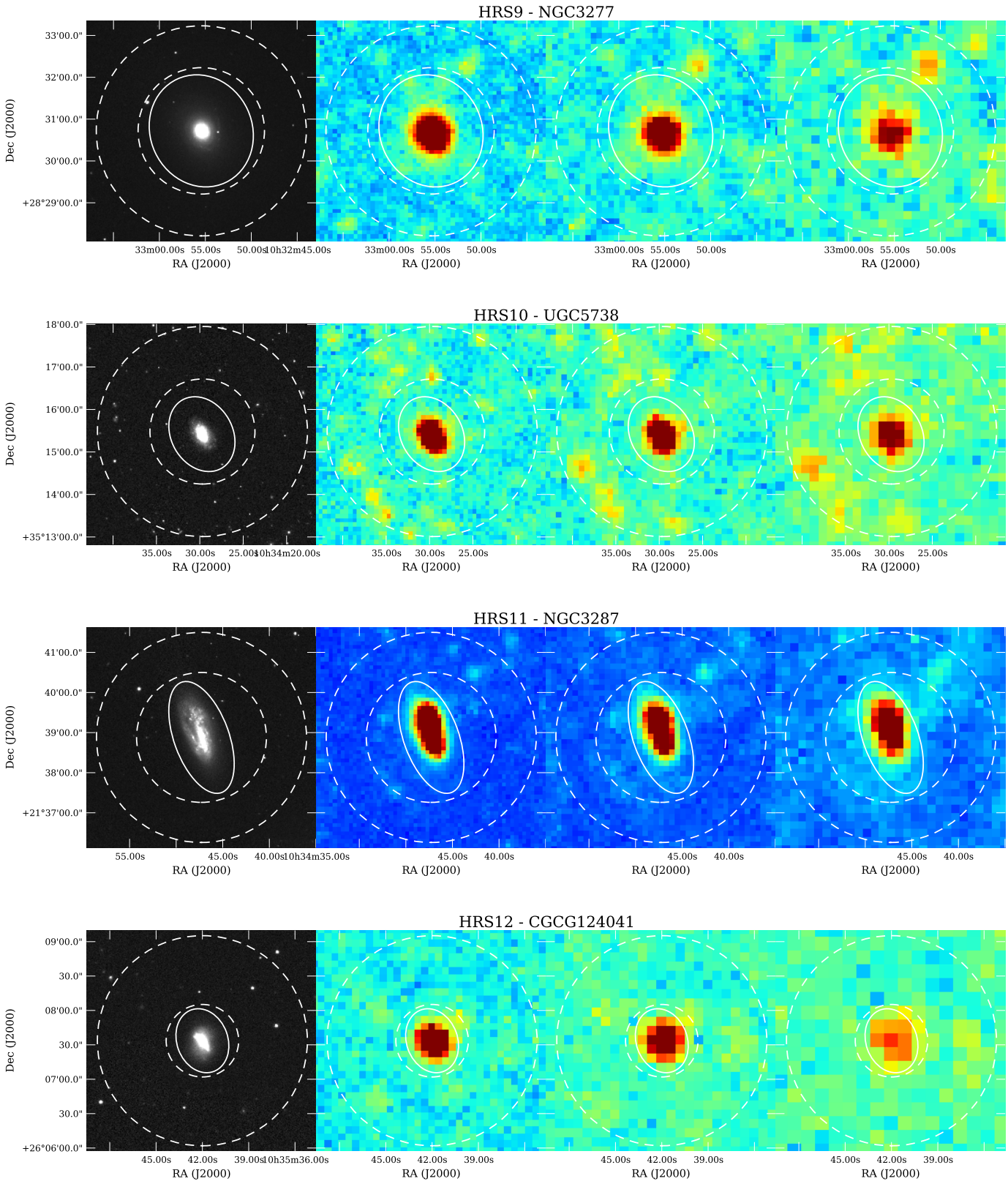

Fig. A.1: Images of the HRS galaxies. From left to right: SDSS *r'* band image, 250, 350, and 500 μm *Herschel* images. The aperture used for the photometry is indicated by the solid line and the annulus, where the background is estimated, is indicated in dashed lines.

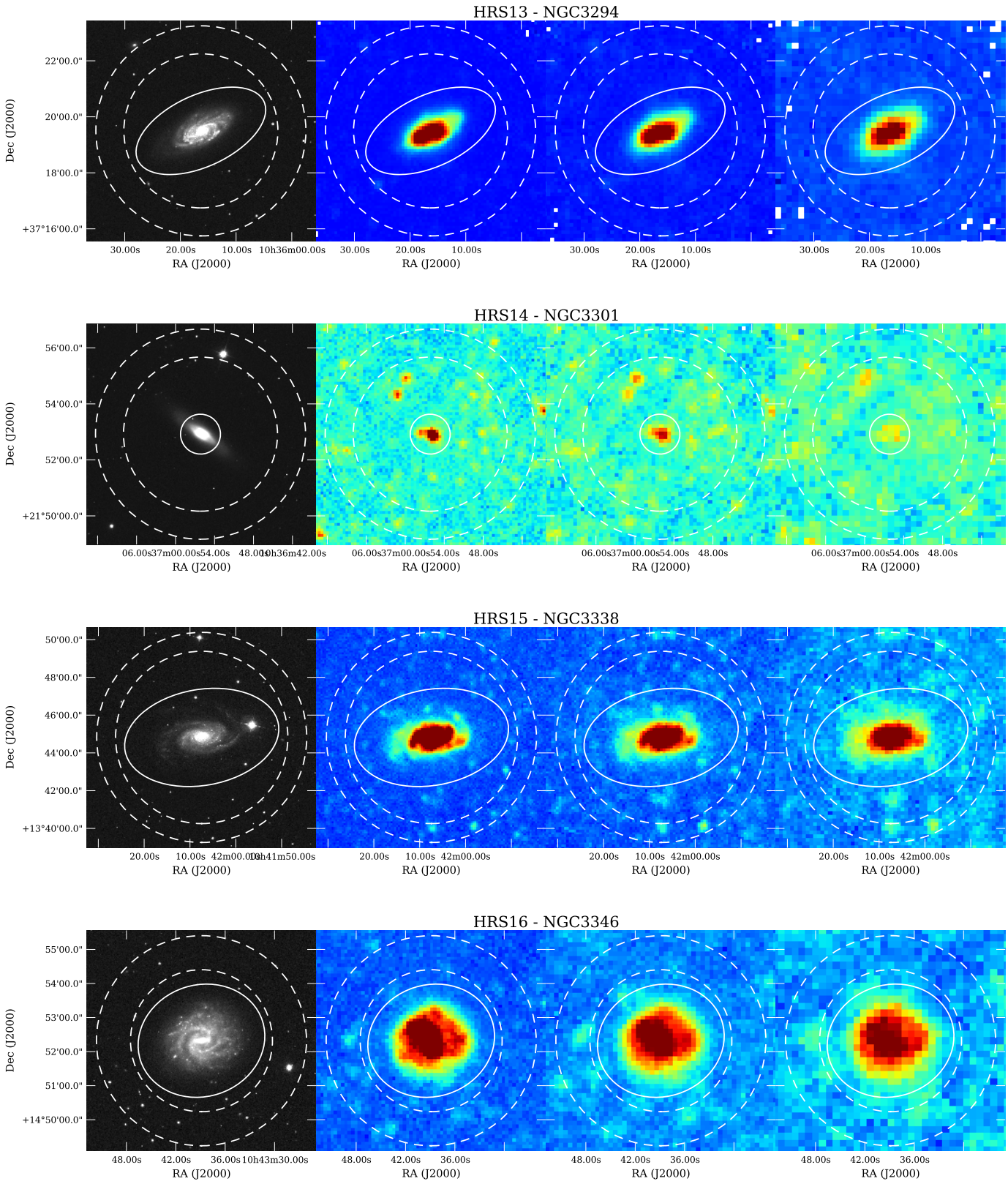

Fig. A.1: Images of the HRS galaxies. From left to right: SDSS *r'* band image, 250, 350, and 500 μm *Herschel* images. The aperture used for the photometry is indicated by the solid line and the annulus, where the background is estimated, is indicated in dashed lines.

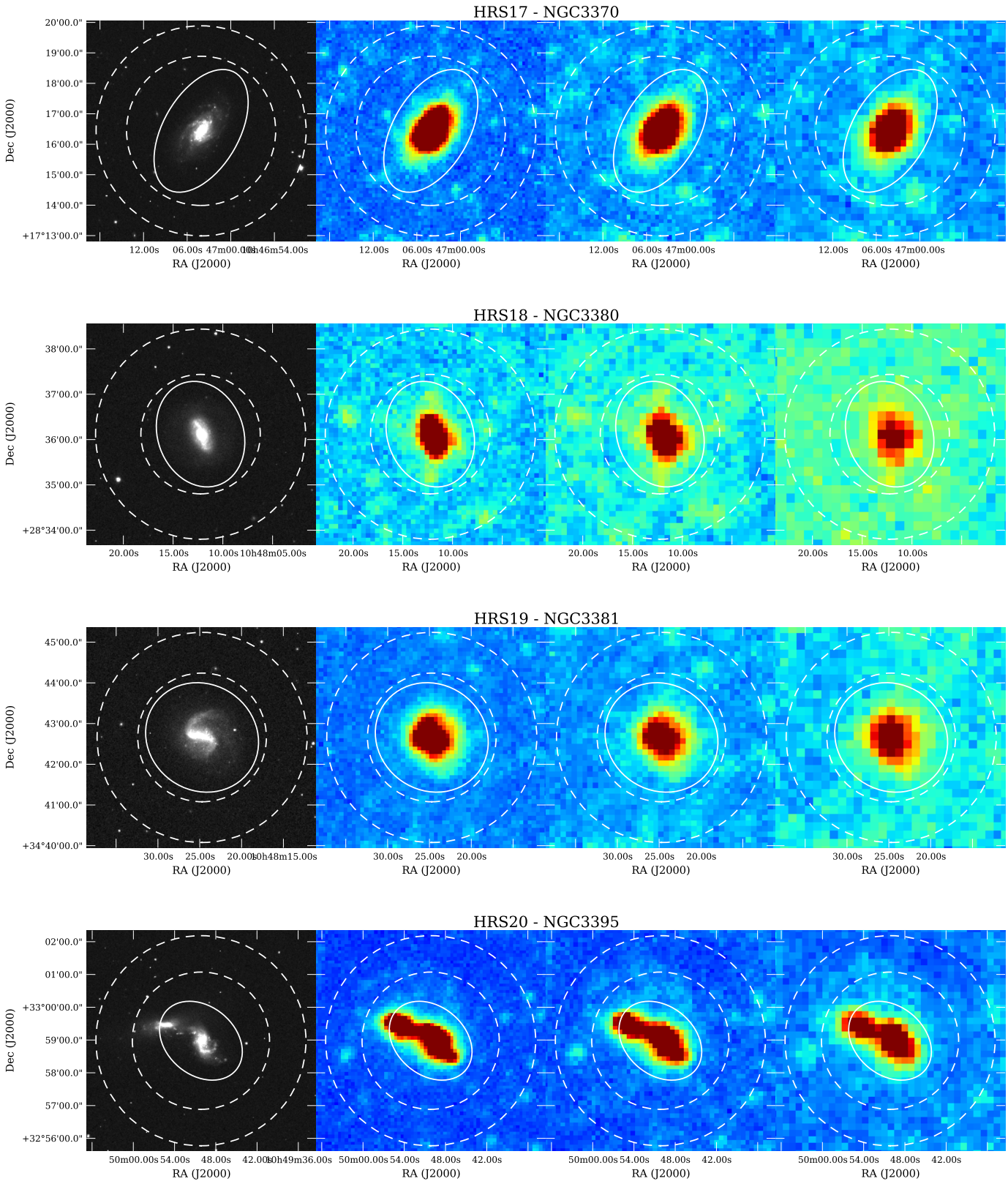

Fig. A.1: Images of the HRS galaxies. From left to right: SDSS *r'* band image, 250, 350, and 500 μm *Herschel* images. The aperture used for the photometry is indicated by the solid line and the annulus, where the background is estimated, is indicated in dashed lines.

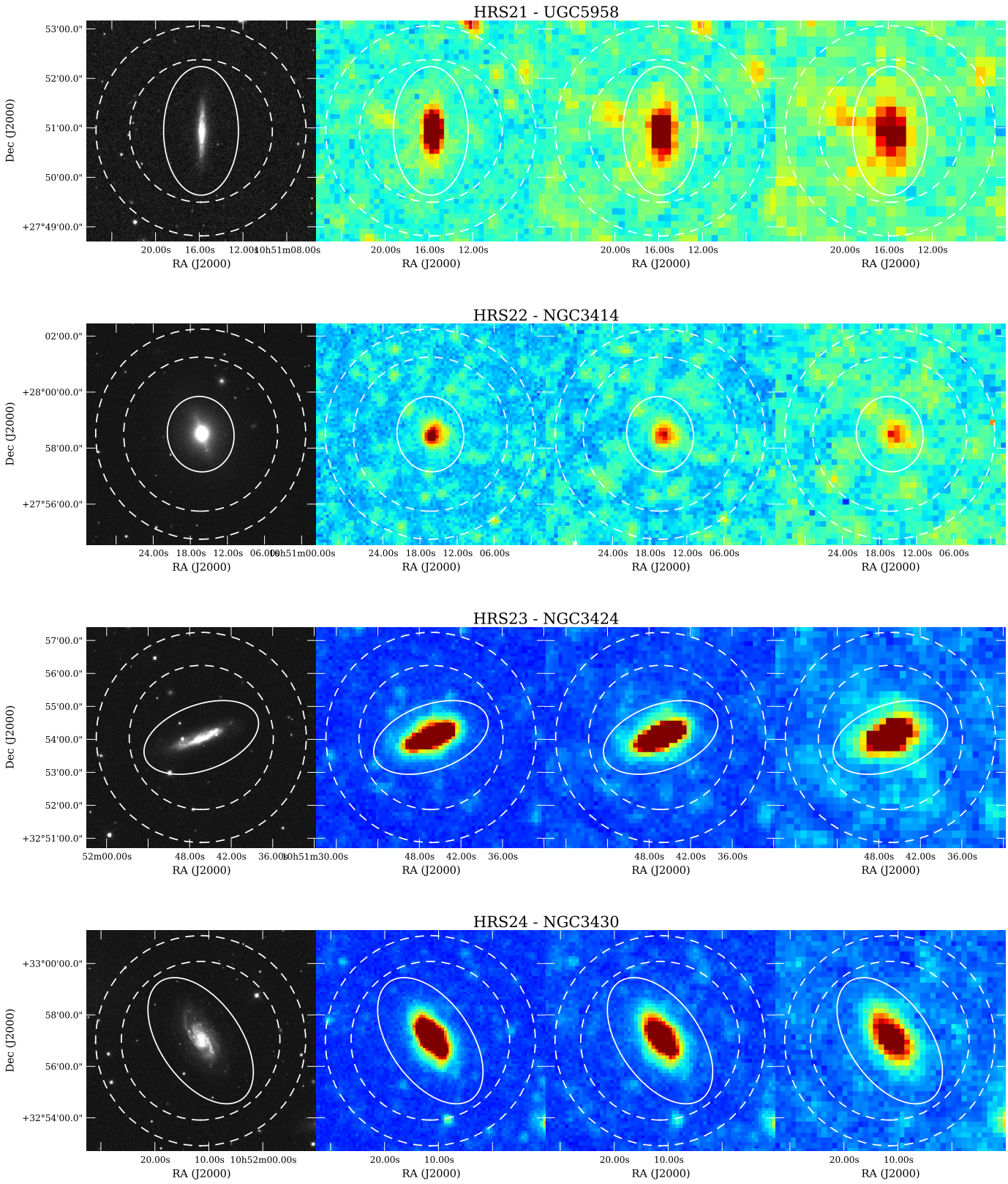

Fig. A.1: Images of the HRS galaxies. From left to right: SDSS *r'* band image, 250, 350, and 500 μm *Herschel* images. The aperture used for the photometry is indicated by the solid line and the annulus, where the background is estimated, is indicated in dashed lines.

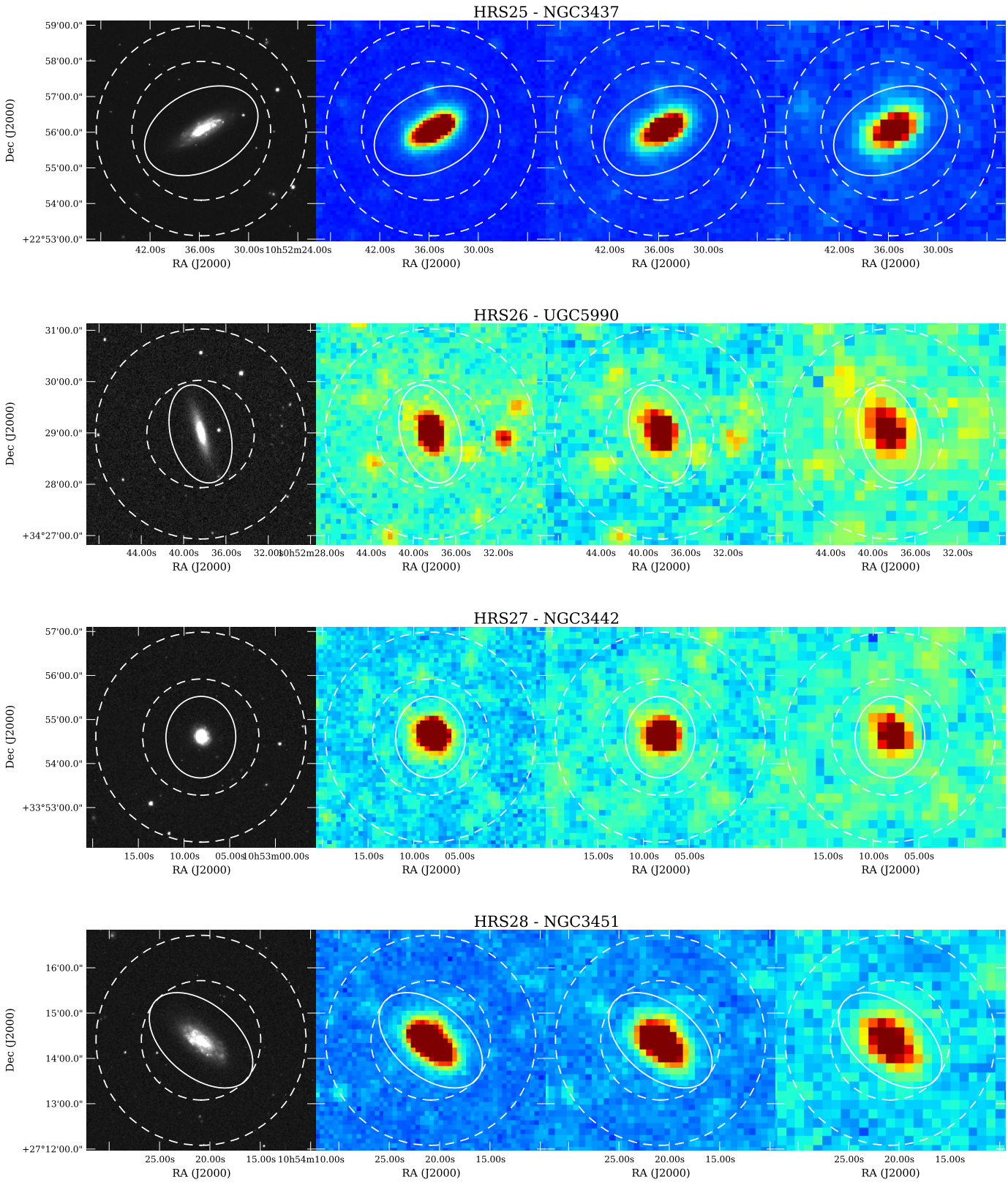

Fig. A.1: Images of the HRS galaxies. From left to right: SDSS *r'* band image, 250, 350, and 500 μm *Herschel* images. The aperture used for the photometry is indicated by the solid line and the annulus, where the background is estimated, is indicated in dashed lines.

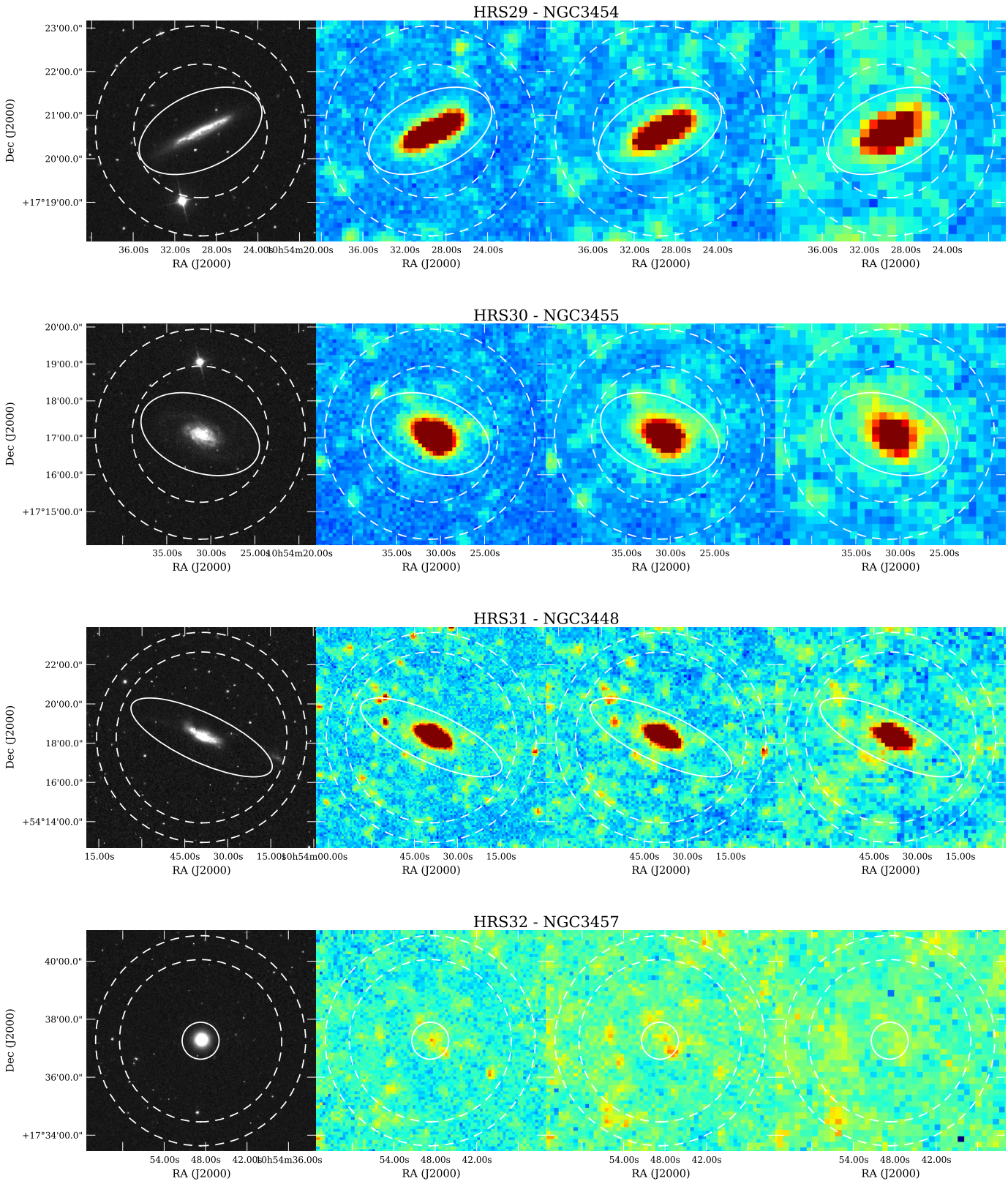

Fig. A.1: Images of the HRS galaxies. From left to right: SDSS *r'* band image, 250, 350, and 500 μm *Herschel* images. The aperture used for the photometry is indicated by the solid line and the annulus, where the background is estimated, is indicated in dashed lines.

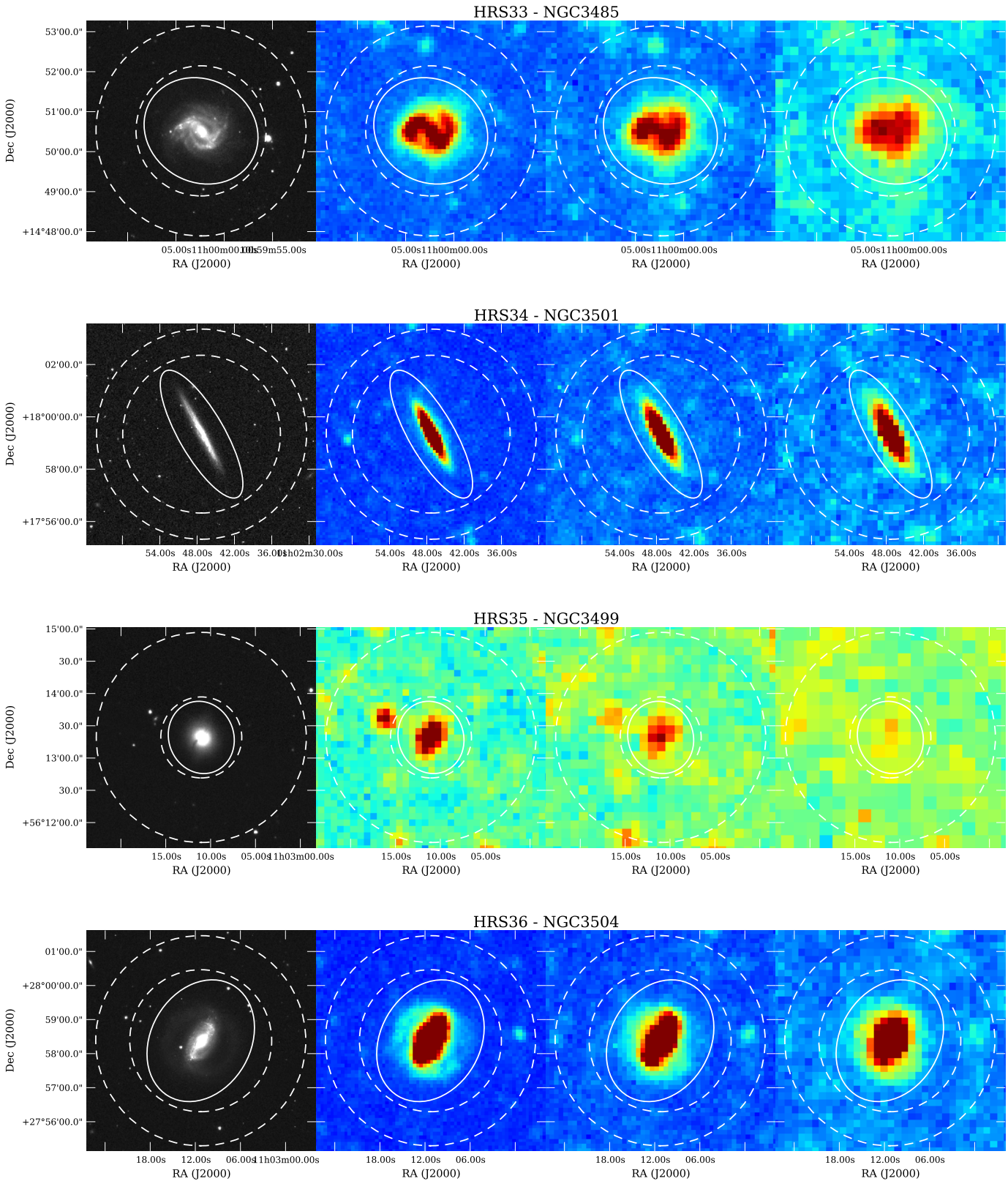

Fig. A.1: Images of the HRS galaxies. From left to right: SDSS *r'* band image, 250, 350, and 500 μm *Herschel* images. The aperture used for the photometry is indicated by the solid line and the annulus, where the background is estimated, is indicated in dashed lines.

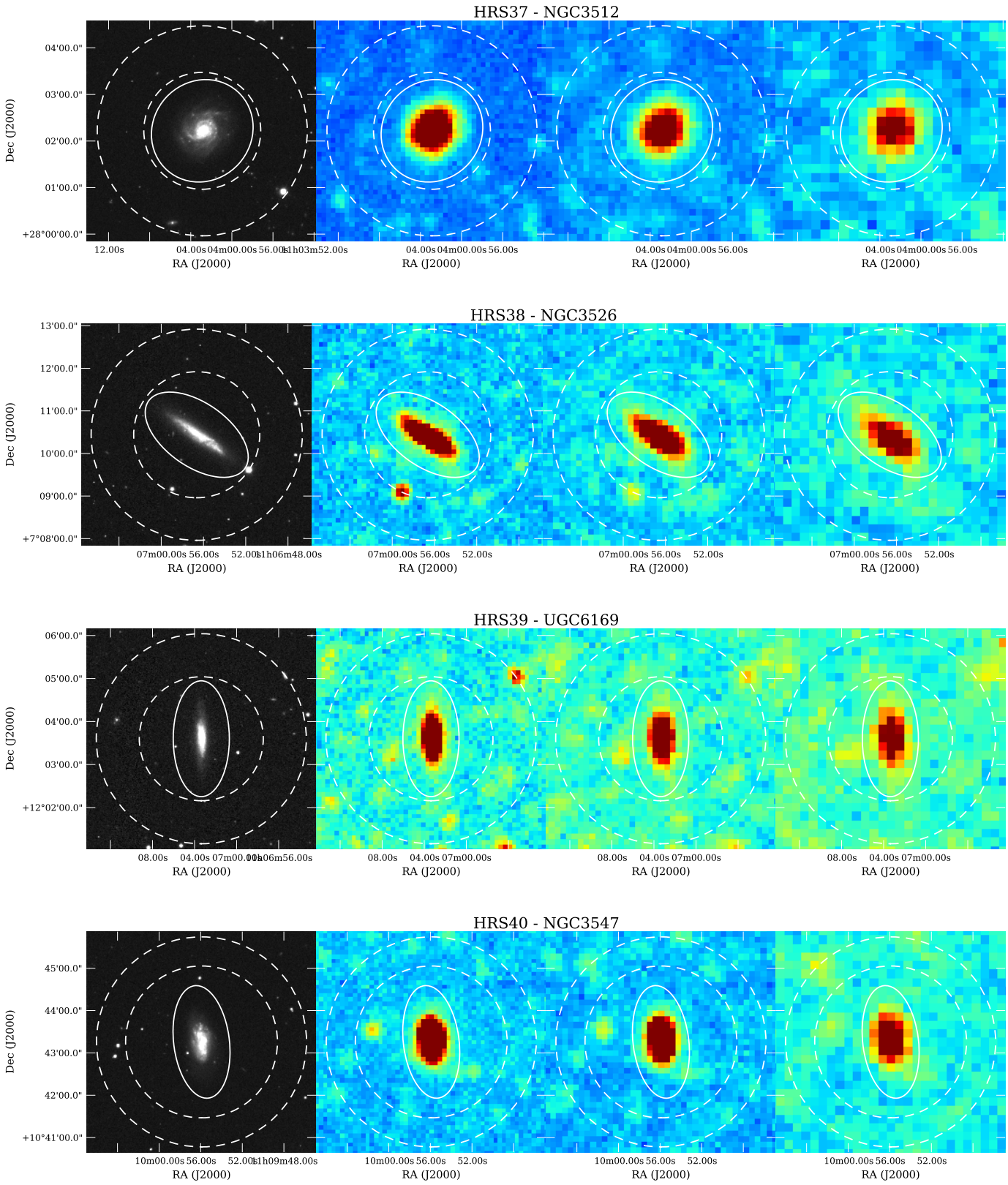

Fig. A.1: Images of the HRS galaxies. From left to right: SDSS *r'* band image, 250, 350, and 500 μm *Herschel* images. The aperture used for the photometry is indicated by the solid line and the annulus, where the background is estimated, is indicated in dashed lines.

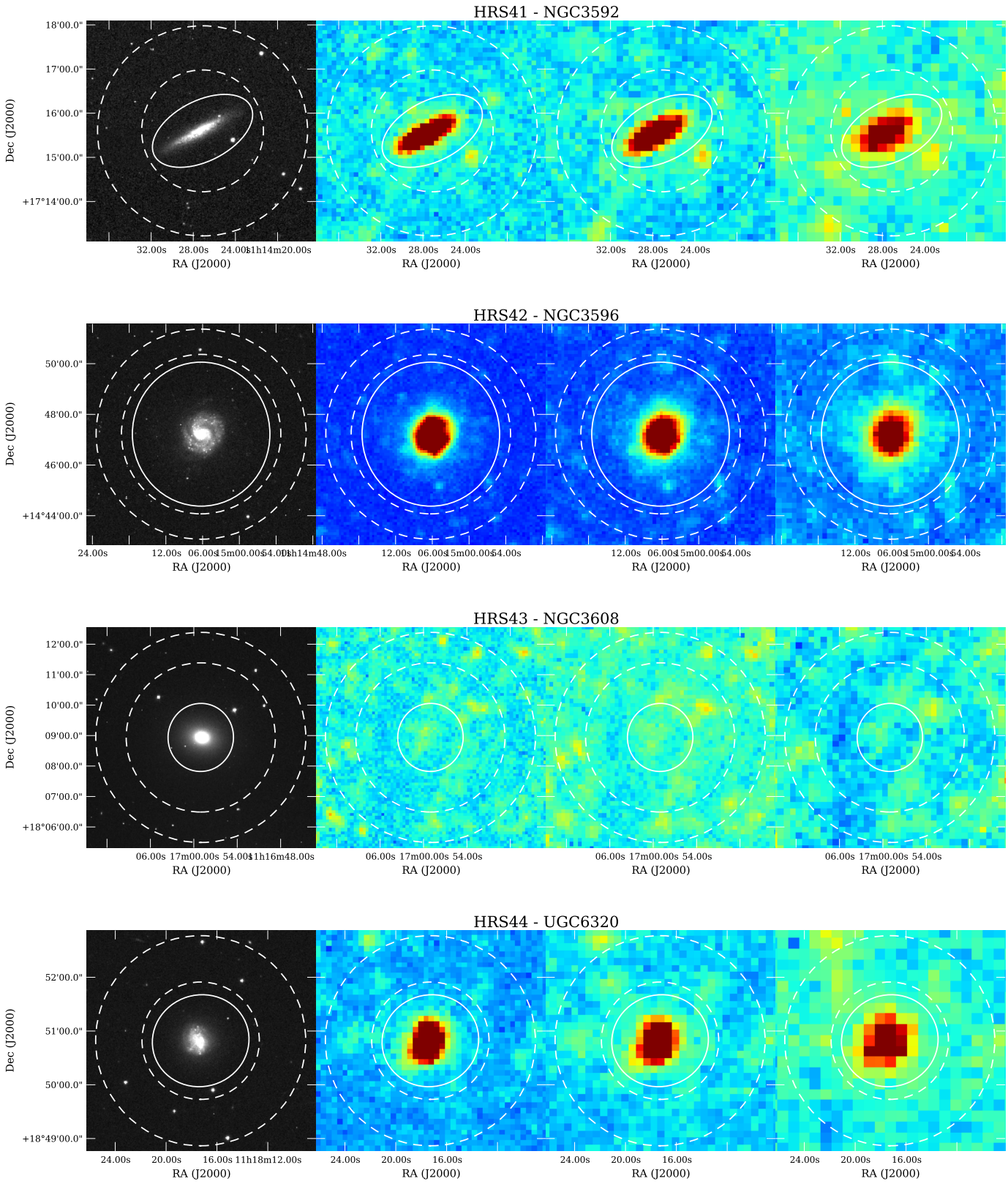

Fig. A.1: Images of the HRS galaxies. From left to right: SDSS *r'* band image, 250, 350, and 500 μm *Herschel* images. The aperture used for the photometry is indicated by the solid line and the annulus, where the background is estimated, is indicated in dashed lines.

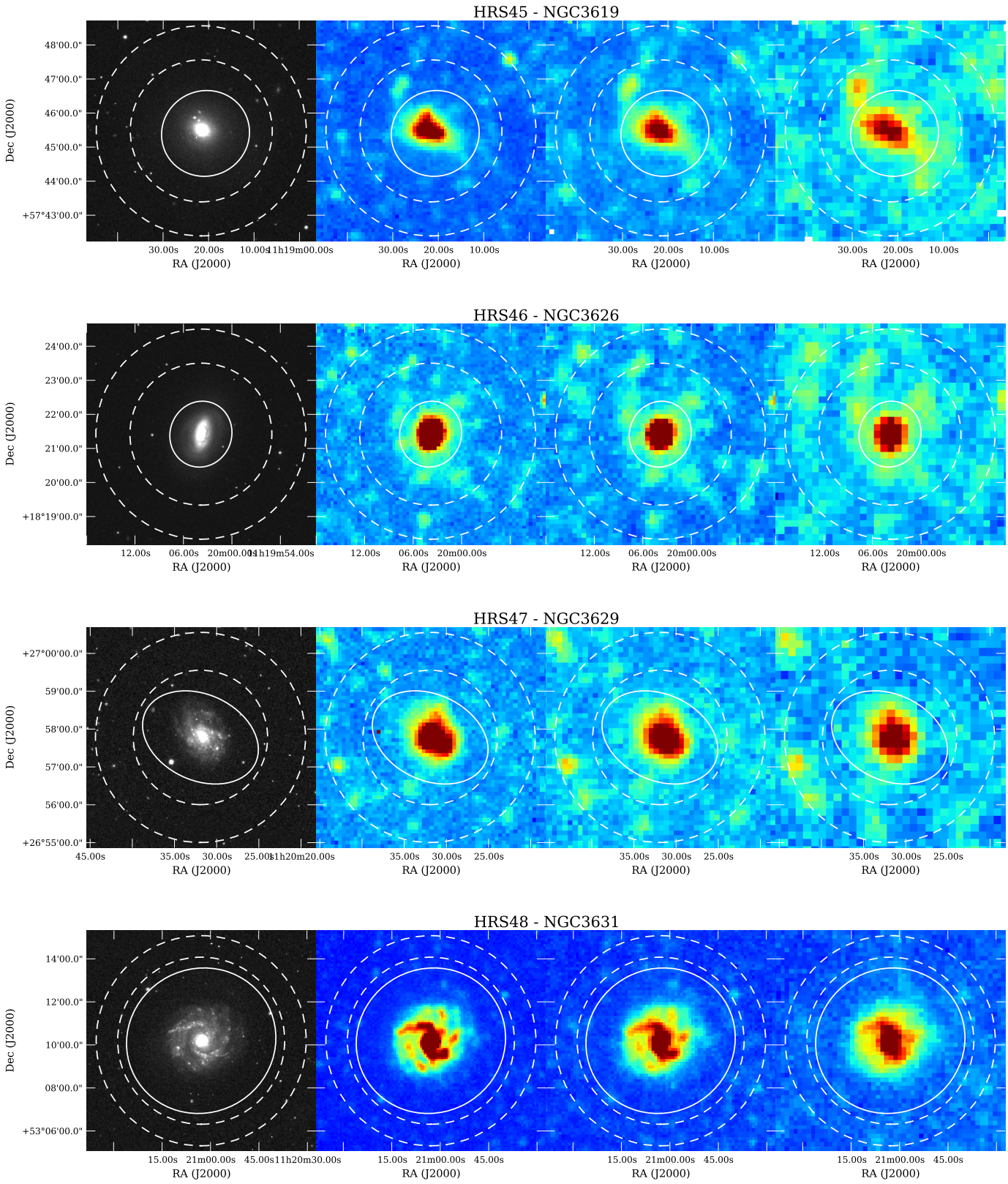

Fig. A.1: Images of the HRS galaxies. From left to right: SDSS *r'* band image, 250, 350, and 500 μm *Herschel* images. The aperture used for the photometry is indicated by the solid line and the annulus, where the background is estimated, is indicated in dashed lines.

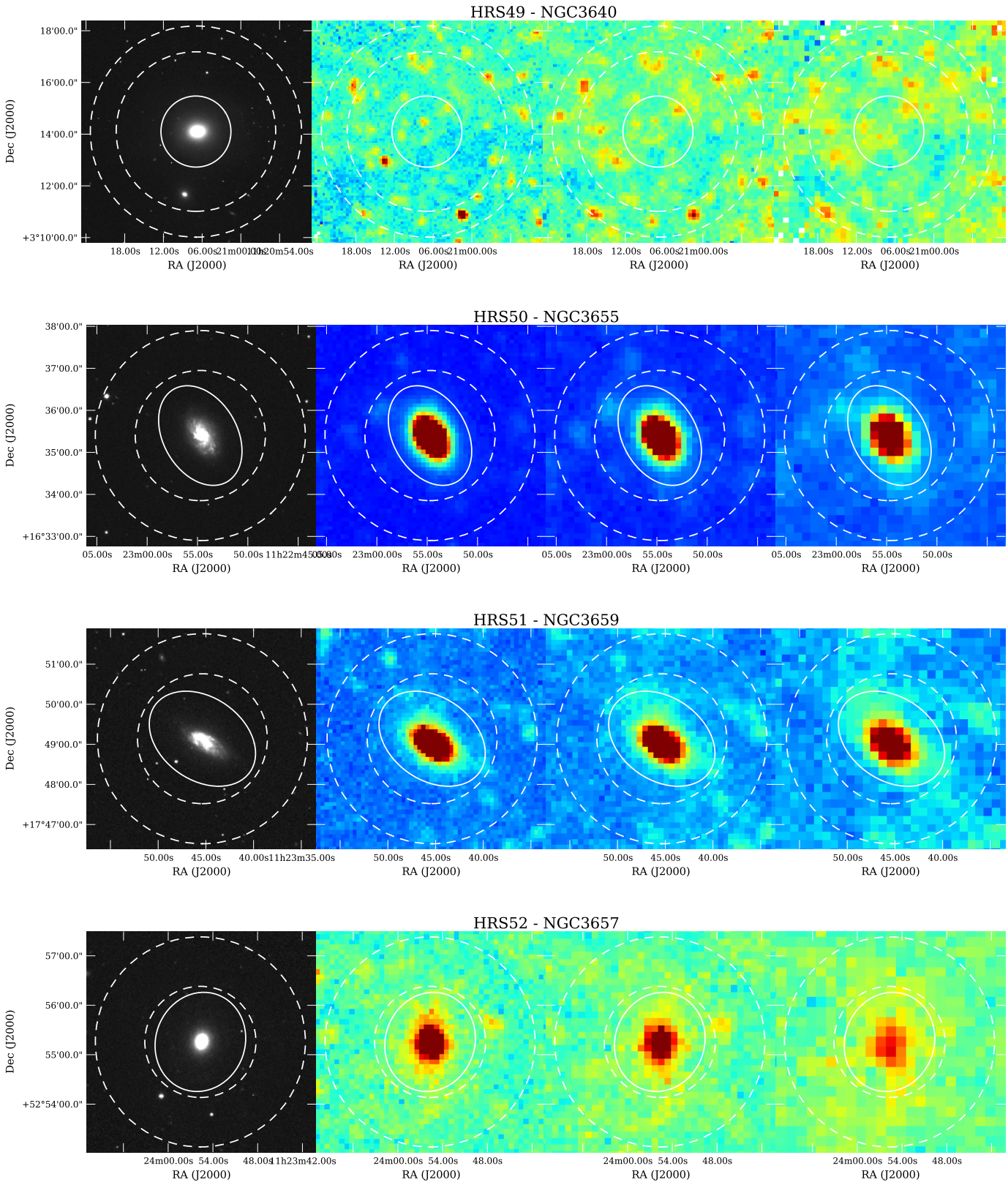

Fig. A.1: Images of the HRS galaxies. From left to right: SDSS *r'* band image, 250, 350, and 500 μm *Herschel* images. The aperture used for the photometry is indicated by the solid line and the annulus, where the background is estimated, is indicated in dashed lines.

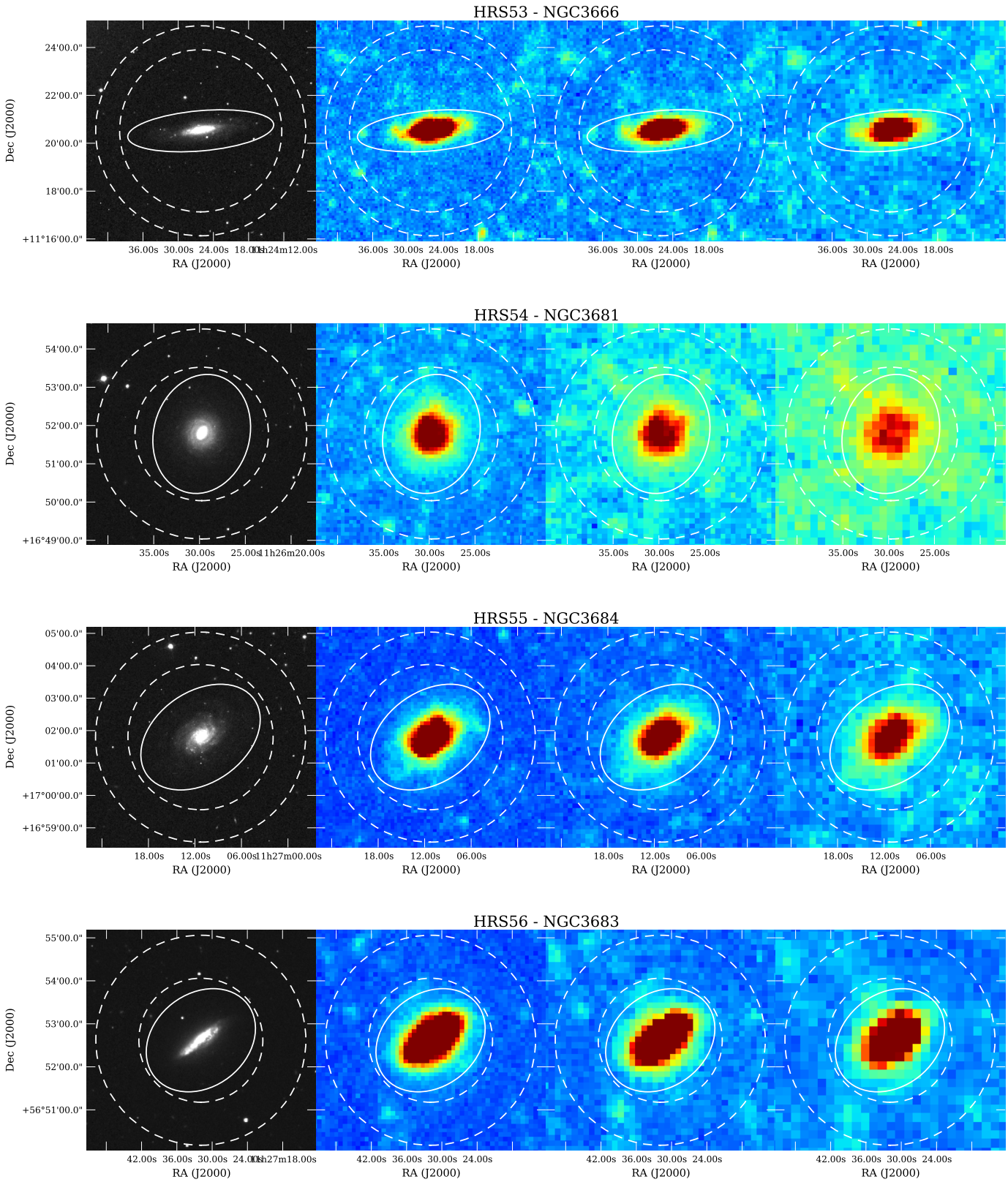

Fig. A.1: Images of the HRS galaxies. From left to right: SDSS *r'* band image, 250, 350, and 500 μm *Herschel* images. The aperture used for the photometry is indicated by the solid line and the annulus, where the background is estimated, is indicated in dashed lines.

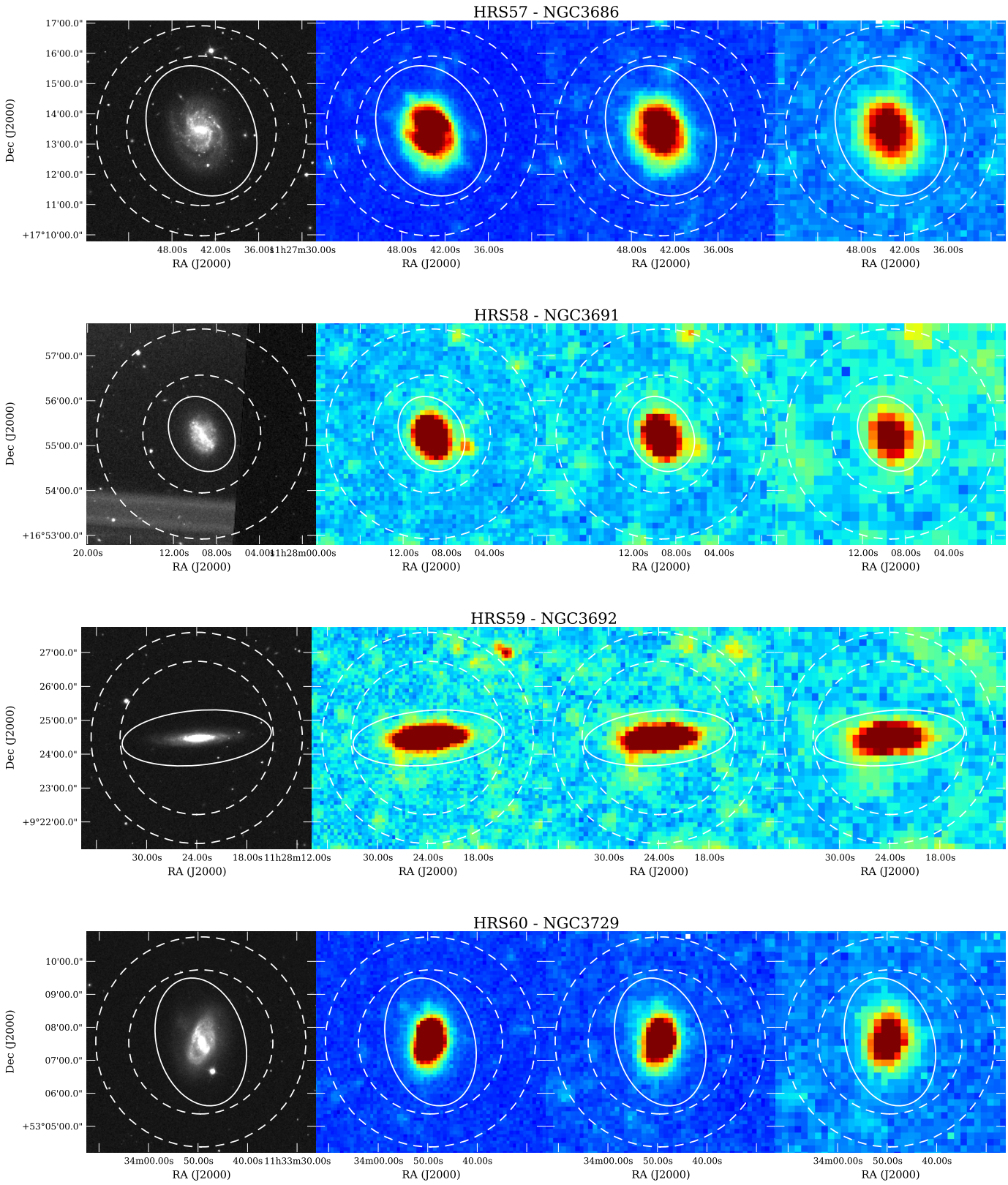

Fig. A.1: Images of the HRS galaxies. From left to right: SDSS *r'* band image, 250, 350, and 500 μm *Herschel* images. The aperture used for the photometry is indicated by the solid line and the annulus, where the background is estimated, is indicated in dashed lines.

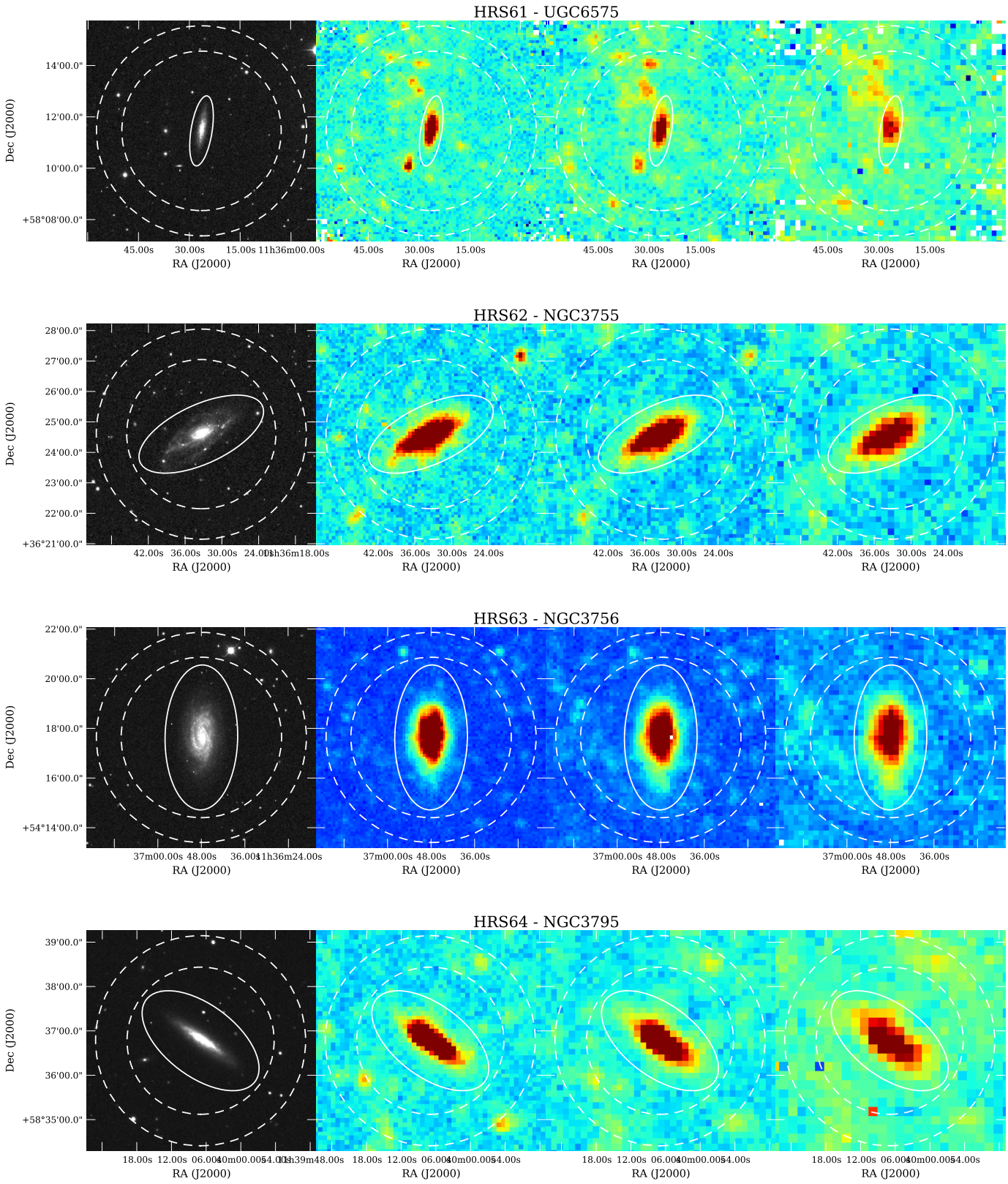

Fig. A.1: Images of the HRS galaxies. From left to right: SDSS *r'* band image, 250, 350, and 500 μm *Herschel* images. The aperture used for the photometry is indicated by the solid line and the annulus, where the background is estimated, is indicated in dashed lines.

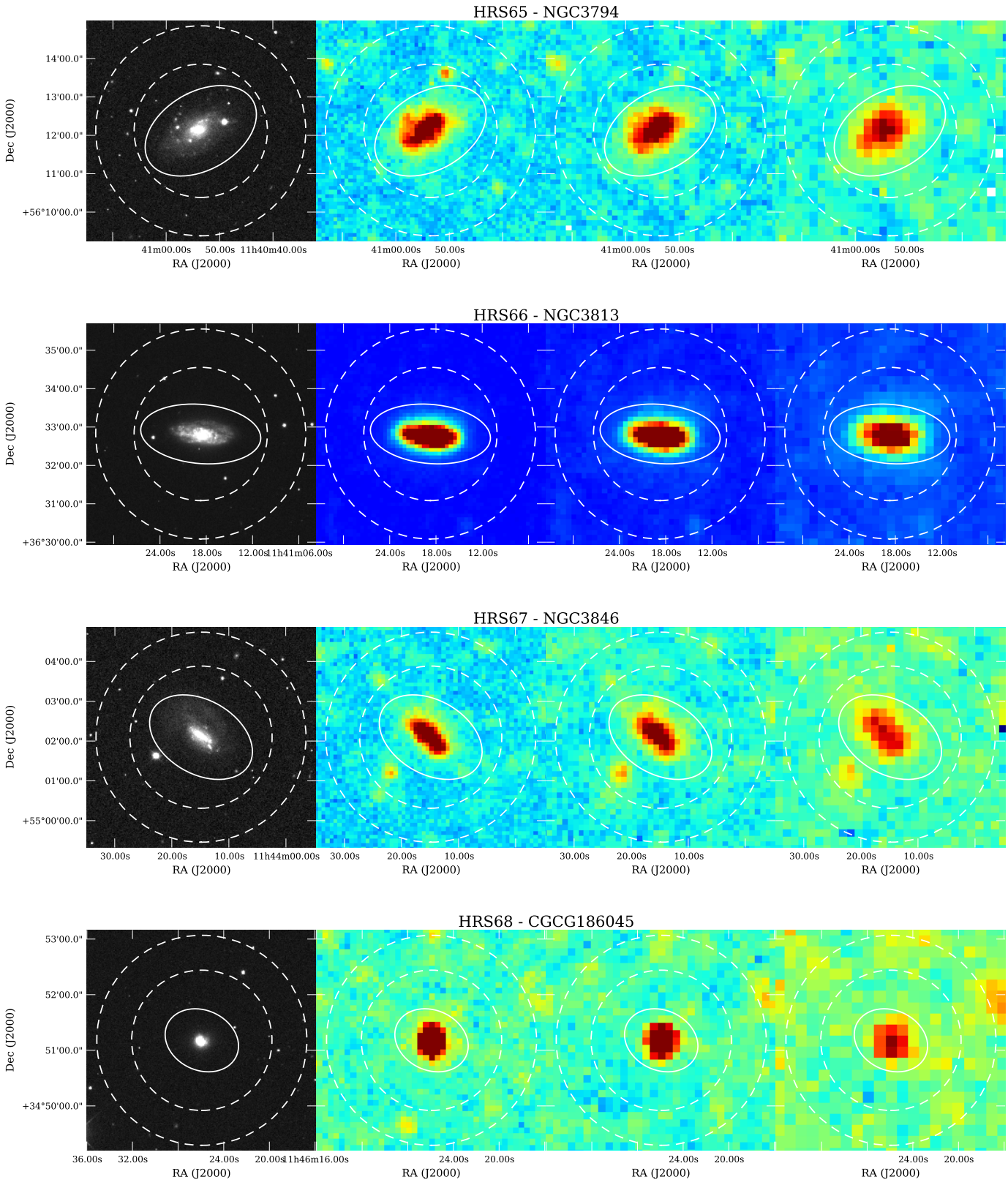

Fig. A.1: Images of the HRS galaxies. From left to right: SDSS *r'* band image, 250, 350, and 500 μm *Herschel* images. The aperture used for the photometry is indicated by the solid line and the annulus, where the background is estimated, is indicated in dashed lines.

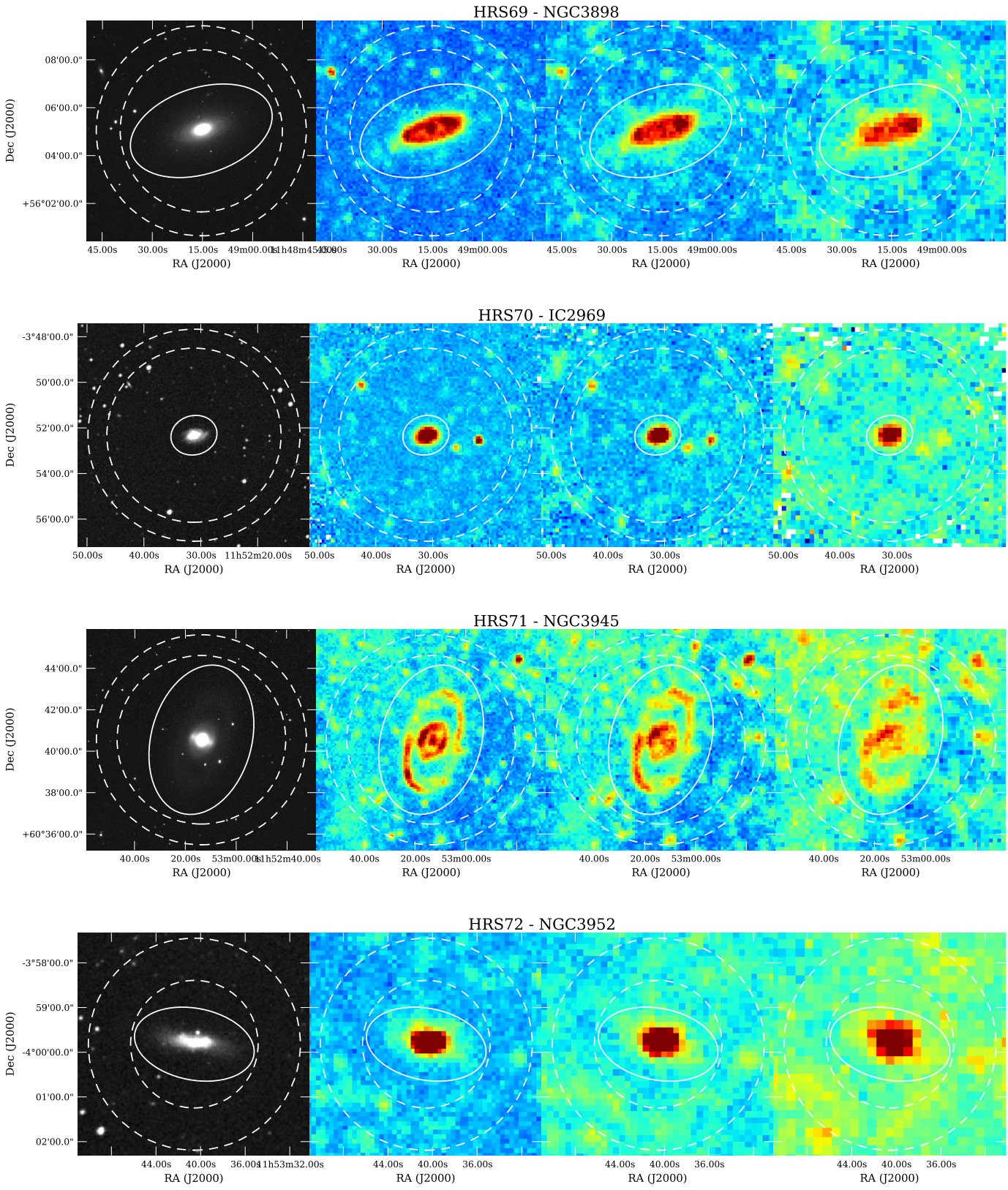

Fig. A.1: Images of the HRS galaxies. From left to right: SDSS *r'* band image, 250, 350, and 500 μm *Herschel* images. The aperture used for the photometry is indicated by the solid line and the annulus, where the background is estimated, is indicated in dashed lines.

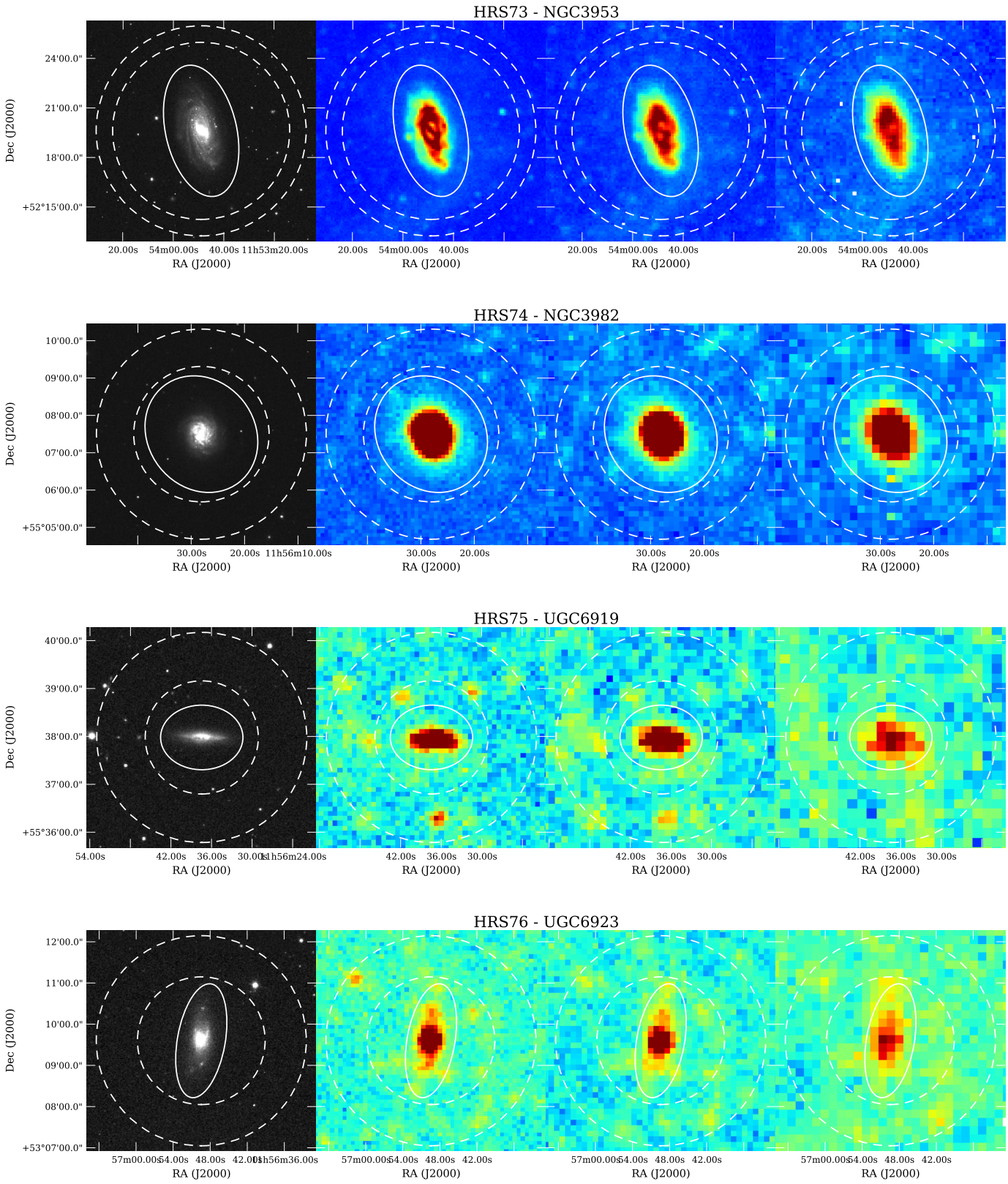

Fig. A.1: Images of the HRS galaxies. From left to right: SDSS *r'* band image, 250, 350, and 500 μm *Herschel* images. The aperture used for the photometry is indicated by the solid line and the annulus, where the background is estimated, is indicated in dashed lines.

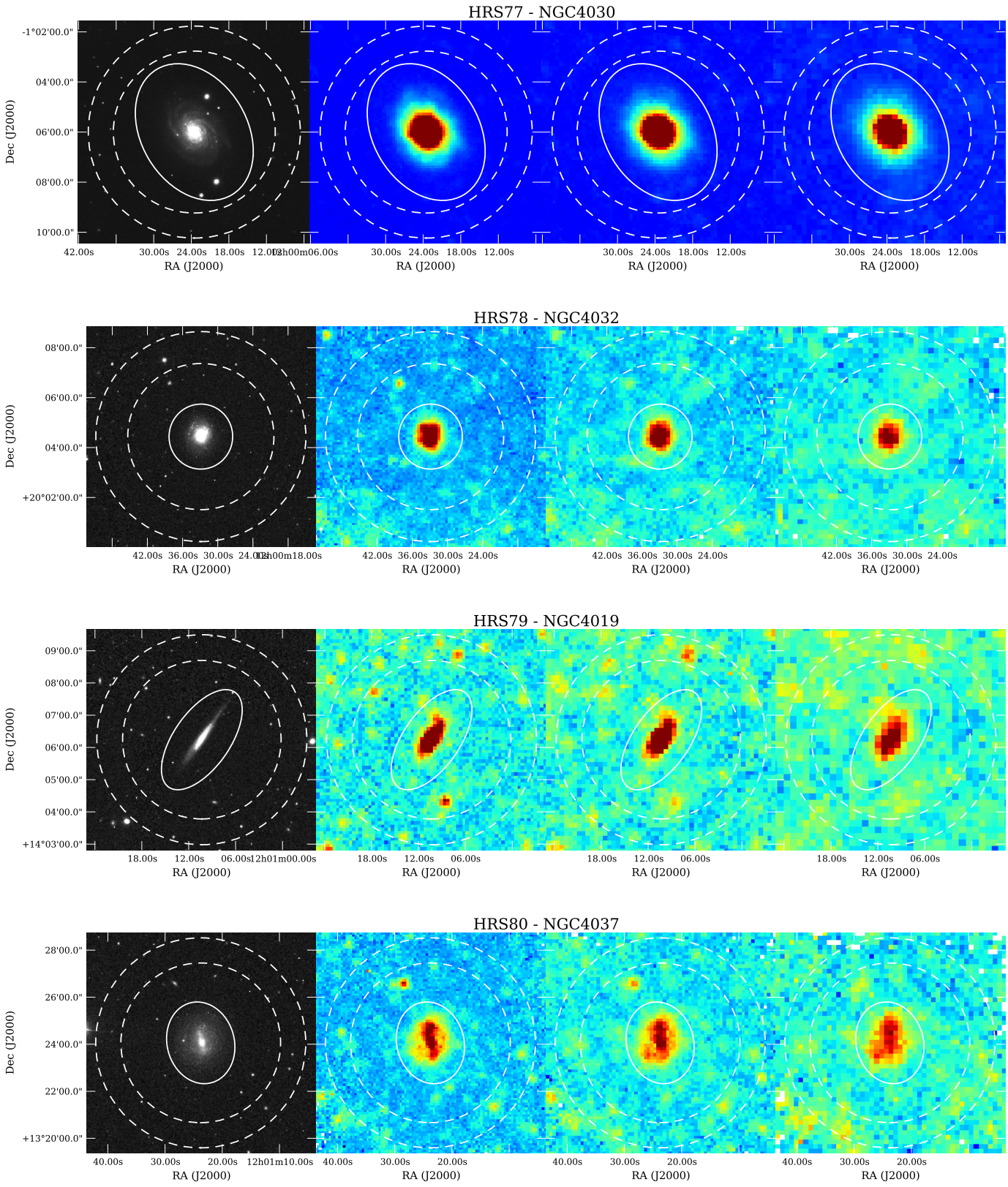

Fig. A.1: Images of the HRS galaxies. From left to right: SDSS *r'* band image, 250, 350, and 500 μm *Herschel* images. The aperture used for the photometry is indicated by the solid line and the annulus, where the background is estimated, is indicated in dashed lines.

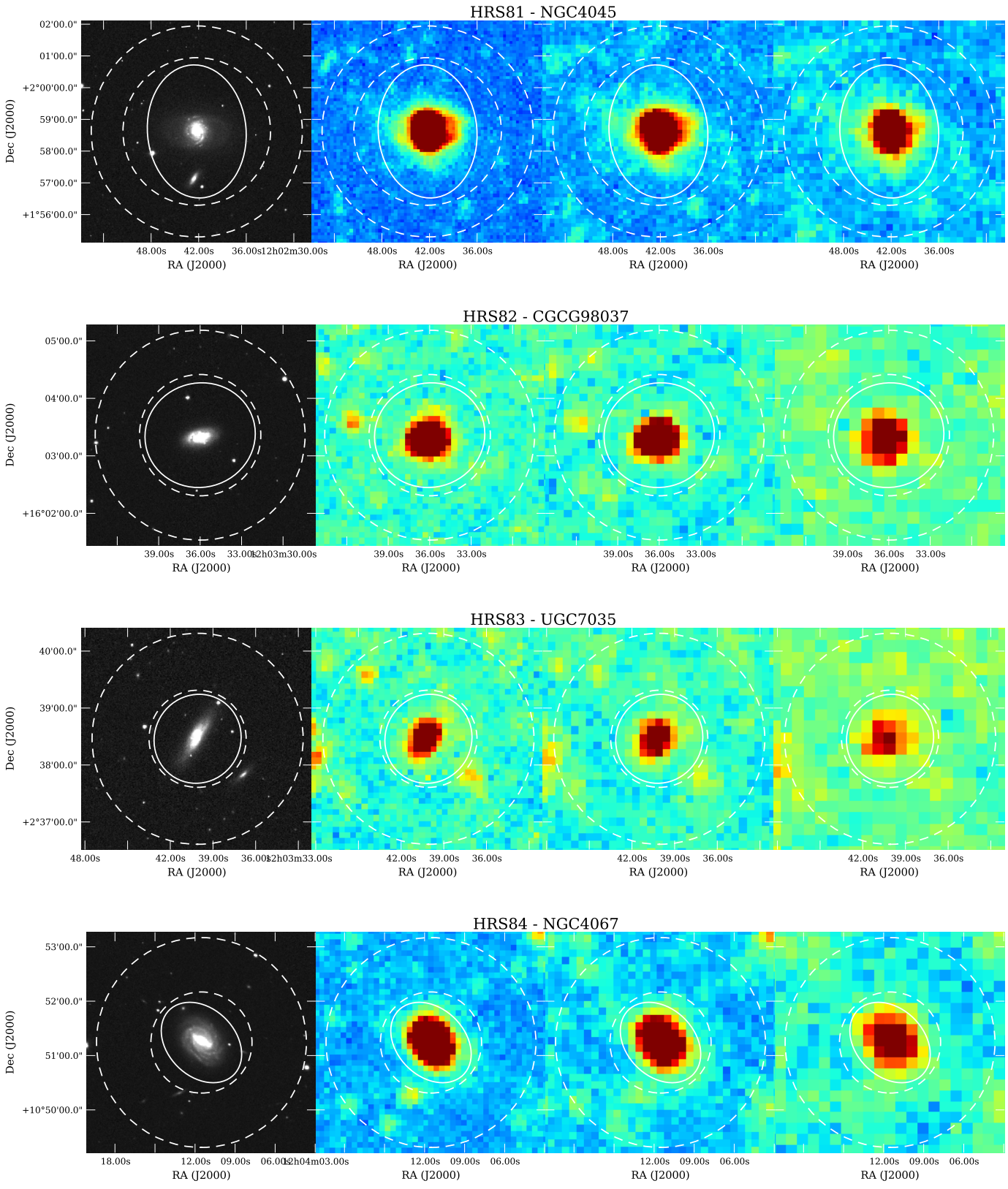

Fig. A.1: Images of the HRS galaxies. From left to right: SDSS *r'* band image, 250, 350, and 500 μm *Herschel* images. The aperture used for the photometry is indicated by the solid line and the annulus, where the background is estimated, is indicated in dashed lines.

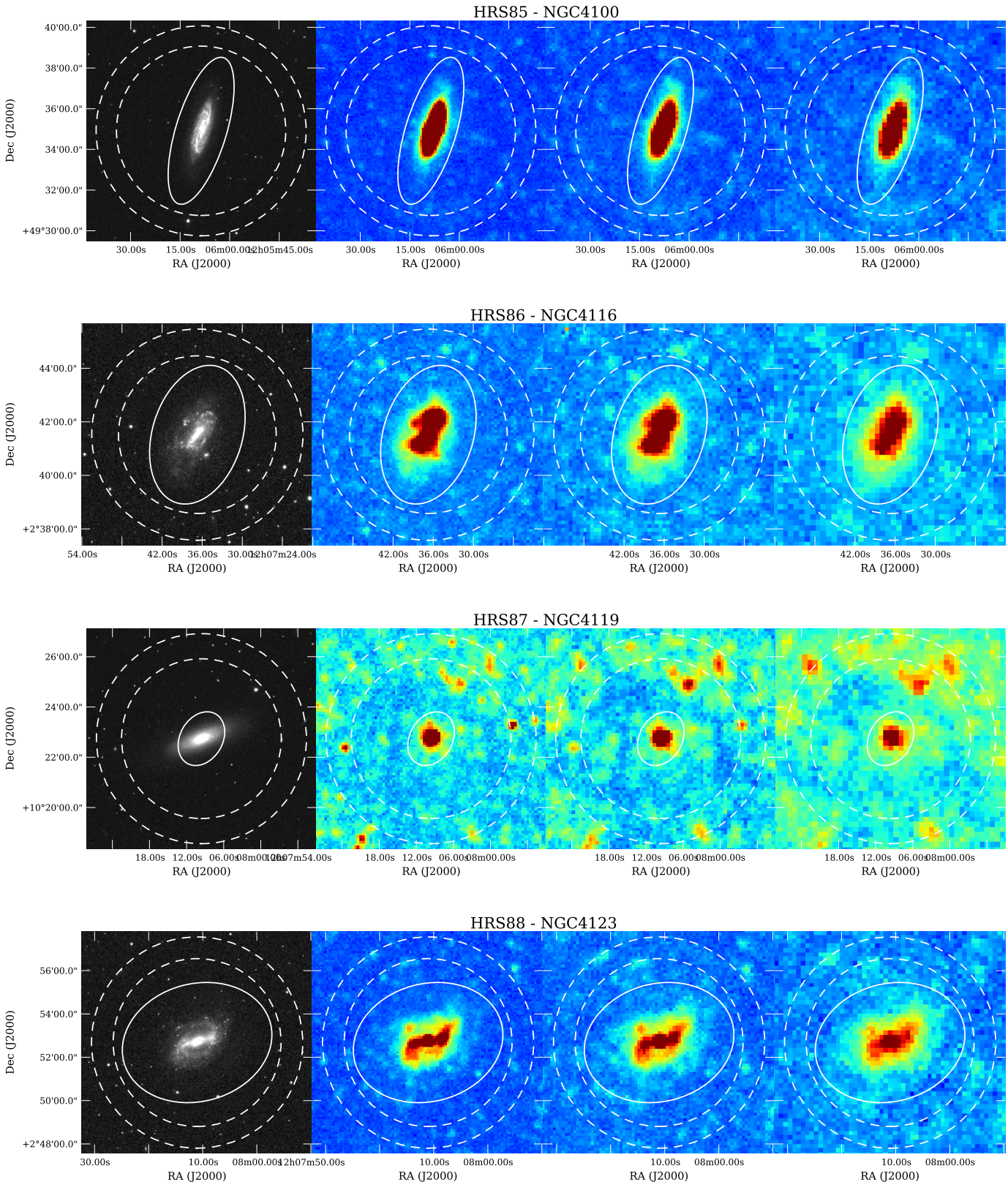

Fig. A.1: Images of the HRS galaxies. From left to right: SDSS *r'* band image, 250, 350, and 500 μm *Herschel* images. The aperture used for the photometry is indicated by the solid line and the annulus, where the background is estimated, is indicated in dashed lines.

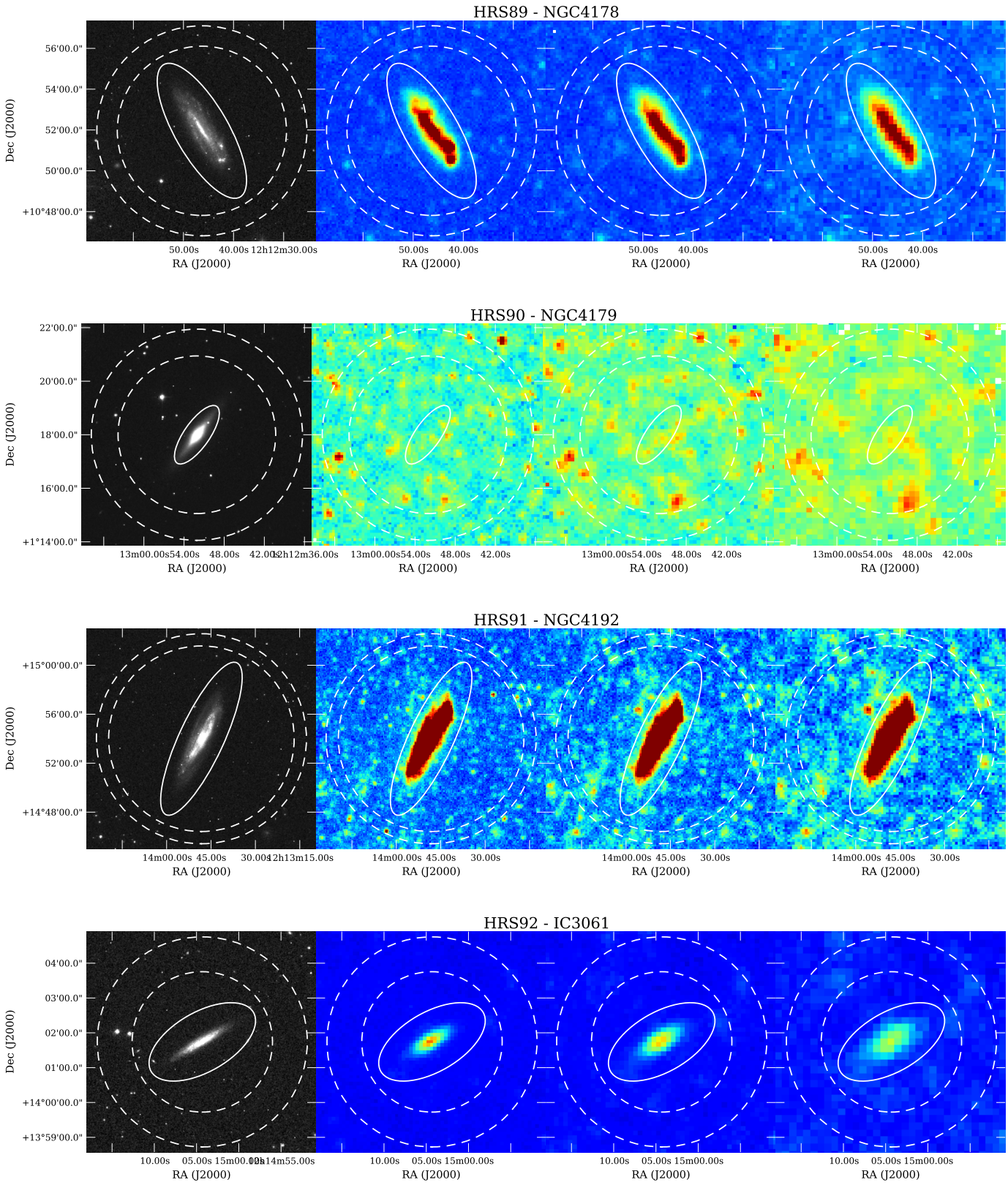

Fig. A.1: Images of the HRS galaxies. From left to right: SDSS *r'* band image, 250, 350, and 500 μm *Herschel* images. The aperture used for the photometry is indicated by the solid line and the annulus, where the background is estimated, is indicated in dashed lines.

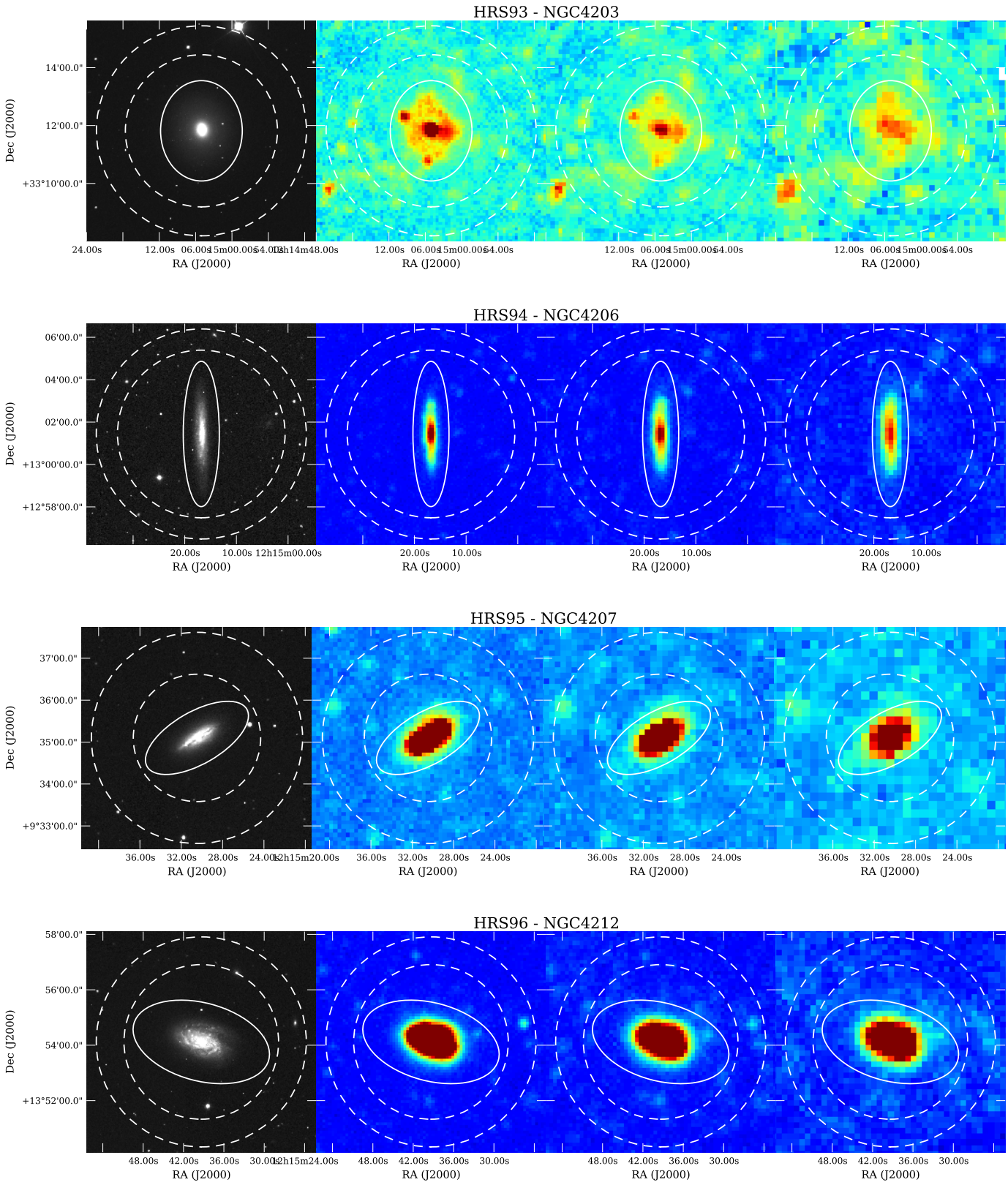

Fig. A.1: Images of the HRS galaxies. From left to right: SDSS *r'* band image, 250, 350, and 500 μm *Herschel* images. The aperture used for the photometry is indicated by the solid line and the annulus, where the background is estimated, is indicated in dashed lines.

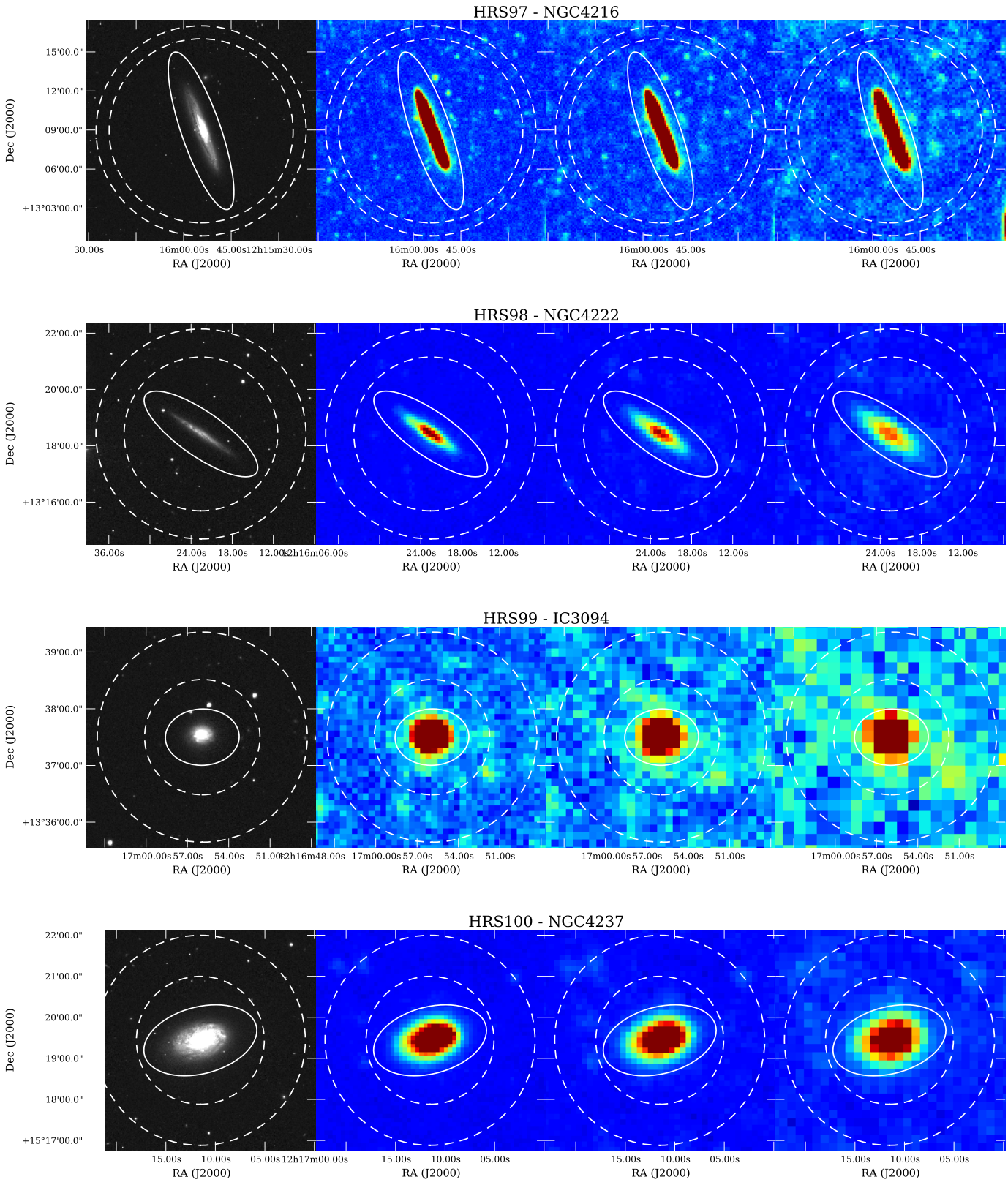

Fig. A.1: Images of the HRS galaxies. From left to right: SDSS *r'* band image, 250, 350, and 500 μm *Herschel* images. The aperture used for the photometry is indicated by the solid line and the annulus, where the background is estimated, is indicated in dashed lines.

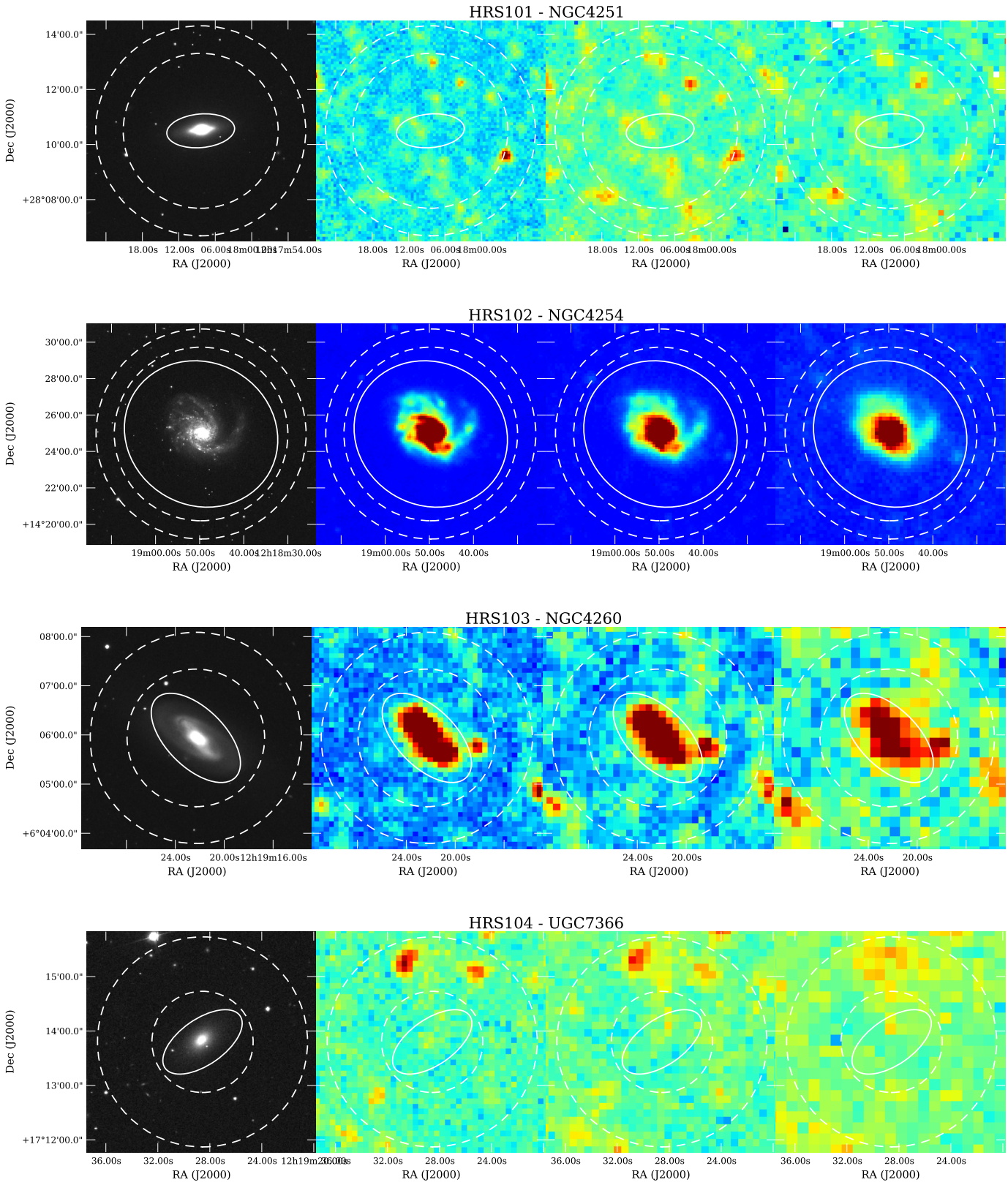

Fig. A.1: Images of the HRS galaxies. From left to right: SDSS *r'* band image, 250, 350, and 500 μm *Herschel* images. The aperture used for the photometry is indicated by the solid line and the annulus, where the background is estimated, is indicated in dashed lines.

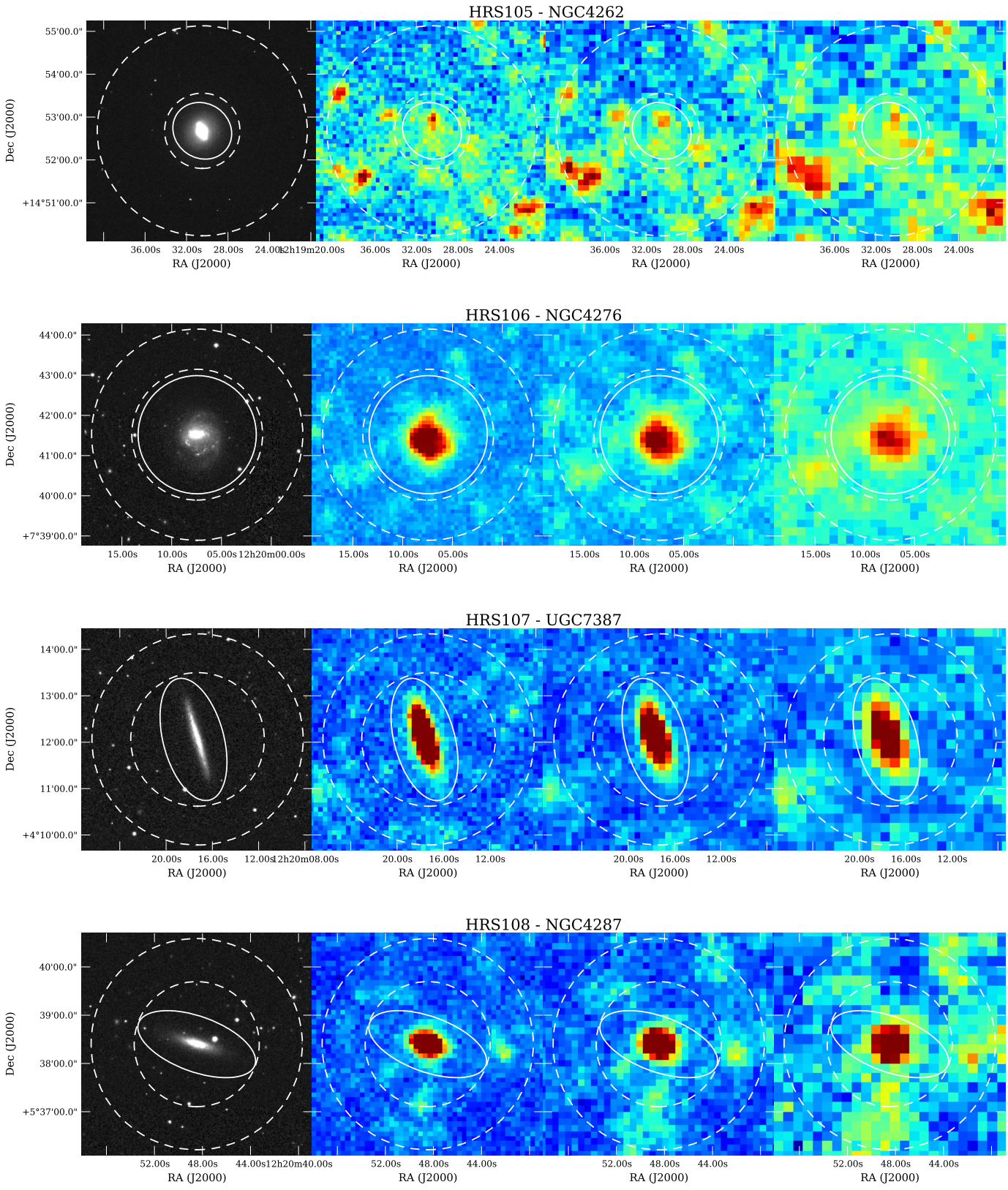

Fig. A.1: Images of the HRS galaxies. From left to right: SDSS *r'* band image, 250, 350, and 500 μm *Herschel* images. The aperture used for the photometry is indicated by the solid line and the annulus, where the background is estimated, is indicated in dashed lines.

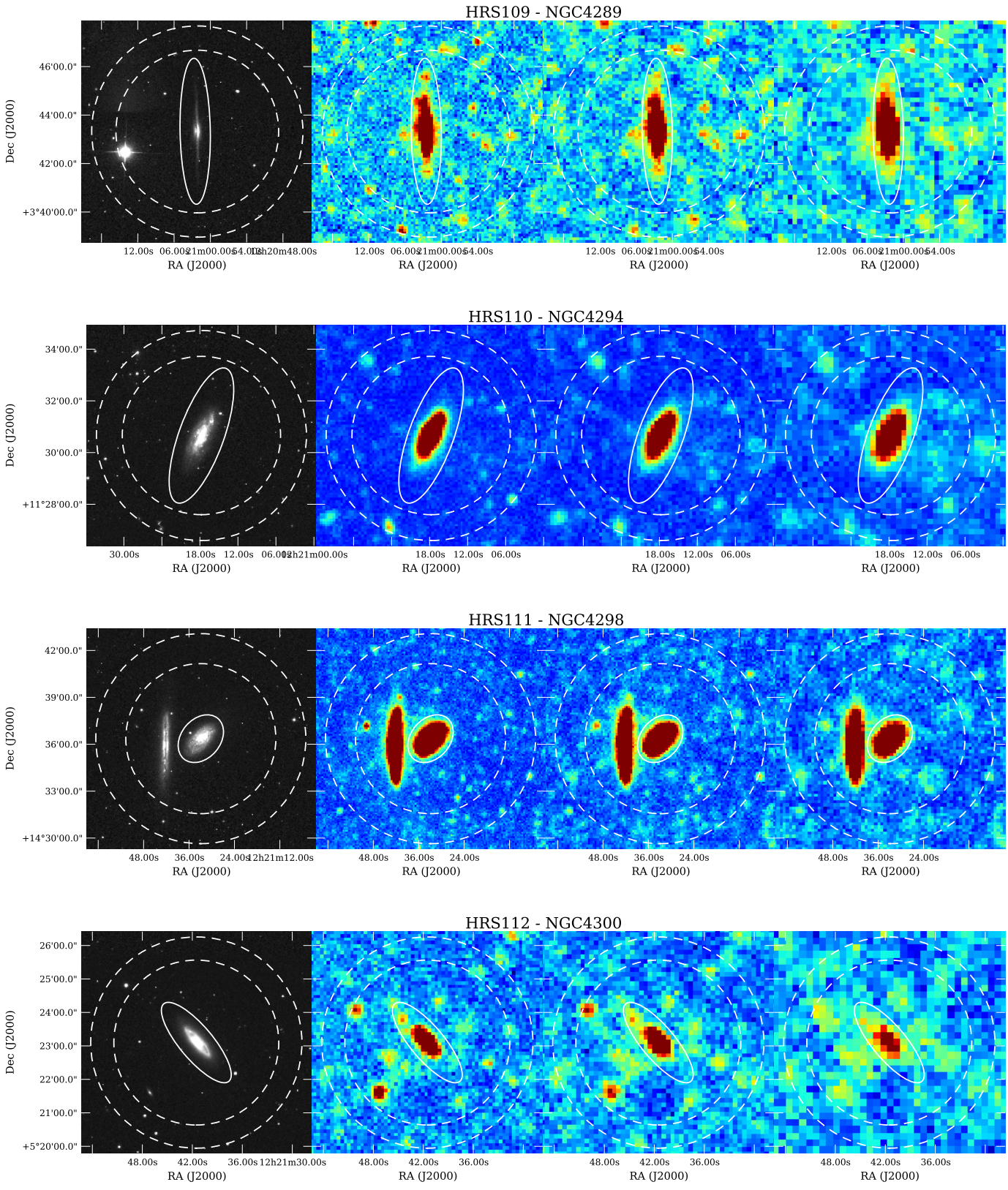

Fig. A.1: Images of the HRS galaxies. From left to right: SDSS *r'* band image, 250, 350, and 500 μm *Herschel* images. The aperture used for the photometry is indicated by the solid line and the annulus, where the background is estimated, is indicated in dashed lines.

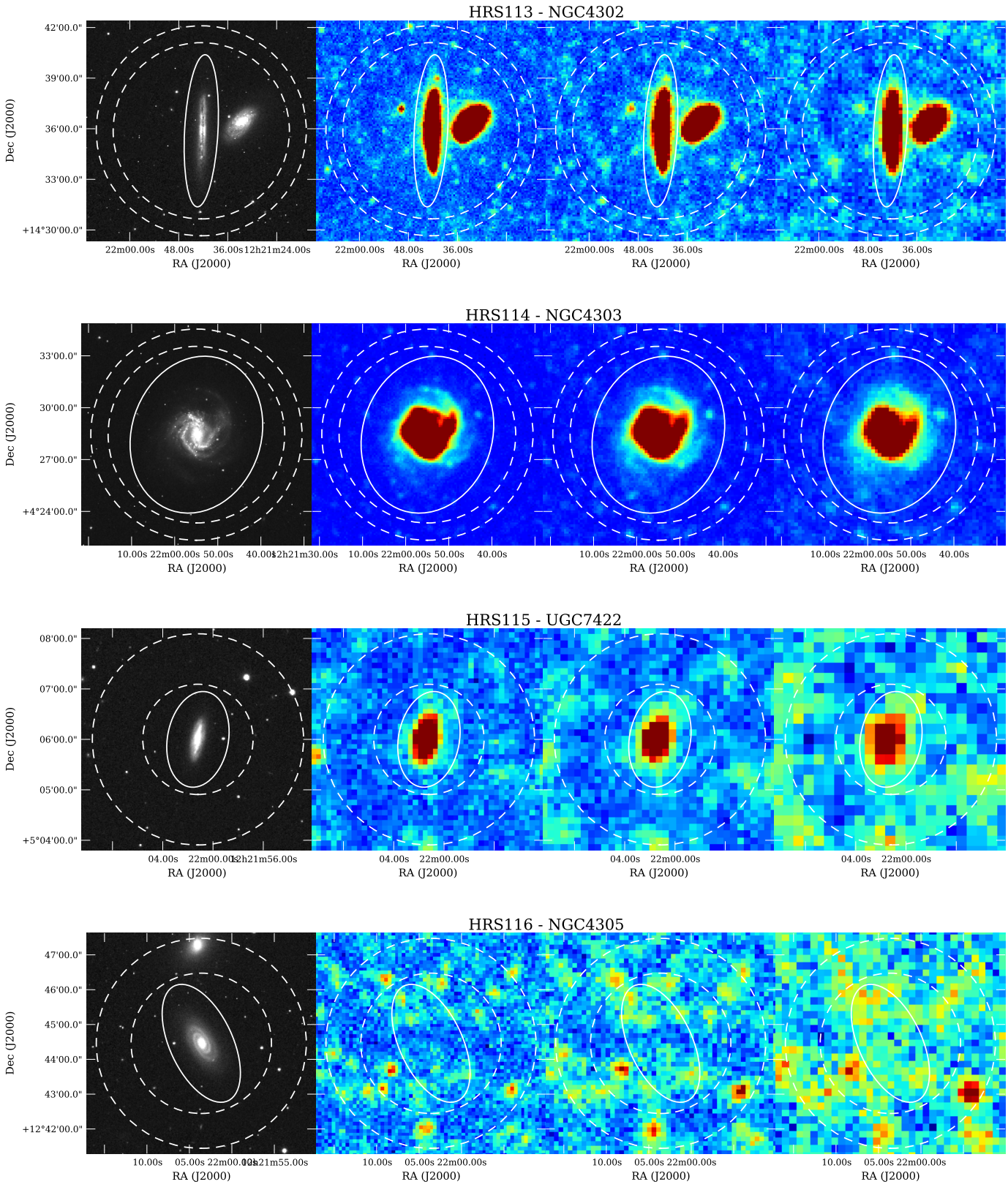

Fig. A.1: Images of the HRS galaxies. From left to right: SDSS *r'* band image, 250, 350, and 500 μm *Herschel* images. The aperture used for the photometry is indicated by the solid line and the annulus, where the background is estimated, is indicated in dashed lines.

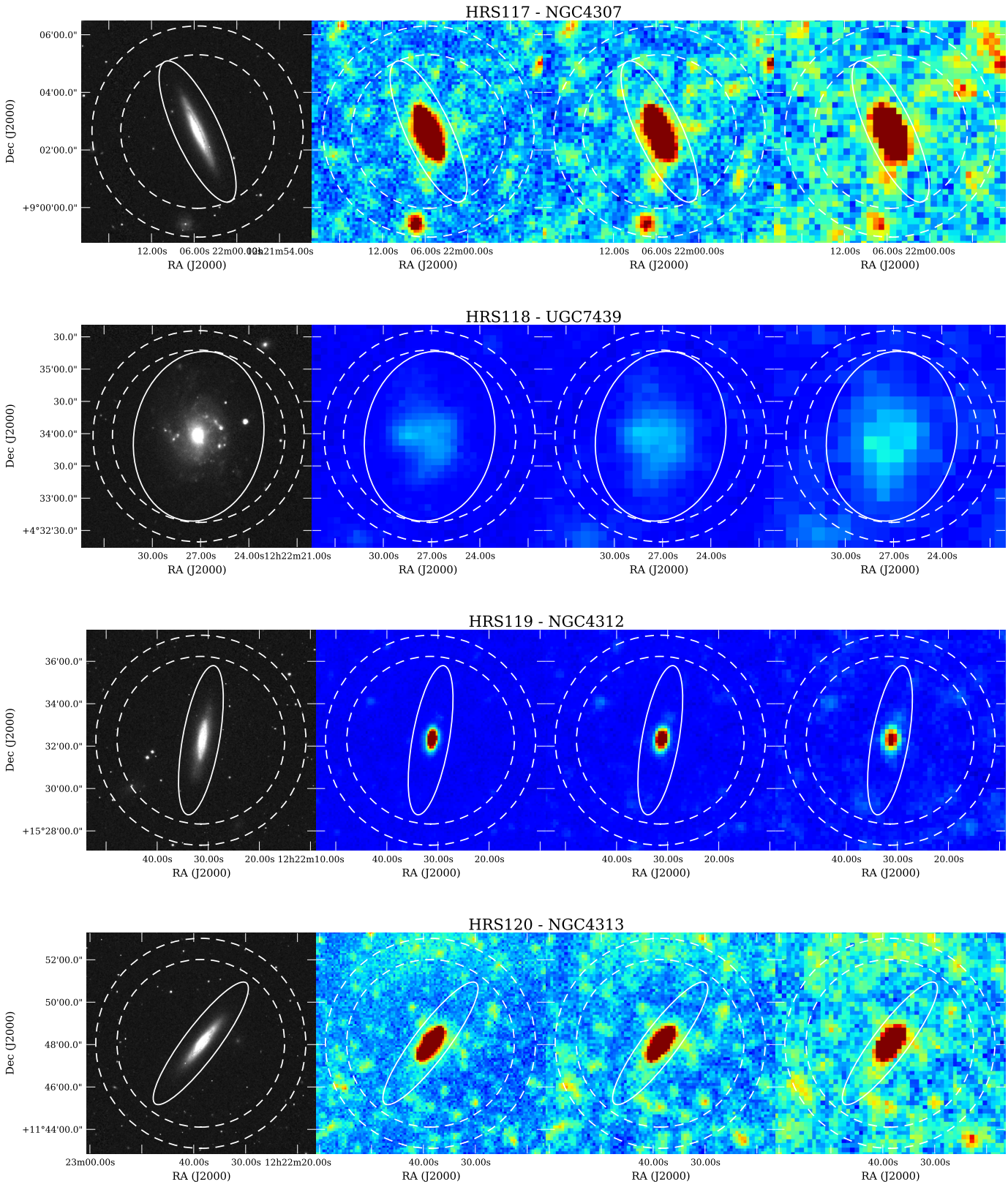

Fig. A.1: Images of the HRS galaxies. From left to right: SDSS *r'* band image, 250, 350, and 500 μm *Herschel* images. The aperture used for the photometry is indicated by the solid line and the annulus, where the background is estimated, is indicated in dashed lines.

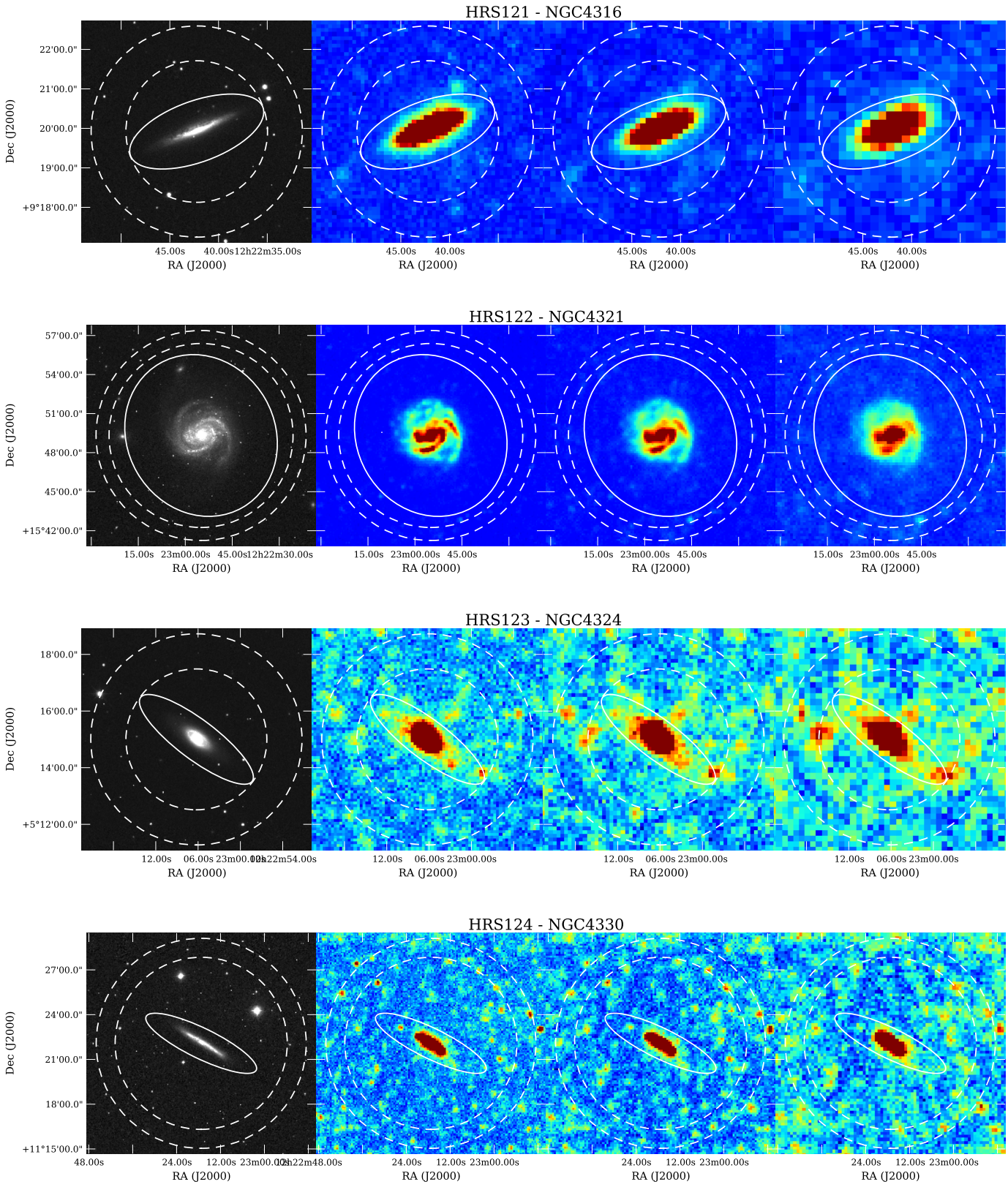

Fig. A.1: Images of the HRS galaxies. From left to right: SDSS *r'* band image, 250, 350, and 500 μm *Herschel* images. The aperture used for the photometry is indicated by the solid line and the annulus, where the background is estimated, is indicated in dashed lines.

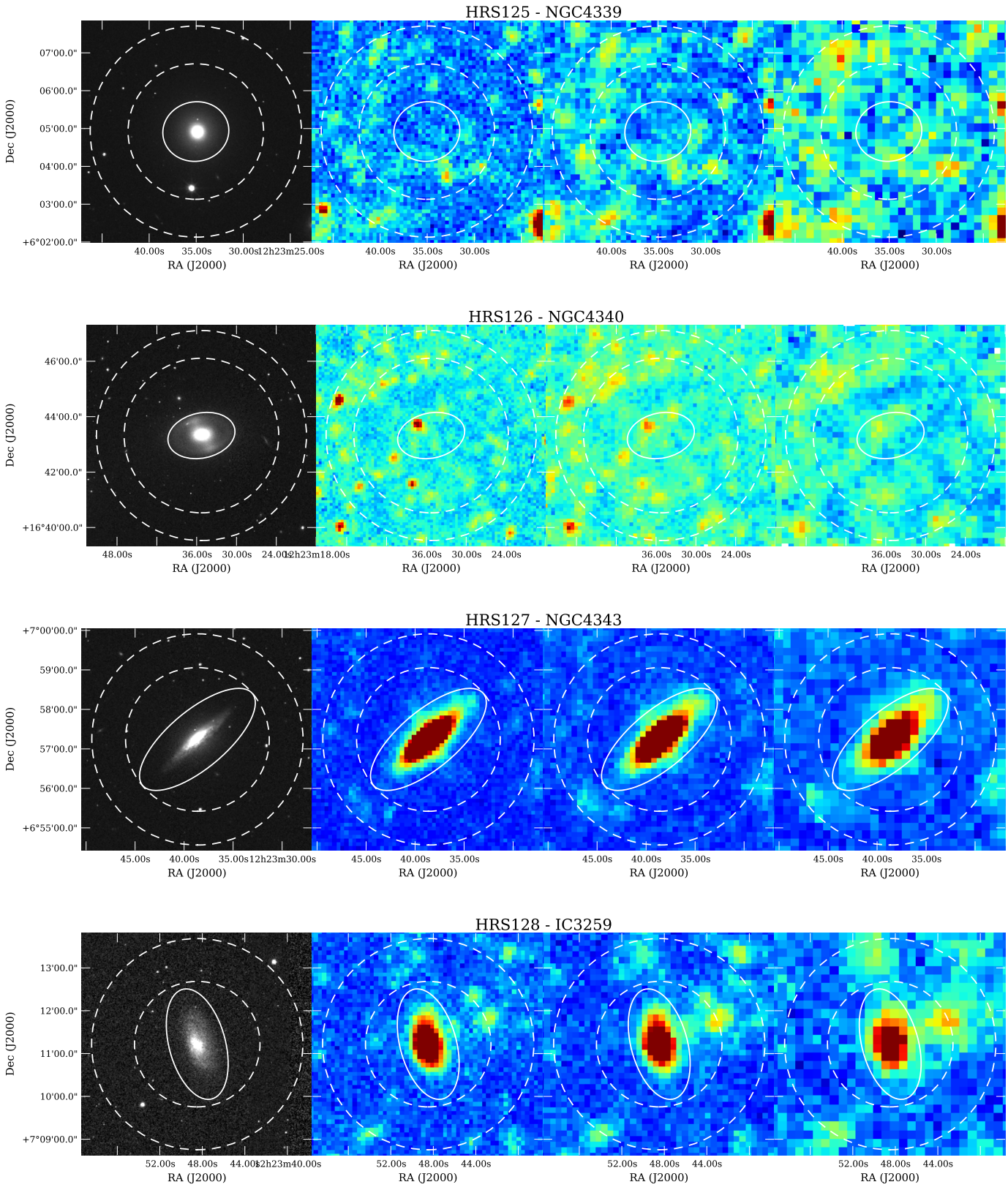

Fig. A.1: Images of the HRS galaxies. From left to right: SDSS *r'* band image, 250, 350, and 500 μm *Herschel* images. The aperture used for the photometry is indicated by the solid line and the annulus, where the background is estimated, is indicated in dashed lines.

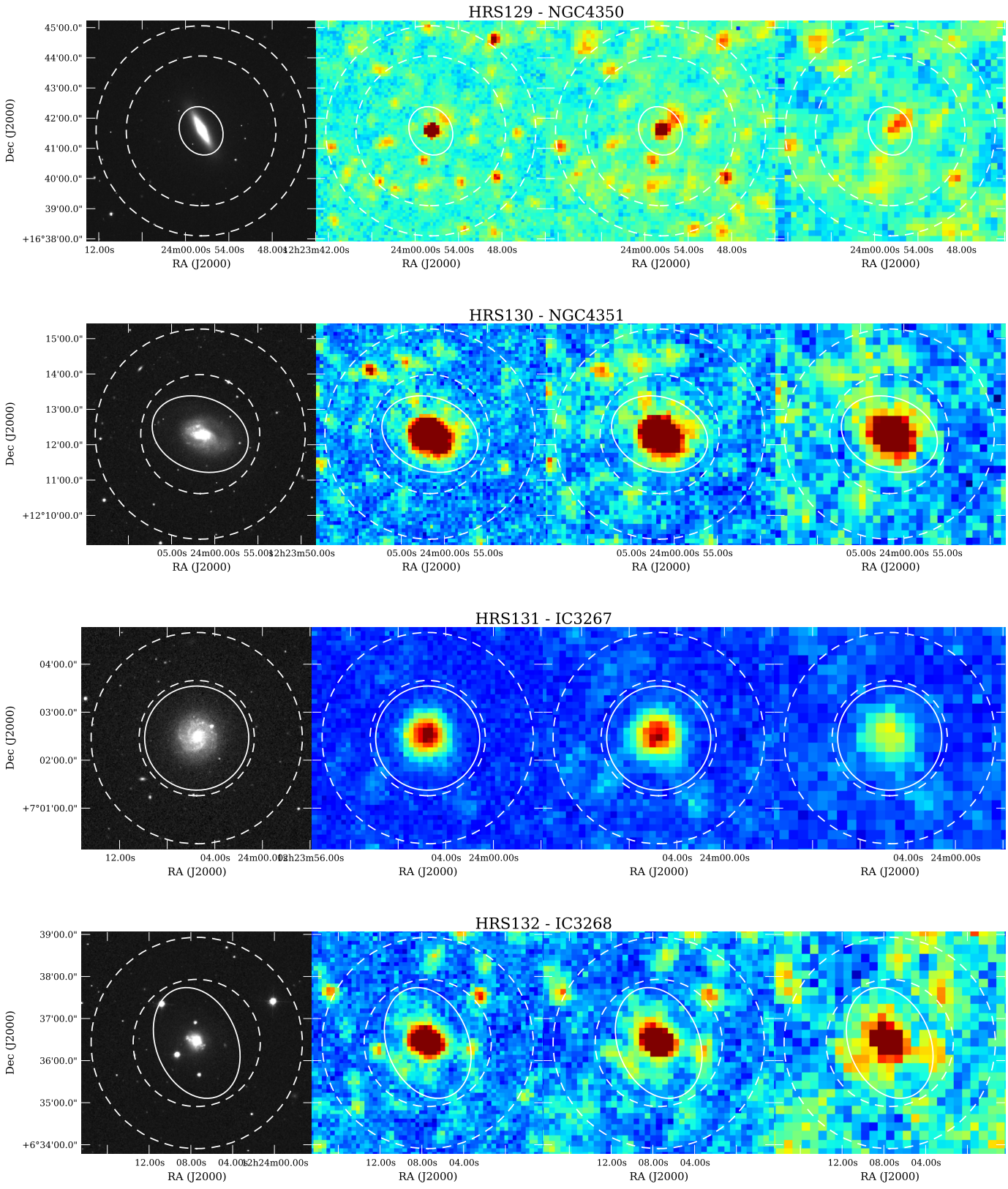

Fig. A.1: Images of the HRS galaxies. From left to right: SDSS *r'* band image, 250, 350, and 500 μm *Herschel* images. The aperture used for the photometry is indicated by the solid line and the annulus, where the background is estimated, is indicated in dashed lines.

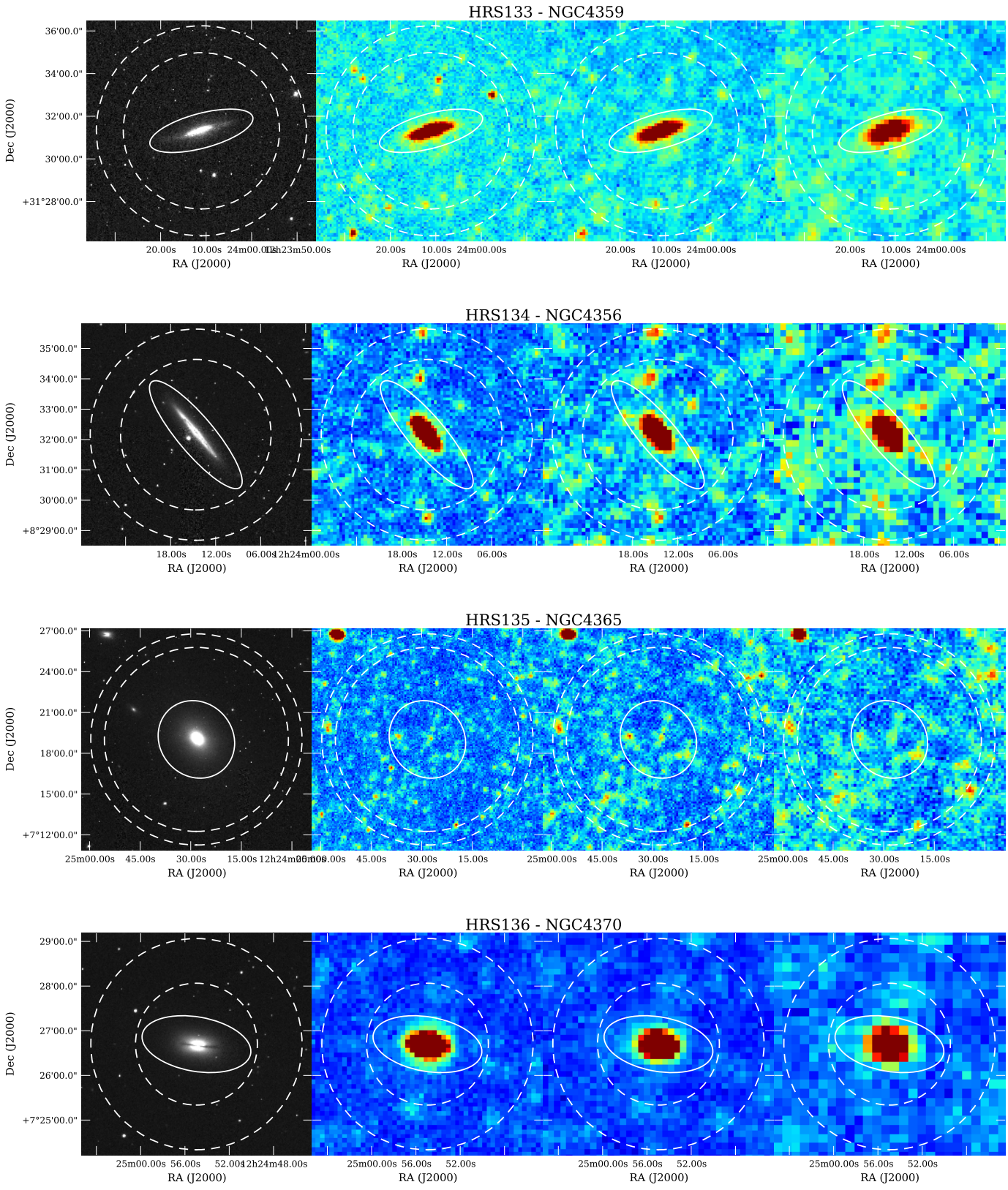

Fig. A.1: Images of the HRS galaxies. From left to right: SDSS *r'* band image, 250, 350, and 500 μm *Herschel* images. The aperture used for the photometry is indicated by the solid line and the annulus, where the background is estimated, is indicated in dashed lines.

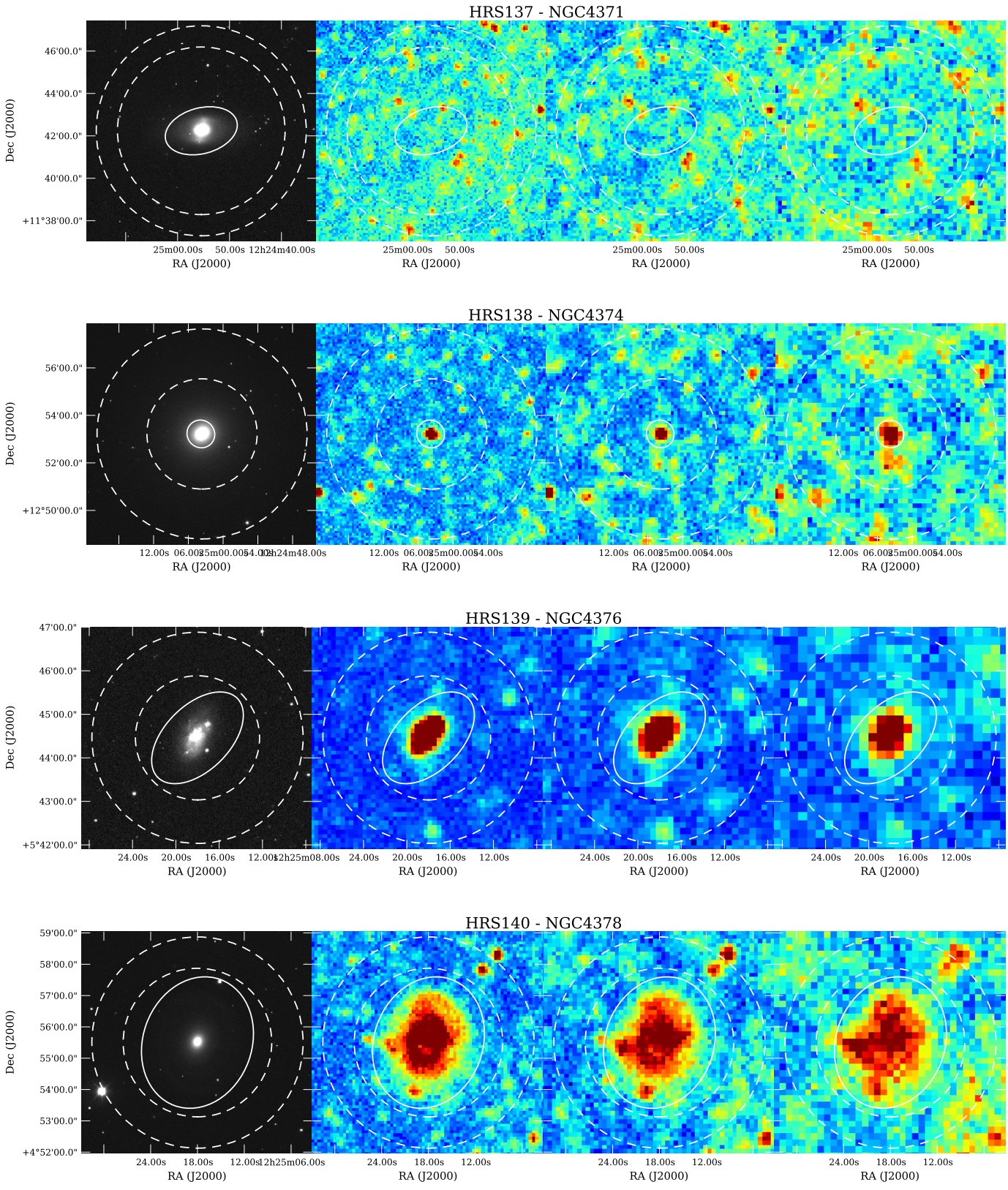

Fig. A.1: Images of the HRS galaxies. From left to right: SDSS *r'* band image, 250, 350, and 500 μm *Herschel* images. The aperture used for the photometry is indicated by the solid line and the annulus, where the background is estimated, is indicated in dashed lines.

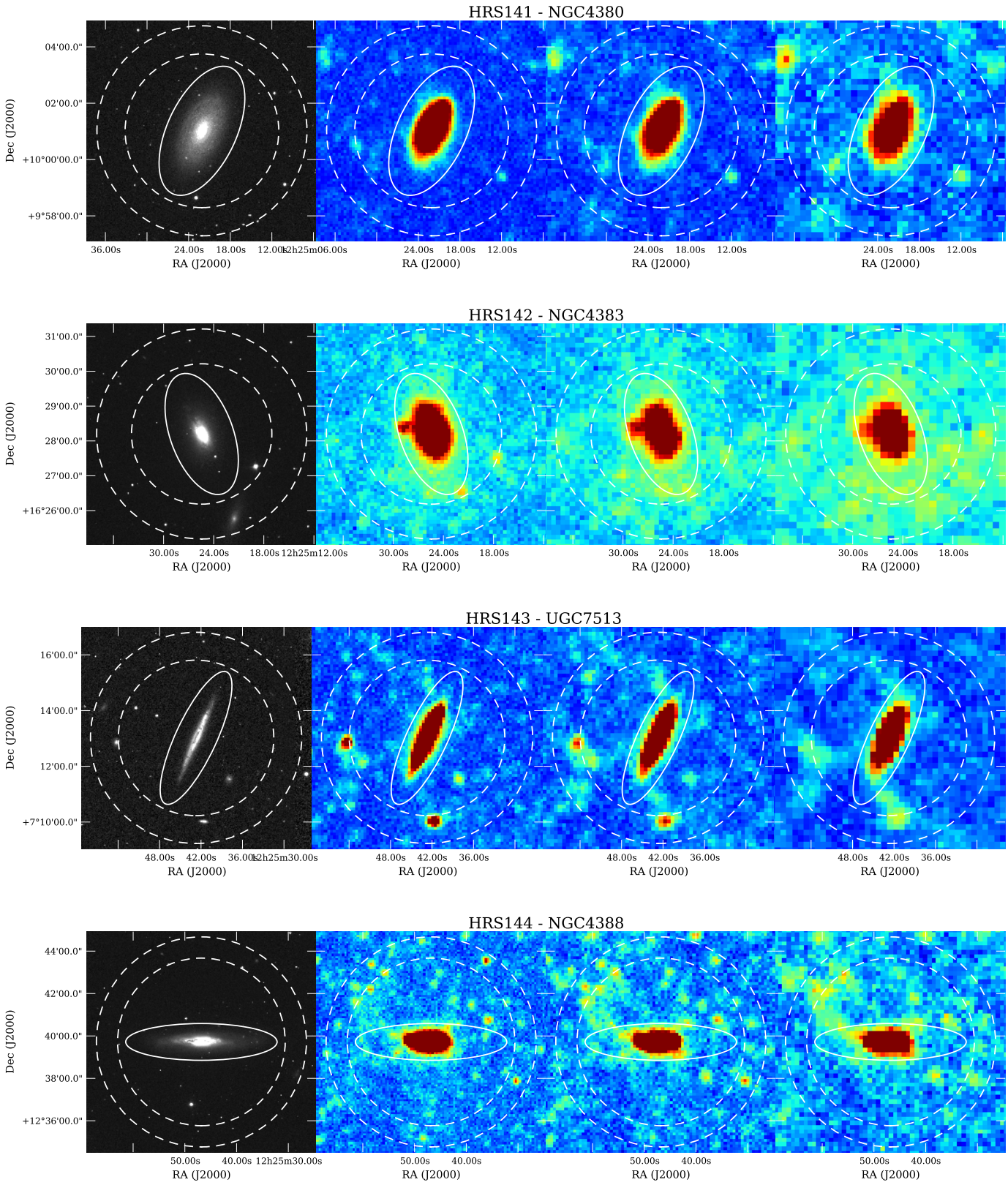

Fig. A.1: Images of the HRS galaxies. From left to right: SDSS *r'* band image, 250, 350, and 500 μm *Herschel* images. The aperture used for the photometry is indicated by the solid line and the annulus, where the background is estimated, is indicated in dashed lines.

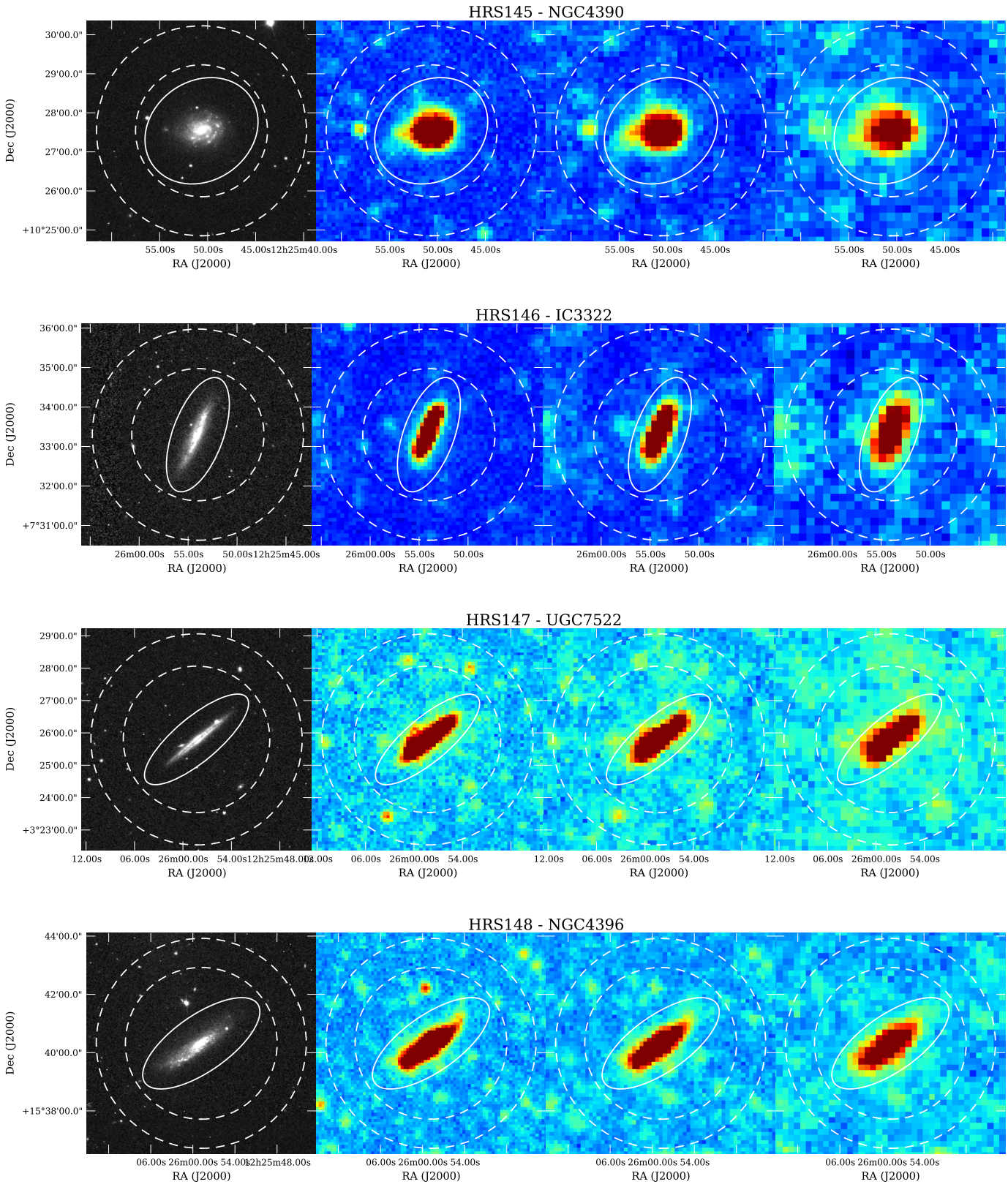

Fig. A.1: Images of the HRS galaxies. From left to right: SDSS *r'* band image, 250, 350, and 500 μm *Herschel* images. The aperture used for the photometry is indicated by the solid line and the annulus, where the background is estimated, is indicated in dashed lines.

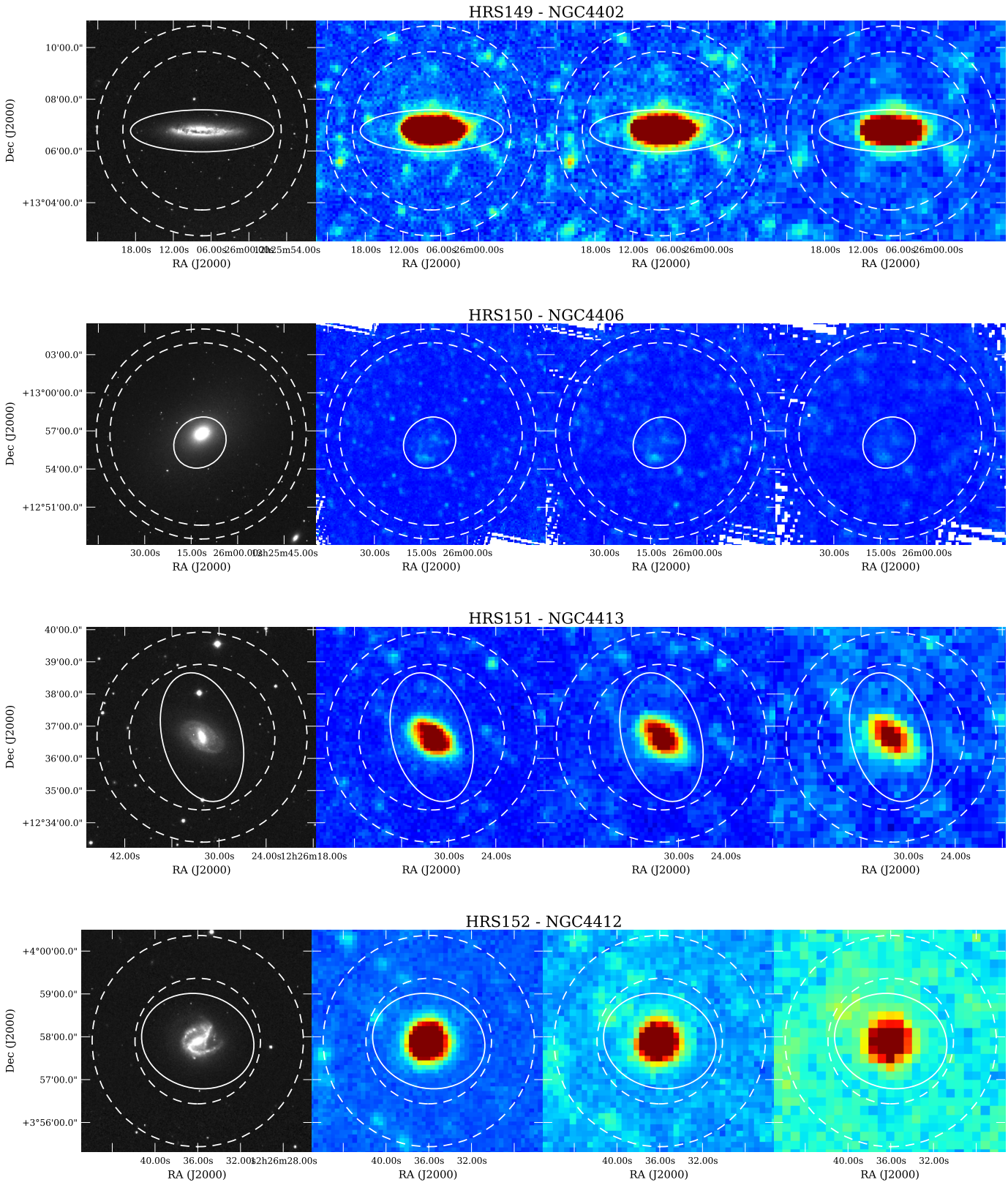

Fig. A.1: Images of the HRS galaxies. From left to right: SDSS *r'* band image, 250, 350, and 500 μm *Herschel* images. The aperture used for the photometry is indicated by the solid line and the annulus, where the background is estimated, is indicated in dashed lines.

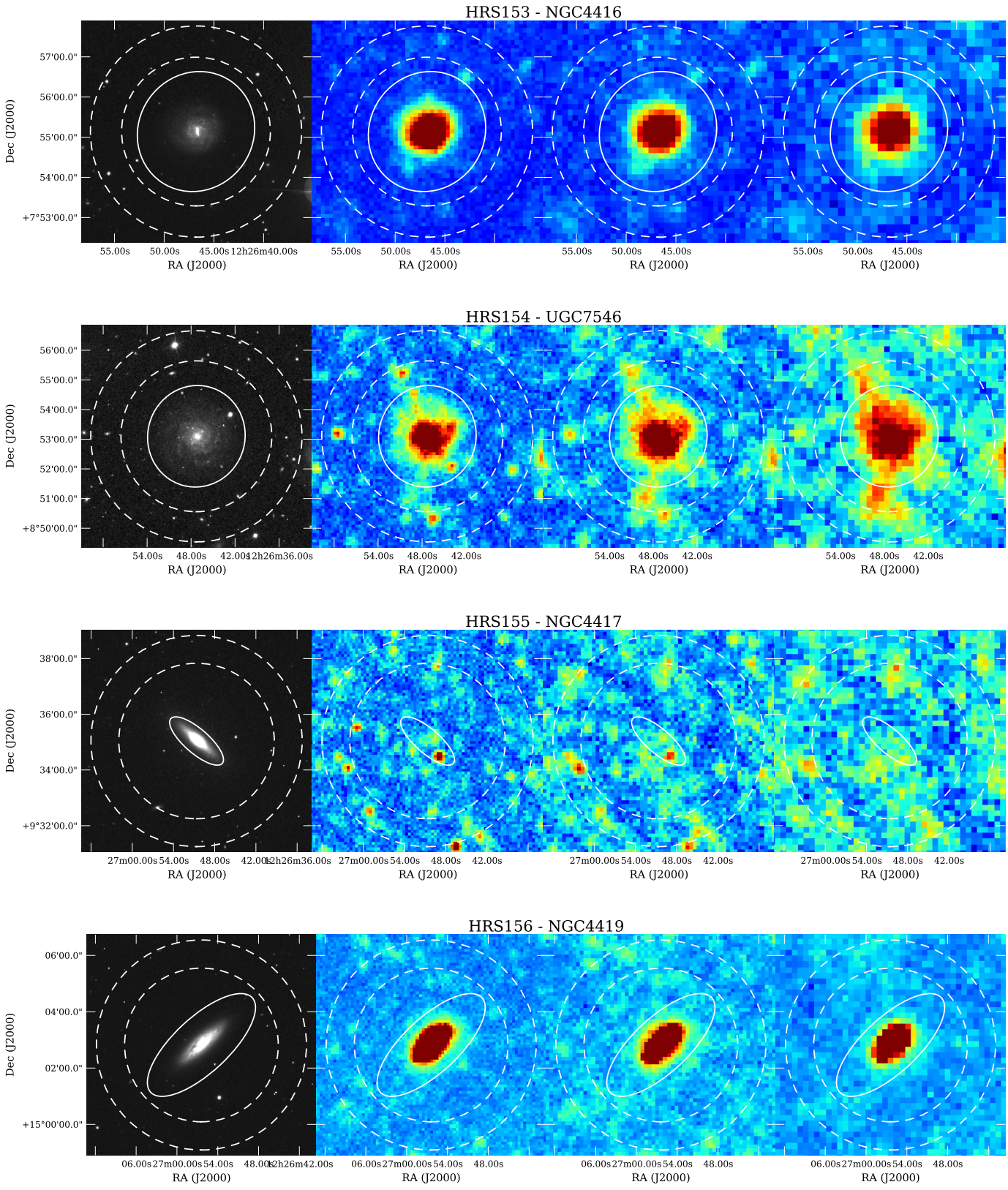

Fig. A.1: Images of the HRS galaxies. From left to right: SDSS *r'* band image, 250, 350, and 500 μm *Herschel* images. The aperture used for the photometry is indicated by the solid line and the annulus, where the background is estimated, is indicated in dashed lines.

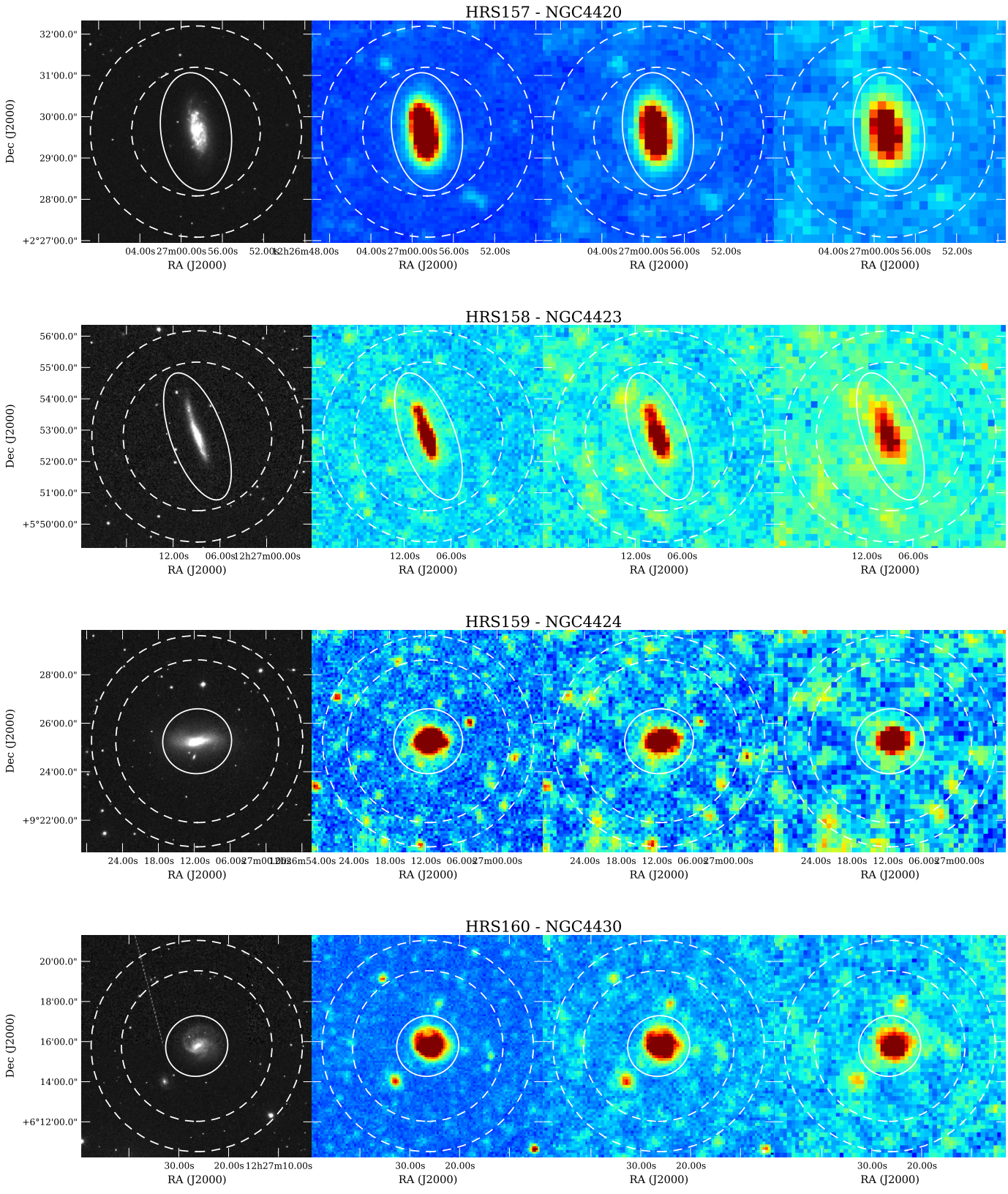

Fig. A.1: Images of the HRS galaxies. From left to right: SDSS *r'* band image, 250, 350, and 500 μm *Herschel* images. The aperture used for the photometry is indicated by the solid line and the annulus, where the background is estimated, is indicated in dashed lines.

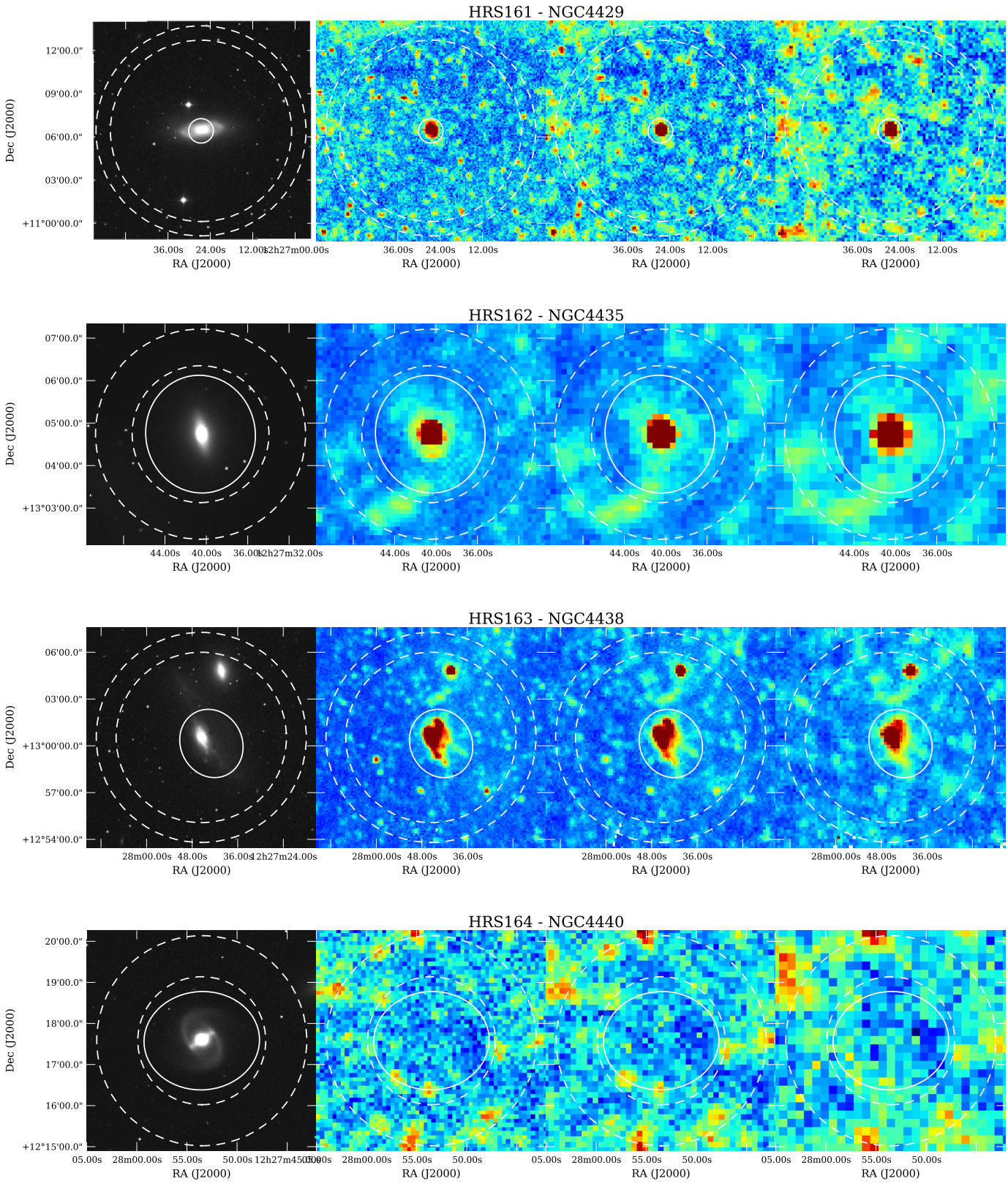

Fig. A.1: Images of the HRS galaxies. From left to right: SDSS *r'* band image, 250, 350, and 500 μm *Herschel* images. The aperture used for the photometry is indicated by the solid line and the annulus, where the background is estimated, is indicated in dashed lines.

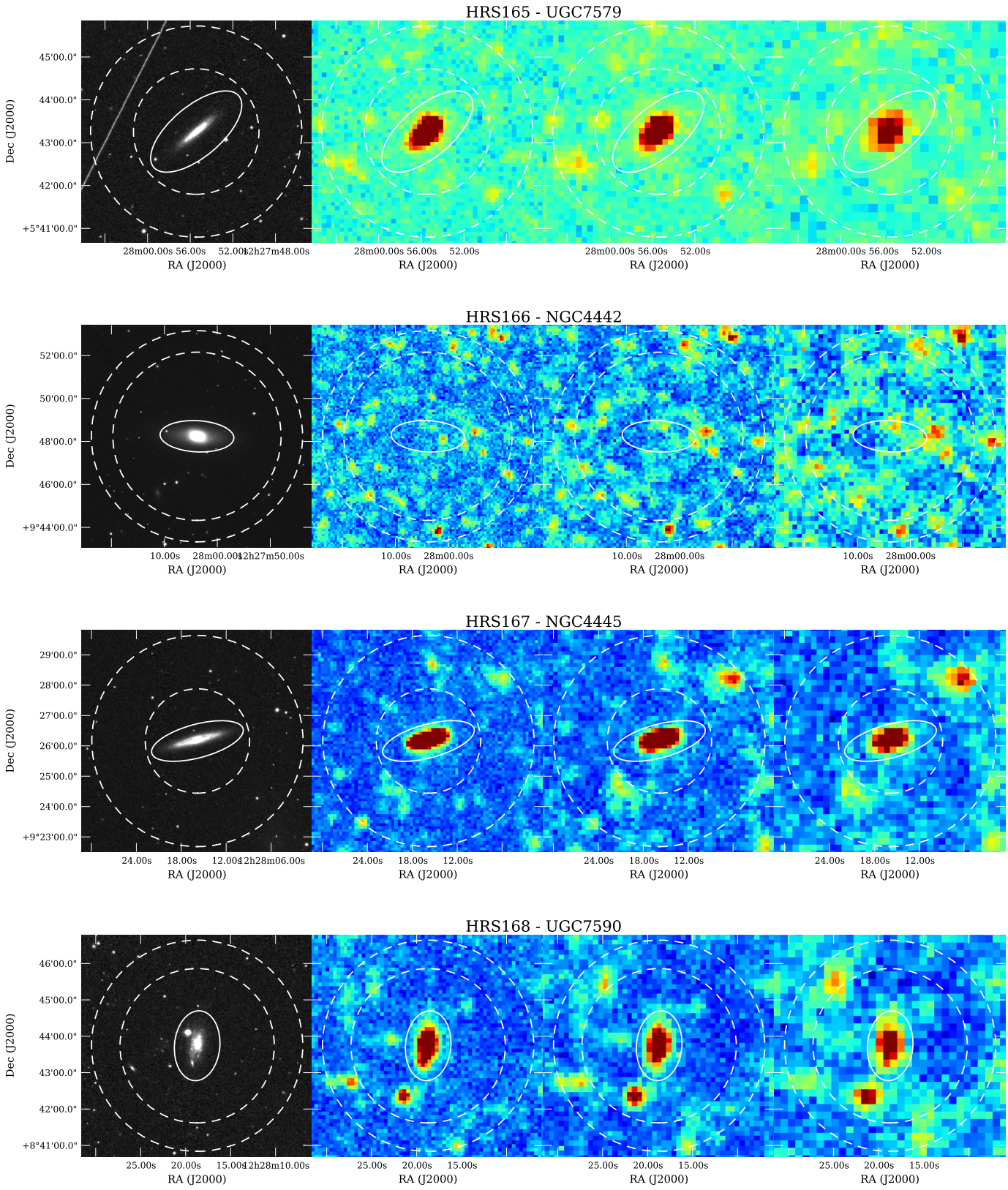

Fig. A.1: Images of the HRS galaxies. From left to right: SDSS *r'* band image, 250, 350, and 500 μm *Herschel* images. The aperture used for the photometry is indicated by the solid line and the annulus, where the background is estimated, is indicated in dashed lines.

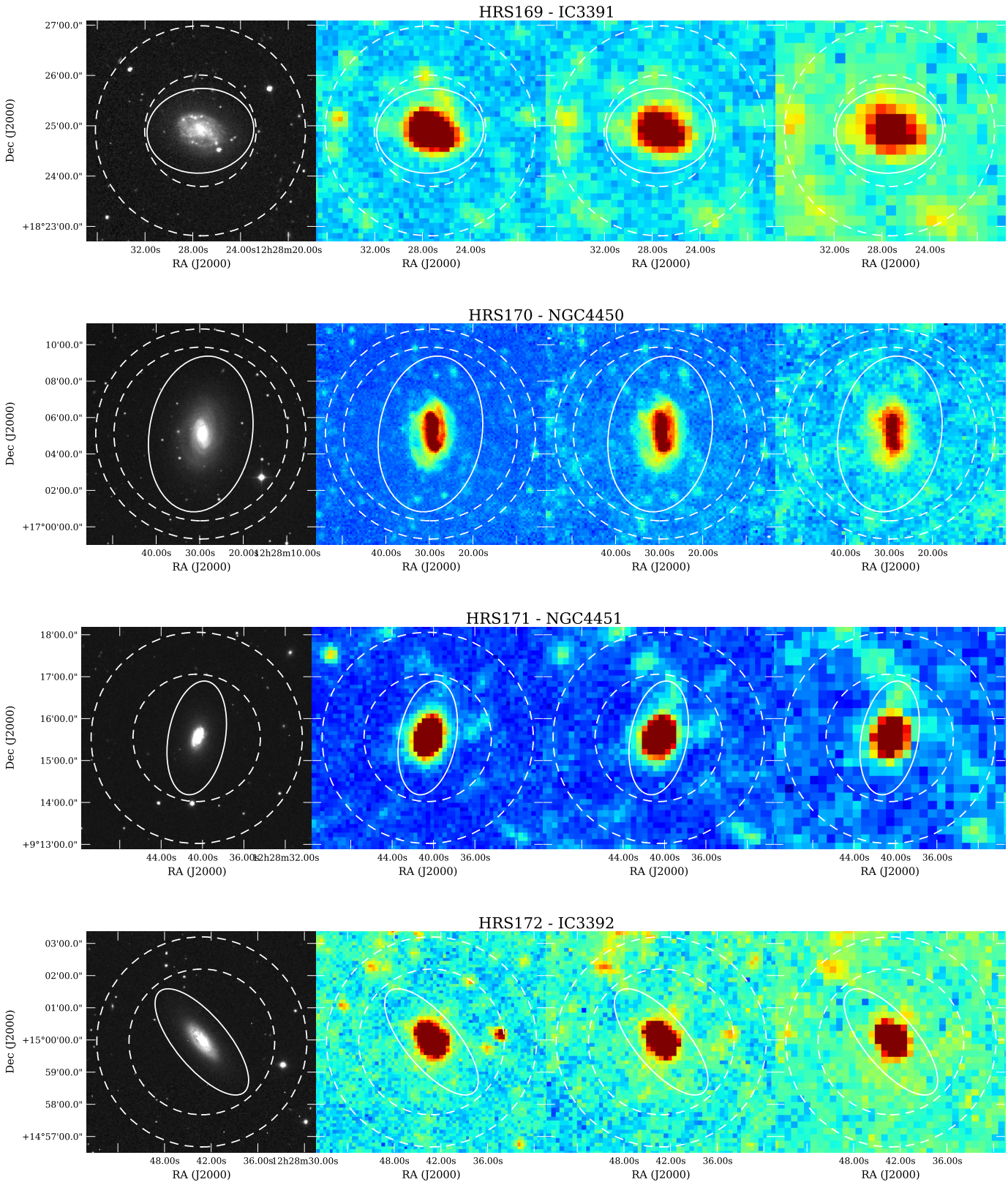

Fig. A.1: Images of the HRS galaxies. From left to right: SDSS *r'* band image, 250, 350, and 500 μm *Herschel* images. The aperture used for the photometry is indicated by the solid line and the annulus, where the background is estimated, is indicated in dashed lines.

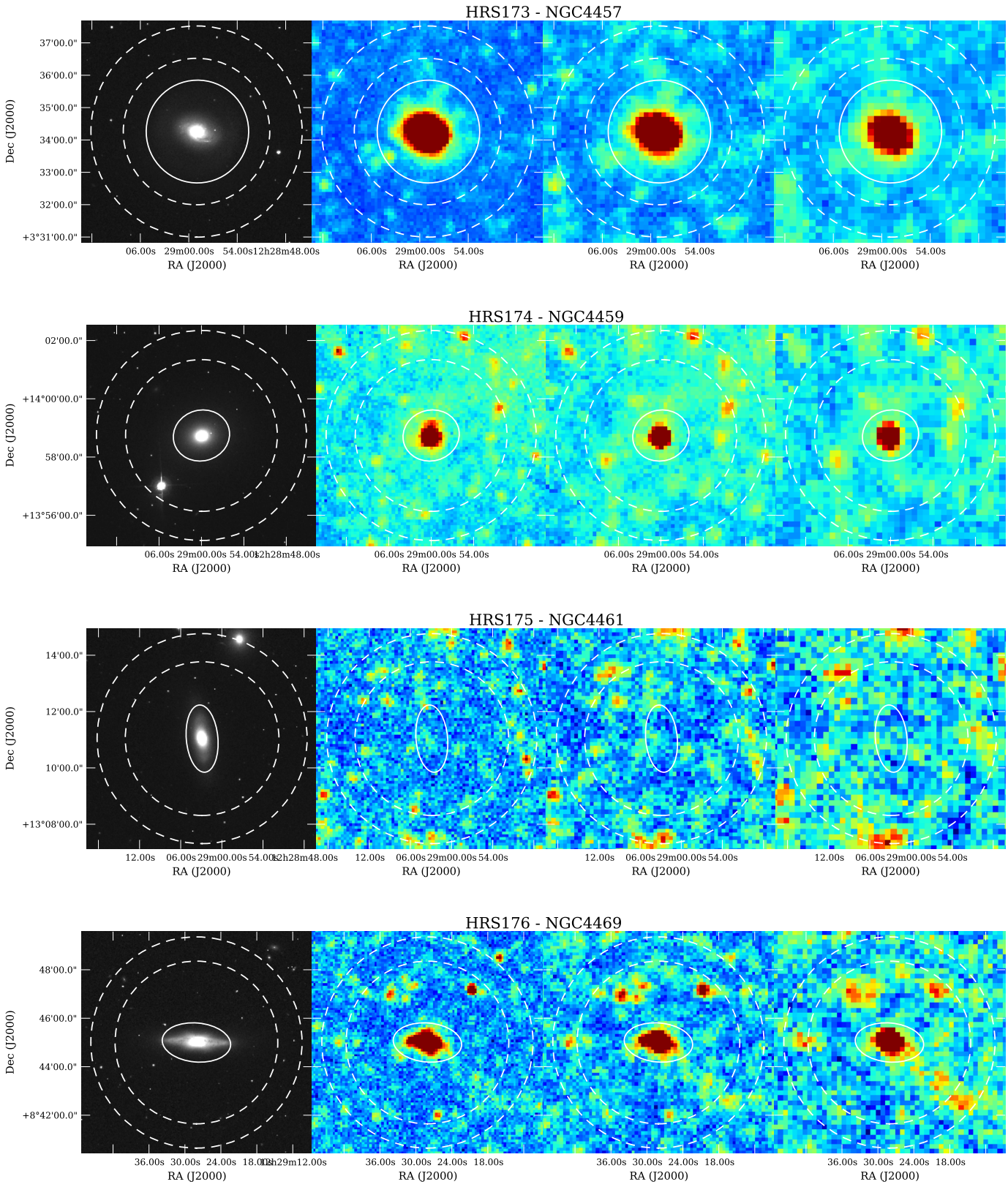

Fig. A.1: Images of the HRS galaxies. From left to right: SDSS *r'* band image, 250, 350, and 500 μm *Herschel* images. The aperture used for the photometry is indicated by the solid line and the annulus, where the background is estimated, is indicated in dashed lines.

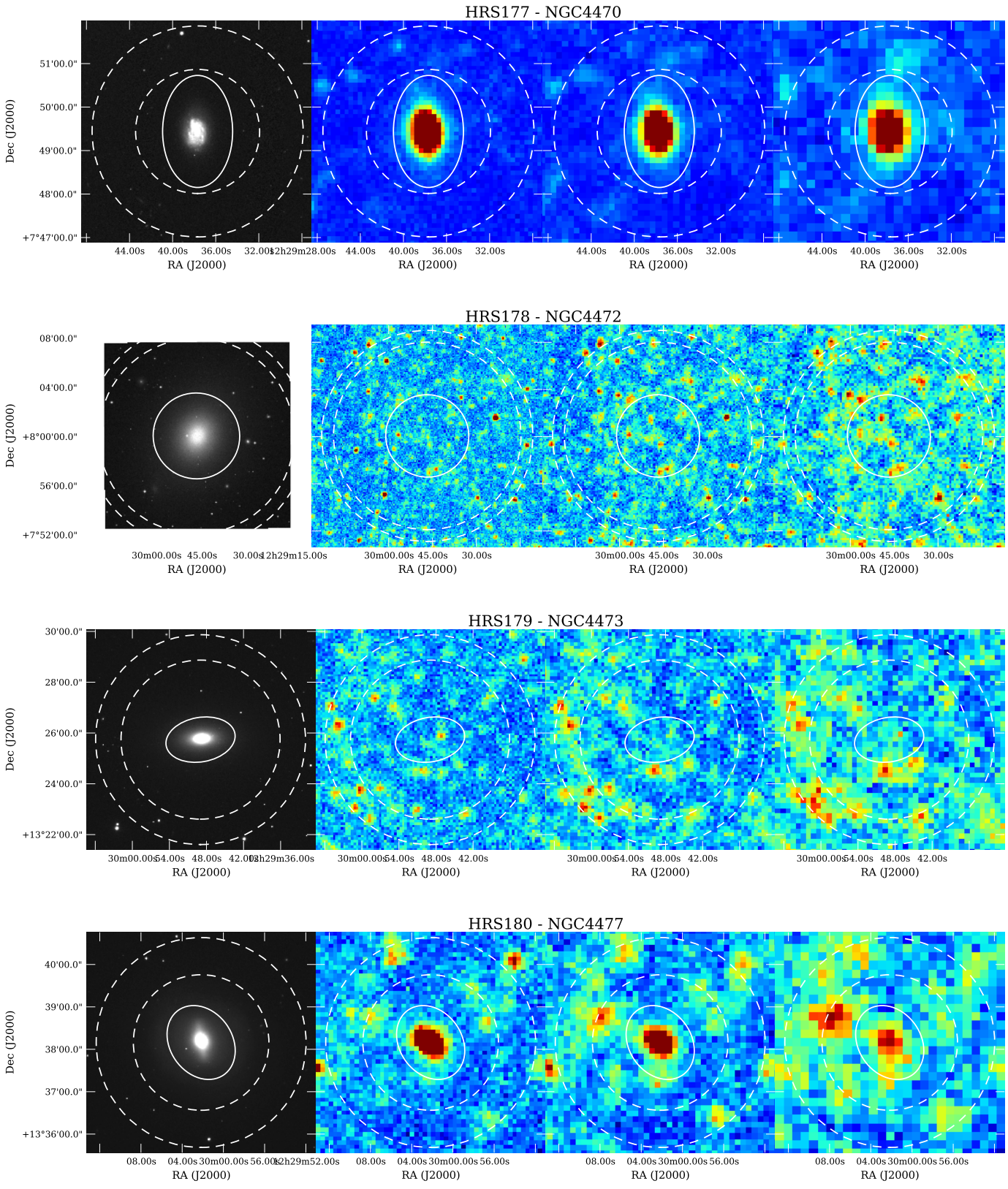

Fig. A.1: Images of the HRS galaxies. From left to right: SDSS *r'* band image, 250, 350, and 500 μm *Herschel* images. The aperture used for the photometry is indicated by the solid line and the annulus, where the background is estimated, is indicated in dashed lines.

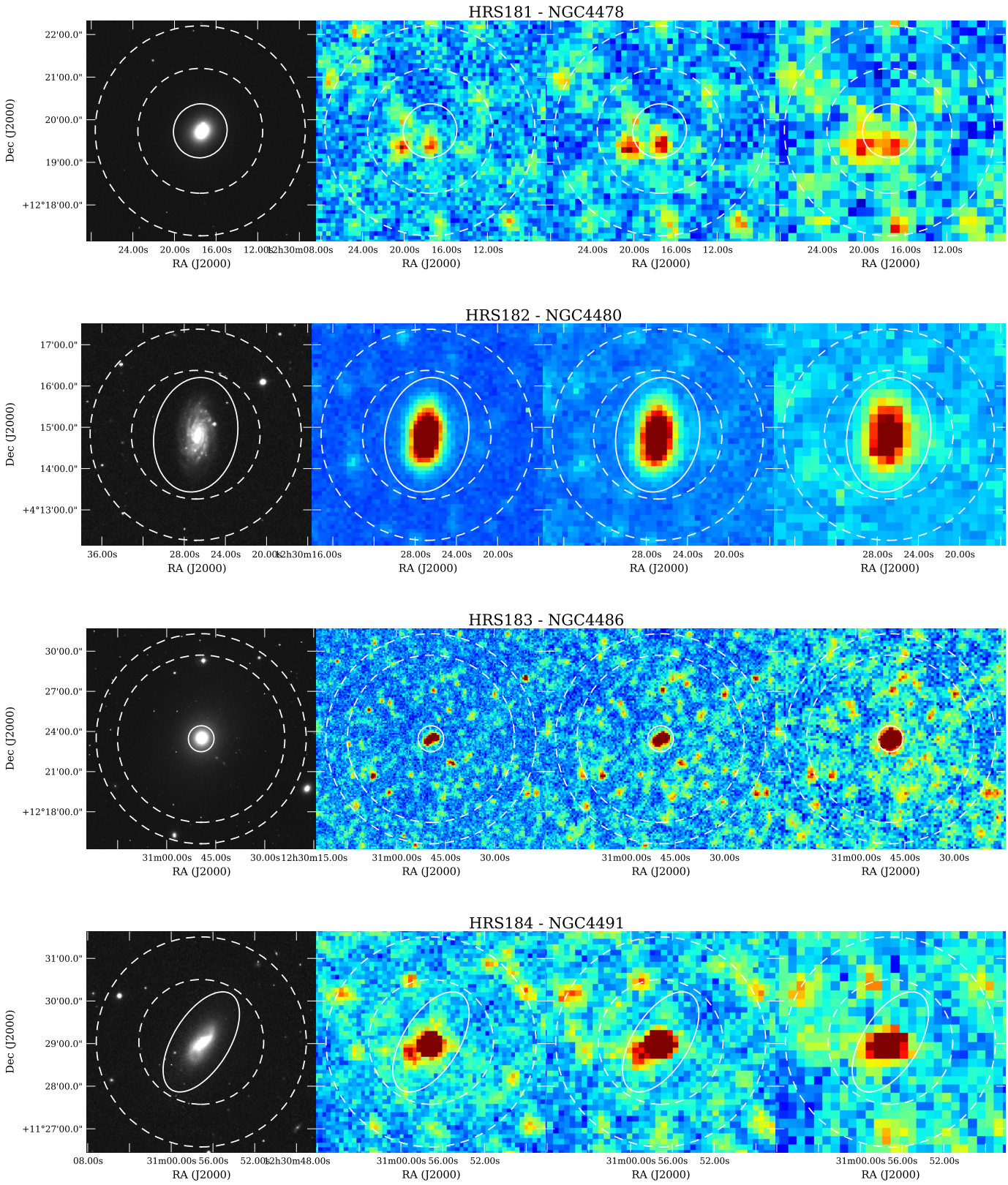

Fig. A.1: Images of the HRS galaxies. From left to right: SDSS *r'* band image, 250, 350, and 500 μm *Herschel* images. The aperture used for the photometry is indicated by the solid line and the annulus, where the background is estimated, is indicated in dashed lines.

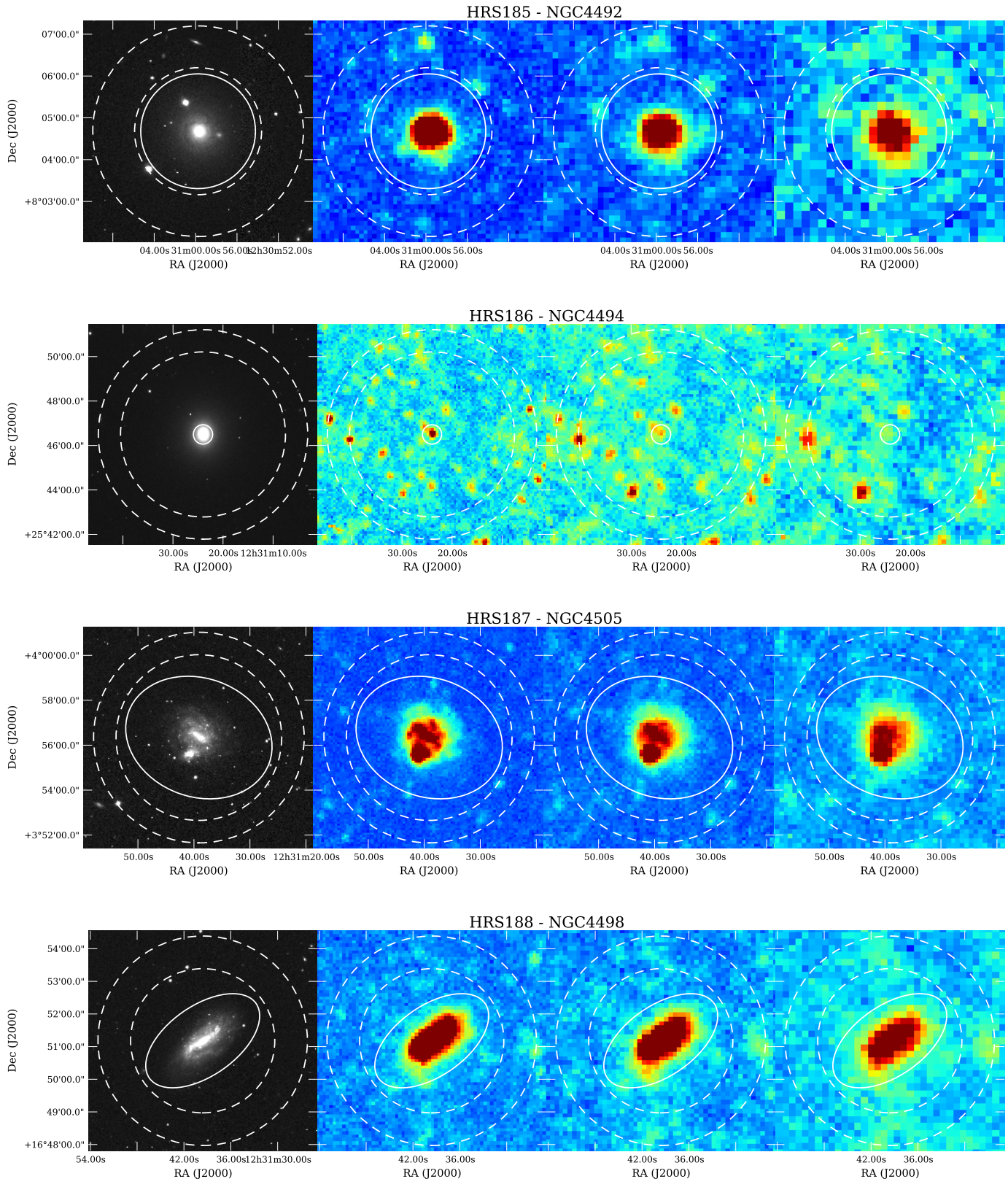

Fig. A.1: Images of the HRS galaxies. From left to right: SDSS *r'* band image, 250, 350, and 500 μm *Herschel* images. The aperture used for the photometry is indicated by the solid line and the annulus, where the background is estimated, is indicated in dashed lines.

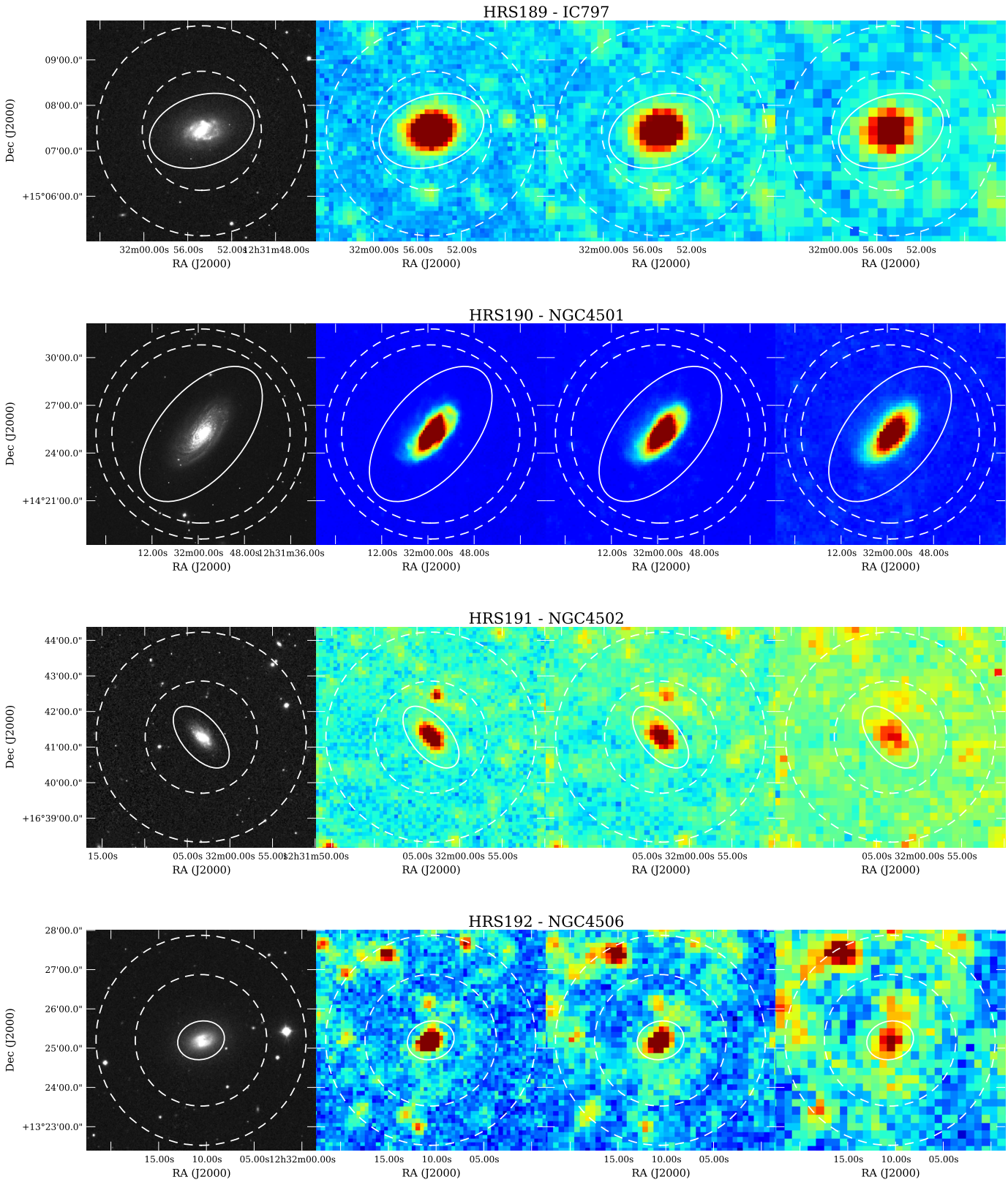

Fig. A.1: Images of the HRS galaxies. From left to right: SDSS *r'* band image, 250, 350, and 500 μm *Herschel* images. The aperture used for the photometry is indicated by the solid line and the annulus, where the background is estimated, is indicated in dashed lines.

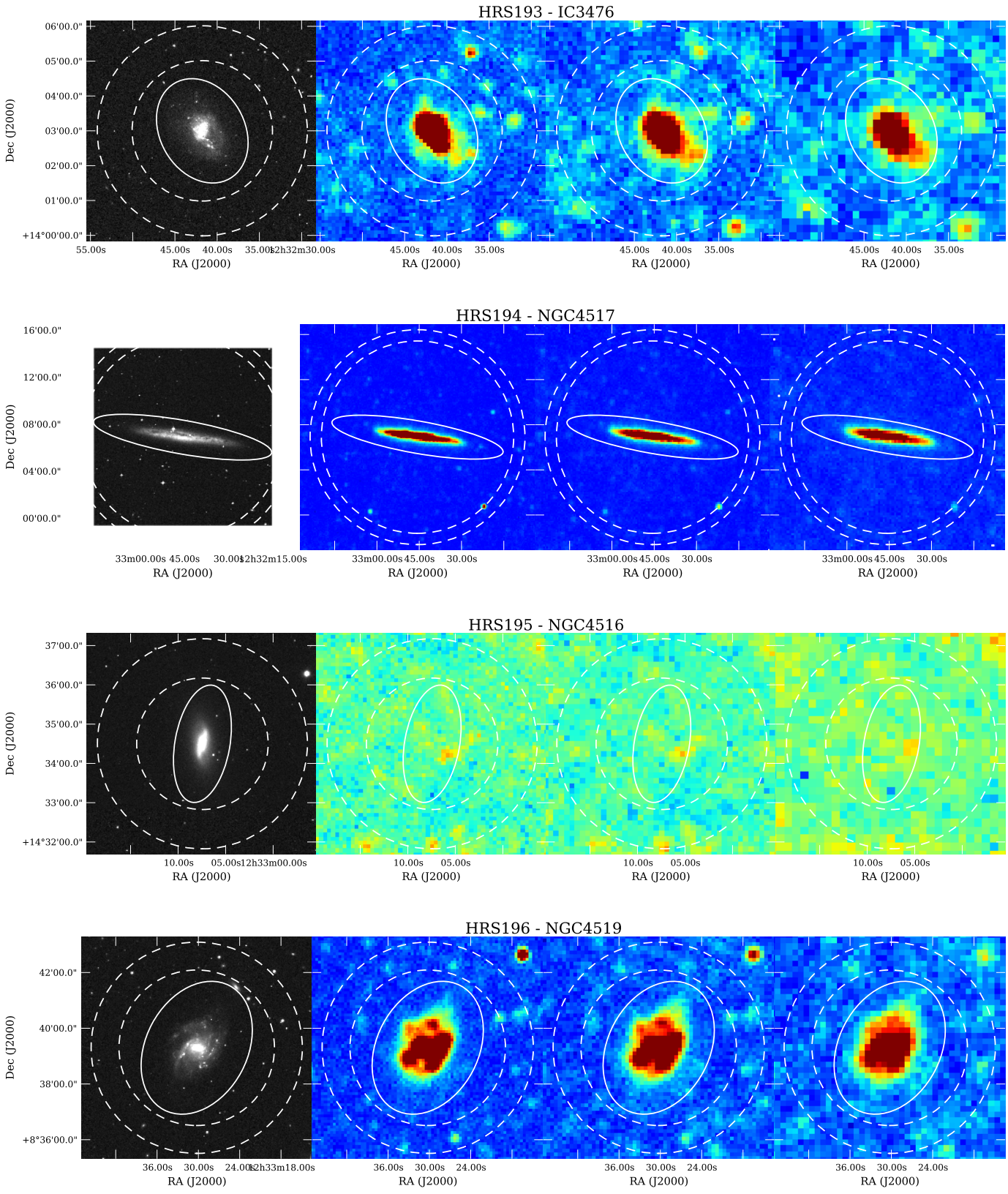

Fig. A.1: Images of the HRS galaxies. From left to right: SDSS *r'* band image, 250, 350, and 500 μm *Herschel* images. The aperture used for the photometry is indicated by the solid line and the annulus, where the background is estimated, is indicated in dashed lines.

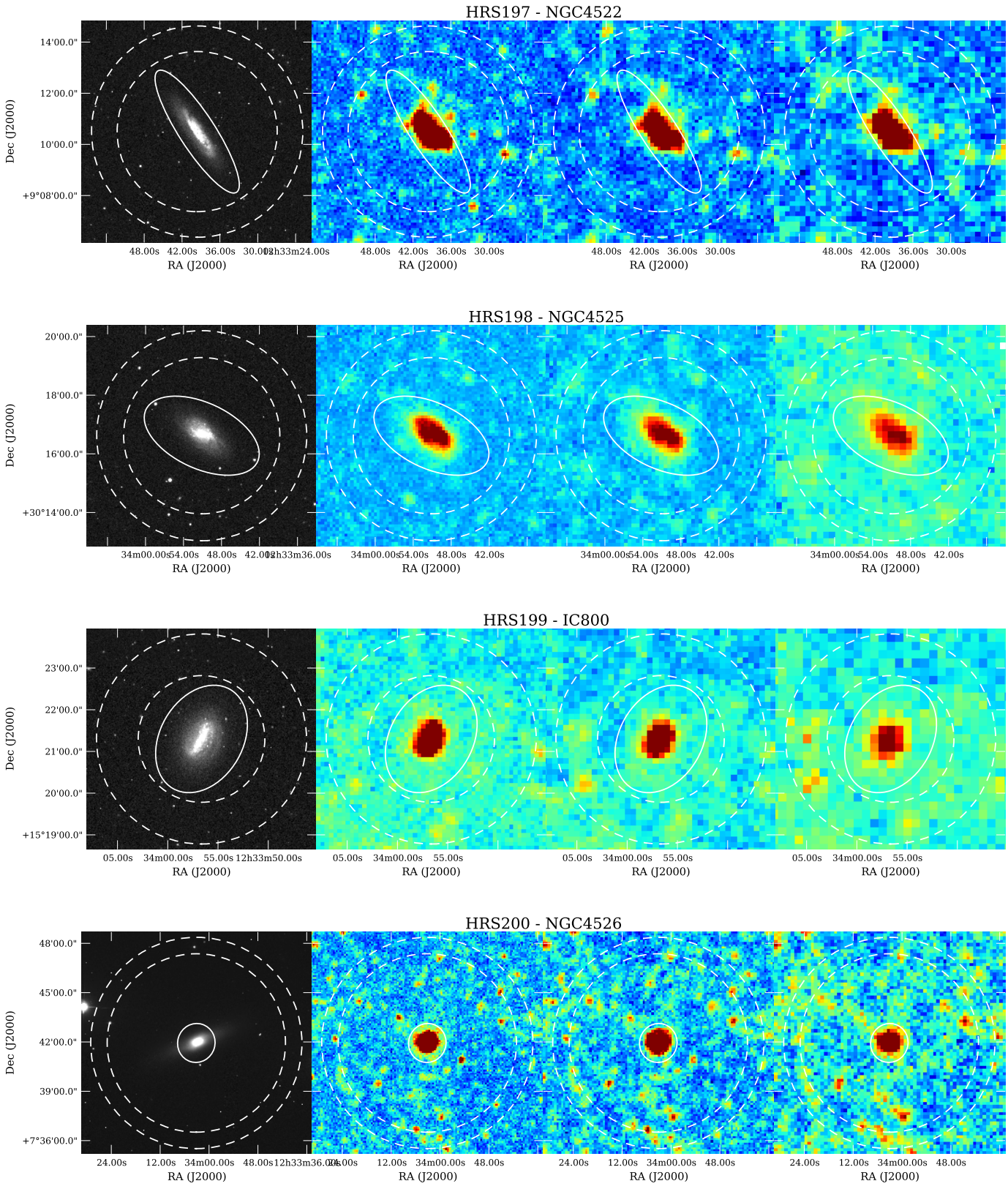

Fig. A.1: Images of the HRS galaxies. From left to right: SDSS *r'* band image, 250, 350, and 500 μm *Herschel* images. The aperture used for the photometry is indicated by the solid line and the annulus, where the background is estimated, is indicated in dashed lines.

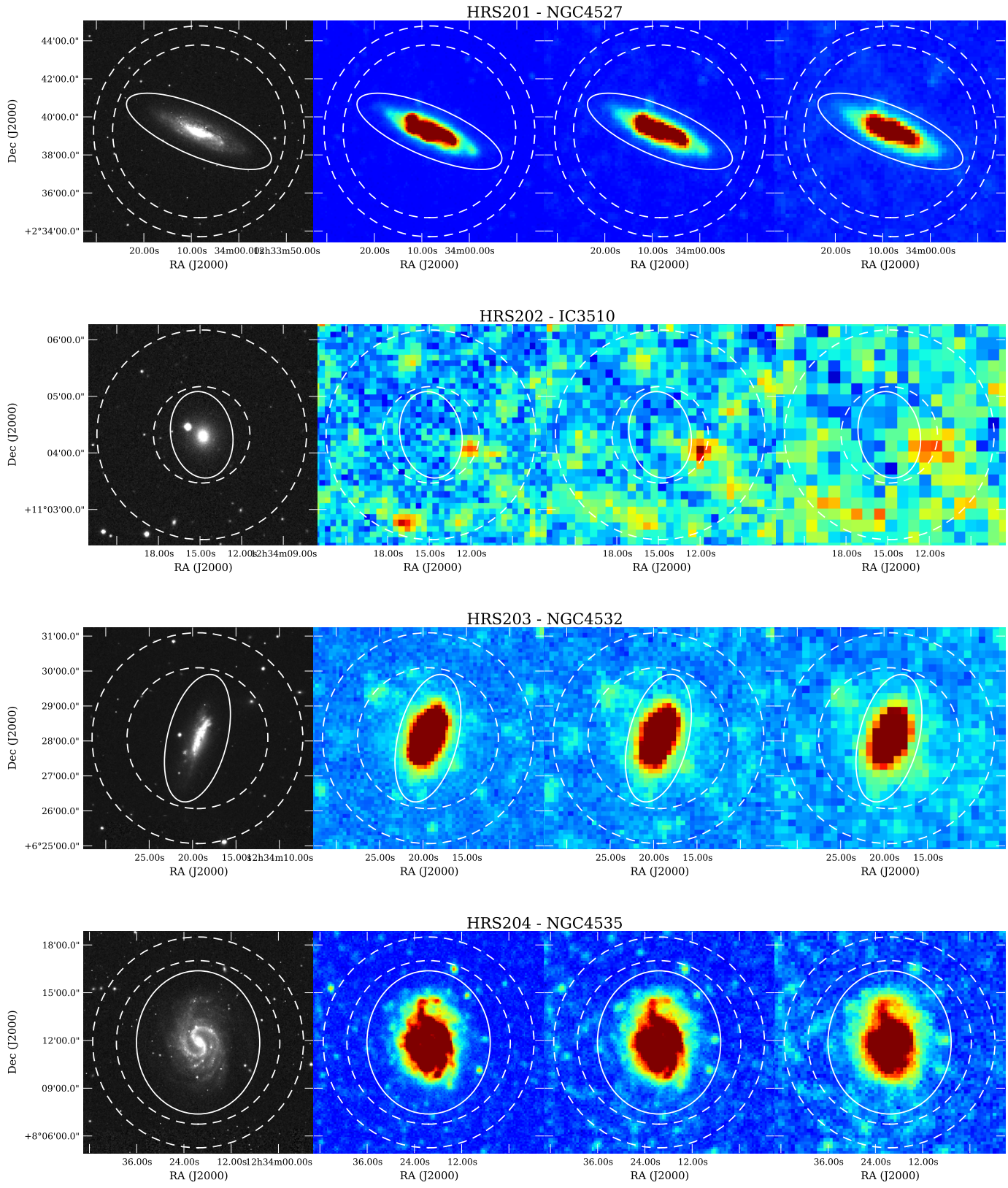

Fig. A.1: Images of the HRS galaxies. From left to right: SDSS *r'* band image, 250, 350, and 500 μm *Herschel* images. The aperture used for the photometry is indicated by the solid line and the annulus, where the background is estimated, is indicated in dashed lines.

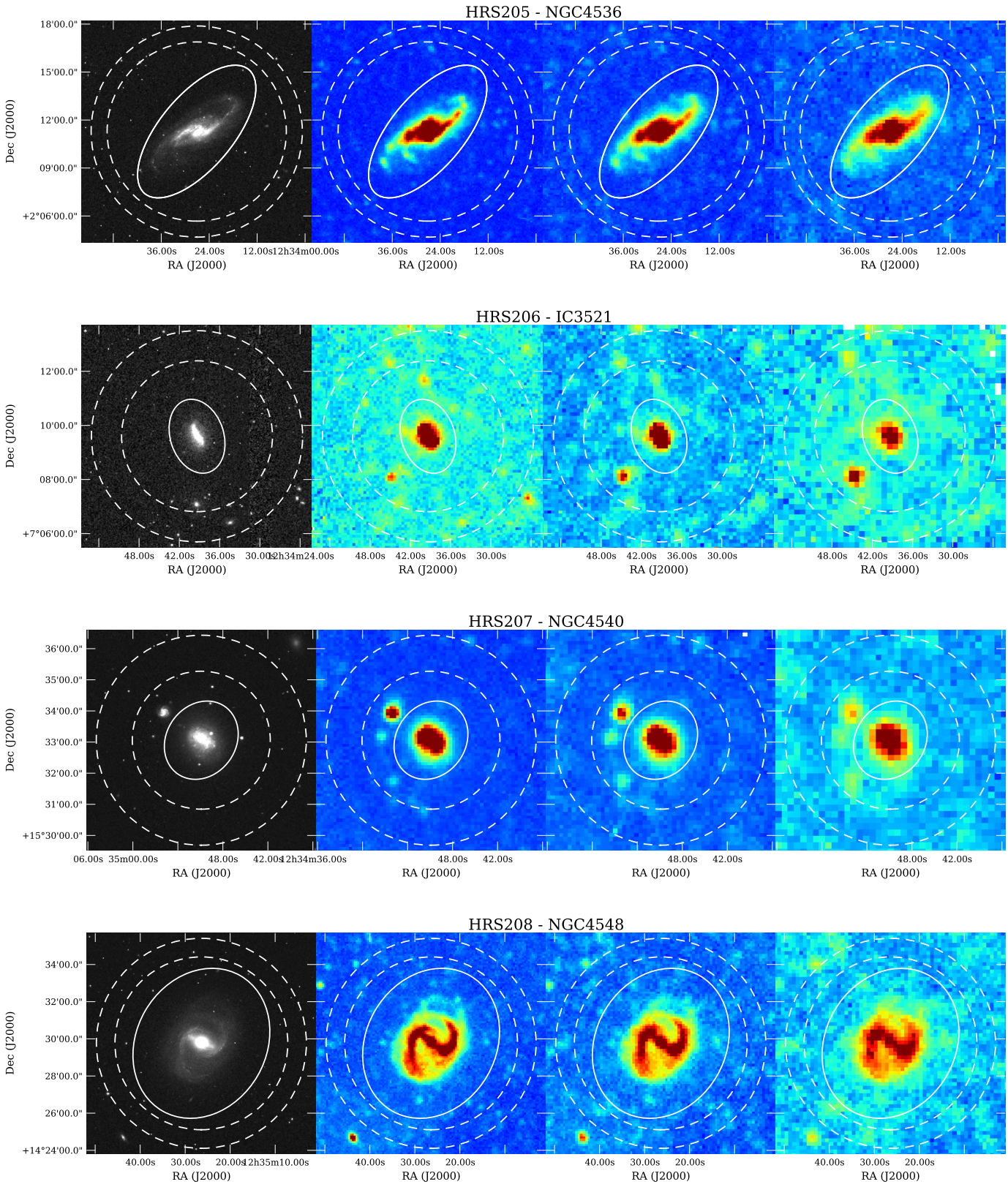

Fig. A.1: Images of the HRS galaxies. From left to right: SDSS *r'* band image, 250, 350, and 500 μm *Herschel* images. The aperture used for the photometry is indicated by the solid line and the annulus, where the background is estimated, is indicated in dashed lines.

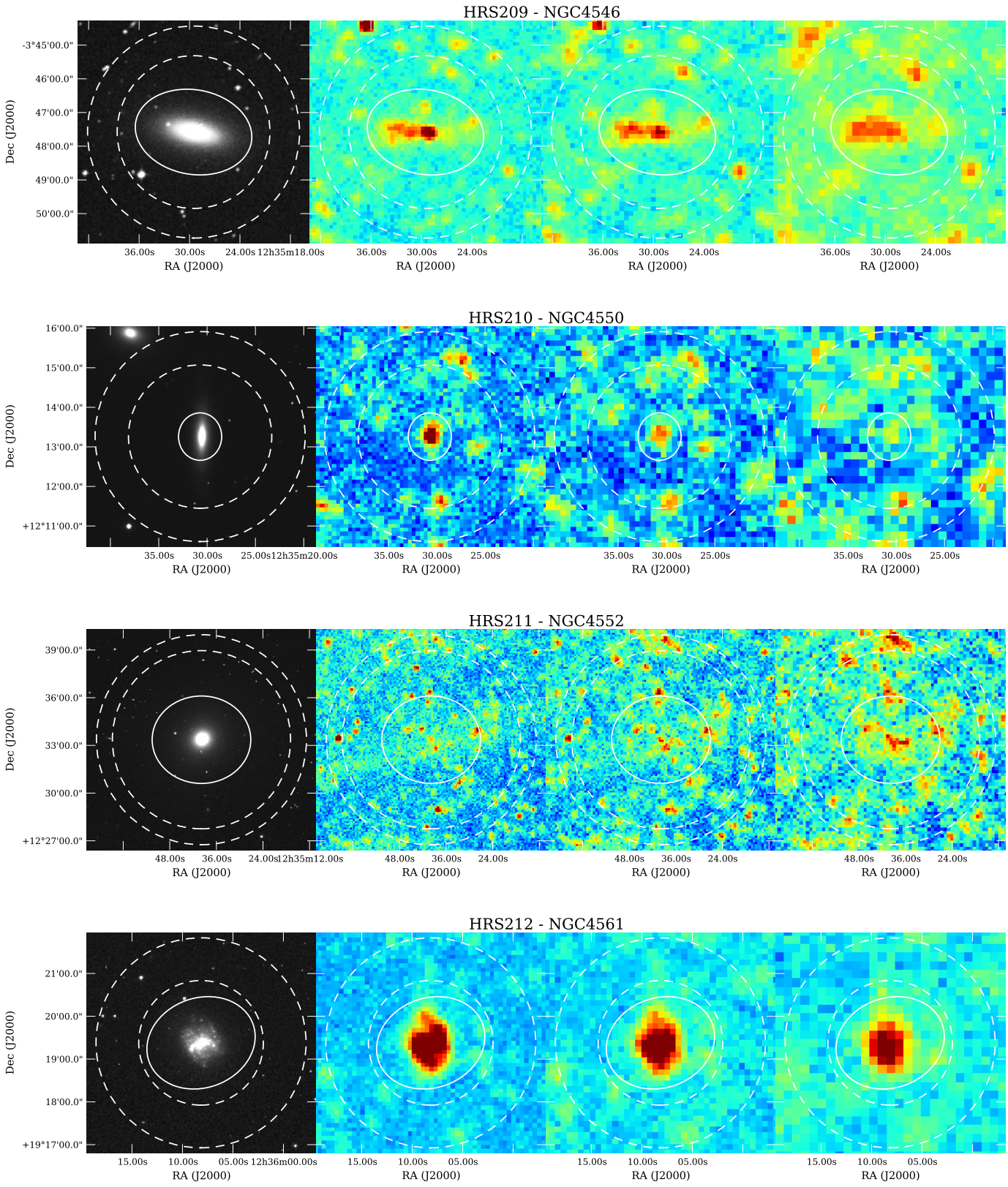

Fig. A.1: Images of the HRS galaxies. From left to right: SDSS *r'* band image, 250, 350, and 500 μm *Herschel* images. The aperture used for the photometry is indicated by the solid line and the annulus, where the background is estimated, is indicated in dashed lines.

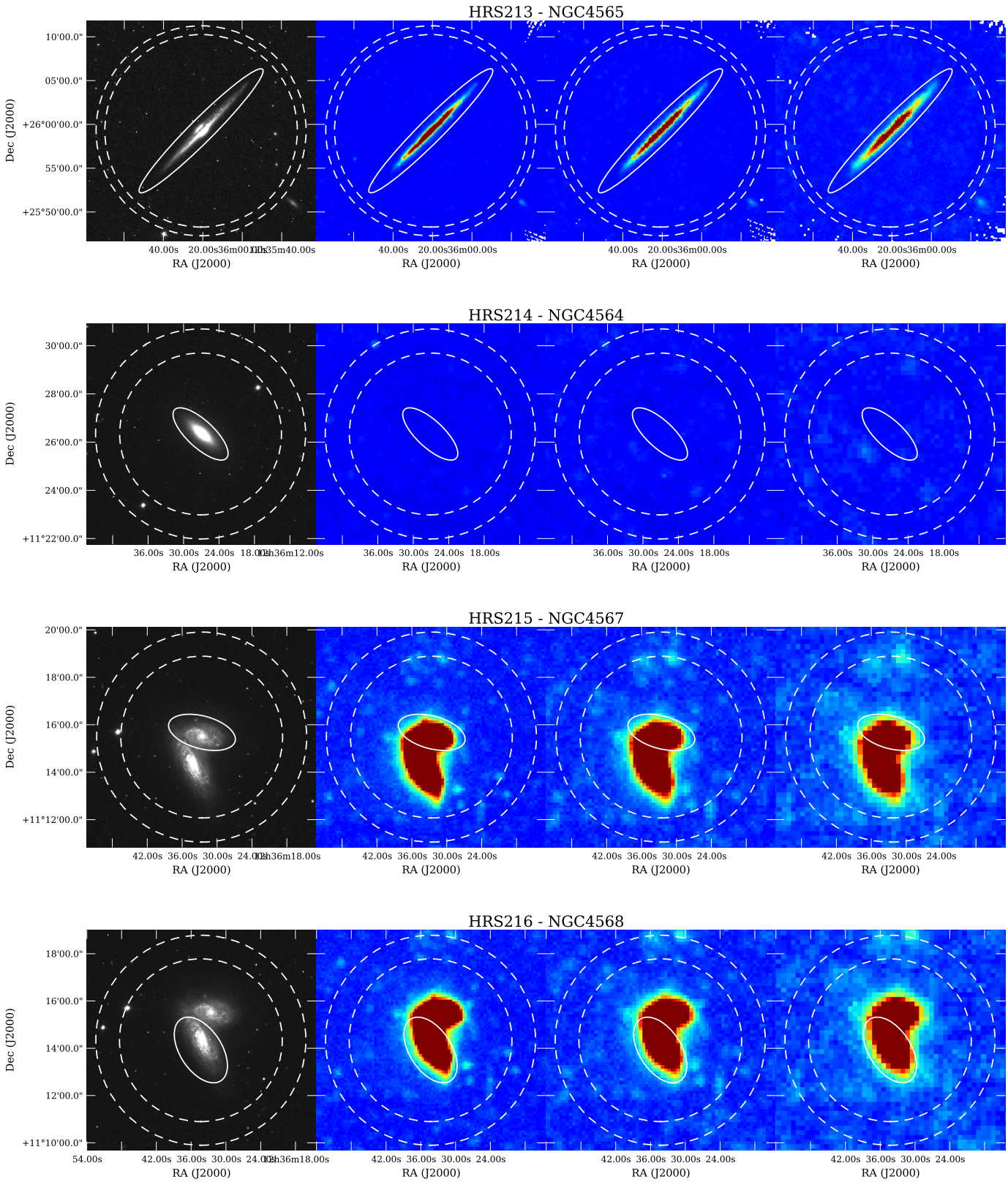

Fig. A.1: Images of the HRS galaxies. From left to right: SDSS *r'* band image, 250, 350, and 500 μm *Herschel* images. The aperture used for the photometry is indicated by the solid line and the annulus, where the background is estimated, is indicated in dashed lines.

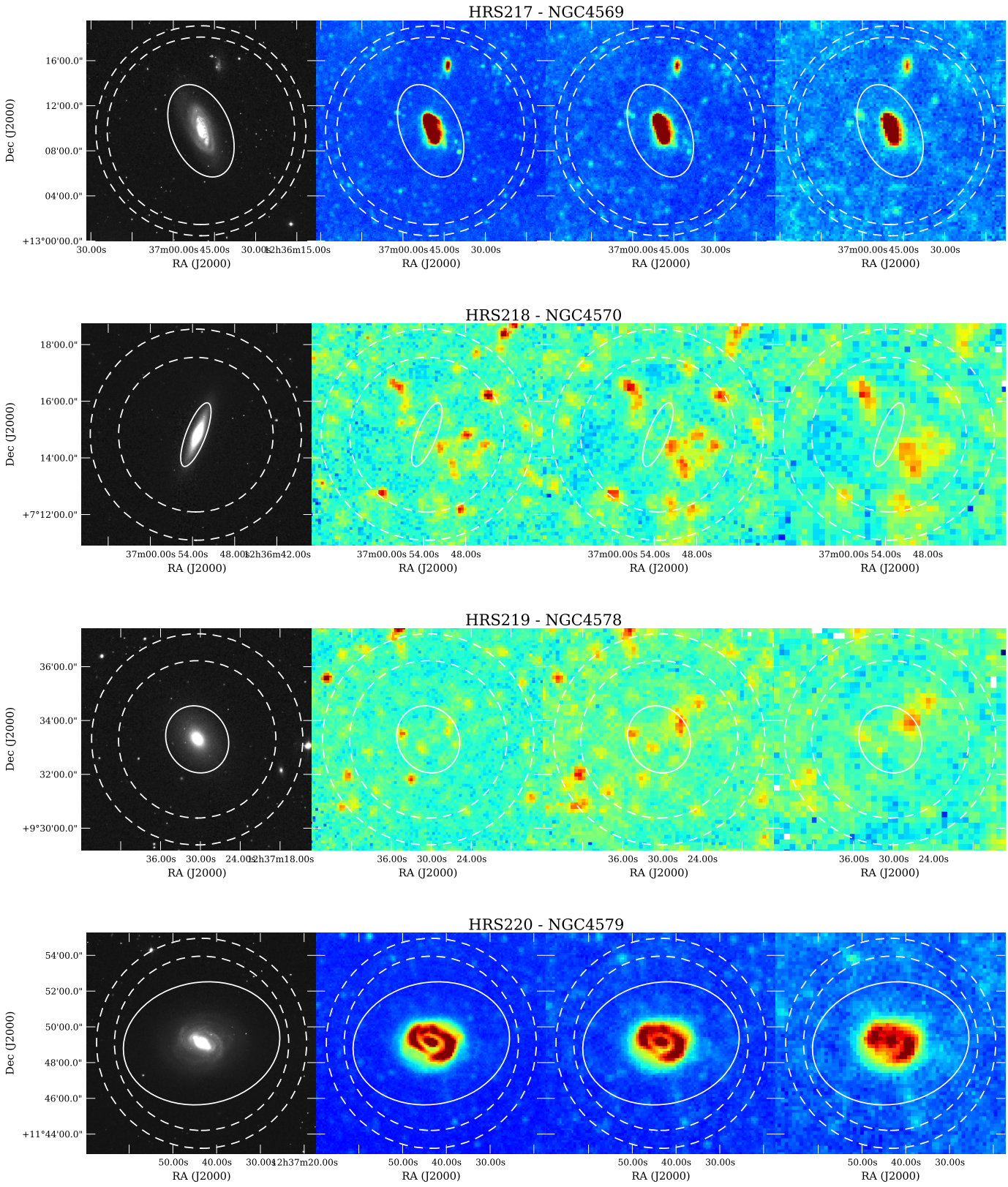

Fig. A.1: Images of the HRS galaxies. From left to right: SDSS *r'* band image, 250, 350, and 500 μm *Herschel* images. The aperture used for the photometry is indicated by the solid line and the annulus, where the background is estimated, is indicated in dashed lines.

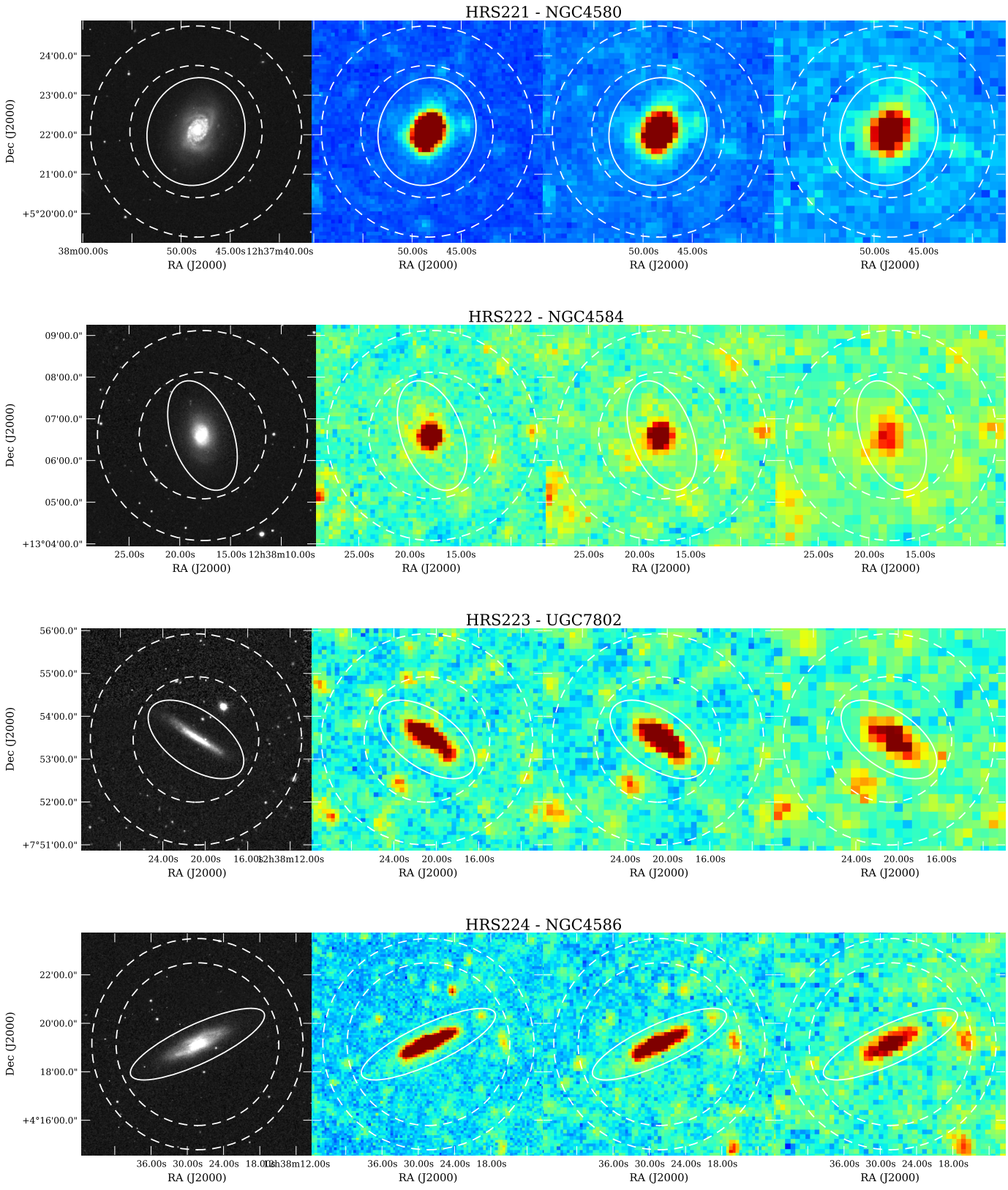

Fig. A.1: Images of the HRS galaxies. From left to right: SDSS *r'* band image, 250, 350, and 500 μm *Herschel* images. The aperture used for the photometry is indicated by the solid line and the annulus, where the background is estimated, is indicated in dashed lines.

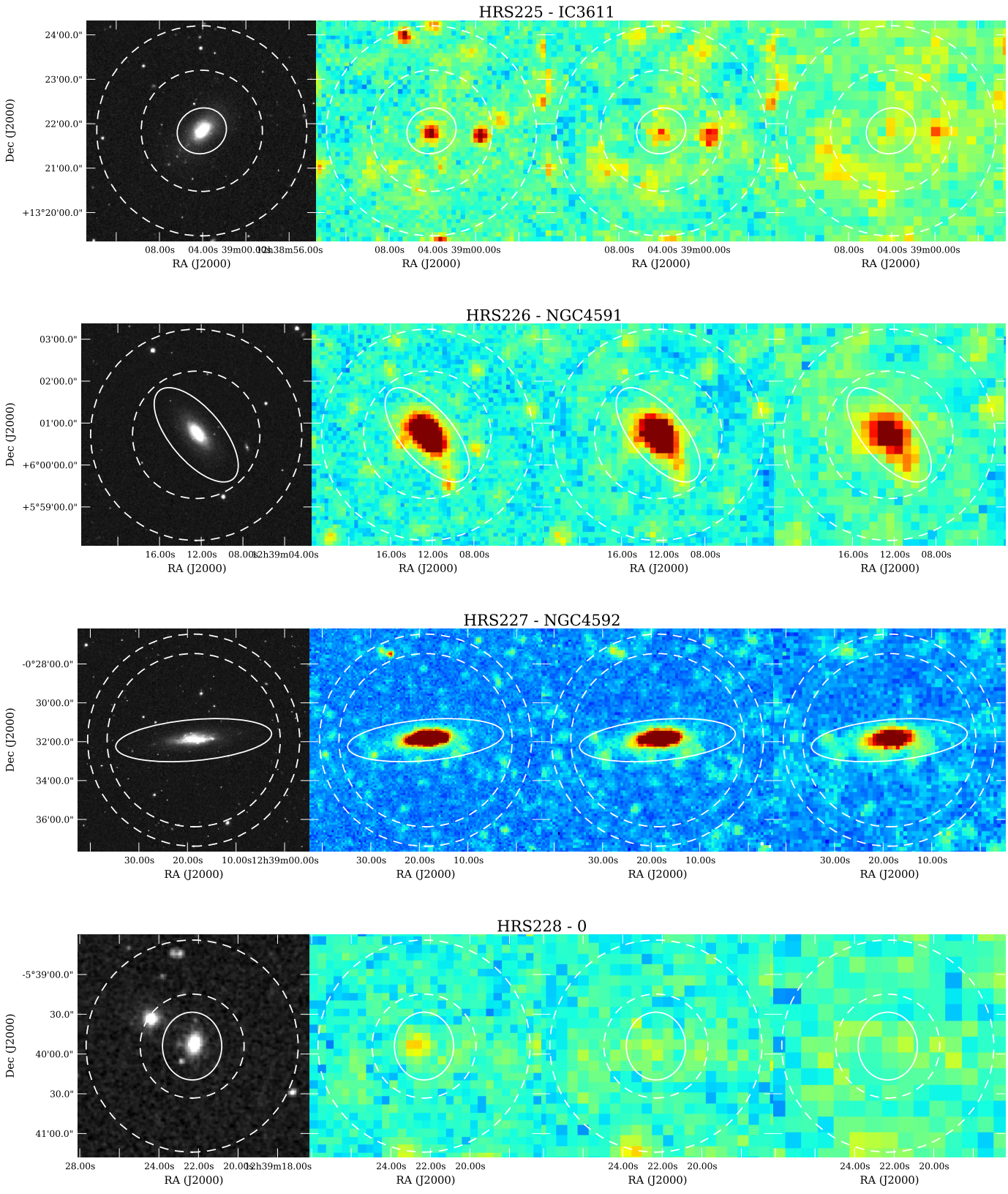

Fig. A.1: Images of the HRS galaxies. From left to right: SDSS *r'* band image, 250, 350, and 500 μm *Herschel* images. The aperture used for the photometry is indicated by the solid line and the annulus, where the background is estimated, is indicated in dashed lines.

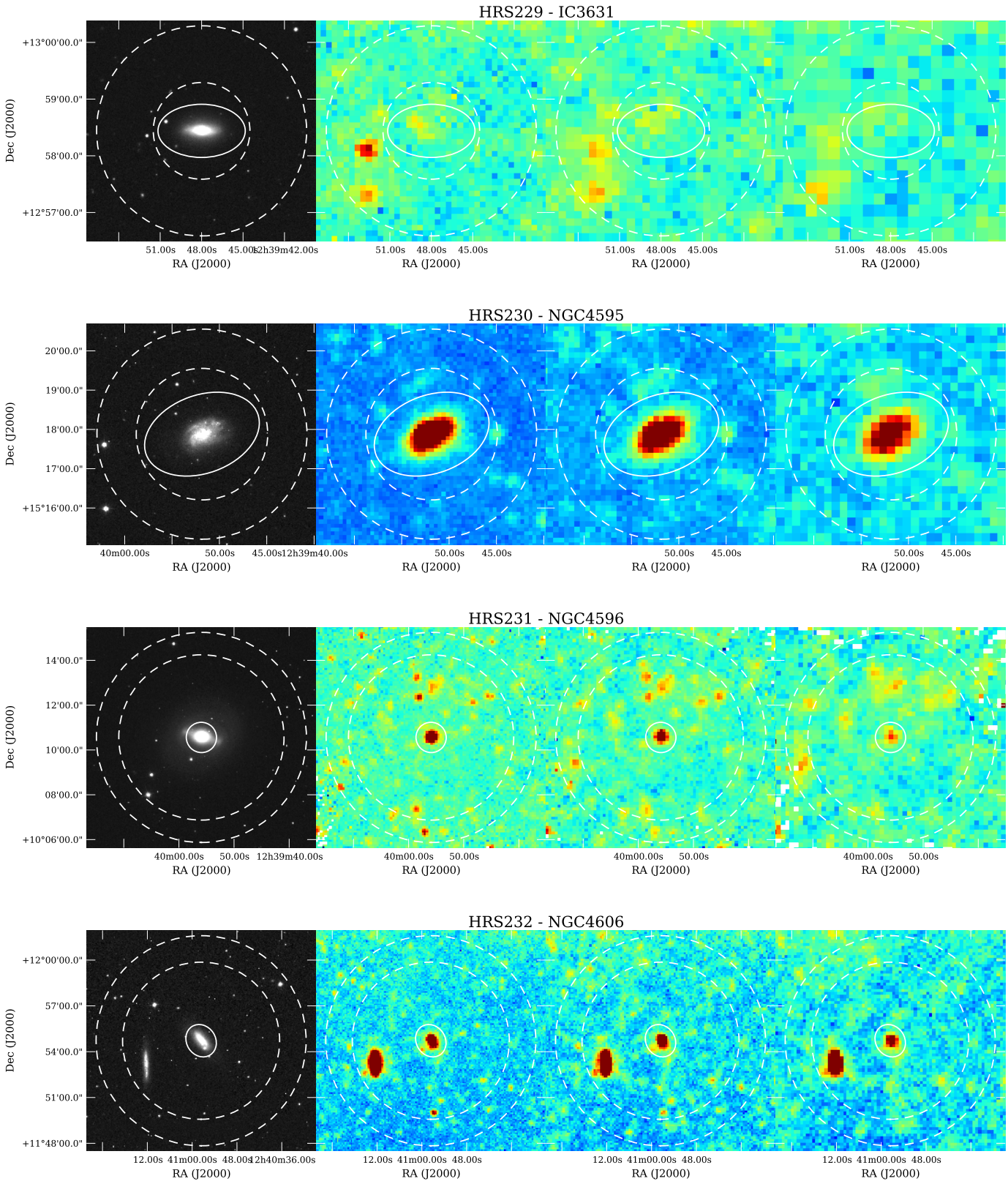

Fig. A.1: Images of the HRS galaxies. From left to right: SDSS *r'* band image, 250, 350, and 500 μm *Herschel* images. The aperture used for the photometry is indicated by the solid line and the annulus, where the background is estimated, is indicated in dashed lines.

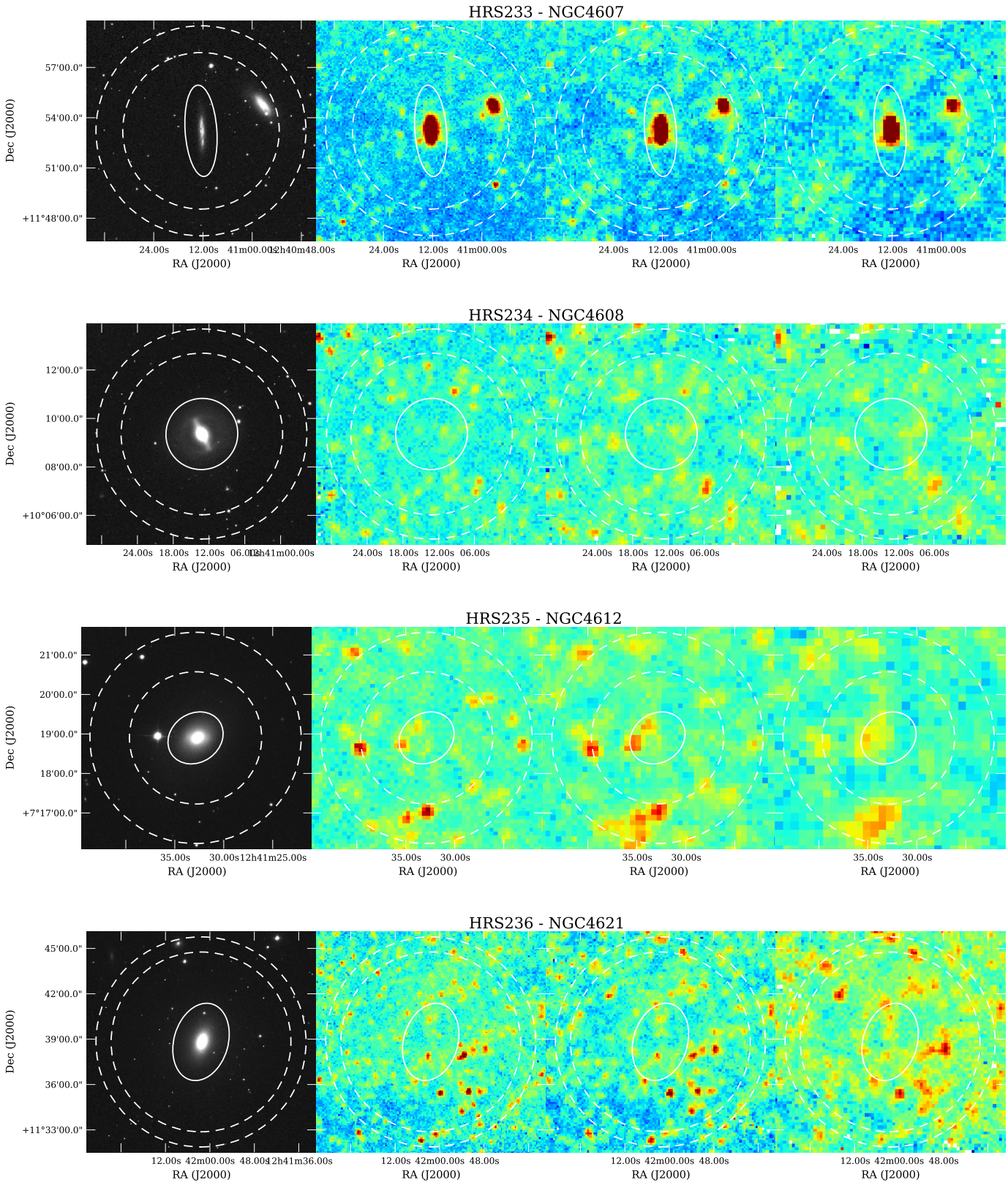

Fig. A.1: Images of the HRS galaxies. From left to right: SDSS *r'* band image, 250, 350, and 500 μm *Herschel* images. The aperture used for the photometry is indicated by the solid line and the annulus, where the background is estimated, is indicated in dashed lines.

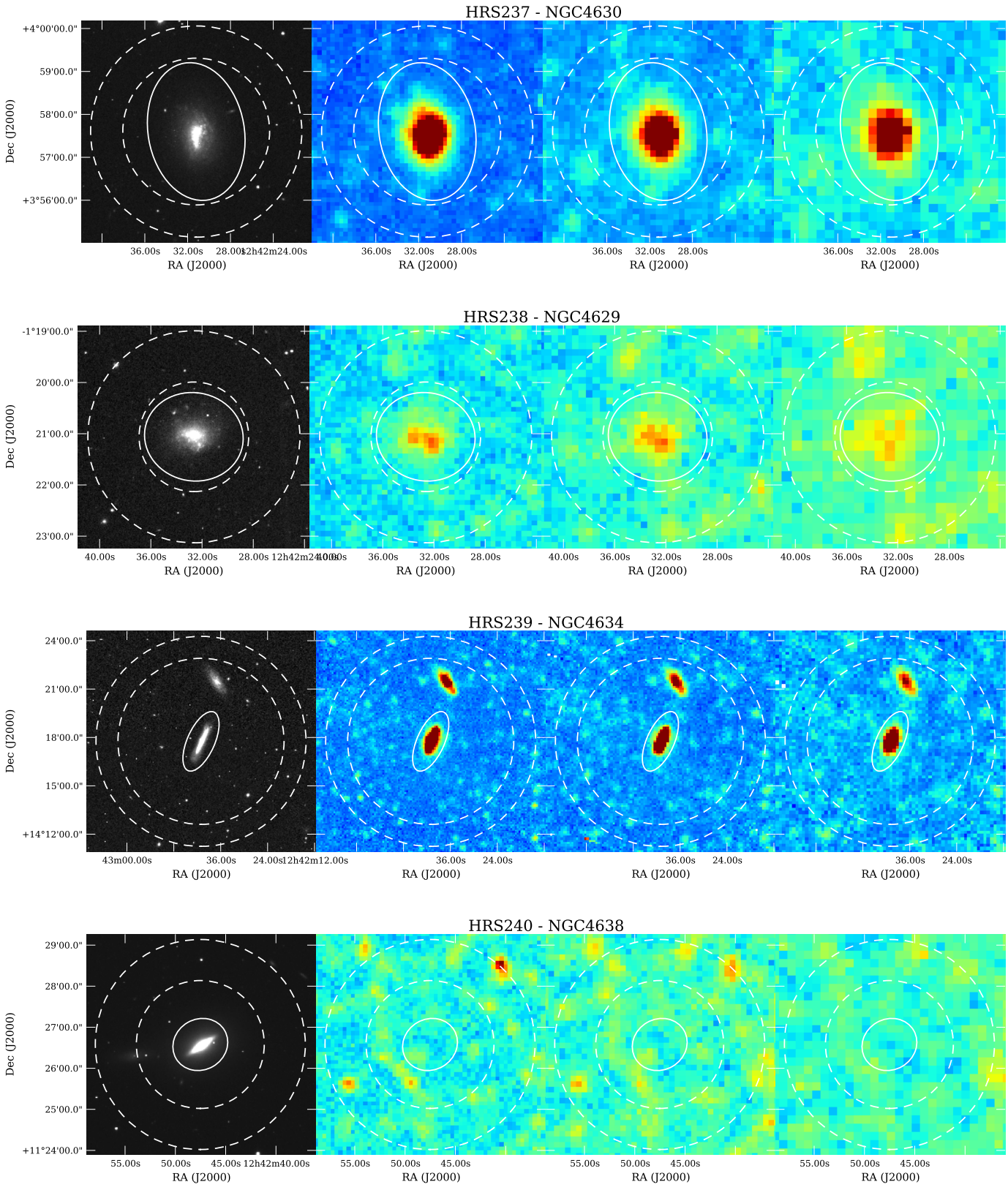

Fig. A.1: Images of the HRS galaxies. From left to right: SDSS *r'* band image, 250, 350, and 500 μm *Herschel* images. The aperture used for the photometry is indicated by the solid line and the annulus, where the background is estimated, is indicated in dashed lines.

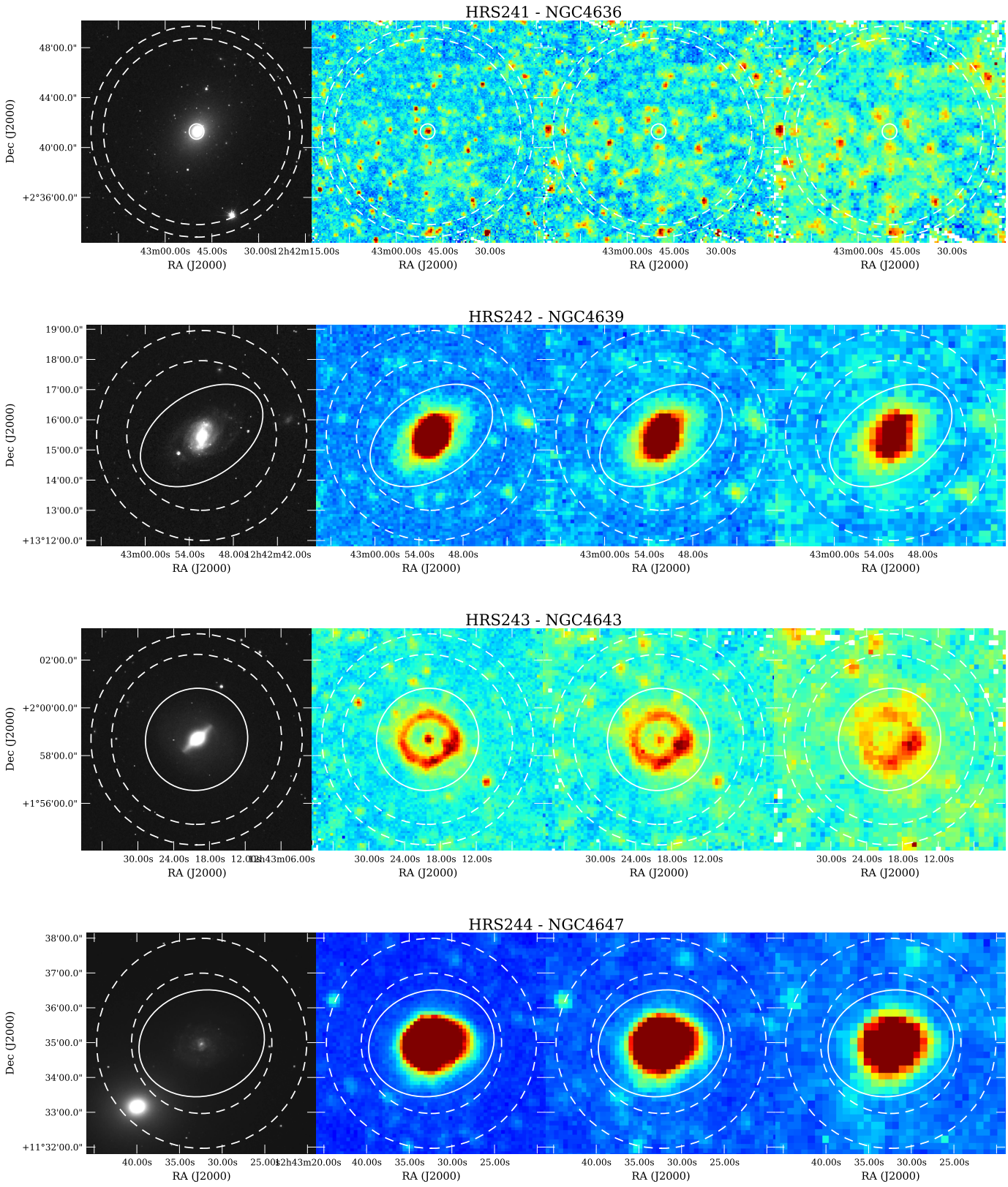

Fig. A.1: Images of the HRS galaxies. From left to right: SDSS *r'* band image, 250, 350, and 500 μm *Herschel* images. The aperture used for the photometry is indicated by the solid line and the annulus, where the background is estimated, is indicated in dashed lines.

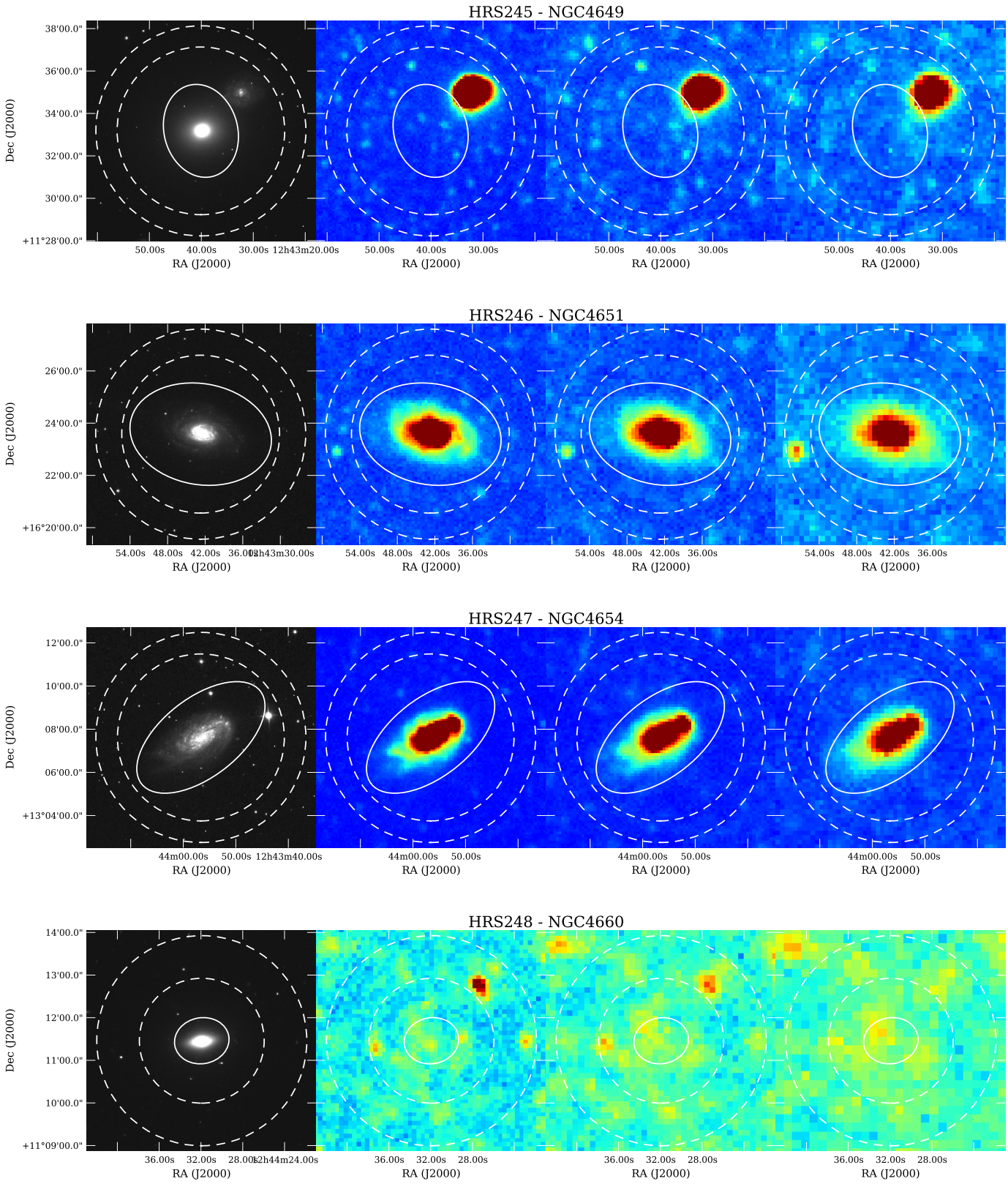

Fig. A.1: Images of the HRS galaxies. From left to right: SDSS *r'* band image, 250, 350, and 500 μm *Herschel* images. The aperture used for the photometry is indicated by the solid line and the annulus, where the background is estimated, is indicated in dashed lines.

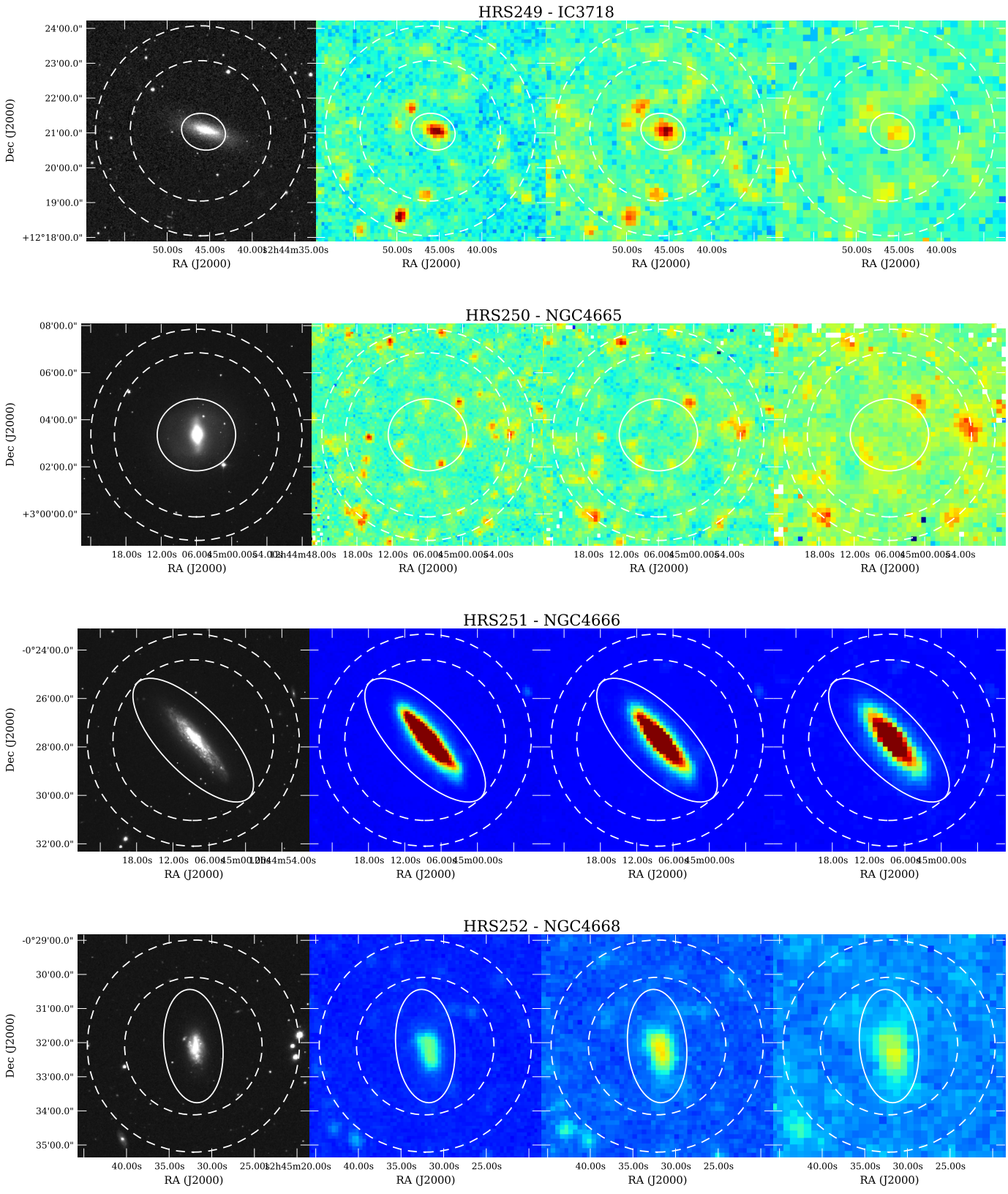

Fig. A.1: Images of the HRS galaxies. From left to right: SDSS *r'* band image, 250, 350, and 500 μm *Herschel* images. The aperture used for the photometry is indicated by the solid line and the annulus, where the background is estimated, is indicated in dashed lines.

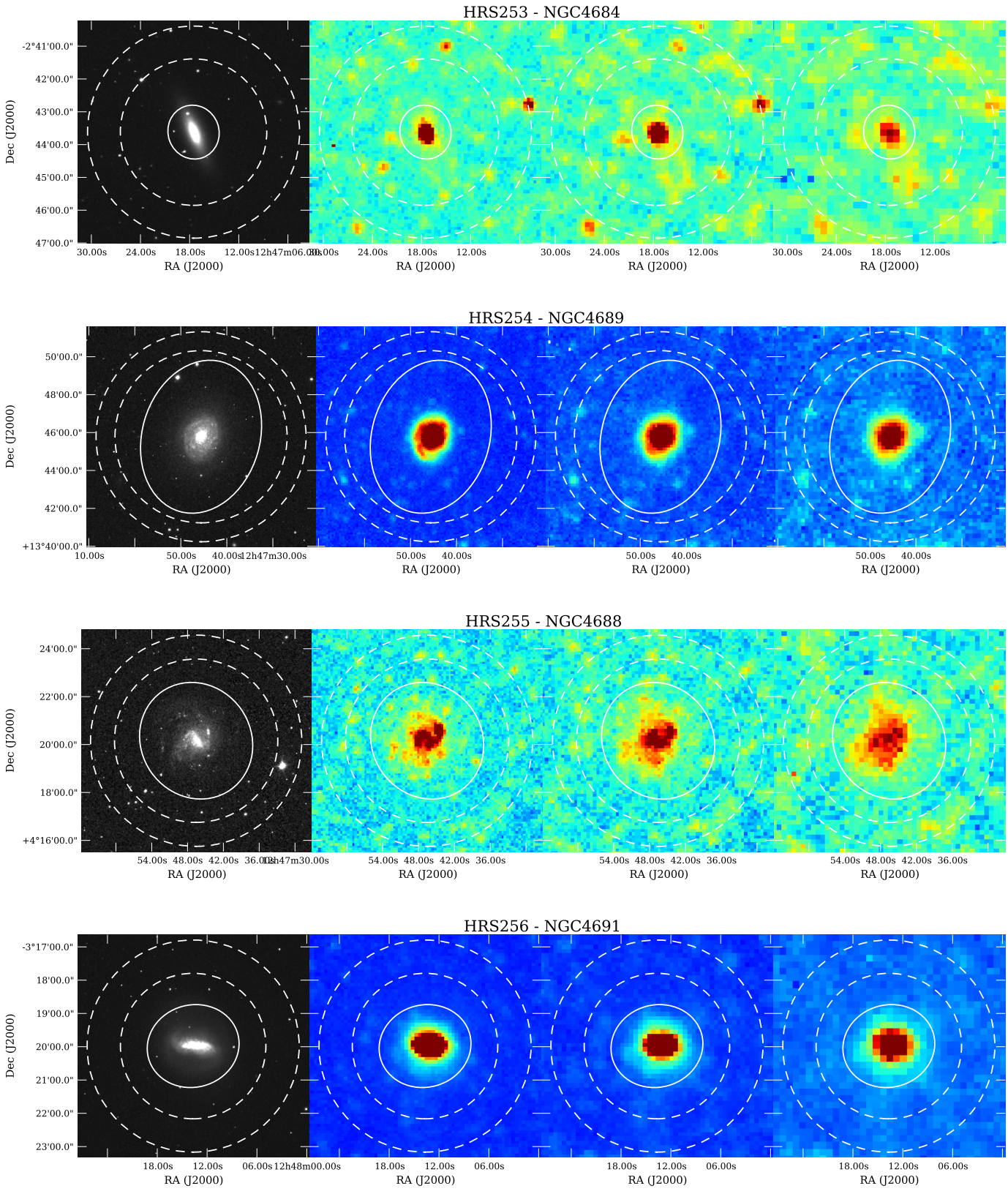

Fig. A.1: Images of the HRS galaxies. From left to right: SDSS *r'* band image, 250, 350, and 500 μm *Herschel* images. The aperture used for the photometry is indicated by the solid line and the annulus, where the background is estimated, is indicated in dashed lines.

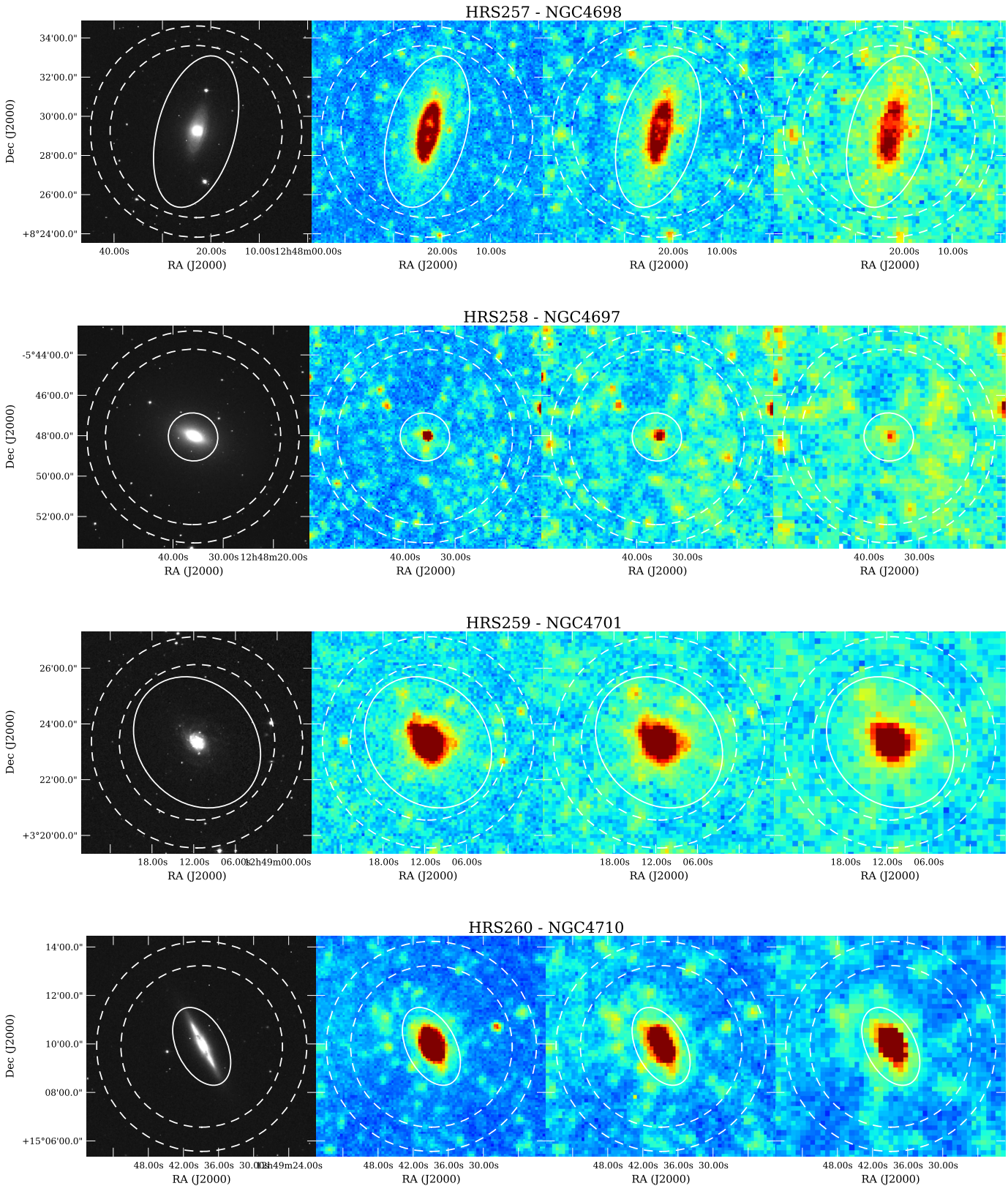

Fig. A.1: Images of the HRS galaxies. From left to right: SDSS *r'* band image, 250, 350, and 500 μm *Herschel* images. The aperture used for the photometry is indicated by the solid line and the annulus, where the background is estimated, is indicated in dashed lines.

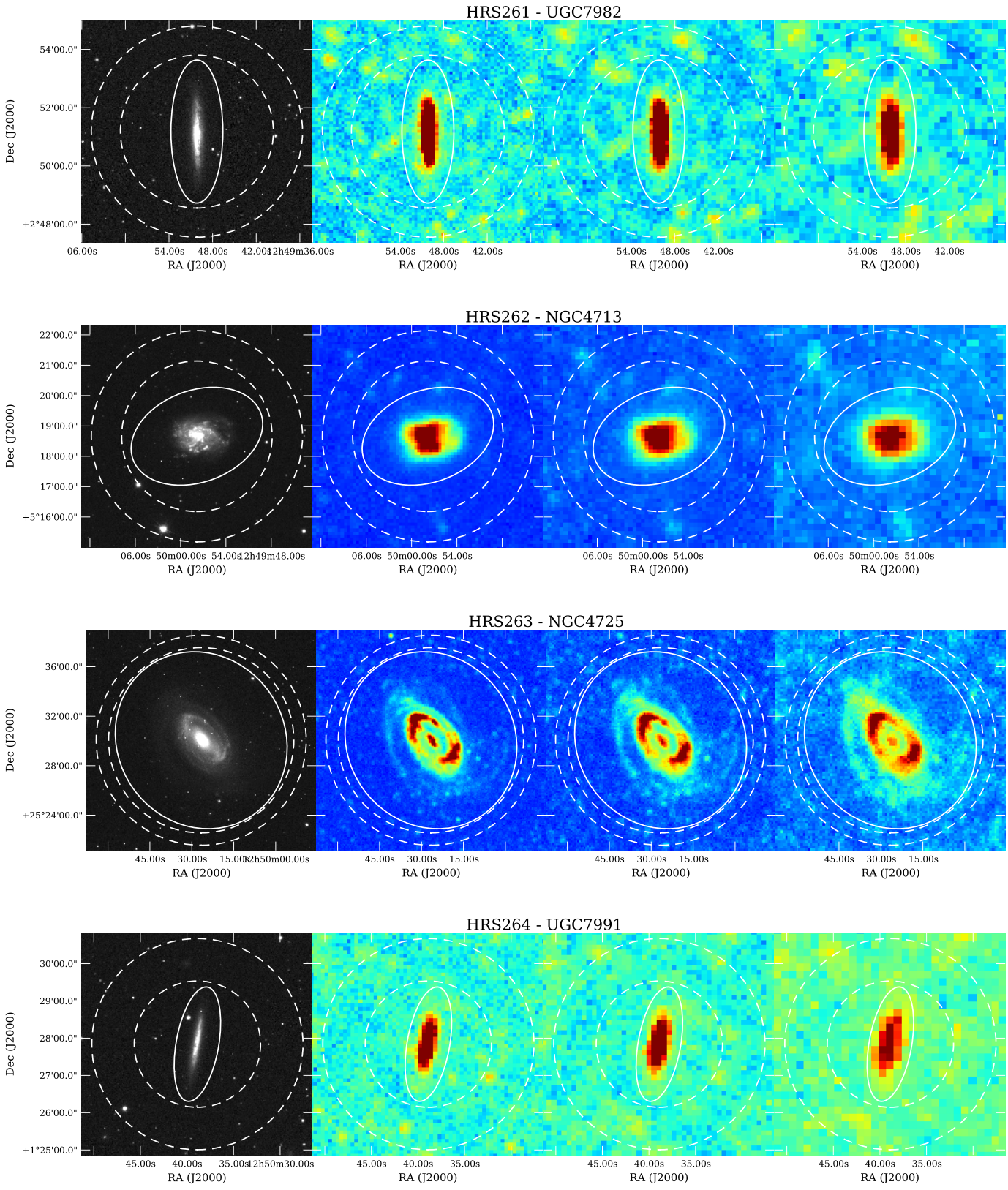

Fig. A.1: Images of the HRS galaxies. From left to right: SDSS *r'* band image, 250, 350, and 500 μm *Herschel* images. The aperture used for the photometry is indicated by the solid line and the annulus, where the background is estimated, is indicated in dashed lines.

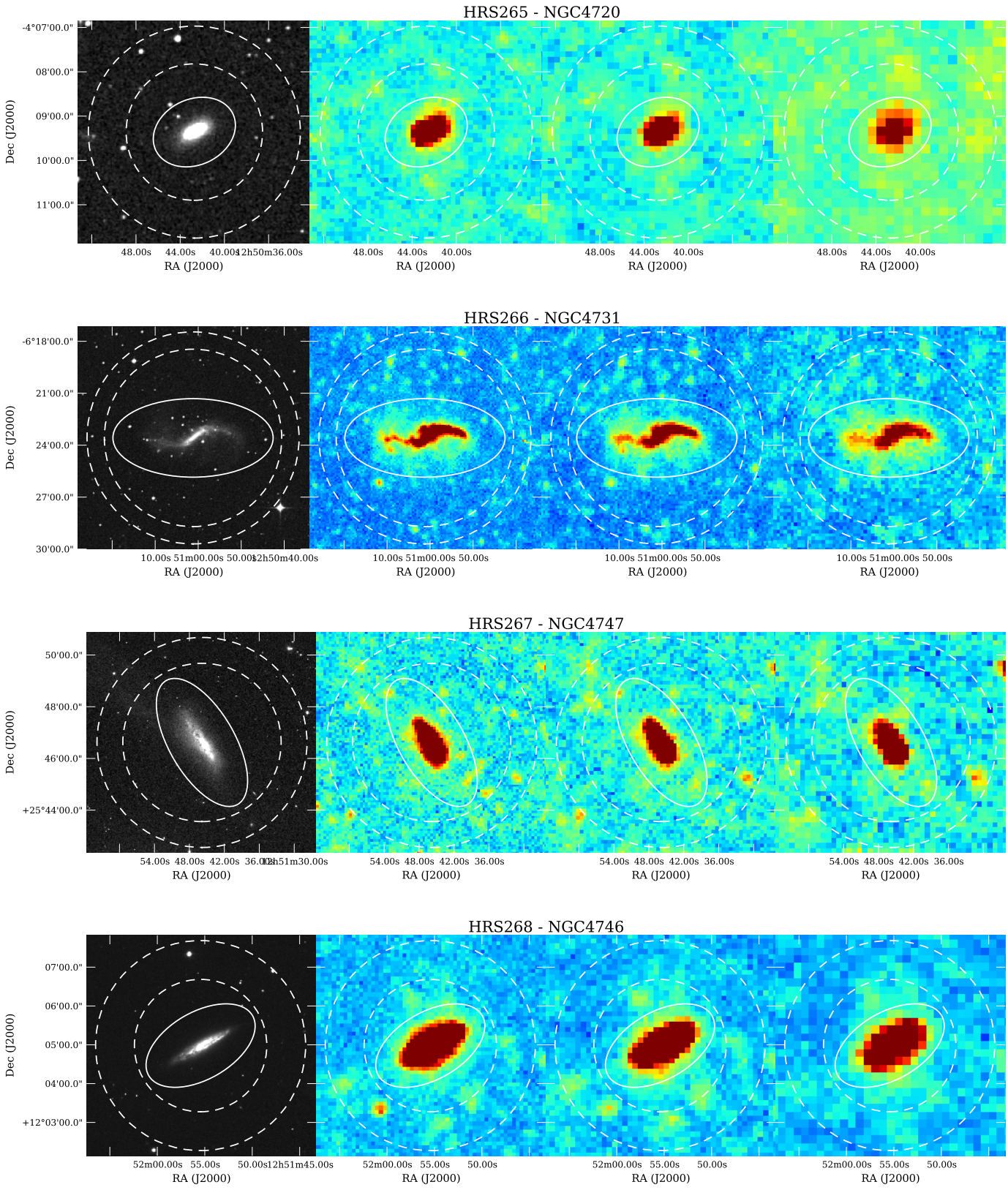

Fig. A.1: Images of the HRS galaxies. From left to right: SDSS *r'* band image, 250, 350, and 500 μm *Herschel* images. The aperture used for the photometry is indicated by the solid line and the annulus, where the background is estimated, is indicated in dashed lines.

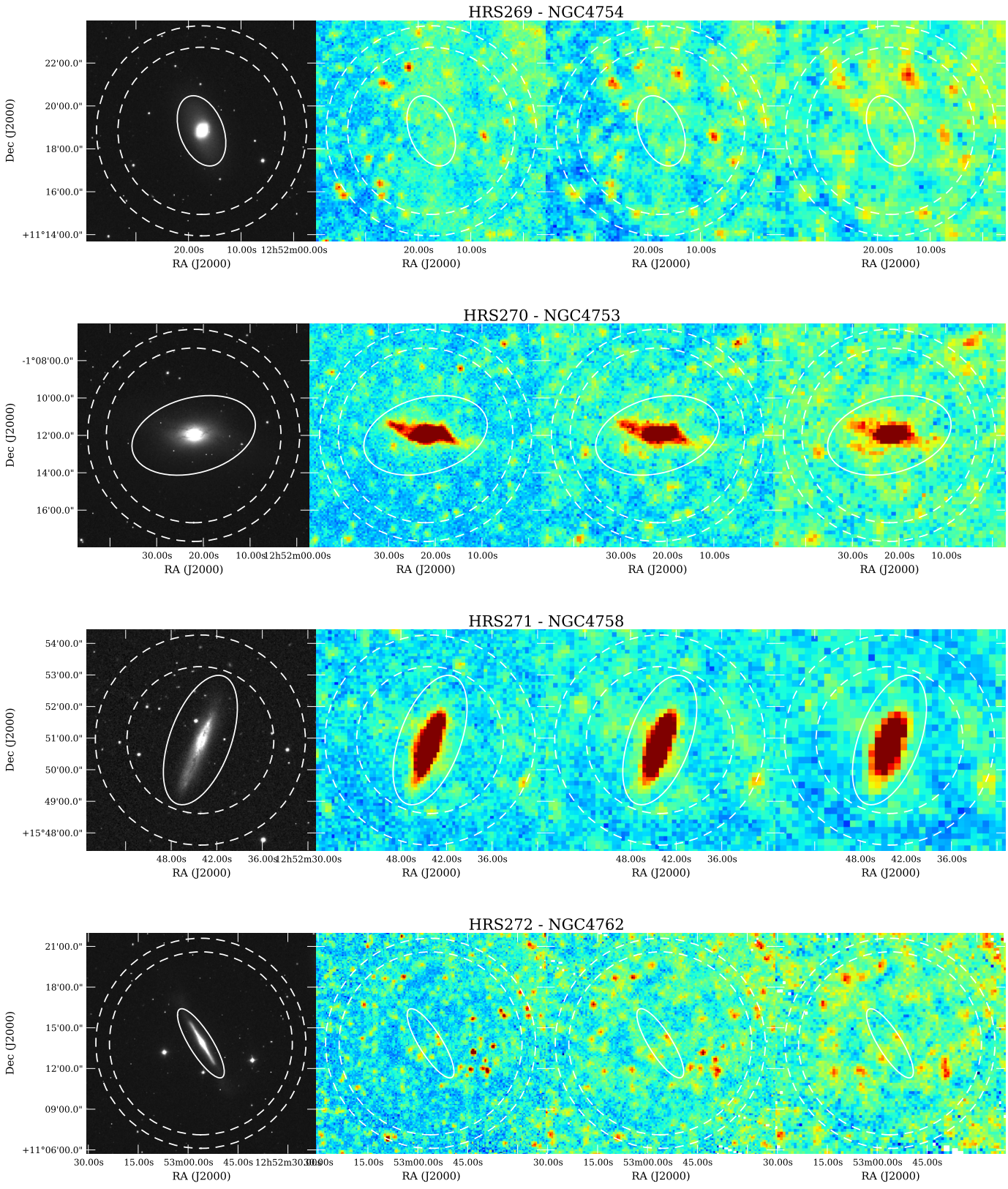

Fig. A.1: Images of the HRS galaxies. From left to right: SDSS *r'* band image, 250, 350, and 500 μm *Herschel* images. The aperture used for the photometry is indicated by the solid line and the annulus, where the background is estimated, is indicated in dashed lines.

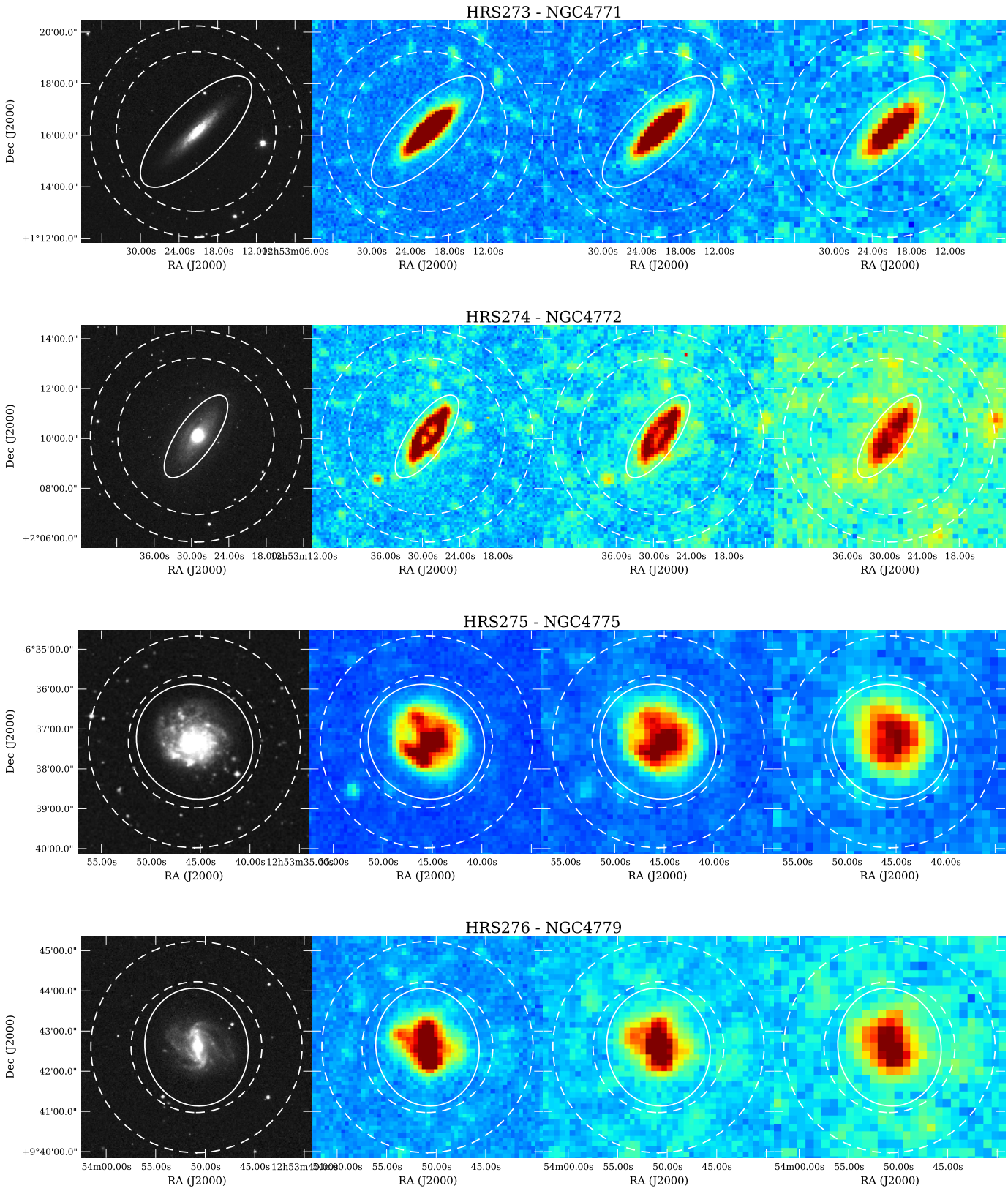

Fig. A.1: Images of the HRS galaxies. From left to right: SDSS *r'* band image, 250, 350, and 500 μm *Herschel* images. The aperture used for the photometry is indicated by the solid line and the annulus, where the background is estimated, is indicated in dashed lines.

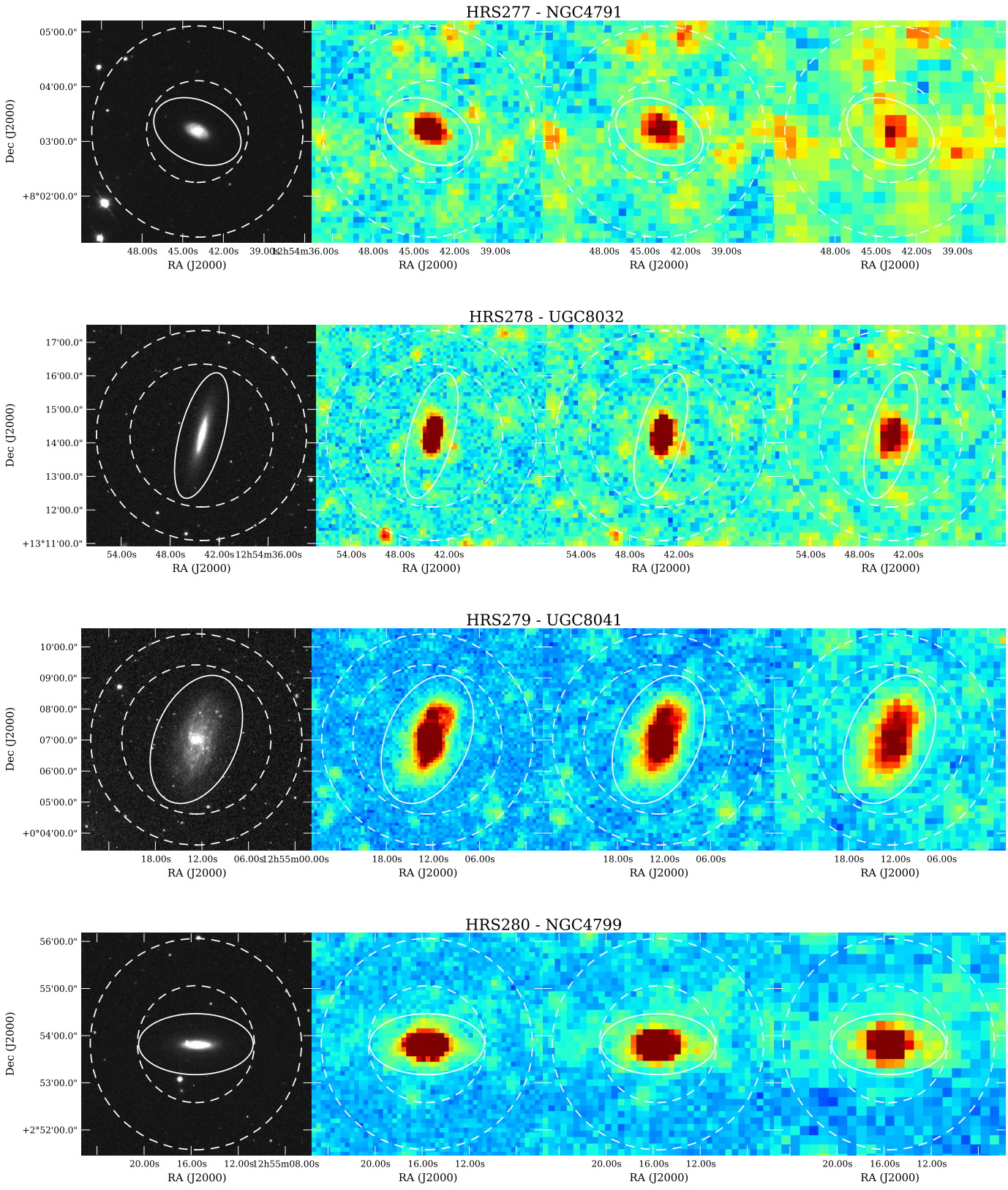

Fig. A.1: Images of the HRS galaxies. From left to right: SDSS *r'* band image, 250, 350, and 500 μm *Herschel* images. The aperture used for the photometry is indicated by the solid line and the annulus, where the background is estimated, is indicated in dashed lines.

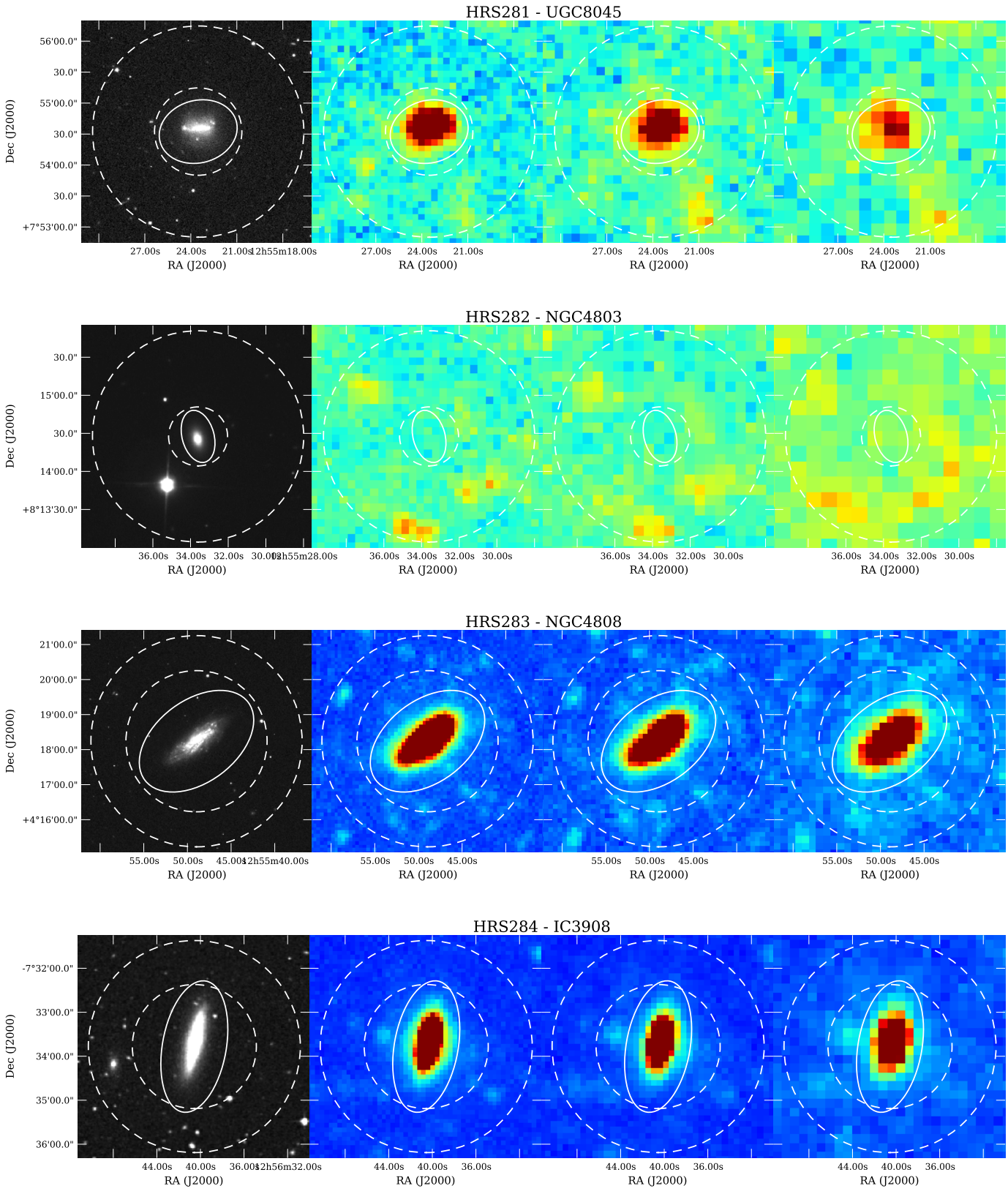

Fig. A.1: Images of the HRS galaxies. From left to right: SDSS *r'* band image, 250, 350, and 500 μm *Herschel* images. The aperture used for the photometry is indicated by the solid line and the annulus, where the background is estimated, is indicated in dashed lines.

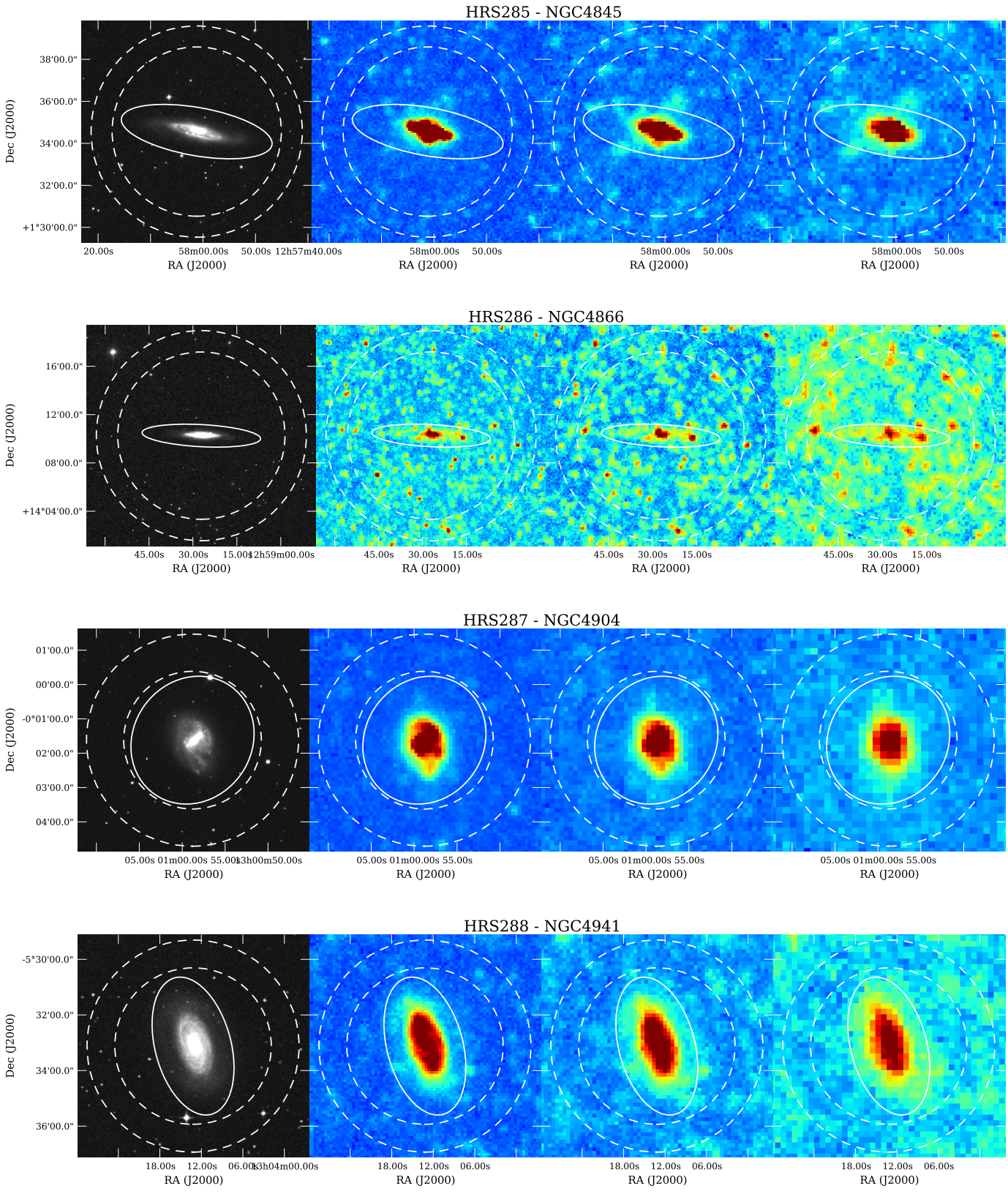

Fig. A.1: Images of the HRS galaxies. From left to right: SDSS *r'* band image, 250, 350, and 500 μm *Herschel* images. The aperture used for the photometry is indicated by the solid line and the annulus, where the background is estimated, is indicated in dashed lines.

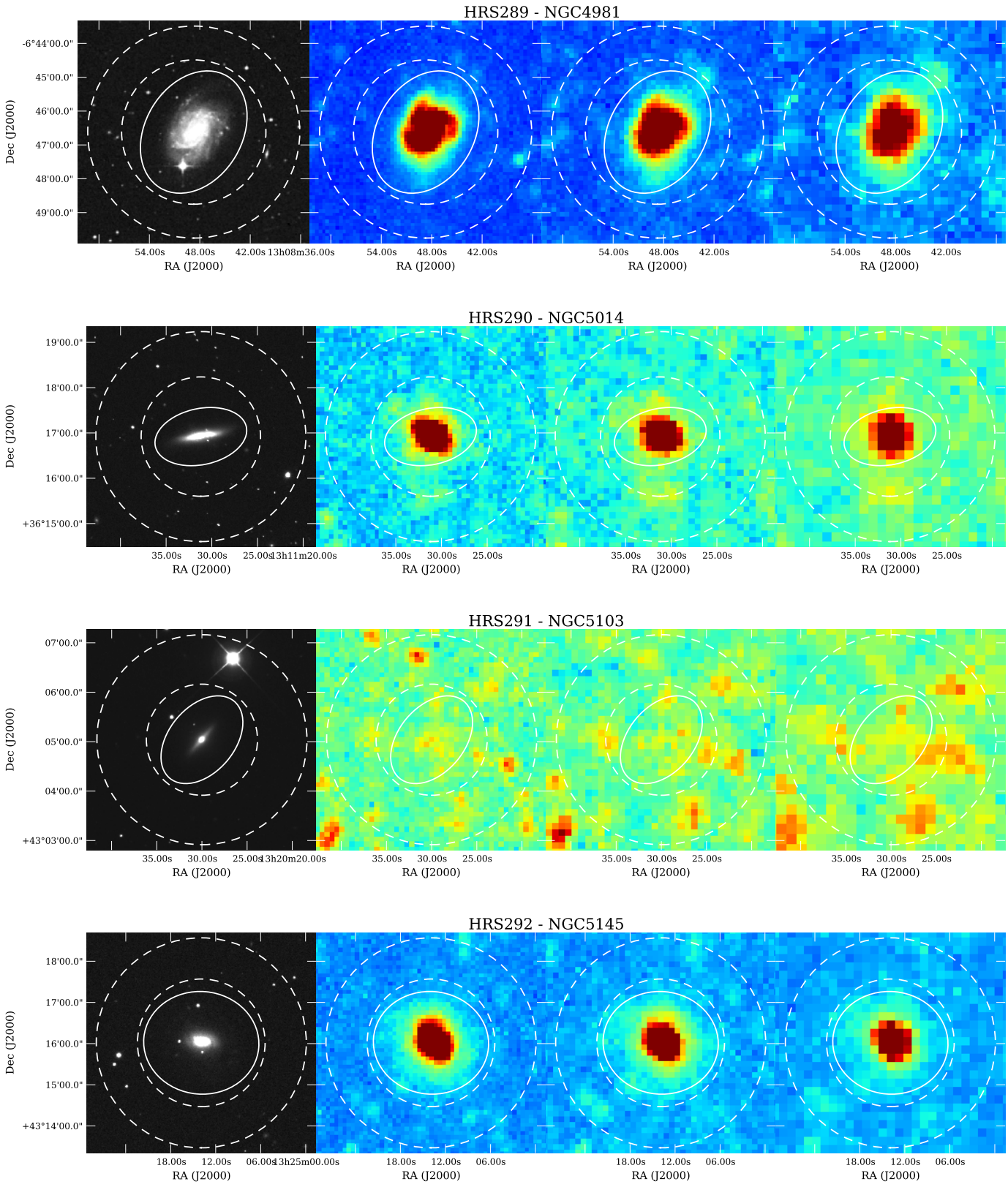

Fig. A.1: Images of the HRS galaxies. From left to right: SDSS *r'* band image, 250, 350, and 500 μm *Herschel* images. The aperture used for the photometry is indicated by the solid line and the annulus, where the background is estimated, is indicated in dashed lines.

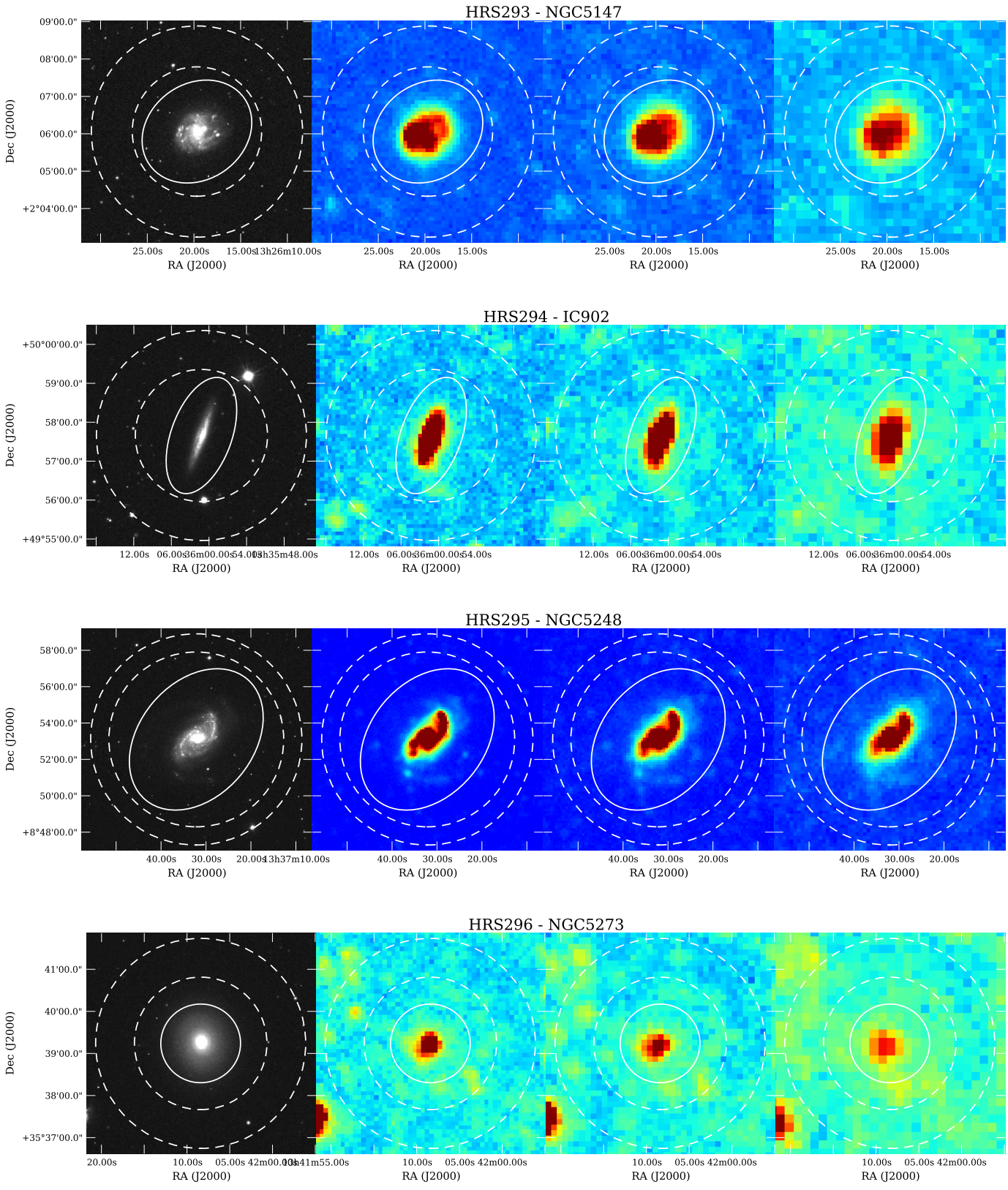

Fig. A.1: Images of the HRS galaxies. From left to right: SDSS *r'* band image, 250, 350, and 500 μm *Herschel* images. The aperture used for the photometry is indicated by the solid line and the annulus, where the background is estimated, is indicated in dashed lines.

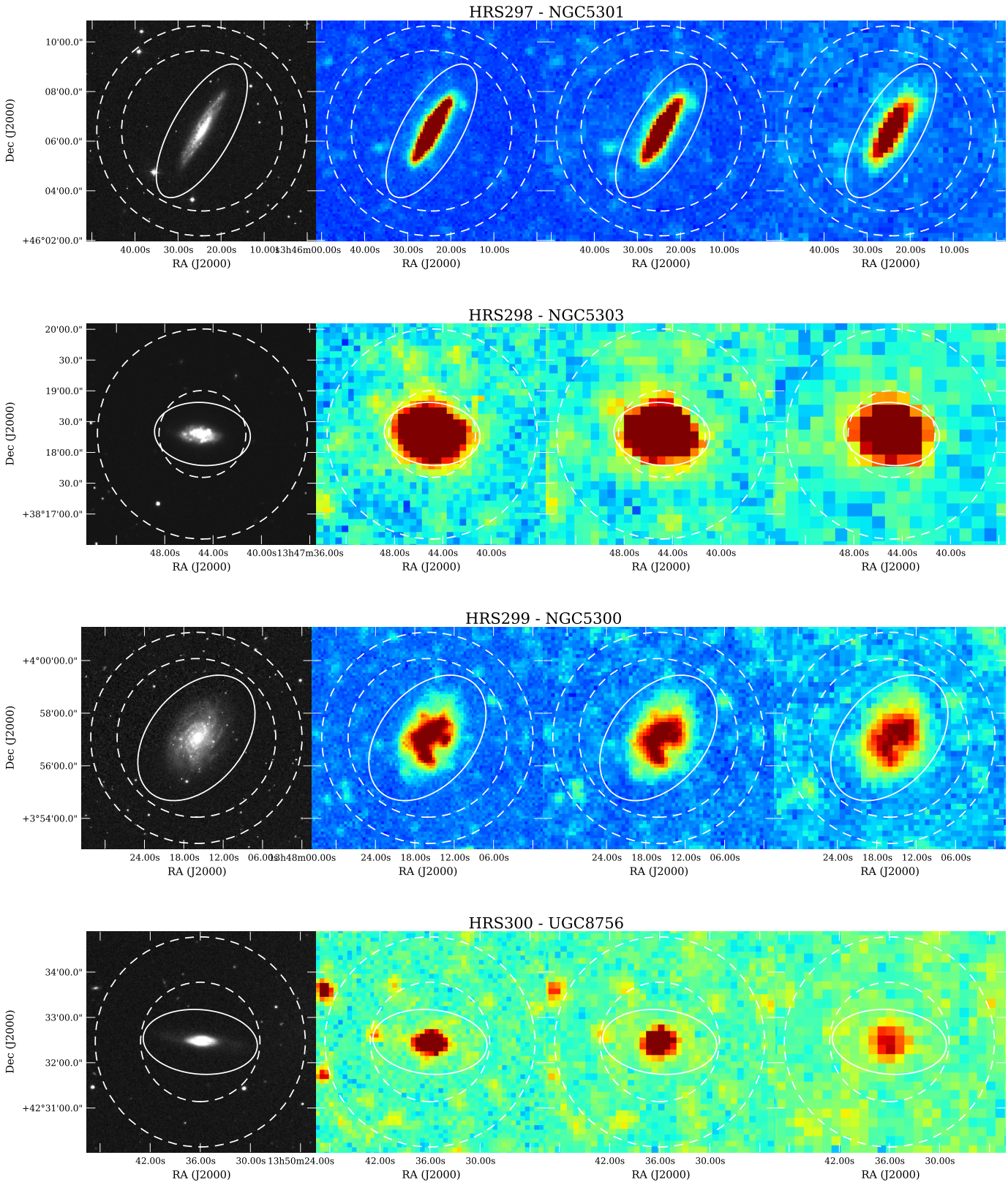

Fig. A.1: Images of the HRS galaxies. From left to right: SDSS *r'* band image, 250, 350, and 500 μm *Herschel* images. The aperture used for the photometry is indicated by the solid line and the annulus, where the background is estimated, is indicated in dashed lines.

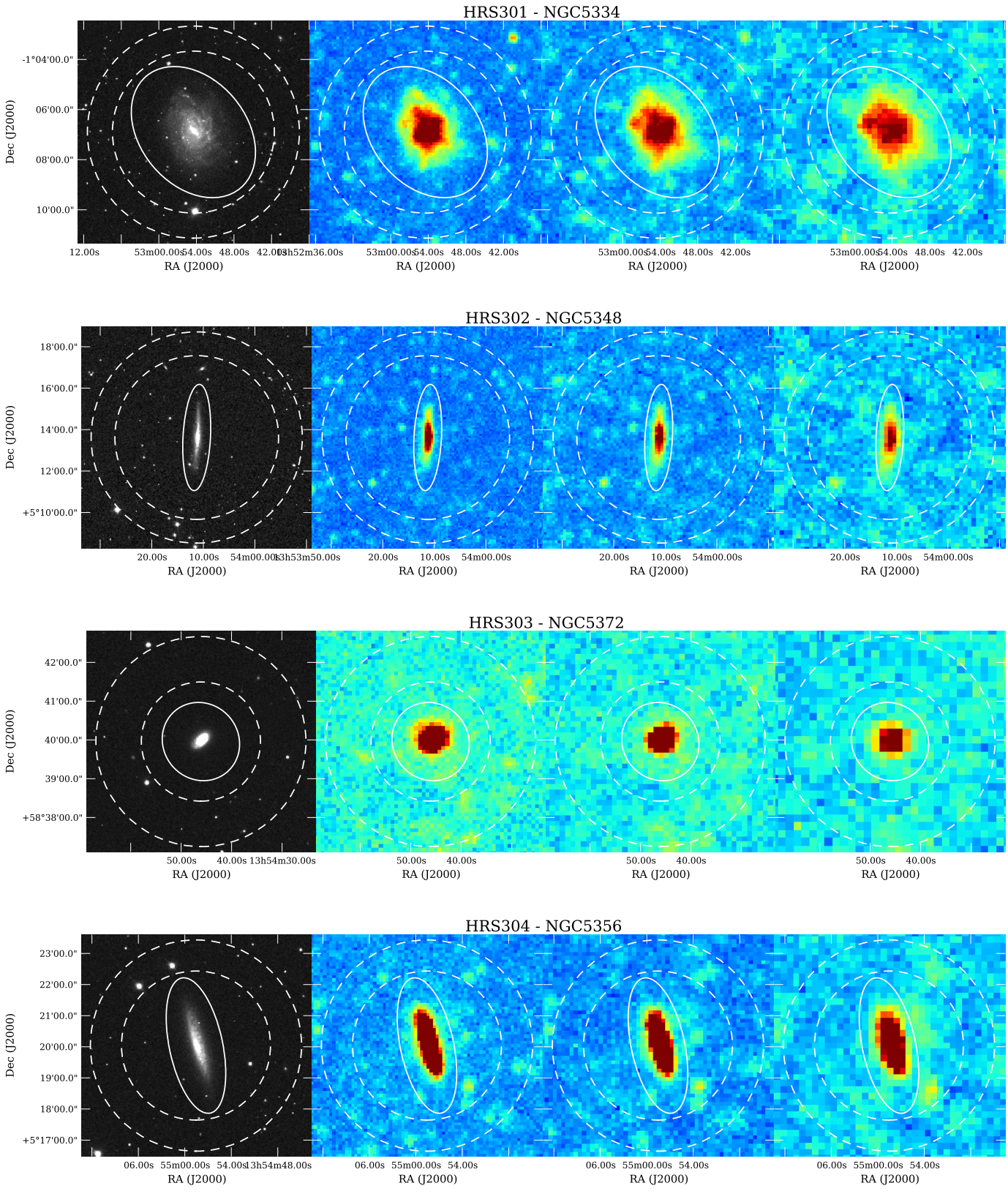

Fig. A.1: Images of the HRS galaxies. From left to right: SDSS *r'* band image, 250, 350, and 500 μm *Herschel* images. The aperture used for the photometry is indicated by the solid line and the annulus, where the background is estimated, is indicated in dashed lines.

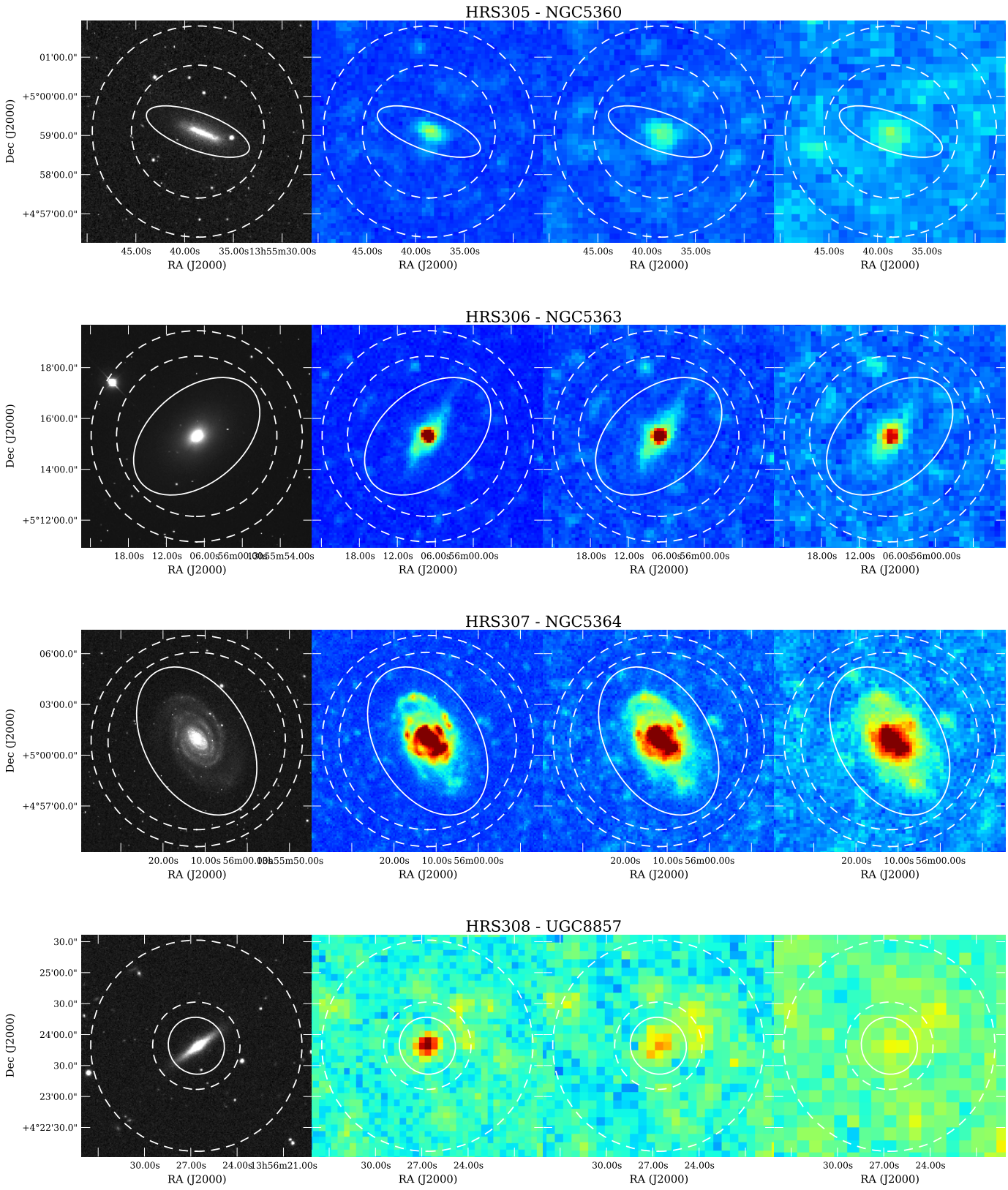

Fig. A.1: Images of the HRS galaxies. From left to right: SDSS *r'* band image, 250, 350, and 500 μm *Herschel* images. The aperture used for the photometry is indicated by the solid line and the annulus, where the background is estimated, is indicated in dashed lines.

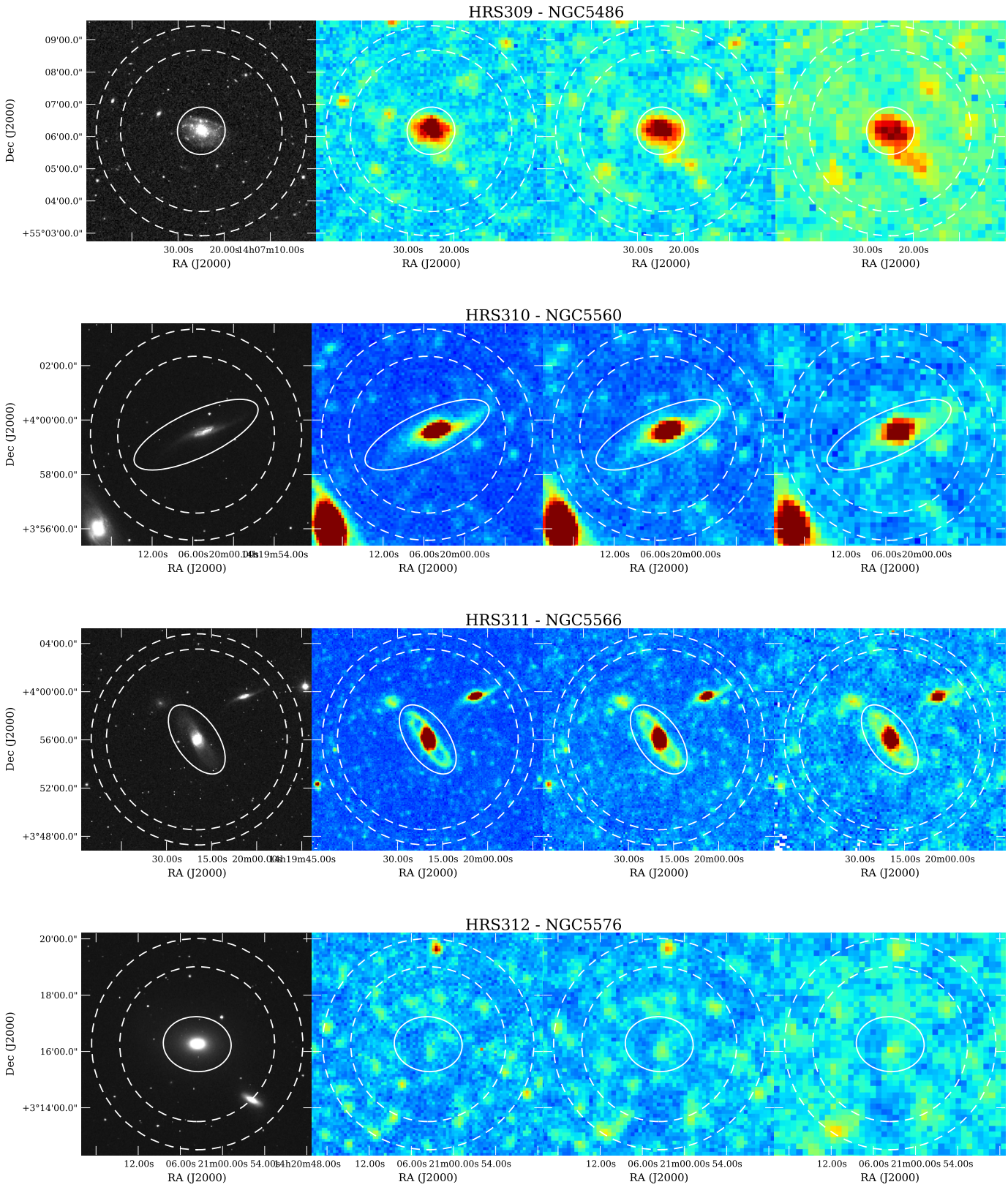

Fig. A.1: Images of the HRS galaxies. From left to right: SDSS *r'* band image, 250, 350, and 500 μm *Herschel* images. The aperture used for the photometry is indicated by the solid line and the annulus, where the background is estimated, is indicated in dashed lines.

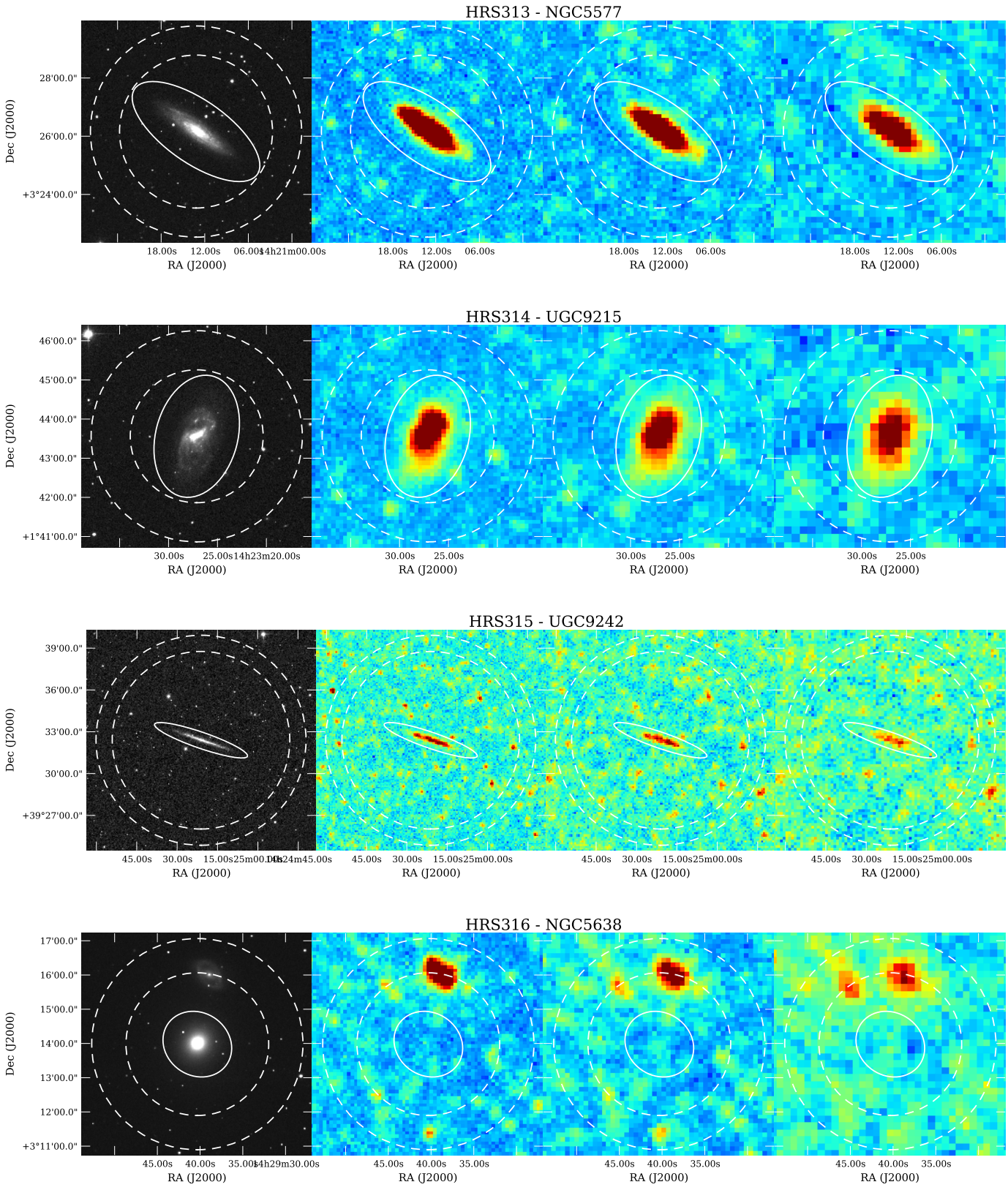

Fig. A.1: Images of the HRS galaxies. From left to right: SDSS *r'* band image, 250, 350, and 500 μm *Herschel* images. The aperture used for the photometry is indicated by the solid line and the annulus, where the background is estimated, is indicated in dashed lines.

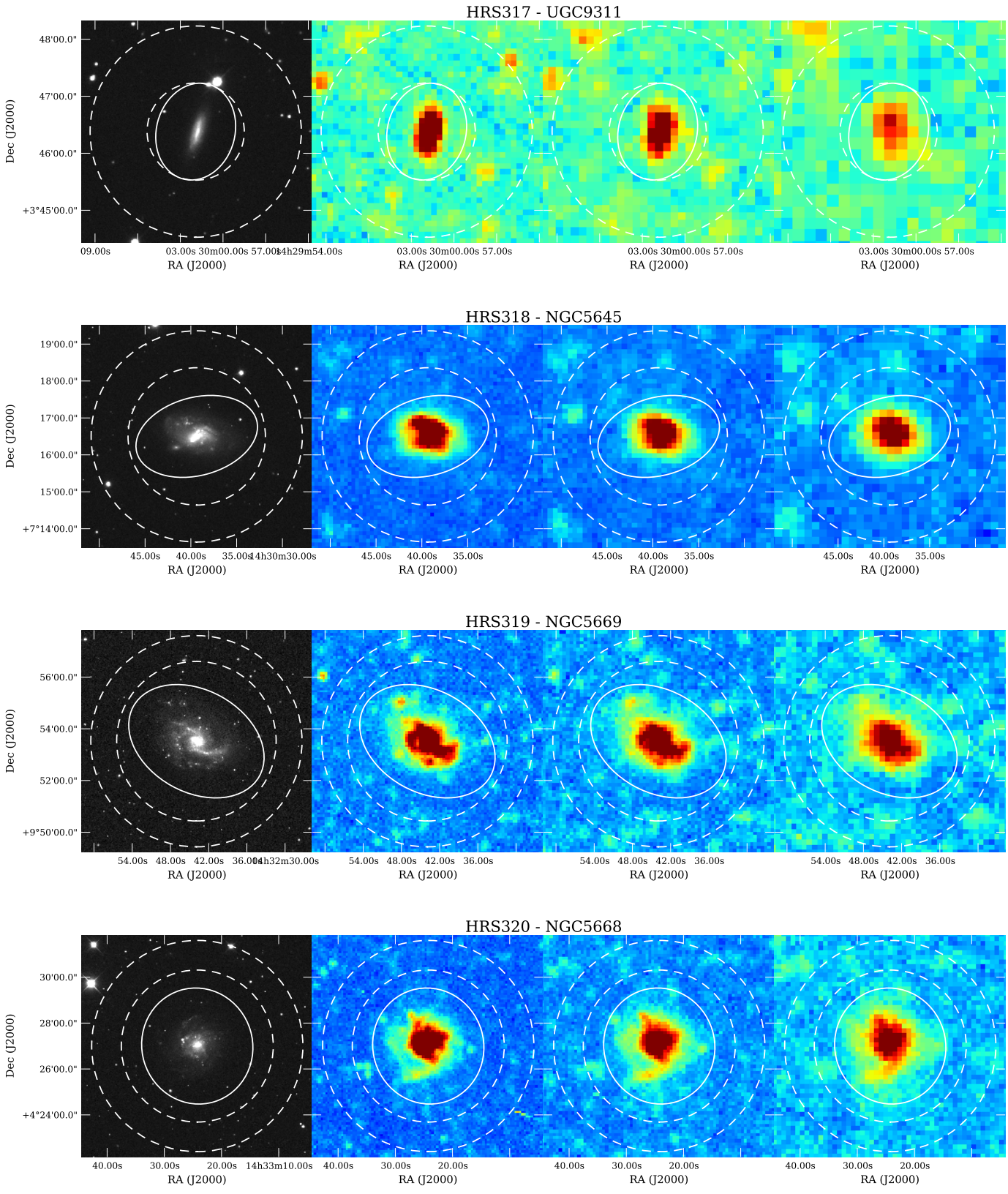

Fig. A.1: Images of the HRS galaxies. From left to right: SDSS *r'* band image, 250, 350, and 500 μm *Herschel* images. The aperture used for the photometry is indicated by the solid line and the annulus, where the background is estimated, is indicated in dashed lines.

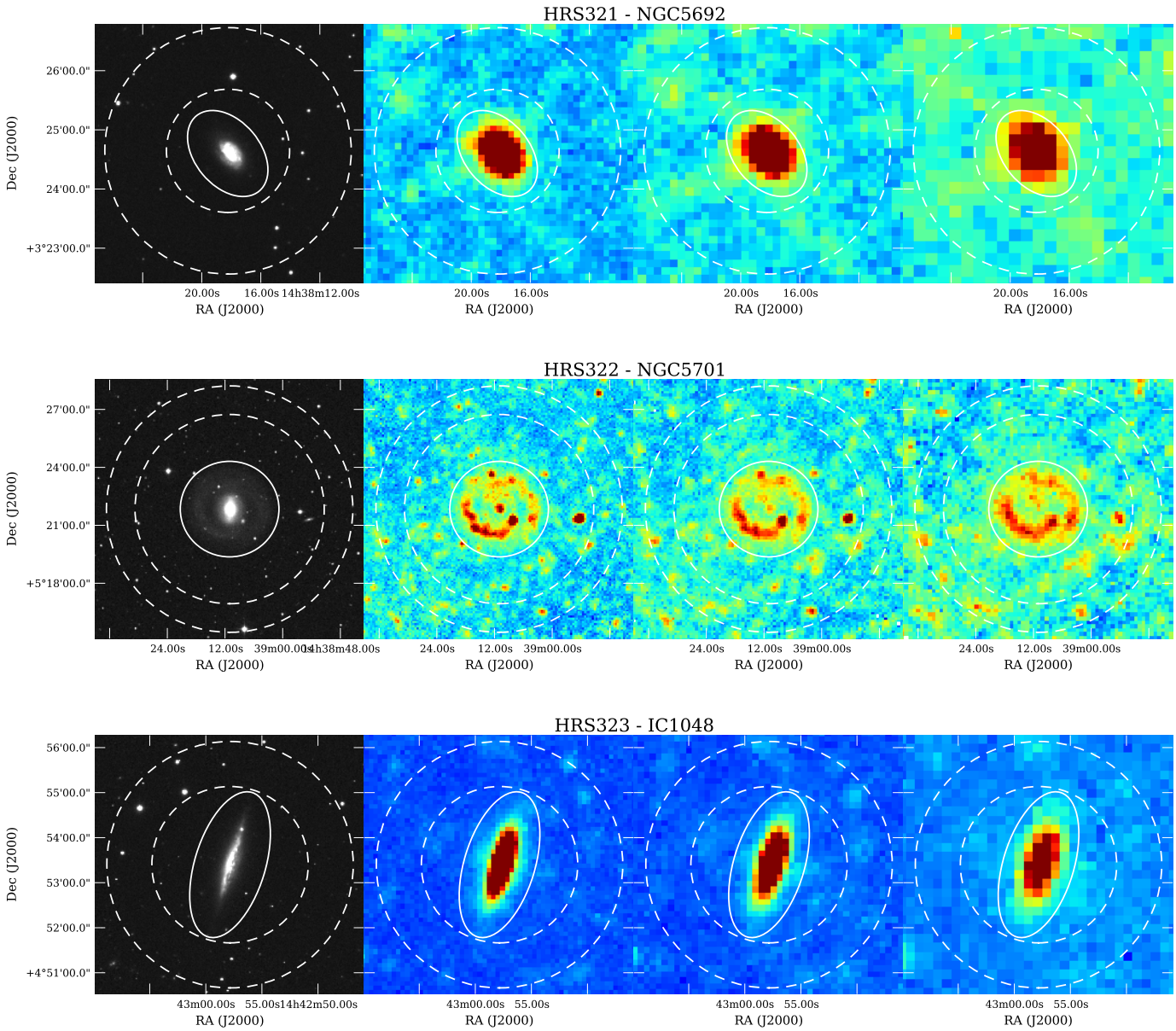

Fig. A.1: Images of the HRS galaxies. From left to right: SDSS *r'* band image, 250, 350, and 500 μm *Herschel* images. The aperture used for the photometry is indicated by the solid line and the annulus, where the background is estimated, is indicated in dashed lines.

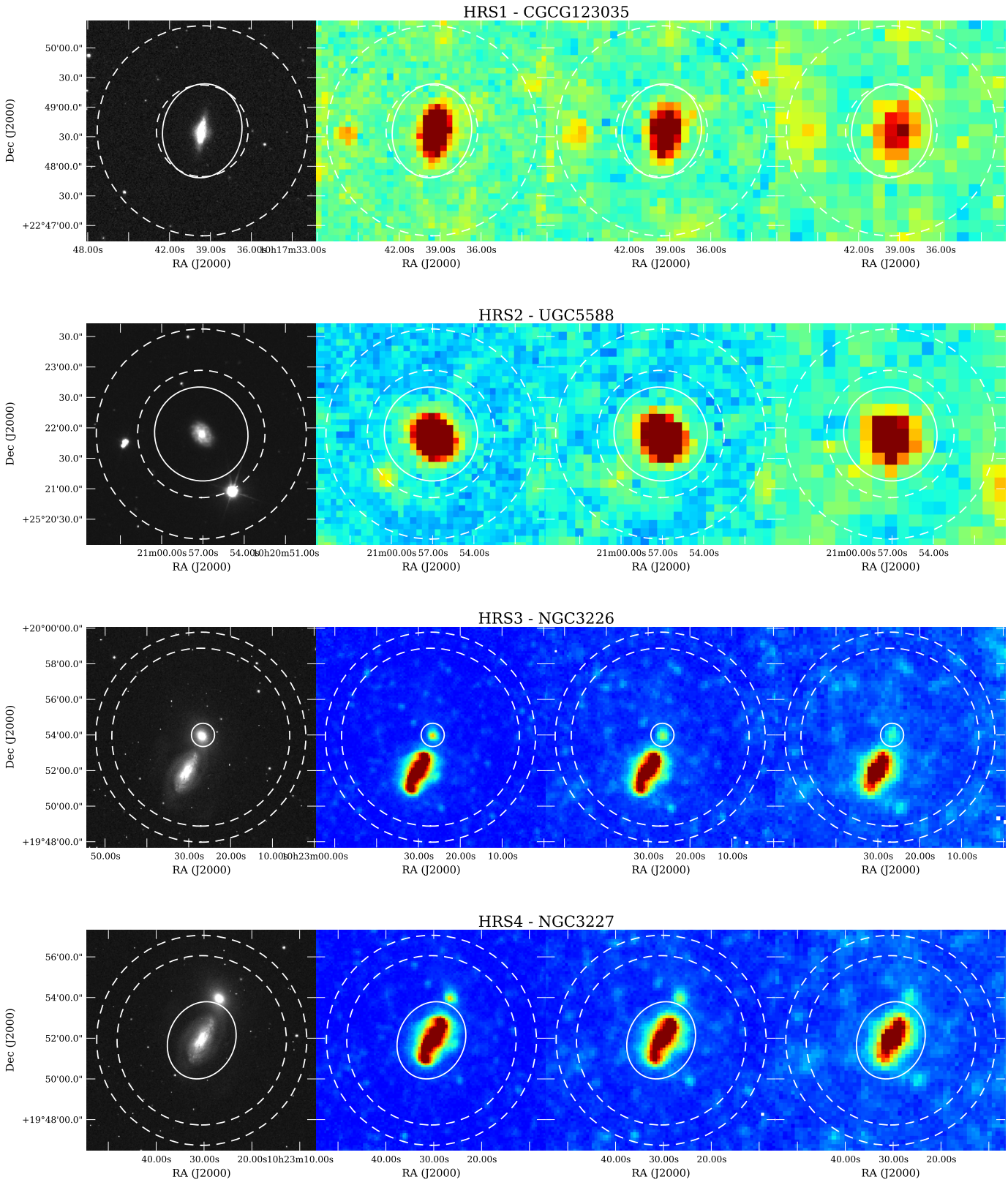

Fig. A.2: Images of 4 HRS galaxies. From left to right: SDSS ***r'* band** image, 250, 350, and 500 μm *Herschel* images. The aperture used for the photometry is indicated by the solid line and the annulus, where the background is estimated, is indicated in dashed lines. The images of all the HRS galaxies are available on Hedam: http://hedam/HRS/index.php.